

# Search for neutral MSSM Higgs bosons in the fully hadronic di-tau decay channel with the ATLAS detector

DISSERTATION

zur Erlangung des akademischen Grades

Doctor rerum naturalium  
(Dr. rer. nat.)

vorgelegt

der Fakultät Mathematik und Naturwissenschaften  
der Technischen Universität Dresden

von

Dipl. Phys. Sebastian Wahrmund  
geboren am 19.06.1986 in Aschersleben



1. Gutachter: Prof. Dr. Arno Straessner
2. Gutachter: Prof. Dr. Stan Lai

Eingereicht am: 31.01.2017

Verteidigt am: 23.06.2017

## Abstract

The search for additional heavy neutral Higgs bosons predicted in Minimal Supersymmetric Extensions of the Standard Model is presented, using the direct decay channel into two tau leptons which themselves decay hadronically. The study is based on proton-proton collisions recorded in 2011 at a center-of-mass energy of 7 TeV with the ATLAS detector at the Large Hadron Collider at CERN. With a sample size corresponding to an integrated luminosity of  $4.5\text{ fb}^{-1}$ , no significant excess above the expected Standard Model background prediction is observed and  $CL_S$  exclusion limits at a 95 % confidence level are evaluated for values of the CP-odd Higgs boson mass  $m_A$  between 140 GeV to 800 GeV within the context of the  $m_h^{\text{max}}$  and  $m_h^{\text{mod}\pm}$  benchmark scenarios. The results are combined with searches for neutral Higgs bosons performed using proton-proton collisions at a center-of-mass energy of 8 TeV recorded with the ATLAS detector in 2012, with a corresponding integrated luminosity of  $19.5\text{ fb}^{-1}$ . The combination allowed an improvement of the exclusion limit at the order of 1 to 3 units in  $\tan\beta$ . Within the context of this study, the structure of additional interactions during a single proton-proton collision (the “underlying event”) in di-jet final states is analyzed using collision data at a center-of-mass energy of 7 TeV recorded with the ATLAS detector in 2010, with a corresponding integrated luminosity of  $37\text{ pb}^{-1}$ . The contribution of the underlying event is measured up to an energy scale of 800 GeV and compared to the predictions of various models. For several models, significant deviations compared to the measurements are found and the results are provided for the optimization of simulation algorithms.





## Kurzdarstellung

Im Rahmen dieser Arbeit wird die Suche nach zusätzlichen schweren und elektrisch neutralen Higgs-Bosonen vorgestellt, wie sie in Minimalen Supersymmetrischen Erweiterungen des Standardmodells der Teilchenphysik vorhergesagt werden. Dabei wurde der Zerfalls der Higgs-Bosonen in zwei Tau-Leptonen untersucht, wobei beide Tau-Leptonen selber in weitere Hadronen zerfallen. Die Studie basiert auf Proton-Proton-Streuereignissen, welche bei einer Schwerpunktsenergie von 7 TeV am ATLAS-Detektor, welcher sich am *Large Hadron Collider* des Kernforschungszentrums CERN befindet, im Jahr 2011 aufgezeichnet wurden. Bei einer integrierten Luminosität von  $4.5 \text{ fb}^{-1}$  konnte kein signifikanter Überschuss an Ereignissen im Vergleich zur Vorhersage des Standardmodells festgestellt werden. Stattdessen wurden  $CL_S$  Ausschlussgrenzen für das  $m_h^{\text{max}}$  sowie das  $m_h^{\text{mod}\pm}$  Szenario bei einem Vertrauensintervall von 95 % für Massen des CP-ungeraden Higgs bosons,  $m_A$ , innerhalb von 140 GeV bis 800 GeV bestimmt. Zusätzlich wurde eine Kombination mit Messergebnissen durchgeführt, die im Jahr 2012 bei Proton-Proton-Streuereignissen mit einer Schwerpunktsenergie von 8 TeV vom ATLAS-Detektor aufgezeichnet wurden. Die integrierte Luminosität der zusätzlichen Daten belief sich auf  $19.5 \text{ fb}^{-1}$ . Durch die Kombination konnte das Ausschlusslimit innerhalb des betrachteten Intervals um 1 bis 3 Einheiten in  $\tan \beta$  verbessert werden. Im Rahmen der Studie wurden außerdem zusätzliche Interaktionen während eines Proton-Proton-Streuereignisses (dem “underlying event”) mit zwei Jets im Endzustand untersucht. Dazu wurden Messdaten mit einer integrierten Luminosität von  $37 \text{ pb}^{-1}$  verwendet die im Jahr 2010 mit dem ATLAS-Detektor aufgezeichnet wurden. Die Beträge aus dem “underlying event” konnten dabei bis zu Energieskalen von 800 GeV vermessen, entfaltet und im Anschluss mit mehreren Vorhersagen aus Monte-Carlo-Modellen verglichen werden. Dabei wurden für einige Modelle teilweise signifikante Abweichungen festgestellt und die erhobenen Messdaten wurden für die Optimierung von Simulationsalgorithmen bereitgestellt.



# Contents

<b>Abstract</b>	<b>v</b>
<b>1 Introduction</b>	<b>1</b>
1.1 Nomenclature and Unit Systems . . . . .	3
<b>2 Standard Model of Particle Physics and Beyond</b>	<b>5</b>
2.1 Standard Model of Particle Physics . . . . .	5
2.1.1 Overview of the Standard Model of Particle Physics . . . . .	5
2.1.2 Spontaneous Breaking of the Electroweak $SU(2)_L \times U(1)_Y$ Symmetry . . .	7
2.1.3 Confinement Property of the Strong Interaction . . . . .	11
2.1.4 Simulation of High-Energy Interactions using Monte Carlo Techniques . .	12
2.2 Minimal Supersymmetric Extension of the Standard Model . . . . .	15
2.2.1 Supersymmetric Extension of the Standard Model . . . . .	15
2.2.2 Introduction to the MSSM . . . . .	17
2.2.3 Higgs Sector of the MSSM . . . . .	19
2.2.4 Production of heavy neutral MSSM Higgs bosons at a hadron collider . .	23
2.2.5 Decay of heavy neutral MSSM Higgs bosons . . . . .	28
2.2.6 MSSM Benchmark Scenarios . . . . .	30
<b>3 The ATLAS experiment at the Large Hadron Collider</b>	<b>35</b>
3.1 The Large Hadron Collider . . . . .	35
3.2 The ATLAS experiment . . . . .	39
3.2.1 Coordinate System . . . . .	40
3.2.2 Inner Detector . . . . .	41
3.2.3 Calorimeter System . . . . .	42
3.2.4 Muon Spectrometer . . . . .	45
3.3 LHC and ATLAS performance during Run 1 . . . . .	48
3.3.1 Data taking during the years 2010 to 2012 at the ATLAS experiment . .	48
<b>4 Particle Reconstruction and Identification</b>	<b>51</b>
4.1 Track and Vertex Reconstruction . . . . .	52
4.2 Reconstruction of Energy Deposits in the Calorimeter . . . . .	53
4.3 Electron Reconstruction and Identification . . . . .	54
4.3.1 Reconstruction and Calibration . . . . .	54
4.3.2 Identification . . . . .	54
4.4 Muon Reconstruction and Identification . . . . .	56
4.5 Jet Reconstruction and Calibration . . . . .	58
4.5.1 Jet Calibration . . . . .	59

4.5.2	Jet Resolution . . . . .	60
4.5.3	Jet Vertex Fraction . . . . .	60
4.5.4	Jet cleaning . . . . .	61
4.6	Tau Reconstruction and Identification . . . . .	64
4.6.1	Reconstruction of hadronically decaying tau leptons . . . . .	66
4.6.2	Energy calibration of hadronically decaying tau leptons . . . . .	66
4.6.3	Distinguishing Tau Leptons and Electrons . . . . .	67
4.6.4	Tau discrimination against QCD-induced jets using early 2012 data . . . .	68
4.6.5	Tau discrimination against QCD-induced jets in 2011 . . . . .	75
4.7	Missing Transverse Momentum and $\sum E_T$ . . . . .	79
4.8	Trigger . . . . .	81
4.8.1	Minimum Bias Trigger . . . . .	83
4.8.2	Jet Trigger . . . . .	83
4.8.3	Muon Trigger . . . . .	84
4.8.4	Tau Trigger . . . . .	86
<b>5</b>	<b>Measurement of the Underlying Event</b>	<b>89</b>
5.1	Underlying Event Analysis . . . . .	92
5.1.1	General Analysis Strategy . . . . .	93
5.1.2	Observables . . . . .	94
5.1.3	Data & Monte Carlo Event Samples . . . . .	98
5.1.4	Event Selection . . . . .	99
5.2	Correction & Unfolding . . . . .	104
5.2.1	Track Observable Corrections . . . . .	105
5.2.2	Iterative Bayesian Unfolding . . . . .	106
5.2.3	Non-collision Background and Merged Vertices . . . . .	110
5.2.4	Systematic Uncertainties . . . . .	116
5.3	Underlying Event Results . . . . .	122
5.3.1	1D Observable Distributions . . . . .	122
5.3.2	Profile Observable Distributions as a function of $p_T^{\text{lead}}$ and $N_{\text{ch}}$ . . . . .	123
5.3.3	Summary . . . . .	132
5.3.4	Comparison with other underlying event measurements . . . . .	133
<b>6</b>	<b>Search for neutral MSSM Higgs bosons</b>	<b>135</b>
6.1	Analysis Overview . . . . .	137
6.1.1	Signal Process . . . . .	137
6.1.2	Background Processes . . . . .	140
6.1.3	Data Sample . . . . .	145
6.1.4	Object Selection . . . . .	145
6.1.5	Event Selection . . . . .	147
6.1.6	Total Transverse Mass . . . . .	150
6.2	Background Estimation . . . . .	151
6.2.1	Pile-up Reweighting . . . . .	152
6.2.2	Trigger Corrections . . . . .	152
6.2.3	Tau Lepton Corrections . . . . .	153

6.2.4	Tau Fakes in Non QCD Multi-jet Background . . . . .	153
6.2.5	QCD Multi-jet Estimation in the Di-Tau Trigger Region . . . . .	154
6.2.6	QCD Multi-jet Estimation in the Single-Tau Trigger Region . . . . .	160
6.3	Measurement of the Tau Misidentification Efficiency . . . . .	164
6.3.1	Overview of the Misidentification Efficiency Measurement . . . . .	164
6.3.2	Results of the Misidentification Efficiency Measurement . . . . .	167
6.4	Measurement of the Tau Identification Transfer Factor . . . . .	177
6.4.1	Overview of the Transfer Factor Measurement . . . . .	177
6.4.2	Results of the Transfer Factor Measurement . . . . .	178
6.5	Validation of the $Z/\gamma^* \rightarrow \tau\tau$ Modeling . . . . .	181
6.6	Systematic Uncertainties . . . . .	184
6.6.1	Determination of the Modeling Uncertainties . . . . .	186
6.7	Measurement Results . . . . .	191
6.8	Limit Setting . . . . .	198
6.8.1	Theoretical Foundation . . . . .	198
6.8.2	Exclusion Limits for the 2011 Data Set . . . . .	206
6.8.3	Exclusion Limits for the combined 2011 and 2012 Dataset . . . . .	215
6.9	Summary and Outlook . . . . .	217
<b>A</b>	<b>Appendix</b>	<b>219</b>
A.1	Standard Model of Particle Physics and MSSM . . . . .	219
A.1.1	MSSM Higgs Boson Sector . . . . .	219
A.2	Reconstruction and Identification . . . . .	220
A.2.1	Tau Identification Against QCD-induced Jets - Observables . . . . .	220
A.3	Underlying Event . . . . .	222
A.3.1	Merged Vertex Effect . . . . .	222
A.3.2	Results for $\sum p_T/\delta\eta\delta\phi$ and $N_{ch}/\delta\eta\delta\phi$ in trans-max and trans-min region . . . . .	223
A.4	Search for neutral MSSM Higgs boson . . . . .	225
A.4.1	Cross Sections for neutral MSSM Higgs bosons . . . . .	225
A.4.2	Background Estimation . . . . .	226
A.4.3	Fail-identification rate for QCD Jets to Hadronic Tau Decays . . . . .	229
A.4.4	Validation of the $Z/\gamma^* \rightarrow \tau\tau$ Modeling . . . . .	232
A.4.5	Signal and Background Samples . . . . .	233
A.4.6	Exclusion Limits . . . . .	238
	<b>List of Figures</b>	<b>243</b>
	<b>List of Tables</b>	<b>247</b>
	<b>Bibliography</b>	<b>249</b>



# 1 Introduction

In the light of modern particle physics, the baryonic matter in the universe is composed of *elementary particles*, physical states which, according to present knowledge, do not contain any further substructure. The properties of these elementary particles and their interactions are the fundamental building blocks to describe the behavior of nature from sub-atomic scales all the way up to the large scales found in the universe.

This concept of atomism, the hypothesis that matter is constructed from fundamental particles which are not further divisible, can be dated back to the ancient Greek philosophers Leucippus and Democritus<sup>1</sup> but has been formulated and employed by other philosophers and scientist throughout the centuries. During the end of the 19th century, the first direct experimental evidence for elementary particles was established with the discovery of the electron by J.J. Thomson [1], who observed a ray of charged particles emitted from a heated cathode. From this point onwards, a series of experiments and discoveries during the 20th and 21th century deepened the understanding about the nature of elementary particles and lead to the modern picture of particle physics. Of significant impact was the development and improvement of particle accelerators and detectors, which allowed the initiation of interactions at sub-atomic length scales in a controlled environment and the study the underlying physics based on the out-coming particle spectra from the scattering process. During the early 20th century, E. Rutherford, H. Geiger and E. Marsden were able to show that the mass of an atom is concentrated in a *nucleus* surrounded by electrons<sup>2</sup>, by scattering an beam of alpha particles at a thin gold foil [2–4]. Further development in collider physics lead, among others, to the discovery of a large number of new (mostly) unstable particles<sup>3</sup>, the “particle zoo”, during the 1950th and 1960th, the discovery of the  $W^\pm$  and  $Z^0$  bosons, as mediators of the weak interaction, at CERN [5–8] during the 1960th and 1970th, the discovery of the top-quark at Tevatron [9] during the 1990th and the recent observation of a Higgs boson at the *Large Hadron Collider* [10,11] in 2012.

The theoretical framework used to described the interactions between elementary particles is known as the *Standard Model of Particle Physics*, containing all known fundamental matter particles and three of the four known fundamental interactions: the strong interaction, the weak interaction and the electro-magnetic interaction. Based in the concepts of quantum field theories, the Standard Model allows predictions for a wide range of interactions between elementary particles which are in excellent agreement with the observations [12]. However, despite the tremendous success of the Standard Model, it is widely assumed that the Standard Model doesn’t provide a full description of nature at quantum level, not in the sense that the Standard Model

---

<sup>1</sup>Which lived, according to the current state of research, during the 5th cent. BCE.

<sup>2</sup>In contrast to the atom model developed by Thomson, which assumed that the electrons of an atom are embedded inside a larger positive structure.

<sup>3</sup>Which are today understood as bound states of quarks and gluons, classified in *mesons* and *baryons*.

is wrong but rather an effective low energy approximation of a more fundamental theory, in a way similar like the theory of classical mechanics can be seen as an approximation of quantum mechanics at larger scales. These considerations are motivated by several open questions of the Standard Model, including: a missing theoretical description of the gravitational force at quantum level, a missing candidate for dark matter or an explanation for the observed mass hierarchy between the different elementary particles. During the last decades, many experiments have been performed to search for hints of new physics beyond the Standard Model but so far without a conclusive observation.

The aim for this study is the search for new physics using proton-proton collisions recorded the ATLAS experiment which is located at the *Large Hadron Collider* at CERN. The search is performed within the context of the *Minimal Supersymmetric Extension of the Standard Model*, which introduces an extended Higgs sector with two additional neutral Higgs bosons. The targeted final state is the decay of the Higgs bosons into two tau leptons, which themselves decay further into bundles of hadrons via the weak interaction. A central part for this study is the reconstruction and identification of the hadronically decaying tau leptons, which was part of the thesis work, as well as the understanding of the possible Standard Model background processes containing themselves two tau leptons or objects which are mis-classified as taus. All studies are performed using measurements recorded during the *Run 1* data taking period of the ATLAS experiment, covering the years 2010, 2011, 2012 and early 2013, at a center-of-mass energy of 7 TeV and 8 TeV. The search for an extended Higgs sector is primarily performed on the dataset recorded in 2011, employing new background estimation techniques which have been developed during *Run 1*. The obtained results are evaluated using statistical methods to allow an interpretation within the context of the Minimal Extension of the Standard Model and to draw conclusions on the agreement between the considered physical models and the observed data.

In addition, a measurement of the *underlying event*, which collectively terms additional interactions during a single proton-proton collision, has been performed using proton-proton collisions recorded with the ATLAS detector in the year 2010. These kinds of measurements allow to study the regime of strong interactions at low energies, which is up to date a field of intensive research because the strong interactions at low energies are typically not predictable via perturbation theory and need to be modeled using phenomenological approaches. Within this thesis, measurements of the underlying event in a di-jet environment are presented and the unfolded<sup>4</sup> distributions are compared with the predictions of various models. Measurements of the underlying event allow a deeper understanding in the structure of strong interactions and are, inter alia, used for the optimization of the simulation of proton-proton interactions.

The thesis is structured in the following way: Chapter 2 will give a brief introduction about the theoretical foundations of the Standard Model and the Minimal Supersymmetric Extension as well as the simulation of proton-proton interactions. Afterwards the experimental setup, including the Large Hadron Collider and the ATLAS experiment, are discussed in Chapter 3 as well as the reconstruction and identification of physical objects from the electrical signals provided by the ATLAS detector in Chapter 4. The next two parts contain the two main analyses:

---

<sup>4</sup>The measured results are corrected for smearing and resolution effects caused by the experimental setup.



starting with the underlying event analysis in Chapter 5, by presenting the event selection and correction procedures as well as the comparison with the underlying event prediction of various Monte Carlo event generators. Within the final Chapter 6, the search for new Higgs bosons is presented: comprising the event selection, various background estimations techniques and auxiliary measurements and the setting of exclusion limits for three different scenarios in the context the Minimal Supersymmetric Extension model.

## 1.1 Nomenclature and Unit Systems

Within the context of this thesis, all physical units are either expressed in terms of *natural units* or the *International System of Units* (SI) [13, 14]. The definition of the natural units systems follows the usual conventions in high energy physics by setting the *reduced*<sup>5</sup> *Planck constant*  $\hbar$ , the *speed of light*  $c$  and the *Boltzmann constant*  $k_B$  dimensionless and equal to one:

$$\hbar = c = k_B = 1. \quad (1.1)$$

In addition, the Lorentz-Heavyside unit system is deployed by setting:

$$\epsilon_0 = \mu_0 = 1, \quad (1.2)$$

where  $\epsilon_0$  and  $\mu_0$  represent the *permittivity and permeability of the free space*, respectively. Since these five constants are set dimensionless and equal to one, they are usually suppressed in equations. For example, the relationship between the energy,  $E$ , the momentum  $p$  and the rest mass,  $m_0$ , of a relativistic particle can be expressed in the form:

$$E^2 = p^2 c^2 + m_0^2 c^4 = p^2 + m_0^2. \quad (1.3)$$

The fundamental electric charge,  $e$ , follows the relation:

$$e = \sqrt{4\pi\alpha_e}, \quad (1.4)$$

where  $\alpha_e \approx 1/137$  represents the electromagnetic fine-structure constant. Quantities of energy, momentum or mass share the same units and are expressed in multiples of *electron volt* (eV):

$$[E] = [p] = [m] = 1 \text{ eV}. \quad (1.5)$$

Quantities of lengths or times also share the same units, which are usually expressed in multiples of  $\text{eV}^{-1}$  in the natural unit system. However, their usage is not so common as for energy related quantities and within this thesis all quantities related to lengths or times are expressed in SI units.

In quantum theory, spin components of elementary particles can be expressed in terms of  $\hbar$ :  $1/2 \cdot \hbar$ ,  $1 \cdot \hbar$ ,  $3/2 \cdot \hbar$ , etc. Similar to the energy relation,  $\hbar$  will be suppressed in the spin notation and (for example) a particle with a spin value of  $\hbar/2$  will be referred to as “spin  $1/2$ ” particle.

<sup>5</sup>The reduced Planck constant is defined as the Planck constant,  $h$ , divided by  $2\pi$ .



# 2 Standard Model of Particle Physics and Beyond

## 2.1 Standard Model of Particle Physics

### 2.1.1 Overview of the Standard Model of Particle Physics

The *Standard Model of Particle Physics* (SM) is a theoretical framework to describe three of the four known fundamental interactions between elementary particles: the strong [15–19] and the electroweak [20–22] interaction<sup>1</sup>, which combines the weak and electromagnetic interaction. All three fundamental forces are described in terms of Quantum field theories: *Quantum Chromo Dynamics* (QCD) for the strong interaction, *Quantum Flavor Dynamics* (QFD) for the electroweak interaction und *Quantum Electrodynamics* (QED) for the electromagnetism, which remains after the electroweak symmetry breaking. Developed predominantly during the 1960s and 1970s, the Standard Model has been tested in a myriad number of experiments during the last decades, proving that the model allows reliable predictions of the three interactions on quantum level<sup>2</sup>.

The theoretical description of the three forces is based on the *gauge symmetry group*

$$\mathrm{SU}(3)_C \times \mathrm{SU}(2)_L \times \mathrm{U}(1)_Y, \quad (2.1)$$

where  $\mathrm{SU}(2)_L \times \mathrm{U}(1)_Y$  corresponds to the theory of electroweak interaction and  $\mathrm{SU}(3)_C$  to the theory of strong interaction. Within this picture, the interactions between two particles are transmitted via spin-one gauge bosons which are closely related to the generators of the corresponding gauge group, summarized in Table 2.1. The strength of each interaction is

Gauge Group	Generators	Gauge Fields	
$\mathrm{U}(1)_Y$	$Y$	$B_\mu$	
$\mathrm{SU}(2)_L$	$T^a = \frac{1}{2}\tau^a$	$W_\mu^a$	$a = 1, 2, 3$
$\mathrm{SU}(3)_C$	$T^\alpha = \frac{1}{2}\lambda^\alpha$	$G_\mu^\alpha$	$\alpha = 1, \dots, 8$

**Table 2.1:** Overview about the gauge field structure in the SM. The generators of the gauge groups are the described by the hypercharge  $Y$ , the Pauli matrices  $\tau^a$  and the Gell-Mann matrices  $\lambda^\alpha$ .

defined by the coupling constants  $g_1$ ,  $g_2$  and  $g_3$  (for the  $\mathrm{U}(1)_Y$ ,  $\mathrm{SU}(2)_L$  and  $\mathrm{SU}(3)_C$  gauge group,

<sup>1</sup>Interactions via the gravitational force are not included in the Standard Model of Particle Physics. The understanding of gravity on a quantum level and the combination of the concepts of general relativity and quantum mechanics are the topic of ongoing studies (see for example [23–25]).

<sup>2</sup>Assuming that the theory behaves perturbative and renormalizable at the considered energies.

respectively) and the charge carried by the involved particles. The structure of the charge is defined by the structure of the gauge group: the charge for the  $U(1)_Y$  group is the scalar *hypercharge*  $Y$ , for the  $SU(2)_L$  group the *weak isospin*  $\mathbf{I}_W$  and for the  $SU(3)_C$  a *color triplet*. Note that the electric charge<sup>3</sup>,  $Q$ , is not a fundamental charge in the SM gauge group, but it can be related to the hypercharge via:

$$Y = 2(Q - I_W^3), \quad (2.2)$$

where  $I_W^3$  represents the third component of the weak isospin. Like the theory of classical electrodynamics, the physical properties of the fields can be expressed in terms of a field strength tensor for each gauge group:

$$B_{\mu\nu} = \partial_\mu B_\nu - \partial_\nu B_\mu \quad (2.3)$$

$$W_{\mu\nu}^a = \partial_\mu W_\nu^a - \partial_\nu W_\mu^a + g_2 \epsilon_{bc}^a W_\mu^b W_\nu^c \quad (2.4)$$

$$G_{\mu\nu}^\alpha = \partial_\mu W_\nu^\alpha - \partial_\nu W_\mu^\alpha + g_3 f_{\beta\gamma}^\alpha W_\mu^\beta W_\nu^\gamma, \quad (2.5)$$

where  $\epsilon_{bc}^a$  represents the antisymmetric tensor and  $f_{\beta\gamma}^\alpha$  the structure constant of the  $SU(3)_C$  group. Given the definition of the field strength tensors, the Lagrangian of the gauge boson fields can be expressed in the form

$$\mathcal{L}_{\text{gauge}} = -\frac{1}{4} G_{\mu\nu}^\alpha G_{\alpha}^{\mu\nu} - \frac{1}{4} W_{\mu\nu}^a W_a^{\mu\nu} - \frac{1}{4} B_{\mu\nu} B^{\mu\nu}. \quad (2.6)$$

Since the  $SU(2)_L$  and  $SU(3)_C$  are non-abelian groups, triple and quartic self-interaction between the gauge bosons of the same group are allowed. The eight fields of the  $SU(3)_C$ ,  $G_\mu^\alpha$ , are identified with the gluon fields of the QCD. The  $SU(2)_L \times U(1)_Y$  gauge fields,  $W_\mu^a$  and  $B_\mu$ , can be related to the physical gauge bosons  $W_\mu^\pm$ ,  $Z_\mu$  and the photon  $A_\mu$ , which will be discussed within the context of the spontaneous breaking of the electroweak symmetry.

The known matter content observed in nature consist of three generations of spin-1/2 fermions, divided into six leptons and six quarks. With respect to the gauge symmetries, the quarks are triplets under  $SU(3)_C$ , while leptons are singlets, which reflects that quarks, in contrast to leptons, carry a color charge and participate in the strong interaction. Left-handed fermions are weak iso-spin doublets, while right-handed fermions are weak iso-spin singlets, representing that only left-handed fermion fields participate in the weak interaction. For the first generation, the iso-spin doublets and singlets are

$$L_1 = \begin{pmatrix} \nu_e \\ e^- \end{pmatrix}_L, \quad e_R^- \quad \text{and} \quad Q_1 = \begin{pmatrix} u \\ d \end{pmatrix}_L, \quad u_R, \quad d_R, \quad (2.7)$$

where the subscripts  $L$  and  $R$  represents the left-handed and right-handed fermion field. A full summary over all three generations is provided in Table 2.2. In addition, each known

---

<sup>3</sup>The electric charge  $Q$  is expressed in multiples of the electric charge of a positron.

particle is accompanied by its corresponding anti-matter partner<sup>4</sup>. Between each generation, the

	Generation			$Q$	$I_W^3$	$Y$
	1 <sup>st</sup>	2 <sup>nd</sup>	3 <sup>rd</sup>			
Quarks	$\begin{pmatrix} u \\ d \end{pmatrix}_L$	$\begin{pmatrix} c \\ s \end{pmatrix}_L$	$\begin{pmatrix} t \\ b \end{pmatrix}_L$	$\begin{pmatrix} +\frac{2}{3} \\ -\frac{1}{3} \end{pmatrix}$	$\begin{pmatrix} +\frac{1}{2} \\ -\frac{1}{2} \end{pmatrix}$	$+\frac{1}{3}$
	$u_R$	$c_R$	$t_R$	$+\frac{2}{3}$	0	$+\frac{4}{3}$
	$d_R$	$s_R$	$b_R$	$-\frac{1}{3}$	0	$-\frac{2}{3}$
Leptons	$\begin{pmatrix} \nu_e \\ e^- \end{pmatrix}_L$	$\begin{pmatrix} \nu_\mu \\ \mu^- \end{pmatrix}_L$	$\begin{pmatrix} \nu_\tau \\ \tau^- \end{pmatrix}_L$	$\begin{pmatrix} 0 \\ -1 \end{pmatrix}$	$\begin{pmatrix} +\frac{1}{2} \\ -\frac{1}{2} \end{pmatrix}$	-1
	$e_R^-$	$\mu_R^-$	$\tau_R^-$	-1	0	-2

**Table 2.2:** Overview about the matter content in the SM. The fermions are presented in their left-handed and right-handed weak isospin doublets and singlets.

corresponding particles share the same quantum numbers, except for a different flavor and an increasing mass value towards the higher generations.

The Lagrangian for the fermion fields can be expressed by

$$\mathcal{L}_{\text{fermion}} = \sum_{j=1}^3 \left( \bar{L}_j i D_\mu \gamma^\mu L_j + \bar{e}_{R_j} i D_\mu \gamma^\mu e_{R_j} + \bar{Q}_j i D_\mu \gamma^\mu Q_j + \bar{u}_{R_j} i D_\mu \gamma^\mu u_{R_j} + \bar{d}_{R_j} i D_\mu \gamma^\mu d_{R_j} \right), \quad (2.8)$$

where  $j$  represents the generation index. The coupling between the fermionic matter field and the gauge bosons is comprised in the *covariant derivative*,

$$D_\mu = \partial_\mu - ig_3 T_\alpha G_\mu^\alpha - ig_2 T_a W_\mu^a - ig_1 \frac{Y}{2} B_\mu. \quad (2.9)$$

The resulting Lagrangian,

$$\mathcal{L} = \mathcal{L}_{\text{fermion}} + \mathcal{L}_{\text{gauge}}, \quad (2.10)$$

is invariant under a local gauge transformation in the  $SU(3)_C \times SU(2)_L \times U(1)_Y$  symmetry group and describes the physics of massless matter and gauge fields.

### 2.1.2 Spontaneous Breaking of the Electroweak $SU(2)_L \times U(1)_Y$ Symmetry

So far, the fermionic matter fields as well as the bosonic gauge fields are treated as massless particles. Since all observed particles, except for photons and gluons, are found to be massive, it is necessary to reflect this property in the SM. Unfortunately, the introduction of simple mass

<sup>4</sup>The neutrino particles are a special case, because the underlying nature of neutrinos is the subject of ongoing studies (for example if neutrinos are Dirac or Majorana fermions). Within this SM overview, neutrinos are treated massless (which is a simplification, because it is known from observations of neutrino oscillations that at least two of the three neutrinos are massive) and right handed neutrinos are neglected.

terms in the form of

$$\sim m_W^2 W_\mu^a W^{a,\mu} \quad \text{or} \quad \sim m_f^2 \psi_f \bar{\psi}_f, \quad (2.11)$$

would violate the invariance of the Lagrangian against the  $SU(2)_L \times U(1)_Y$  electroweak symmetry. The solution to this problem is the concept of the *spontaneous breaking of the electroweak symmetry* [26–30] into the remaining electromagnetic symmetry  $U(1)_Q$ ,

$$SU(2)_L \times U(1)_Y \longrightarrow U(1)_Q, \quad (2.12)$$

which was proposed during the mid 1960s. The baseline is the introduction of an  $SU(2)_L$  doublet<sup>5</sup>

$$\Phi = \begin{pmatrix} \phi^+ \\ \phi^0 \end{pmatrix}, \quad (2.13)$$

consisting of two complex scalar fields: a charged field  $\phi^+$  and a neutral field  $\phi^0$ , each with a hypercharge of  $Y_\phi = 1$ . The corresponding Lagrangian can be expressed in the form

$$\mathcal{L}_{\text{Higgs}} = (D^\mu \Phi)^\dagger (D_\mu \Phi) \underbrace{-\mu^2 \Phi^\dagger \Phi - \lambda(\Phi^\dagger \Phi)^2}_{-V(\Phi)}. \quad (2.14)$$

For values  $\mu^2 < 0$ , the “Higgs” potential will develop a non-zero vacuum expectation value (VEV),  $\nu$ , in the neutral component (illustrated for the one-dimensional case in Figure 2.1),

$$\langle 0 | \Phi | 0 \rangle = \begin{pmatrix} 0 \\ \frac{\nu}{\sqrt{2}} \end{pmatrix}, \quad (2.15)$$

with

$$\nu^2 = -\frac{\mu^2}{\lambda}. \quad (2.16)$$

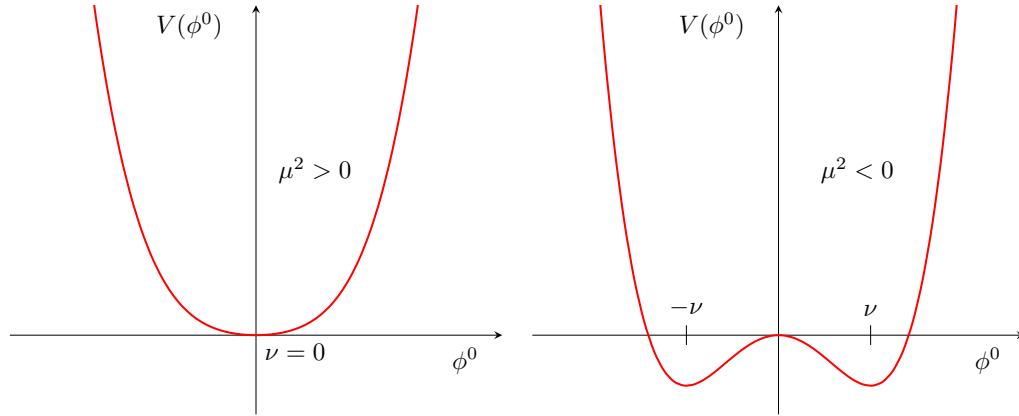


**Figure 2.1:** Illustration of the vacuum expectation value of the scalar Higgs potential in the case of one-dimension for  $\mu^2 > 0$  and  $\mu^2 < 0$ .

However, the VEV of the charged component is still forced to zero to preserve the electromagnetic gauge symmetry  $U(1)_Q$  and to be therefore in agreement with the experimental observations.

<sup>5</sup>Within the literature, the doublets or the single components are commonly referred to as “Higgs field”, referring to one of the main authors P. W. Higgs.

For the full complex field,  $\phi^0$ , the Higgs potential will develop a concentric (“Mexican-hat” like) form in the complex plane, illustrated in Figure 2.2.

Four spin-zero bosons can be associated with the four degree of freedoms in the Higgs doublet: one electrically neutral *Goldstone boson*  $G^0$ , two electrically charged Goldstone bosons  $G^\pm$  and the Higgs field  $h$ . The Goldstone bosons themselves are not observed but rather “absorbed” by the  $W^\pm$  and  $Z$  bosons to create their longitudinal components and to generate their mass values. The observed gauge bosons can be related to the gauge bosons of the unbroken  $SU(2)_L \times U(1)_Y$  symmetry:

$$W^\pm = \frac{1}{\sqrt{2}} (W_\mu^1 \mp iW_\mu^2) \quad (2.17)$$

and

$$\begin{pmatrix} A_\mu \\ Z_\mu \end{pmatrix} = \begin{pmatrix} \cos \theta_W & \sin \theta_W \\ -\sin \theta_W & \cos \theta_W \end{pmatrix} \begin{pmatrix} B_\mu \\ W_\mu^3 \end{pmatrix}, \quad (2.18)$$

where  $\theta_W$  represents the *Weinberg angle*,

$$\cos \theta_W = \frac{g_2^2}{\sqrt{g_1^2 + g_2^2}} = \frac{m_W}{m_Z}, \quad (2.19)$$

which describes the mixing between the  $B_\mu$  and  $W_\mu^3$  field. Given the definitions above, it is possible to obtain gauge boson mass terms,

$$m_W^2 W_\mu^+ W^{-\mu} + \frac{1}{2} m_Z^2 Z_\mu Z^\mu + \frac{1}{2} m_A^2 A_\mu A^\mu, \quad (2.20)$$

where

$$m_W = \frac{\nu}{2} g_2, \quad m_Z = \frac{\nu}{2} \sqrt{g_1^2 + g_2^2} \text{ and } m_A = 0. \quad (2.21)$$

While the gauge bosons of the weak interaction obtain mass values via the Goldstone bosons, the photon  $A_\mu$  remains massless after the symmetry breaking, reflecting that the  $U(1)_Q$  gauge symmetry is still unbroken. Following the relation between the VEV and the  $W^\pm$  mass, it is possible to estimate the value of the VEV via the Fermi constant,  $G_F$ ,

$$\nu^2 = \frac{2m_W}{g_2} = \frac{1}{\sqrt{2}G_F} \simeq (246 \text{ GeV})^2. \quad (2.22)$$

Fermion masses are obtained via the *Yukawa interaction* with the Higgs field,

$$\mathcal{L}_{\text{Yukawa}} = -\lambda_e \bar{L} \Phi e_R - \lambda_d \bar{Q} \Phi d_R - \lambda_u \bar{Q} \tilde{\Phi} u_R + \text{h.c.}, \quad (2.23)$$

where  $\lambda_e$ ,  $\lambda_u$  and  $\lambda_d$  represent the *Yukawa couplings* for the electron, up-quark and down-quark, respectively. The couplings are directly proportional to the mass of the particle:

$$m_e = \frac{\nu}{\sqrt{2}} \lambda_e, \quad m_u = \frac{\nu}{\sqrt{2}} \lambda_u \text{ and } m_d = \frac{\nu}{\sqrt{2}} \lambda_d. \quad (2.24)$$

The remaining two generations of fermions are described by the same structure.

The remaining degree of freedom translates into the *Higgs boson*,  $h$ , which is an additional

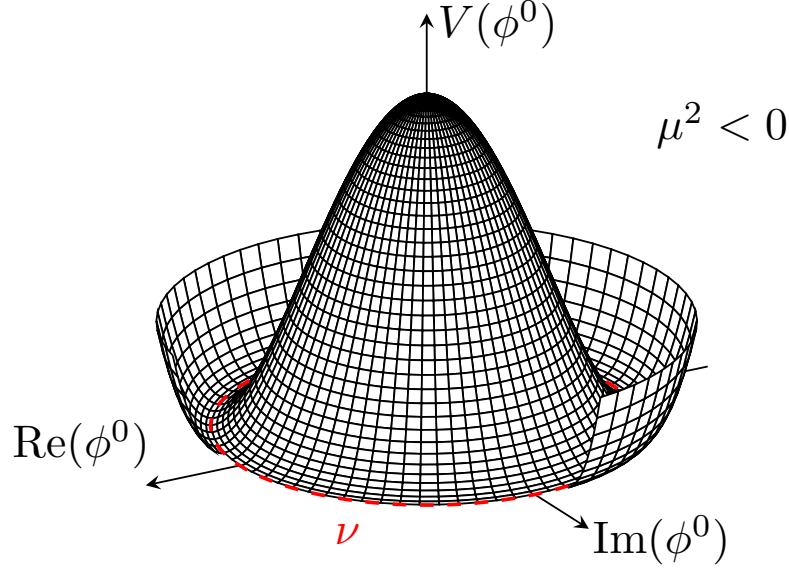


**Figure 2.2:** Illustration of the scalar Higgs potential for  $\mu^2 < 0$ .

particle postulated by the mechanism of symmetry breaking. Following the Lagrangian for the Higgs field,

$$\frac{1}{2}(\partial_\mu h)^2 - \lambda\nu^2 h^2 - \lambda\nu h^3 - \frac{\lambda}{4}h^4, \quad (2.25)$$

the Higgs boson mass at tree level can be expressed with

$$m_h^2 = 2\lambda\nu^2, \quad (2.26)$$

which is a free parameter in the SM. The Lagrangian also allows triple and quartic Higgs self-interactions with a coupling strength of

$$g_{hhh} = 3i\frac{m_h^2}{\nu} \text{ and } g_{hhhh} = 3i\frac{m_h^2}{\nu^2}. \quad (2.27)$$

Similar, the interaction strengths between the Higgs bosons and fermions,  $f$ , as well as gauge bosons,  $W^\pm$  and  $Z$ , are proportional to the mass of the involved particles [31]:

$$g_{hff} = i\frac{m_f}{\nu}, \quad (2.28)$$

$$g_{hW^+W^-} = -2i\frac{m_W^2}{\nu}, \quad g_{hZZ} = -2i\frac{m_Z^2}{\nu}, \quad (2.29)$$

$$g_{hhW^+W^-} = -2i\frac{m_W^2}{\nu^2}, \quad g_{hhZZ} = -2i\frac{m_Z^2}{\nu^2}. \quad (2.30)$$

Given the definitions above, the full Lagrangian of the SM can be written in the form:

$$\mathcal{L}_{\text{SM}} = \mathcal{L}_{\text{fermion}} + \mathcal{L}_{\text{gauge}} + \mathcal{L}_{\text{Higgs}} + \mathcal{L}_{\text{Yukawa}}, \quad (2.31)$$

which preserves gauge invariance under  $\text{SU}(3)_C \times \text{SU}(2)_L \times \text{U}(1)_Y$ , while allowing massive physical gauge boson states and fermions due to the spontaneous breaking of the electroweak symmetry  $\text{SU}(2)_L \times \text{U}(1)_Y$ . The remaining electromagnetic gauge symmetry  $\text{U}(1)_Q$  and the gauge symmetry



of the strong interaction  $SU(3)_C$  remain unbroken in the SM.

The search for the SM Higgs boson was a subject of various studies over the past  $\sim$  five decades, including studies from LEP, SLC and Tevatron [32–34] in the pre-LHC area. At this point, no observation of a SM Higgs boson like particle could be claimed<sup>6</sup> and constraints on the Higgs mass from direct and indirect searches have been set. At the end of Run 1 in 2012, the ATLAS and CMS collaborations are able to state the observation of a SM Higgs boson [10,11] like particle with a mass value of  $m_h = 125.09 \pm 0.21$  (stat.)  $\pm 0.11$  (syst.) GeV [35]. Down to the present day, the measured properties of the new particle are in good agreement with the predictions of the SM Higgs boson [36].

### 2.1.3 Confinement Property of the Strong Interaction

Neither quarks nor gluons have been observed as free particles so far, instead interactions with quark/gluon final states resolve into bunches of hadrons and mesons, referred to as *jets*. This particular phenomenon is known as *confinement property of the strong interaction* which has its origin in the structure of the QCD gauge symmetry group. In contrast to the photons of the QED, gluons are allowed to participate in self-interactions (see Eq. (2.5)) which reflects the fact that the gluons carry a color charge<sup>7</sup> due to the non-abelian nature of the  $SU(3)_C$ .

The effects can be expressed in terms of the *running coupling strength*  $\alpha_s(Q^2)$ , reflecting the strength of the strong interaction at a certain energy scale  $Q^2$ , which has been determined in various scattering experiments [12], presented in Figure 2.3. With an increase of the energy

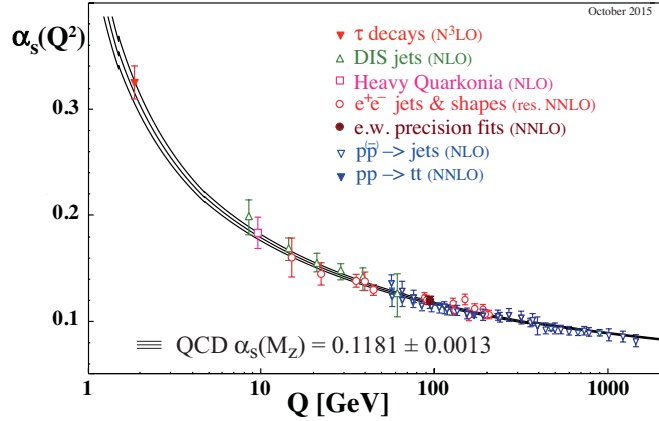


**Figure 2.3:** Summary of measurements for coupling strength  $\alpha_s(Q^2)$  [12].

scale  $Q$ , the coupling strength is significantly reduced and thus leading to a weaker coupling between quarks and gluons (for example inside of a proton) which is known as *asymptotic freedom*. In contrast, gluons and quarks are strongly coupled for relatively low energy scales, thus the separation of quarks and gluons from a bound state will increase the amount of gluon radiation and quark anti-quark pair production and subsequently leading to the development of new

<sup>6</sup>In the latest Tevatron results, an excess with a global significance of  $3.1\sigma$  has been observed in a mass window of 120 GeV to 135 GeV, which is compatible with the observation by ATLAS and CMS.

<sup>7</sup>The photons, in contrast, do not carry any electric charge and thus self-interactions between photons (at leading order) are prohibited.

hadronic bound states (baryons and mesons). This *hadronisation* process conceals the quarks and gluons and results in the observed hadron jets. Except for the top quark, all known quarks and gluons are affected by the hadronisation process. The top quark is a special case, because the proper life time of a top quark is lower than typical timescales for hadronisation processes (due to its high mass) and thus the top quark decays before a bound top quark state is formed.

This confinement property also applies to sub-sequent decays of particles into quarks, for example a tau lepton decaying into quarks via the weak interaction will resolve into a jet of baryons and mesons in the final state.

### 2.1.4 Simulation of High-Energy Interactions using Monte Carlo Techniques

The simulation of high-energy scattering processes is an important tool for many tasks in the field of particle physics. One of the most common tasks is the comparison between measurements and the predictions from various models (either the SM or other hypotheses) even in complicated regions of the phase-space which are only numerically accessible. In addition, simulations are used in a wide scope of activities including the optimization of background selections and estimations, training and tuning of reconstruction methods and algorithms and the planning and evaluation of new detector designs and concepts. In general, the simulations are performed using *Monte Carlo (MC) techniques*. During the past decades, a wide range of different *Monte Carlo event generators* has been developed, covering various numbers of possible scattering processes at different levels of perturbation theory. The choice of a certain generator usually depends on the considered process and measurement and is discussed in the corresponding analysis sections. In this section, a brief review about the general concepts of the simulation of proton-proton interactions is presented.

The simulation of a certain scattering process

$$p_1 p_2 \rightarrow \mathbf{X} , \quad (2.32)$$

with two protons  $p_1$  and  $p_2$  in the initial state and a set of particles  $\mathbf{X}$  in the final state, comprises several sub-activities which need to be modelled, including: the hard scattering process including possible contributions from higher orders of perturbation theory, additional photon and gluon bremsstrahlung, hadronisation of final state quarks and gluons, the structure of the incoming protons, multiple parton interactions and interactions with the beam remnants (underlying event) and the decay of instable particles (usually hadrons and tau leptons). All sub-activities together form a complex collision landscape, which is modelled by separating the simulation into different distinguishable phases. The cross section,  $\sigma(p_1 p_2 \rightarrow \mathbf{X})$ , for the considered process is factorized in

$$\sigma(p_1 p_2 \rightarrow \mathbf{X}) \sim \sum_{ij} \int dx_1 \int dx_2 f_i^1(x_1, \mu_F^2) f_j^2(x_2, \mu_F^2) \hat{\sigma}_{ij \rightarrow \mathbf{X}}(x_1, x_2, \mu_F^2, \mu_R^2) , \quad (2.33)$$

where  $i, j$  are the corresponding parton indices and  $\hat{\sigma}_{ij}$  the corresponding cross section at parton level [12], which is commonly referred to as *parton* or *matrix element* level. The parton level

cross section is usually provided up to a fixed order in perturbation theory. The proton structure is parameterized by the parton distribution function (PDF),  $f_i^a(x, Q^2)$ , which represents the probability to find a parton  $i$  within the proton  $a$  carrying a momentum fraction  $x$  of the total proton momentum. In general, the PDFs are functions of the considered energy scale  $Q^2$  and are derived from measurements of deep-inelastic-scattering processes [37, 38]. The parameter  $\mu_F^2$  and  $\mu_R^2$  represent the factorization and renormalization scale, respectively.

Electric and/or color charged particles in the initial and final state can emit additional radiation in form of photons or gluons. These *initial or final state radiations* are either incorporated into the matrix element (up to a certain order in perturbation theory) or modelled using a *parton-shower* algorithm. A parton shower allows to add an arbitrary number of additional radiation (which is an approximation for the exact perturbative expansion) but need to be modelled phenomenologically and matched to the matrix element calculation.

Quarks/gluons in the final state are bundled into hadrons to account for the hadronisation effect of the QCD. The underlying fragmentation process is not evaluable via perturbation theory but rather modelled using a phenomenological approach, which can differ between the various MC event generator frameworks. Additional contributions from multiple parton scatterings or interactions with the beam remnants are not covered by the factorization approach and need to be included using phenomenological models (e.g. [39]).

In order to compare the predictions of the MC generators with measurements, which are recorded within an experimental setup, it is necessary to take various effects during the measurement process itself into account, collectively referred to as *detector simulation*. The detector simulation process includes: the limited acceptance, efficiency and resolution of the detector components, the influence of the trigger decision on the collected data sample, effects originating from reconstruction, calibration and identification algorithms and additional sources of background processes which relate to the experimental setup.

The simulation of the ATLAS detector is performed using the GEANT4 [40, 41] software package which has been embedded within the ATLAS software framework *Athena* [42], based on the *Gaudi* [43, 44] framework, developed by the LHCb collaboration. Starting from the particle spectra produced by the MC event generators, the interactions of the particles with the magnetic fields (which are generated within the volume of the tracking detectors) and with the actual detector material is simulated [45]. Subsequent decays of particles during the detector simulation are considered. The considered geometry of the ATLAS detector incorporates the conditions of the real detector, e.g. alignment of detector components or the temperature within the detector [45]. Subsequently, the resulting energy deposits within the individual detector modules are translated into the expected voltages and currents, which are digitized to create an output format which is comparable with the output of the real detector. In the final step, the digitized samples are passed to the same reconstruction and trigger algorithms as the measured data samples. Only particles with a proper lifetime of  $c\tau > 10$  mm are declared to be stable enough to reach active detector material and are passed to the detector simulation [45]. The decay of particles with a shorter lifetime is instead simulated within the MC event generation process.

During the detector simulation, additional background sources are added, including: effects of multiple proton-proton scatterings during the same bunch crossing (in-time pile-up) and adjacent bunch crossings (out-of-time pile-up), background from interactions of the remaining gas in the cavern and background from additional interactions within the beam pipe [46].

## 2.2 Minimal Supersymmetric Extension of the Standard Model

Up to this point the *Standard Model of Particle Physics* has been introduced as the fundamental theoretical framework to describe strong and electroweak interactions in the context of quantum field theories. Recent measurements at the LHC substantiate again the statement that the SM is capable of describing the physics even up to energy scales of several TeV and with the discovery of a SM-like Higgs boson, possibly the last missing component of the SM has been found. However, even in the light of its tremendous success, it is commonly expected that the SM will not be valid all the way up to the Planck scale ( $\sim 10^{19}$  GeV) and instead it is assumed that the SM is an effective low-energy approximation of some (still unknown) more fundamental theory. The related physics is usually referred to as physics *Beyond the Standard Model* (BSM).

BSM theories are motivated by open question of the SM itself or by indications for new physics provided by different measurements, including<sup>8</sup>:

- the absence of a quantum theory of gravity in the SM,
- the hierarchy (or fine-tuning) effect in the SM Higgs sector,
- a possible unification of forces at large energies, usually referred to as *Grand Unified Theory* (GUT),
- discrepancies between the measurement of the anomalous magnetic moment of the muon and the SM prediction at the level of three standard deviations [49–51],
- a missing candidate for dark matter.

Over the past decades various BSM models have been developed. Although a great effort in finding BSM effects has been performed so far, no experimental evidences of BSM physics has been found. One large group of BSM models include *Supersymmetric* extensions of the SM, which allow to relate fermion fields with boson fields [52]. The roots of supersymmetry extend back to the early 1970s, when the foundation of the supersymmetric algebra was developed [53–55]. From this point onwards a rich development of supersymmetric theories within the context of relativistic quantum field theories started<sup>9</sup> in order to use supersymmetric models as description for physics at high energies [56,57].

### 2.2.1 Supersymmetric Extension of the Standard Model

The baseline for a *supersymmetric* extensions of the SM is the introduction of a symmetry between fermionic and bosonic states, denoted as *supersymmetry* (*SUSY*). The corresponding operator  $Q$  allows a transformation between both states [58]:

$$Q |\text{boson}\rangle = |\text{fermion}\rangle \quad (2.34)$$

$$Q |\text{fermion}\rangle = |\text{boson}\rangle , \quad (2.35)$$

<sup>8</sup>A good overview about the implications of these results, among others, can be for example found in Refs. [47,48].

<sup>9</sup>A more detailed overview of the development of supersymmetry can be found in Ref. [52].

in which the operator changes the spin of the corresponding particle in units of  $1/2$ . Each fundamental particle in the Standard Model will receive its corresponding *superpartner* due to this transformation. The operator  $Q$  itself and its Hermitian conjugate,  $Q^\dagger$ , must satisfy the following relations:

$$\{Q, Q^\dagger\} = P^\mu \quad (2.36)$$

$$\{Q, Q\} = \{Q^\dagger, Q^\dagger\} = 0 \quad (2.37)$$

$$[P^\mu, Q] = [P^\mu, Q^\dagger] = 0, \quad (2.38)$$

where  $P^\mu$  represents the generator of the four-momentum and  $[X, Y]$  and  $\{X, Y\}$  are the commutator and anti-commutator relations, respectively.

Fermions,  $f$ , in the SM (quarks and leptons) are composed of a left and right handed component,  $f_L$  and  $f_R$ , and each has its own supersymmetric partner with spin zero. Partners for the fermions are denoted as *scalar quarks* (squarks) and *scalar leptons* (sleptons) and are usually marked with a tilde (“ $\sim$ ”). The scalar fermions participate in same gauge interactions as their SM counterparts. The fermionic and bosonic state of a single particle can be combined to a *chiral supermultiplet*.

The superpartners of the spin one gauge bosons, usually denoted as *gauginos*, are fermions with spin  $1/2$  and are combined with their SM counterparts in *gauge* or *vector supermultiplets*.

Superpartners to the Higgs scalar fields are logically fermionic states and are represented together with the SM parts in chiral multiplets. A superpartner for a Higgs field is, like the gauge bosons partners, denoted with *higgsino*. To avoid gauge anomalies [58] it is necessary that (at least) two chiral multiplets exists, which subsequently lead to a quite rich Higgs sector in SUSY theories. The details of the Higgs sector will be discussed in Section 2.2.3 for the minimal supersymmetric extension of the SM.

If SUSY would be perfectly realized in nature, then each SUSY particle would have the same mass and quantum numbers as their SM counterparts, except for the spin. This includes the electric charge, the weak isospin and a possible color charge. In this case, no additional fundamental parameter would be introduced by SUSY and (except for the superpotential) the physics content would be determined by the SUSY and gauge invariance.

But no supersymmetric partners of the known SM particles have been observed so far [12]. In fact, the Higgs boson candidate, which was discovered in 2012 by the ATLAS and CMS collaborations, is the first observed candidate for a fundamental scalar particle.

In consequence, SUSY can only be realized as a broken symmetry in nature, in which the masses of the SUSY particles are shifted towards higher values. This can be achieved by adding SUSY breaking terms to the Lagrangian density, resulting in an effective SUSY theory valid for a relatively low energy scale. Due to the ignorance about the true fundamental physic of the SUSY breaking mechanism, the SUSY breaking is parametrized [59], leading to an increased

number of additional parameters of the theory. One of the most widely considered versions is the *Minimal Supersymmetric Standard Model* (MSSM), which will be discussed in greater detail in the following sections.

## 2.2.2 Introduction to the MSSM

The *Minimal Supersymmetric Standard Model* is a possible extension of the Standard Model of particle physics. It is based on the general SUSY deliberations, discussed in Section 2.2.1, and specified by the four following assumptions [59]:

1. The gauge group of the MSSM is the same as in the Standard model:

$$\mathrm{SU}(3)_C \times \mathrm{SU}(2)_L \times \mathrm{U}(1)_Y , \quad (2.39)$$

which is the minimal possible gauge group for an extension of the SM. This requirement leads to the following particle content: the usual gauge bosons of the SM,  $G_a^\mu$  (gluons) and  $W_b^\mu/B^\mu$  (gauge bosons of the electro-weak symmetry) and their super-partners:  $\tilde{G}_a$  (gluinos),  $\tilde{W}_b$  (winos) and  $\tilde{B}$  (bino), with  $a = 1 \dots 8$  and  $b = 1, 2, 3$ .

2. No additional generation of fermions (either leptons or quarks) is assumed, so any additional SUSY particles are the super-partners of the corresponding SM fermions. This ensures the minimal possible particle content of the SUSY model. In addition, two super-fields for the Higgs sector are introduced, which separately generate masses to particles with positive or negative isospin. The introduction of two fields leads to five physical Higgs bosons in the MSSM: two CP-even Higgs bosons,  $h$  and  $H$ , one CP-odd boson,  $A$ , and two charged bosons,  $H^\pm$ .

3. The following discrete symmetry, denoted as the *R-parity* [60], should be preserved:

$$R_p = (-1)^{2s+3B+L} , \quad (2.40)$$

where  $s$  is the spin quantum number and  $B$  and  $L$  are the baryon and lepton numbers, respectively. Given the definition in Eq. (2.40), the R-parity is positive for SM particles and negative for their super-partners. The conservation of  $R_p$  leads to the following consequences:

- Lepton and baryon numbers are conserved.
  - Supersymmetric particles are always produced in pairs.
  - The decay of SUSY particles need to contain an odd number of SUSY particles. The lightest particle in the SUSY sector is therefore stable and can provide a possible candidate for dark matter.
4. The breaking of SUSY should be provided by a minimal set of additional terms [59], including the mass terms for gauginos, scalar fermions, Higgs bosons, bilinear terms between the Higgs bosons and trilinear couplings between the Higgs bosons and scalar fermions.

A SUSY model following the four assumptions above is usually referred to as the *unconstrained* MSSM.

Although the unconstrained MSSM is already designed as a minimal extension of the SM, it still introduces a large number ( $> 100$  [61]) of new unknown parameter to the theory<sup>10</sup>. The large number of parameters complicate the interpretation of experimental results in the context of the unconstrained MSSM. It is therefore useful to reduce the number of free parameter to 22 by assuming the following additional requirements [59].

1. The SUSY breaking terms are assumed to be real. This ensures that, beside the CMK and PMNS mechanism, no CP violation processes are possible within the context of the theory [59].
2. Mass matrices for scalar fermions and coupling matrices for trilinear couplings are assumed to be diagonal.
3. The mass terms and trilinear couplings for the first and second scalar fermion generation are assumed to be equal.

This model is often referred to as *phenomenological* MSSM (pMSSM). The remaining 22 parameters of the pMSSM are:

- The mass of the CP-odd Higgs boson,  $m_A$ , and the Higgs mixing parameter  $\mu$ . Alternatively it is also possible to use the two Higgs mass parameter  $m_{H_1}^2$  and  $m_{H_2}^2$  instead.
- The ratio of the vacuum expectation values,  $v_1$  and  $v_2$ , of the two Higgs doublets:

$$\tan \beta = \frac{v_2}{v_1} . \quad (2.41)$$

- Mass parameters for the gauginos (bino, wino and gluino):  $M_1, M_2, M_3$ .
- Mass parameters and trilinear couplings for the first (and therefore also the second) generation of scalar fermions:  $m_{\tilde{q}}, m_{\tilde{u}_R}, m_{\tilde{d}_R}, m_{\tilde{l}}, m_{\tilde{e}_R}$  and  $A_u, A_d, A_e$ , with

$$\tilde{q} = \begin{pmatrix} \tilde{u}_L \\ \tilde{d}_L \end{pmatrix} \text{ and } \tilde{l} = \begin{pmatrix} \tilde{\nu}_L \\ \tilde{e}_L \end{pmatrix} . \quad (2.42)$$

- Mass parameters and trilinear couplings for the third generation:  $m_{\tilde{Q}}, m_{\tilde{t}_R}, m_{\tilde{b}_R}, m_{\tilde{L}}, m_{\tilde{\tau}_R}$  and  $A_t, A_b, A_\tau$ , with

$$\tilde{Q} = \begin{pmatrix} \tilde{t}_L \\ \tilde{b}_L \end{pmatrix} \text{ and } \tilde{L} = \begin{pmatrix} \tilde{\nu}_L \\ \tilde{\tau}_L \end{pmatrix} . \quad (2.43)$$

Within the context of this thesis the experimental results of the Higgs boson searches are interpreted in certain *benchmark scenarios* of the MSSM. In these scenarios, the number of free parameters is further reduced to two:  $m_A$  and  $\tan \beta$ , by fixing the remaining parameters using additional assumptions or limits from previous experimental measurement. An overview about the benchmark scenarios used is presented in Section 2.2.6.

---

<sup>10</sup>In addition to the 19 a-priori unknown parameters of the SM.



### 2.2.3 Higgs Sector of the MSSM

The Higgs sector of the MSSM is slightly more complicated than in the SM. Instead of one complex doublet of scalar Higgs fields, one needs to introduce two doublets  $H_1$  and  $H_2$  with

$$H_1 = \begin{pmatrix} H_1^0 \\ H_1^- \end{pmatrix} , \quad H_2 = \begin{pmatrix} H_2^+ \\ H_2^0 \end{pmatrix} . \quad (2.44)$$

Both doublets are complex scalar fields, which lead to eight degrees of freedom. Two doublets are necessary to ensure that the theory is free of chiral or Adler-Bradeen-Jachiw anomalies [59]. A higher number of doublets is in principle possible but a rotation in the field space can ensure that only  $H_1$  and  $H_2$  have a non-vanishing vacuum expectation value [62].

The fields  $H_1$  and  $H_2$  generate the masses of the matter particles with negative or positive weak iso-spin independently, in contrast to the SM, in which the masses of the fermions are generated by the same Higgs field, independent of the iso-spin.

The potential of the Higgs sector,  $V_H$ , in the MSSM can be written in the following form [58, 59]:

$$\begin{aligned} V_H = & (|\mu|^2 + m_{H_1}^2) |H_1|^2 + (|\mu|^2 + m_{H_2}^2) |H_2|^2 \\ & - \mu B (H_1^- H_2^+ - H_1^0 H_2^0 + \text{h.c.}) \\ & + \frac{g_1^2 + g_2^2}{8} (|H_1|^2 - |H_2|^2)^2 + \frac{1}{2} g_2^2 |H_1^{-*} H_1^0 + H_2^{0*} H_2^+|^2 , \end{aligned} \quad (2.45)$$

in which

$$|H_1|^2 = |H_1^0|^2 + |H_1^-|^2 \quad (2.46)$$

$$|H_2|^2 = |H_2^0|^2 + |H_2^+|^2 . \quad (2.47)$$

The parameters  $g_1$  and  $g_2$  represent the gauge couplings of the  $U(1)_Y$  and  $SU(2)_L$  symmetry, respectively.

Like the SM, the electro-weak symmetry  $SU(2)_L \times U(1)_Y$  should be broken at the minimum of the Higgs potential but not the QED symmetry. Using the freedom of gauge transformation in  $SU(2)_L$  allows to set the vacuum expectation value of one of the charged components to zero:  $\langle H_1^- \rangle = 0$ . The VEV of the second charged component,  $\langle H_2^+ \rangle = 0$ , is subsequently also vanishing at the minimum of the potential [58, 59]:

$$\frac{\partial V_H}{\partial H_1^-} = 0 . \quad (2.48)$$

The vanishing VEVs of the charged components ensures an unbroken potential of the electromagnetic sector of the theory [58, 59].

To break the electro-weak symmetry, the VEVs of the neutral components acquire non-vanishing

values [59]:

$$\langle H_1^0 \rangle = \frac{v_1}{\sqrt{2}} \quad , \quad \langle H_2^0 \rangle = \frac{v_2}{\sqrt{2}} \quad , \quad (2.49)$$

in which  $v_1$  and  $v_2$  are related via:

$$v^2 = (v_1^2 + v_2^2) = \frac{4m_Z^2}{g_1^2 + g_2^2} = (246 \text{ GeV})^2 \quad , \quad (2.50)$$

at lowest order of perturbation theory. The ratio of the vacuum expectation values is usually defined as  $\tan \beta$ , with:

$$\tan \beta = \frac{v_2}{v_1} \quad . \quad (2.51)$$

Evaluating the Higgs potential at its minimum with respect to the neutral components,

$$\frac{\partial V_H}{\partial H_1^0} = 0 \quad , \quad \frac{\partial V_H}{\partial H_2^0} = 0 \quad ,$$

allows to gain conditions for  $B$  and  $\mu^2$  as functions of  $m_{H_1}^2$ ,  $m_{H_2}^2$  and  $\tan \beta$ . Developing the Higgs potential around the minimum leads to the physical Higgs fields: three of the eight degrees of freedom can be associated with the Nambu–Goldstone bosons,  $G^0$  and  $G^\pm$ , which will give masses and longitudinal polarization modes to the gauge bosons  $Z^0$  and  $W^\pm$  [58]. The remaining degrees of freedom introduce five Higgs scalar mass eigenstates [58]: three neutral Higgs bosons,  $h$ ,  $H$  and  $A$ , as well as the two charged Higgs bosons  $H^\pm$ . Assuming an expansion in the neutral parts of the Higgs fields (separated in the real and imaginary part) [59]:

$$H_1 = \frac{1}{\sqrt{2}} \begin{pmatrix} v_1 + H_1^0 + iP_1^0 \\ H_1^- \end{pmatrix} \quad , \quad H_2 = \frac{1}{\sqrt{2}} \begin{pmatrix} H_2^+ \\ v_2 + H_2^0 + iP_2^0 \end{pmatrix} \quad , \quad (2.52)$$

one obtains the following relations [59] between the gauge eigenstates and the mass eigenstates:

$$\begin{pmatrix} H \\ h \end{pmatrix} = \begin{pmatrix} \cos \alpha & \sin \alpha \\ -\sin \alpha & \cos \alpha \end{pmatrix} \begin{pmatrix} H_1^0 \\ H_2^0 \end{pmatrix} \quad (2.53)$$

$$\begin{pmatrix} G^0 \\ A \end{pmatrix} = \begin{pmatrix} \cos \beta & \sin \beta \\ -\sin \beta & \cos \beta \end{pmatrix} \begin{pmatrix} P_1^0 \\ P_2^0 \end{pmatrix} \quad , \quad \begin{pmatrix} G^\pm \\ H^\pm \end{pmatrix} = \begin{pmatrix} \cos \beta & \sin \beta \\ -\sin \beta & \cos \beta \end{pmatrix} \begin{pmatrix} H_1^\pm \\ H_2^\pm \end{pmatrix} \quad . \quad (2.54)$$

The mixing angle  $\beta$  is defined via the ratio of VEVs according to eq. (2.51). At tree level, two parameters are sufficient to fix the Higgs boson mass values. It is common to choose  $m_A$  and  $\tan \beta$  as the free parameters, which leads to the relations [59]:

$$m_{h,H}^2 = \frac{1}{2} \left( m_A^2 + m_Z^2 \mp \sqrt{(m_A^2 + m_Z^2)^2 - 4m_A^2 m_Z^2 \cos^2 2\beta} \right) \quad (2.55)$$

$$m_{H^\pm}^2 = m_A^2 + m_W^2 \quad . \quad (2.56)$$

This also defines the mixing angle  $\alpha$  with:

$$\alpha = \frac{1}{2} \arctan \left( \tan 2\beta \frac{m_A^2 + m_Z^2}{m_A^2 - m_Z^2} \right) \quad , \quad -\frac{\pi}{2} < \alpha < 0 \quad . \quad (2.57)$$

The mass values of the  $A$ ,  $H$  and  $H^\pm$  bosons are unbounded, but the mass of the (light<sup>11</sup>)  $h$  boson has an upper bound of

$$m_h < m_Z |\cos(2\beta)| \quad (2.58)$$

at tree level. Consequently the maximum allowed mass values would be  $m_h = m_Z$  ( $|\cos(2\beta)| = 1$ ) but the parameter space for such a light MSSM Higgs boson is already largely excluded by the MSSM Higgs searches at LEP [63].

If the MSSM is realized in nature, the mass value of  $h$  is expected to be larger than  $m_Z$  which is possible when taking radiative corrections into account. Corrections at higher order of perturbation theory modify the Higgs boson masses. In particular, the mass of the lightest Higgs boson,  $m_h$ , can be increased above the Z-boson mass boundary up to a maximum value of:

$$m_h^{\max} \sim 130 - 140 \text{ GeV} . \quad (2.59)$$

This allows to raise the mass of the light MSSM Higgs boson above the exclusion limit of LEP and it also allows a possible interpretation of the new particle, discovered by ATLAS and CMS [10,11], to be the light MSSM Higgs boson. These corrections depend on the top-sector and bottom-sector as well as the mixing between the corresponding SUSY particles. The number of parameters necessary to provide a full description of the MSSM Higgs sector increases and the additional parameters are usually fixed within certain *benchmark scenarios* to allow an interpretation of experimental results.

In contrast, the mass values of the four remaining heavy Higgs bosons ( $A$ ,  $H$ ,  $H^\pm$ ) will degenerate and converge to the value of  $m_A$ ,

$$m_A \simeq m_H \simeq m_{H^\pm} . \quad (2.60)$$

The evolution of the neutral, CP-even Higgs boson masses,  $m_h$  and  $m_H$ , are presented in Figure 2.4 as a function of  $m_A$  for two different values of  $\tan\beta$  in the  $m_h^{\max}$  benchmark scenario. The left plot presents the low mass region, showing the saturation of the  $h$  boson mass around 130 GeV, while the right plot shows the same distribution for a larger range in  $m_A$ , emphasizing the degeneration for  $m_A$  and  $m_H$  in the *decoupling limit* of the MSSM:

$$m_A \gg m_Z \text{ and } \tan\beta \gg 1 . \quad (2.61)$$

The corresponding distributions for the  $m_h^{\text{mod}\pm}$  benchmark scenarios can be found in Section A.1.1.

### Coupling of the neutral MSSM Higgs bosons to SM particles

The physics of the MSSM Higgs sector is not only affected by the mass parameters of the Higgs bosons but also by their interaction strengths to other particles.

Yukawa interactions between the scalar Higgs boson fields and fermion fields are parameterized

<sup>11</sup>The choice that  $h$  is the lighter one of both neutral, CP-even bosons is a convention.

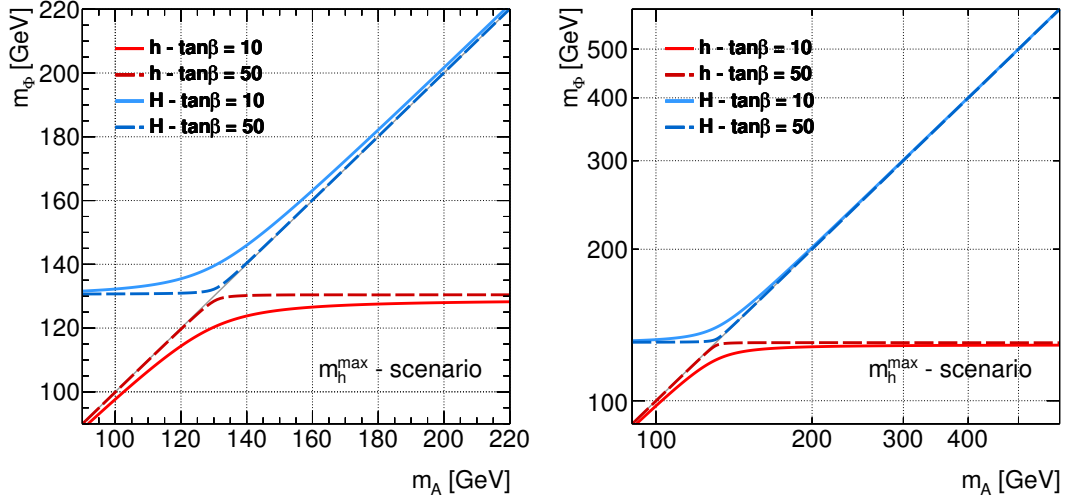


**Figure 2.4:** Development of the neutral, CP-even Higgs boson masses,  $m_h$  and  $m_H$ , as a function of  $m_A$  for two different values in  $\tan\beta$ . Both plots are produced for the  $m_h^{\max}$  benchmark scenario. The benchmark points are provided by the *LHC Higgs Cross Section Working Group* [64, 65].

using a *superpotential*  $W$  [58, 59]. The Yukawa couplings to *down-type* and *up-type* fermions<sup>12</sup> can be expressed in the following terms [59]:

$$\begin{aligned} \Phi = h : \quad g_{hdd} &= -i \frac{m_d}{v} \frac{\sin \alpha}{\cos \beta}, & g_{huu} &= i \frac{m_u}{v} \frac{\cos \alpha}{\sin \beta} \\ \Phi = H : \quad g_{Hdd} &= i \frac{m_d}{v} \frac{\cos \alpha}{\cos \beta}, & g_{Hu u} &= i \frac{m_u}{v} \frac{\sin \alpha}{\sin \beta} \\ \Phi = A : \quad g_{Add} &= \gamma_5 \frac{m_d}{v} \tan \beta, & g_{Auu} &= \gamma_5 \frac{m_u}{v} \frac{1}{\tan \beta}. \end{aligned} \quad (2.62)$$

Including radiative corrections [59, 66], the coupling structure shows a quite different behavior for values of  $m_A$  below or above  $m_h^{\max}$ . If  $m_A < m_h^{\max}$ , the couplings of the  $h$  boson are enhanced/suppressed for down-type/up-type fermions, while the couplings for the  $H$  boson are close to the Higgs-fermion couplings predicted in the SM. In contrast, for  $m_A > m_h^{\max}$  (especially in the decoupling limit), both CP-even Higgs bosons switch their behavior. The coupling parameters of the light Higgs boson  $h$  to SM fermions will develop towards the couplings of a pure SM Higgs boson without a supersymmetry extension of the Higgs-sector [59]. Except for the sign, the neutral CP-even and CP-odd Higgs bosons show the same coupling structure. The couplings to up-type fermions are suppressed with  $\cot \beta$  while the couplings to down-type fermions are enhanced by  $\tan \beta$  [59]. Consequently, with increasing values of  $\tan \beta$  the couplings to up-type fermions will vanish and the couplings to down-type will play a dominant role in the production and decay mechanisms of  $A$  and  $H$ . Especially the interactions with bottom quarks and tau leptons will become more interesting as these are the heaviest down-type quarks/leptons in the SM. These general behaviors of the Higgs bosons persist even after taking radiative corrections into account [59].

Interactions between the Higgs bosons and SM gauge bosons are parametrized in the kinematic terms of the two Higgs fields. Trilinear couplings between one Higgs boson and two gauge

<sup>12</sup>Fermions with negative or positive iso-spin, denoted with a “ $d$ ” or “ $u$ ” superscript, respectively.

bosons are only allowed for the two neutral CP-even Higgs bosons:  $hZZ$ ,  $HZZ$ ,  $hW^+W^-$  and  $HW^+W^-$ . Trilinear interactions with the CP-odd A boson ( $AWW$ ,  $AZZ$ ) and the charged Higgs bosons ( $H^\pm W^\pm Z$ ) are not permitted due to CP invariance [59]. No (direct) couplings to photons are allowed due to fact that the photon is massless. The couplings themselves are proportional to the mass of the corresponding gauge bosons and to the sine or cosine of the difference between the two mixing angles of the Higgs sector, depending on whether the gauge boson couples to  $h$  or  $H$ :

$$\begin{aligned} \text{coupling to } h &\sim \sin(\beta - \alpha) , \\ \text{coupling to } H &\sim \cos(\beta - \alpha) . \end{aligned}$$

Like the couplings to fermions, the couplings between  $h$  and  $H$  behave contrary to each other. In the decoupling limit, the couplings between the SM gauge boson and the heavy Higgs boson will vanish, while the coupling parameters to the light Higgs boson are converging towards the SM values.

Trilinear couplings between one Higgs boson and two gauge bosons are strongly suppressed by the requirement of CP invariance, which demands that the Higgs bosons involved need to have an opposite parity [59]. Only two interaction for neutral Higgs boson are allowed:  $AZh$  and  $AZH$ , which are proportional to  $\cos(\beta - \alpha)$  for  $h$  and  $\sin(\beta - \alpha)$  for  $H$ . Additional interactions are possible if one of the bosons is charged:  $W^\pm H^\pm \Phi$  with  $\Phi \in \{h, H, A\}$ ,  $ZH^+H^-$ , and  $\gamma H^+H^-$  [59].

Quartic couplings between Higgs bosons and gauge bosons offer a complex spectrum of possible interactions, but are not relevant in the context of this thesis.

In summary, the MSSM Higgs sector in the decoupling limit is characterized by the following properties:

1. The light CP-even Higgs boson  $h$  receives its maximal mass value,  $m_h^{\max}$ , and its couplings converge towards to the couplings of the SM Higgs boson.
2. The mass values between the heavier neutral Higgs bosons  $H$  and  $A$  degenerate and the coupling structure between both Higgs bosons becomes similar: the couplings to SM gauge bosons vanish and the couplings to down-type/up-type fermions are enhanced/suppressed with  $\tan\beta$ .

The resulting SM-like Higgs boson  $h$ , with a mass  $\lesssim m_h^{\max}$ , is therefore effectively decoupled from the high mass Higgs sector of the MSSM.

#### 2.2.4 Production of heavy neutral MSSM Higgs bosons at a hadron collider

The main production channels for the neutral MSSM Higgs bosons in a hadron collider environment are similar to the ones for the pure SM Higgs boson. Within the context of this thesis, the *production in association with heavy quarks* (especially b-quarks) and the *gluon-gluon fusion* process are the most important production channels. Production channels including interactions

with vector bosons  $V \in \{Z, W^\pm\}$ , either the associated production with  $V$  or the vector boson fusion, are less relevant in the decoupling limit, since the interactions are strongly suppressed or even forbidden by CP invariance.

### Production in association with heavy quarks

The production of neutral MSSM Higgs bosons in association with heavy quarks is dominated by Higgs radiation processes off top or bottom quarks. The final state is usually characterized by a  $t\bar{t}$  or  $b\bar{b}$  pair in addition to the produced Higgs boson, either via a quark/anti-quark annihilation process,  $q\bar{q} \rightarrow t\bar{t}/b\bar{b} + \Phi$ , or a gluon-gluon fusion process,  $gg \rightarrow t\bar{t}/b\bar{b} + \Phi$ , in the initial state. Two example Feynman diagrams at lowest order in perturbation theory are shown in Figure 2.5, where  $\Phi$  represents one of the three neutral Higgs bosons:  $\Phi = h, H, A$ . For the b-quark associated

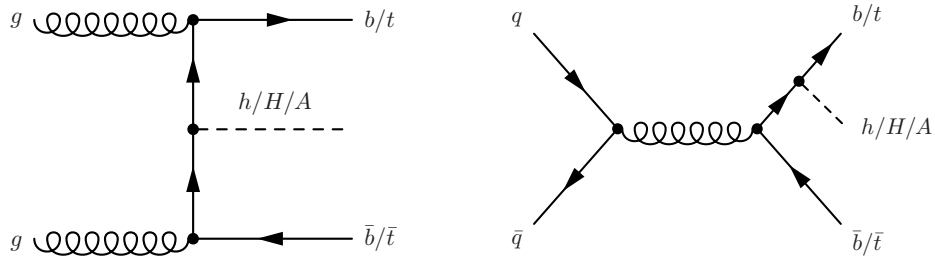


**Figure 2.5:** Feynman diagrams for the heavy neutral MSSM Higgs bosons production in association with an  $t\bar{t}$  or  $b\bar{b}$  pair in the final state.

production, processes with no additional quark,  $b\bar{b} \rightarrow \Phi$ , or one b-quark,  $gb \rightarrow \Phi$ , in the final state are also allowed. The corresponding Feynman diagrams are presented in Figure 2.6.

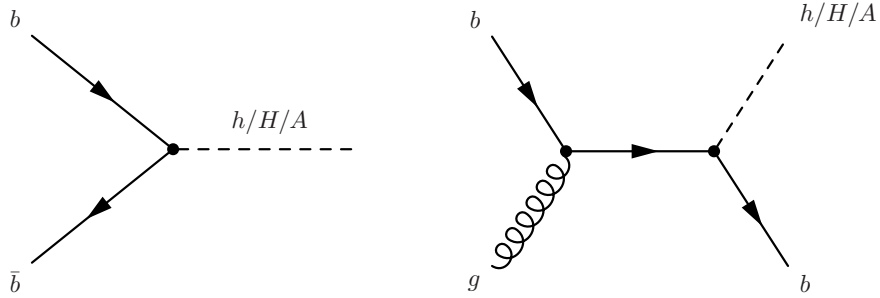


**Figure 2.6:** Feynman diagrams for the heavy neutral MSSM Higgs bosons production in association with one or zero additional b-quark in the final state.

The general features of the cross sections are similar to the SM cross sections, but are modified by the different couplings of the MSSM Higgs bosons to the top and bottom quarks:  $g_{\Phi t\bar{t}}$  and  $g_{\Phi b\bar{b}}$ . In the decoupling limit, the cross sections for  $h$  are almost SM like and the top-quark associated production is therefore the dominating process, due to the large mass of the top quark. For  $H$  the cross section of the top quark associated production is smaller than the SM one due to the suppression of the couplings to up-type quarks. In contrast, the coupling to bottom quarks is enhanced and the Higgs boson production in association with b-quarks becomes the dominant production process for high values of  $\tan\beta$  [59, 67].

The cross sections for the b-associated production of neutral MSSM Higgs bosons and for the production via gluon-gluon fusion (which will be discussed in the next section) are shown for two different values of  $\tan\beta$  in Figure 2.7. For high values of  $\tan\beta$  (in this example  $\tan\beta = 30$ ) the b-associated production becomes the major production mechanism over (almost) the full mass range, when compared to the gluon-gluon fusion production process. The production cross sections for the CP-odd boson  $A$  are very similar compared to the CP-even  $H$  boson in the decoupling limit. With increasing values of  $\tan\beta$  the differences between the cross sections are further reduced and only at low values of  $\tan\beta$  a significant difference between the CP-odd and the CP-even Higgs boson can be observed. Around the critical point of  $m_A = m_h^{\max}$  one can nicely observe the transition between the behaviors of the two CP-even bosons.

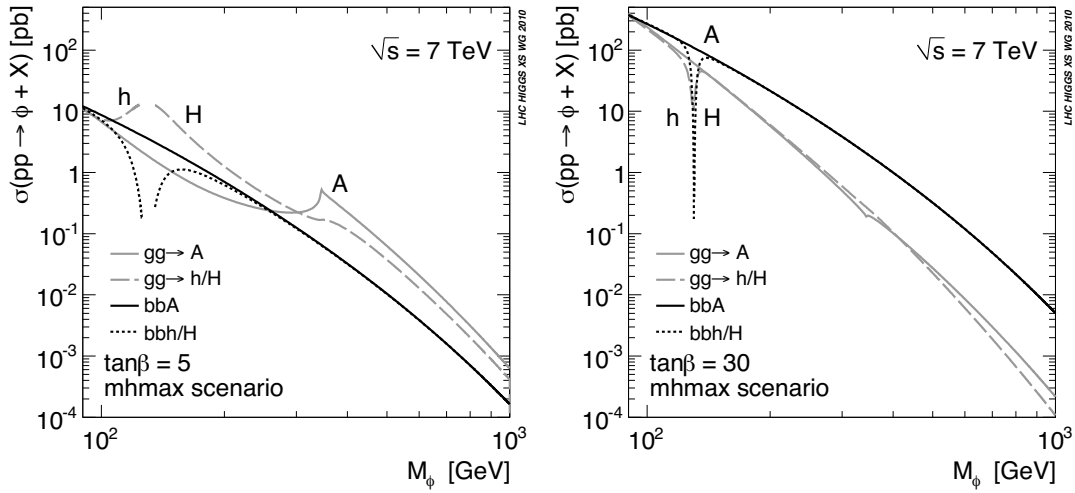


**Figure 2.7:** Production cross sections for the neutral MSSM Higgs bosons  $h$ ,  $H$  and  $A$  are shown as a function of the corresponding Higgs boson mass,  $M_\Phi$ , and for a relative small values of  $\tan\beta = 5$  (left) and a quite large value of  $\tan\beta = 30$  (right). The cross sections are calculated within the  $m_h^{\max}$  benchmark scenario. Both results are taken from [67].

Corrections at higher orders in the perturbation theory will modify the b-associated cross sections [67]: the dominant groups are the NLO QCD corrections [68, 69] (which are of the order of 20 % to 45 % at the LHC, depending on the Higgs mass considered) but also electro-weak corrections [70] and corrections due to SUSY particles are taken into account [71].

The calculation of the inclusive total cross section for the Higgs production can be performed in two different schemes: either the *five flavor scheme* (5FS), where the b-quarks are considered as possible partons in the proton, or the *four flavor scheme* (4FS), where the b-quarks are not considered. If all orders of the perturbation theory would be considered, the results for the cross sections using the 4FS and 5FS would be identical, but at a finite order of perturbation theory the cross sections calculated using the two schemes will show differences due to the different ways how the terms in the perturbation series are ordered. Within the context of this thesis, a method to combine the results of both schemes is applied, suggested by R. Harlander, M. Krämer and M. Schumacher [72].

In this method the cross sections for the 4FS and the 5FS are combined by the weight  $w$ :

$$\sigma_{\text{comb.}} = \frac{\sigma^{4\text{FS}} + w \cdot \sigma^{5\text{FS}}}{1 + w}, \quad (2.63)$$

where

$$w = \ln \frac{m_\Phi}{m_b} - 2 \quad (2.64)$$

depends on the mass of the Higgs bosons,  $m_\Phi$ , divided by the mass of the bottom quark,  $m_b$ . For small Higgs mass values the 4FS will dominate the combined cross section, while the 5FS will provide the major part for large Higgs mass values. Around a mass of 100 GeV, both schemes will be equally weighted in the combination, which is in accord with the fact the both schemes provide similar results at around this mass value.

### Gluon-gluon fusion

The production of neutral MSSM Higgs boson via *gluon-gluon fusion* is an important process, especially for smaller values of  $\tan \beta$ , compared to the b-associated production. Because gluons are massless, the Higgs bosons will not couple directly to them. Like the coupling to photons, the interaction  $gg \rightarrow \Phi$  is performed via a fermion (or boson) loop, illustrated in Figure 2.8. Dominant contributions arise from top and bottom quark loops (like in the SM) but additional contributions from SUSY particles are possible (e.g. stop and sbottom loops for the  $h, H$  production).

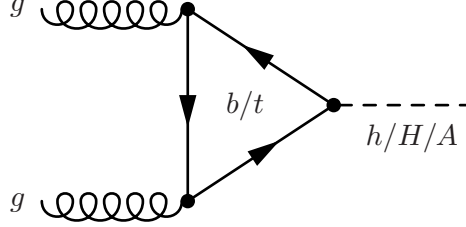


**Figure 2.8:** Feynman diagram for neutral MSSM Higgs production via gluon-gluon fusion with a bottom and top-quark loop.

The cross section for the gluon-gluon fusion process in the MSSM is similar to the SM cross section but the portions of top/bottom loops contributing to the cross section differ depending on the couplings of the Higgs bosons to top and bottom quarks [59]. With increasing values of  $\tan \beta$ , the couplings of the Higgs bosons to top quarks will become more and more suppressed while the couplings to bottom quarks are enhanced. Subsequently the contribution of bottom quarks to the cross section will increase and will become more dominant compared to the SM case. However, the top quark Yukawa coupling is stronger than the bottom quark coupling (neglecting the  $\tan \beta$  effect) due to the high mass of the top quark. If  $\tan \beta$  is small, the loss in the cross section due to the suppression of the top quark Yukawa coupling cannot be compensated yet by the enhancement of the bottom quark contributions. The resulting minimum of the MSSM cross sections is expected around  $\tan \beta \sim 6 - 8$  [59]. Consequently, for relatively small values of  $\tan \beta$  the MSSM cross section will be smaller than the SM one but it will surpass the SM cross section with increasing values of  $\tan \beta$  [59].



Higher order corrections for the gluon-gluon fusion process are dominantly positive and add large contributions to the production process. QCD corrections can increase the total cross section by about 50 % to 100 % depending on the considered  $\tan\beta$  region [67]. The NLO corrections are calculated in the heavy quark limit as well as including the full dependence on the quark masses. In addition to the SM QCD correction, contributions from SUSY QCD interactions are considered which can have a non-negligible effect on the cross section for increasing values of  $\tan\beta$ . These corrections are elaborated by several groups and an overview can be found for example in [59,67]. The evolution of the cross sections as a function of  $m_A$  is shown in Figure 2.7.

### Production including vector boson interactions

The interaction vertex with one Higgs boson and two gauge bosons allows two different production mechanisms for Higgs bosons at a hadron collider: the Higgs production in association with a vector boson, also termed *Higgs-strahlung*, and the production via fusion of two vector bosons. An example Feynman diagram for each process is shown in Figure 2.9. At lowest order in perturbation theory, only the production modes for the CP-even Higgs bosons  $h$  and  $H$  are allowed, because the CP invariance forbids a direct coupling of the CP-odd  $A$  to two vector bosons. The cross sections are proportional to the SM cross sections for the given processes, but

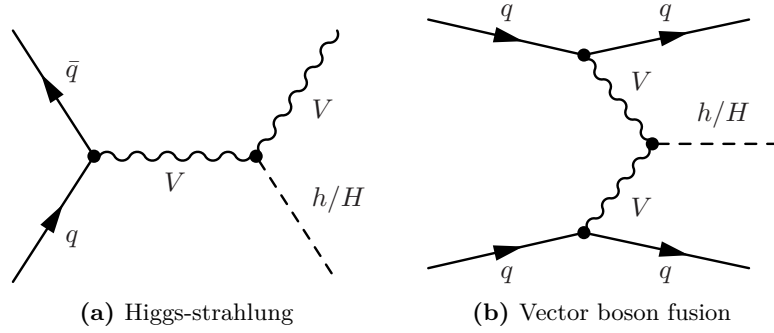


**Figure 2.9:** Primary production mechanisms for neutral MSSM Higgs boson at lowest order of perturbation theory including vector boson interactions, with  $V \in \{Z, W^\pm\}$ .

weighted with the squared coupling of the involved Higgs boson to two vector bosons [59]:

$$\sigma_{\text{MSSM}} = g_{\Phi VV}^2 \times \sigma_{\text{SM}} \quad \Phi \in \{h, H\}. \quad (2.65)$$

Additional radiative corrections from the SUSY sector can also cause deviations from the SM cross sections. This includes additional QCD corrections originating from squarks and gluinos as well as contributions from heavy quark loops to the Higgs-strahlungs process [59] (especially from b-quarks, because the coupling to down-type quarks is usually enhanced).

The cross section dependence on the coupling  $g_{\Phi VV}$  defines its main behavior. For low values of  $m_A$  the coupling of the light  $h$  to two vector bosons is suppressed and consequently also the corresponding cross sections. In the decoupling limit, the coupling  $g_{hVV}$  will converge to the SM value (because  $\sin(\beta - \alpha) \simeq 1$ ) and the cross sections will become close to the SM ones. The light MSSM boson will effectively act like to SM Higgs boson as expected in the decoupling limit.

In contrast to the light  $h$  boson, the cross sections for the heavy  $H$  boson (with  $m_H \sim m_A$  in the decoupling limit), will decrease, because  $\cos(\beta - \alpha) \rightarrow 0$ . In consequence, for high masses of  $A/H$  the production of  $H$  via vector boson interactions will vanish and these production channels become irrelevant for heavy neutral MSSM Higgs boson searches.

### 2.2.5 Decay of heavy neutral MSSM Higgs bosons

The decay modes and rates of the MSSM Higgs bosons are (like the production mechanisms) determined by the couplings and therefore depend on the considered region in the MSSM parameter space. For this study only decays in SM particles are considered and the SUSY particles are assumed to be too heavy to contribute significantly to the branching fractions<sup>13</sup>.

Within the decoupling limit of the MSSM, the light CP-even boson,  $h$ , will acquire its maximum mass value,  $m_h^{\max}$ , and will show a SM like Higgs coupling structure. Subsequently the  $h$  will decay like a SM Higgs boson dominantly in  $b\bar{b}$  and  $WW^*$ , in which one  $W$  boson is off-shell. The total decay width of the light Higgs boson will be of the order of a few MeV.

The couplings of the heavier neutral Higgs bosons,  $A$  and  $H$ , are strongly enhanced toward down-type fermion and suppressed for other particles for large values of  $\tan\beta$ . The dominant decay channels are therefore the decay to  $b\bar{b}$ , with a branching fraction of about 90 %, and the decay in  $\tau^+\tau^-$ , with a branching fraction of roughly 10 %:

$$\begin{aligned}\mathcal{B}(\Phi \rightarrow b\bar{b}) &\simeq 90 \% \quad , \quad \Phi = A, H \\ \mathcal{B}(\Phi \rightarrow \tau^+\tau^-) &\simeq 10 \% .\end{aligned}$$

The ratio,  $R$ , between the branching fractions of the  $b\bar{b}$  and  $\tau^+\tau^-$  decay channel can be expressed in the SM with

$$R = \frac{\mathcal{B}(h \rightarrow b\bar{b})}{\mathcal{B}(h \rightarrow \tau^+\tau^-)} = \frac{3m_b^2(m_h)}{m_\tau^2} , \quad (2.66)$$

where  $m_b(Q)$  represents the running b-quark mass at an energy scale  $Q$ , taking the leading SM QCD corrections into account, and  $m_\tau$  represents the mass of the tau lepton [73]. This result is also valid for models in which the structure of the Higgs sector is like the SM, including the MSSM [73]. Within the decoupling limit, the ratio is expected to be constant at tree level [59].

A small fraction of Higgs bosons can also decay into  $t\bar{t}$ , once the mass values of the bosons are large enough to kinematically allow the decay channel. The total decay widths of the heavy MSSM Higgs bosons,  $\Gamma(\Phi = A, H)$ , are of the order of 1 GeV to 10 GeV, depending on  $\tan\beta$ . The development of the various branching ratios as a function of the Higgs boson masses are presented in Ref. [59] and the relevant distributions are summarized in Figure 2.10. While  $b\bar{b}$  and  $\tau^+\tau^-$  decays are dominating in the decoupling limit, the behavior changes towards lower values of  $\tan\beta$  and Higgs boson masses. The branching ratios for  $H$  and  $A$  are almost identical for high values of  $\tan\beta$ , once the  $m_H$  (and therefore  $m_A$ ) is above the critical point  $m_h^{\max}$ . For low values

---

<sup>13</sup>Nevertheless, supersymmetric particles can still affect the branching ratio via loop contribution, e.g. corrections to the fermion mass terms [59].

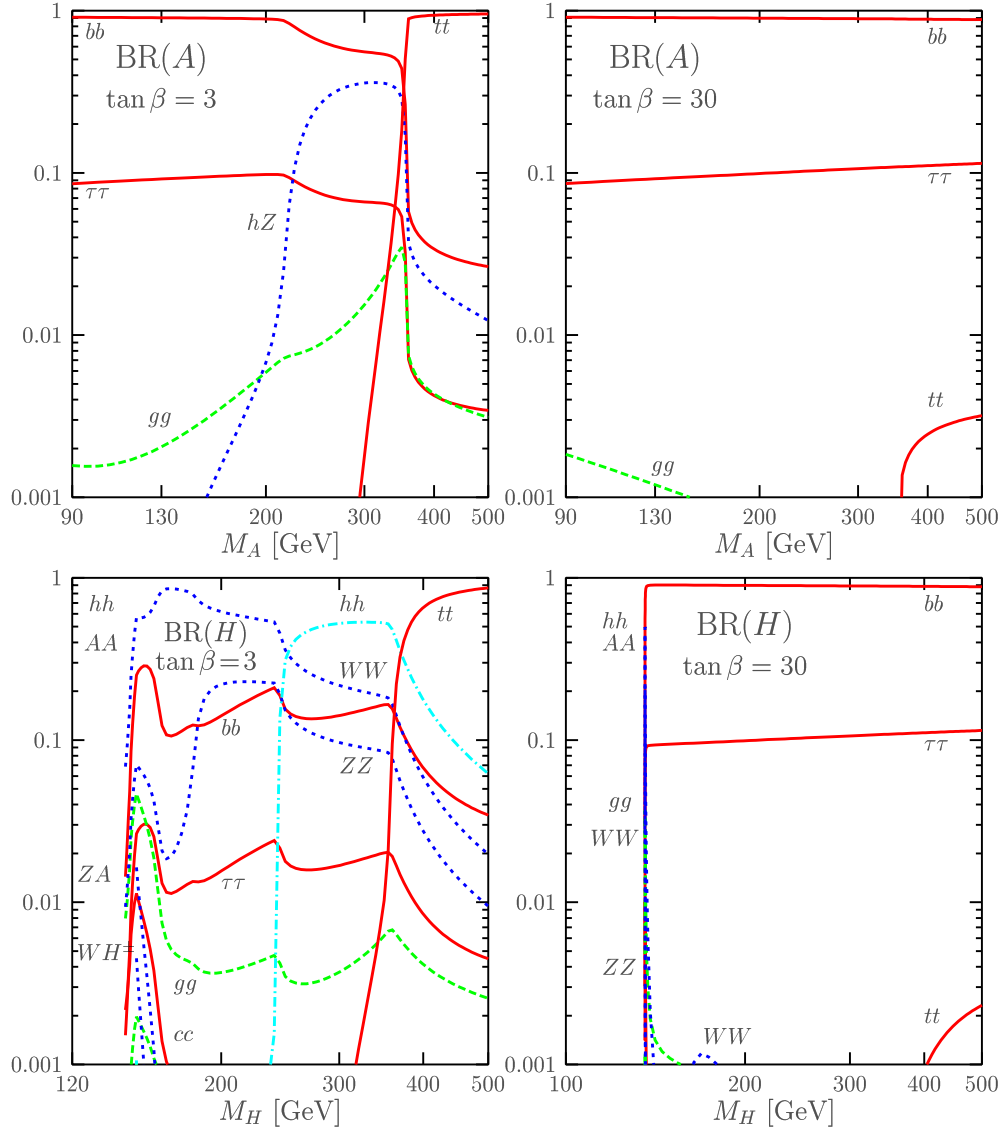


**Figure 2.10:** The development of the branching ratios for the CP-odd Higgs boson  $A$  (top) and the CP-even Higgs boson  $H$  (bottom) are presented as a function of the corresponding boson mass parameter. The branching ratios are shown for a low value of  $\tan \beta = 3$  (left) and a relative large value of  $\tan \beta = 30$  (right). The results are taken from Ref. [59].

of  $\tan \beta$ , the decay spectrum becomes more diverse for both bosons and the differences between  $A$  and  $H$  become more visible due to the different CP behavior of both bosons<sup>14</sup>. In the case of small  $\tan \beta$  values, the  $t\bar{t}$  channel becomes the dominant decay mode for high Higgs masses, because the coupling suppression to up-type fermion is not strong enough to compensate for the increased coupling due to the large top quark mass.

The  $b\bar{b}$  and  $\tau^+\tau^-$  decay channels allow therefore to probe a wide range of the MSSM parameter space, especially in the decoupling limit. Within this thesis the  $\tau^+\tau^-$  decay channel is probed. Although the branching ratio is relatively small compared to the  $b\bar{b}$  channel, the expected background contribution from SM processes is significantly larger for the search based on the  $b\bar{b}$  decay channel compared to the  $\tau^+\tau^-$  decay channel.

### 2.2.6 MSSM Benchmark Scenarios

The large number of additional parameters, introduced by the breaking of SUSY, leads to practical limitations for experimental analyses and their interpretation in the context of SUSY related studies (e.g. searches for new SUSY particles). The high dimensionality of the corresponding parameter space makes a complete scan based on experimental results very difficult. In a benchmark scenario only a small number of SUSY parameters is variable, the rest of the parameters is fixed. This allows a scan over a smaller parameter space and an interpretation of experimental results within the given scenario.

As discussed in Section 2.2.3, the mass parameter of the lightest, CP even, Higgs boson  $h$  can be expressed in terms of the mass of the CP odd Higgs boson,  $m_A$ , the ratio of the vacuum expectation values  $\tan \beta$  and the mass of the Z-boson,  $m_Z$  on tree level. This results in an upper bound of the Higgs boson mass of

$$m_h \leq m_Z. \quad (2.67)$$

Corrections from higher orders in perturbation theory raise the upper bound to  $m_h \lesssim 135 \text{ GeV}$  [74], with an uncertainty of up to 3 GeV.

Radiative corrections allow other particles of the MSSM to add contribution to  $m_h$ , which need to be considered. The dominant contributions originate from interactions to scalar top or scalar bottom particles via the trilinear couplings,  $A_t$  and  $A_b$ , respectively.

$$\mathcal{M}_t^2 = \begin{pmatrix} m_{t_L}^2 + m_t^2 + \cos 2\beta \left( \frac{1}{2} - \frac{2}{3} \sin^2 \theta_w \right) m_Z^2 & m_t X_t^* \\ m_t X_t & m_{t_R}^2 + m_t^2 + \frac{2}{3} \cos 2\beta \sin^2 \theta_w m_Z^2 \end{pmatrix} \quad (2.68)$$

$$\mathcal{M}_b^2 = \begin{pmatrix} m_{b_L}^2 + m_b^2 + \cos 2\beta \left( -\frac{1}{2} + \frac{2}{3} \sin^2 \theta_w \right) m_Z^2 & m_b X_b^* \\ m_b X_b & m_{b_R}^2 + m_b^2 - \frac{1}{3} \cos 2\beta \sin^2 \theta_w m_Z^2 \end{pmatrix}, \quad (2.69)$$

where the parameter  $X_t$  and  $X_b$  contain the trilinear couplings:

$$m_t X_t = m_t (A_t - \mu \cot \beta) \quad (2.70)$$

$$m_b X_b = m_b (A_b - \mu \tan \beta). \quad (2.71)$$

<sup>14</sup>CP invariance restricts the possible decay modes for the CP-odd boson as discussed in the coupling section.

Here the parameter  $\mu$  denotes the Higgs mixing and  $\theta_W$  the weak mixing (Weinberg) angle

$$\cos \theta_W = \frac{m_W}{m_Z}. \quad (2.72)$$

For the benchmark scenarios considered, the masses of the stop and sbottom<sup>15</sup> are assumed to be equal<sup>16</sup> [75]:

$$m_{\tilde{t}_L} = m_{\tilde{t}_R} = m_{\tilde{b}_L} = m_{\tilde{b}_R} := M_{\text{SUSY}}. \quad (2.73)$$

Similar considerations are incorporated for the scalar superpartner of tau leptons and neutrinos and the squarks and sleptons of the first and second generation. Again, the diagonal entries of the mass matrices containing the SUSY breaking terms are assumed to be equal for the stau/sneutrino and for the squarks/sleptons of the first and second generation:

$$m_{\tilde{\tau}_{L/R}} = m_{\tilde{\nu}_\tau} := M_{\tilde{t}_3} \quad (2.74)$$

$$m_{\tilde{e}_{L/R}} = m_{\tilde{\nu}_e} = m_{\tilde{\mu}_{L/R}} = m_{\tilde{\nu}_\mu} := M_{\tilde{t}_{1,2}} \quad (2.75)$$

$$m_{\tilde{u}_{L/R}} = m_{\tilde{d}_{L/R}} = m_{\tilde{c}_{L/R}} = m_{\tilde{s}_{L/R}} := M_{\tilde{q}_{1,2}}. \quad (2.76)$$

The trilinear coupling of the Higgs bosons with tau and stau particles is denoted as  $A_\tau$ .

In addition the light Higgs boson mass depends on the mass of the gluino (at two-loop order corrections),  $m_{\tilde{g}}$ , and the masses of the gauginos  $M_1$  and  $M_2$ . For the scenarios considered, the mass  $M_1$  is fixed at the GUT scale and can be expressed in terms of  $M_2$ :

$$M_1 = \frac{5 \sin^2 \theta_W}{3 \cos^2 \theta_W} M_2. \quad (2.77)$$

The masses of the first and second generation squarks and sleptons have only a minor impact and are fixed to the following values [75] for all benchmark scenarios considered:

$$M_{\tilde{t}_{1,2}} = 1500 \text{ GeV} \quad (2.78)$$

$$M_{\tilde{q}_{1,2}} = 500 \text{ GeV}. \quad (2.79)$$

The couplings to the first and second generation scalar fermions are neglected [75]. They enter the off-diagonal elements of the mass matrices always multiplied with the mass of the corresponding SM fermions and the masses of the first and second generation fermions can be neglected compared to that of the third generation.

Within the context of this thesis, two benchmark scenarios are considered, the  $m_h^{\text{max}}$  and  $m_h^{\text{mod}}$  scenario. The  $m_h^{\text{mod}}$  scenario is furthermore divided into a  $m_h^{\text{mod}+}$  and  $m_h^{\text{mod}-}$  case. In both cases the parameters  $m_A$  and  $\tan \beta$  are free parameters of the benchmark models and the rest of the parameters is fixed. The full list of parameter settings for both scenarios can be found in Table 2.3.

<sup>15</sup>The states  $\tilde{t}_L$ ,  $\tilde{t}_R$ ,  $\tilde{b}_L$  and  $\tilde{b}_R$  are the superpartners to the left and right handed top and bottom quarks, respectively.

<sup>16</sup>The mass parameters of the  $\tilde{t}_L$  and  $\tilde{b}_L$  particles are anyway equal due to gauge invariance under SU(2).

**The  $m_h^{\max}$  benchmark scenario** The  $m_h^{\max}$  benchmark scenario was first introduced within the context of the MSSM Higgs boson searches at LEP [63, 76, 77] in order to derive conservative exclusion limits for  $m_A$  and  $\tan\beta$ . The mixing in the stop sector,  $X_t$ , is adjusted to ensure that the radiative corrections will maximize  $m_h$  as a function of  $\tan\beta$ . With the observation of a possible Higgs candidate with a mass of  $m_{\text{Higgs}}^{\text{obs}} \sim 125.5$  GeV, it seems natural to identify the new particle with the lightest MSSM Higgs boson (within the context of MSSM Higgs searches). The  $m_h^{\max}$  scenario does not really support this interpretation, because  $m_h$  will be (by construction) usually higher (above 130 GeV for  $\tan\beta \geq 10$  [75]). As a result, only a small region in the  $m_A$ - $\tan\beta$  phase-space will allow a light Higgs-boson around 125 GeV. This problem is avoided in the  $m_h^{\text{mod}}$  scenario. However, the  $m_h^{\max}$  scenario is still used to calculate conservative bounds for the MSSM Higgs boson searches and it allows an easy comparison with previous measurements.

Within this thesis an updated version of the  $m_h^{\max}$  scenario [75] is utilized, in which the latest measurements of the top quark mass and limits from direct SUSY searches at the LHC are considered (in particular new limits on gluino searches).

**The  $m_h^{\text{mod}}$  benchmark scenario** The  $m_h^{\text{mod}}$  scenario is a modified version of the  $m_h^{\max}$  scenario, in which the mixing of the stop sector,  $X_t$ , is reduced compared to  $m_h^{\max}$  [75]. This allows a mass of the lightest Higgs boson close to the mass of the observed particle,

$$m_h \approx m_{\text{Higgs}}^{\text{obs}}, \quad (2.80)$$

over a reasonable range in the  $m_A$ - $\tan\beta$  space. Two different version of the scenario were proposed in [75], the  $m_h^{\text{mod}+}$  and  $m_h^{\text{mod}-}$  scenario, in which the sign of  $X_t$  is either positive or negative, respectively. Both scenarios differ in their agreement to other experiment results (which are sensitive to SUSY contributions). The  $m_h^{\text{mod}+}$  tends to provide better results when compared to measurements of the anomalous magnetic dipole moment of the muon ( $g-2$ ), while  $m_h^{\text{mod}-}$  shows a better agreement with measurements in B-physics [75].

Parameter	Unit	$m_h^{\max}$	$m_h^{\text{mod}+}$	$m_h^{\text{mod}-}$
$m_t$	GeV	173.2	173.2	173.2
$M_{\text{SUSY}}$	GeV	1000	1000	1000
$M_{\tilde{l}_3}$	GeV	1000	1000	1000
$m_{\tilde{g}}$	GeV	1500	1500	1500
$M_2$	GeV	200	200	200
$\mu$	GeV	200	200	200
$X_t^{\text{OS}}/M_{\text{SUSY}}$	–	2.0	1.5	-1.9
$X_t^{\overline{\text{MS}}}/M_{\text{SUSY}}$	–	$\sqrt{6}$	1.6	-2.2
$A_X$	–	$A_t = A_b = A_\tau$		

**Table 2.3:** Parameter settings for the  $m_h^{\max}$ ,  $m_h^{\text{mod}+}$  and  $m_h^{\text{mod}-}$  MSSM benchmark scenarios. The parameter  $m_A$  and  $\tan\beta$  are the two remaining variable parameters. The parameter  $X_t^{\text{OS}}$  and  $X_t^{\overline{\text{MS}}}$  are evaluated in the on-shell and  $\overline{\text{MS}}$  scheme, respectively. The results are taken from Ref. [75].





# 3 The ATLAS experiment at the Large Hadron Collider

## 3.1 The Large Hadron Collider

The *Large Hadron Collider* (LHC) [78] is a quasi-circular particle-particle accelerator which is operated by CERN<sup>1</sup>. With a circumference of 26.7 km, the LHC is constructed in the former tunnel of the LEP [79] collider which is located 45 m to 170 m below the surface. The physics program of the LHC involves collisions between either two proton beams with a center-of-mass energy up to  $\sqrt{s} = 14$  TeV or two beams of lead nuclei with energies up to 5.5 TeV per nucleon pair.

Since protons are bound states of quarks and gluons, a collision between two protons will be composed of several sub-interactions between the elementary particles. Although the majority of interactions at the LHC are QCD-based scattering processes, the production of all SM particles is allowed in proton-proton interactions: e.g. the production of electro-weak gauge bosons, top and bottom quarks, Higgs bosons and even possible new resonances predicted by BSM theories. The rate,  $R_{\text{evt}}$ , at which a certain process or event occurs at the LHC is defined by:

$$R_{\text{evt}} = \frac{dN_{\text{evt}}(t)}{dt} = \sigma_{\text{evt}}(pp \rightarrow X) \times L, \quad (3.1)$$

where  $N_{\text{evt}}(t)$  is the expected mean number of events,  $\sigma_{\text{evt}}$  the cross section for the given process and  $L$  represents the *instantaneous luminosity* of the LHC. The luminosity is a machine parameter which depends on the given beam configuration and is a measure for the beam density. The total number of expected events within a certain time interval,  $N_{\text{evt}}(t_0 + \Delta t)$ , can be obtained via integration:

$$N_{\text{evt}}(t_0 + \Delta t) = \sigma_{\text{evt}} \times \int_{t_0}^{t_0 + \Delta t} L dt = \sigma_{\text{evt}} \times L_{\text{int}}, \quad (3.2)$$

where  $L_{\text{int}}$  represents the *integrated luminosity*.

Resonances, which are produced during the proton-proton interactions, will most likely decay into lighter particles until the final decay products are stable enough<sup>2</sup> to reach active detector material. Six main experiments are located along the LHC ring in order to detect and measure the out-coming particle spectra:

---

<sup>1</sup>The *European Organization for Nuclear Research*, "*Conseil Européen pour la Recherche Nucléaire*" (CERN), is located between the French-Swiss border in the near of Geneva, Switzerland. It was founded in 1954 and it is today one of the largest European institutions in the field of particle physics.

<sup>2</sup>Beside particles which are stable at a fundamental level (at the current knowledge) like protons, electrons or photons, also particles with a large enough lifetime are able to reach the active detector elements including pions, kaons, neutrons and muons.

- two high luminosity, multi-purpose detectors: ATLAS [80] and CMS [81], which are designed for proton-proton collisions up to an instantaneous luminosity of  $L = 10^{34} \text{ cm}^{-2} \text{ s}^{-1}$  and lead-lead collisions at a design luminosity of  $L = 10^{27} \text{ cm}^{-2} \text{ s}^{-1}$ ,
- one experiment with focus on heavy ion physics: ALICE [82],
- one experiment specialized to study  $B$  hadron physics (with a focus on rare decays and CP violating processes) in proton-proton collisions: LHCb [83] at a design luminosity of  $L = 10^{32} \text{ cm}^{-2} \text{ s}^{-1}$ ,
- the LHCf experiment [84] which allows measurements of neutral particle spectra at high regions in pseudorapidity ( $\eta > 8.4$ ),
- and the TOTEM [85] experiment, which allows measurements of the total proton-proton collision cross section using a luminosity independent method<sup>3</sup> as well as elastic and diffractive scattering processes in proton-proton collisions.

In contrast to particle- anti-particle accelerators like Tevatron or LEP, the LHC is a particle-particle accelerator and therefore needs two separated rings to accommodate two counter-rotating proton/lead beams. The LHC can be subdivided into 16 sections: eight arched and eight straight sections which are arranged in an alternating pattern. A schematic overview of the LHC can be found in Figure 3.1. Four of the straight segments contain the main experiments<sup>4</sup> and the corresponding beam crossing points. Two of these segments also contain the injection structures for both beams. The rest of the straight elements contain several supporting devices necessary for the accelerator operations: e.g. collimation systems, radio-frequency (RF) cavities for beam acceleration and a beam dump system [78].

A complex, superconducting magnet system, based on NbTi Rutherford cable technology [78], is utilized at the LHC to control the direction and the spread of the two beams. During the LHC operation the magnets are cooled down below 2 K, using superfluid helium, to ensure a superconducting state, generating magnetic fields with a strength<sup>5</sup> up to 8 T. Since two independent beam lines are necessary for a particle-particle collider, most magnets are designed following a “two-in-one” concept in which both beam lines share the same cold mass and cryostat system. The bending of the beams is achieved by 1232 dipole magnets which are primarily implemented in the arched sections of the LHC. In addition  $\sim 4800$  corrector magnets are installed to control the properties of the beams including quadrupole, sextupole as well as octupole designs.

The probability for scattering processes between accelerated protons and the remaining gas atoms inside the beam pipes need to be reduced to ensure a reasonable beam lifetime and to avoid additional background sources in the experiments. The reduction is achieved by a beam vacuum system, which ensures residual gas densities normalized to hydrogen below  $10^{15} \text{ H}_2 \text{ m}^{-3}$  in the beam pipes and below  $10^{13} \text{ H}_2 \text{ m}^{-3}$  around the interaction points of the experiments [78].

---

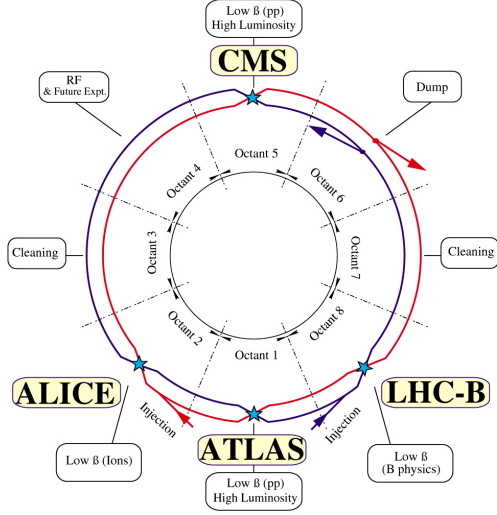
<sup>3</sup>The total proton-proton cross section and the luminosity are measured simultaneously with the TOTEM detector [85].

<sup>4</sup>The TOTEM experiment is embedded within the CMS detector and the LHCf experiment is located near the ATLAS detector.

<sup>5</sup>For comparison: other accelerator experiments, e.g. Tevatron [87], were also using superconducting NbTi technology, usually cooled down to  $\sim 4.2 \text{ K}$  with magnetic fields up to 5 T.

In addition to the vacuum system for the beam pipes, two more vacuum systems are utilized at the LHC for insulation purposes of the cryogenic and helium systems. The vacuum requirements for the insulation systems are looser compared to the beam vacuum, requiring a pressure around  $10^{-6}$  mbar at operation temperature.

### LHC LAYOUT



CERN AC\_EI2-4A\_V18/9/1997

**Figure 3.1:** Schematic overview of the LHC layout in the former LEP tunnel [86].

Before the proton bunches are injected into the LHC rings, they are pre-accelerated in several substeps using the accelerator complex at CERN, illustrated in Figure 3.2. The protons, which are acquired by ionization of hydrogen, are first accelerated up to 50 MeV in the LINAC2 accelerator. Afterwards the protons are subsequently passed to the *Proton-Synchrotron-Booster* (PSB), the *Proton-Synchrotron* (PS) and the *Super-Proton-Synchrotron* (SPS) which accelerate the protons up to an energy of 1.4 GeV, 25 GeV and 450 GeV [78], respectively. From the SPS the protons are injected into the LHC and accelerated to the aimed center-of-mass energy.

bunches with a spacing time of  $t_{bs} \approx 25$  ns between each bunch [78], which leads to a bunch crossing frequency of

$$f_{bc} = \frac{1}{t_{bs}} = 40 \text{ MHz} . \quad (3.3)$$

The expected transverse (normalized) emittance,  $\epsilon_n$ , of a proton bunch is around  $3.75 \mu\text{m}$  [78]. Assuming that the beam density follows a Gaussian profile, the instantaneous luminosity of the LHC can be expressed in the following term:

$$L = \frac{N_b^2 n_b f_{rev} \gamma_r}{4\pi \epsilon_n \beta^*} F , \quad (3.4)$$

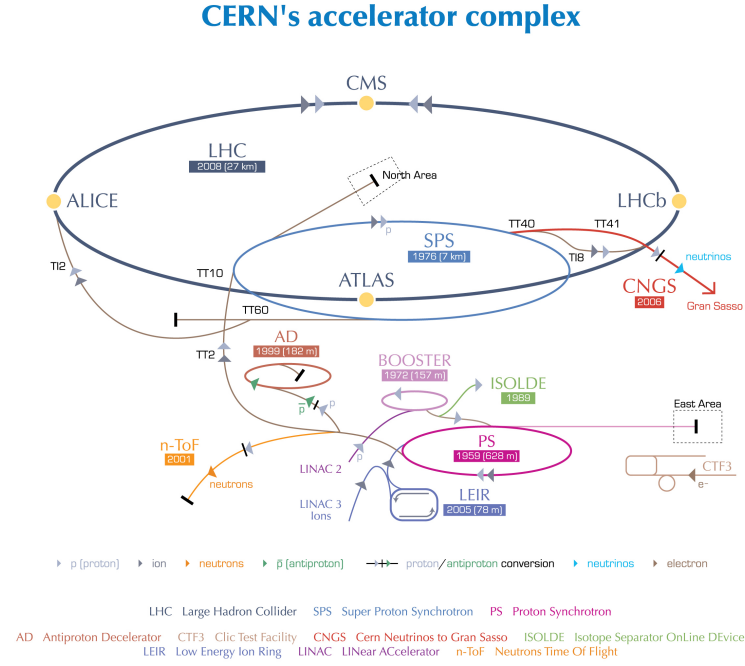
where  $f_{rev}$  represents the revolution frequency,  $\gamma_r$  the relativistic gamma factor and  $\beta^*$  the value of the beta function at the collision point [78]. Since both beams are running in separate beam lines, it is necessary to cross both beams at the desired interaction point in order to trigger the collisions. Subsequently the proton bunches will not collide head on but instead under a certain

<sup>6</sup>During the first years of operation, the LHC was running at much lower luminosities (and center-of-mass energies) and therefore lower number of bunches and larger time spacing.

angle, which affects the instantaneous luminosity. This effect is considered by the correction factor  $F$ . During the crossing of two proton bunches, several proton-proton interactions are possible. The effect of multiple proton-proton collisions is usually referred to as *pile-up*. The expected number of collisions per bunch crossing,

$$E[N_{\text{coll}}] = \langle N_{\text{coll}} \rangle = \mu, \quad (3.5)$$

strongly depends on the beam parameter setting chosen.



European Organization for Nuclear Research | Organisation européenne pour la recherche nucléaire

© CERN 2008

**Figure 3.2:** Schematic overview of the accelerator complex at CERN [88].

The pile-up interactions introduce a new source of unavoidable background by adding additional contributions of tracks and energy deposits which need to be taken into account during the reconstruction, calibration and identification of particles in the experiments.

## 3.2 The ATLAS experiment

The ATLAS<sup>7</sup> detector [80] is a multi-purpose particle detector located at point 1 of the LHC ring. ATLAS was designed to allow a wide range of high-precision measurements and searches for new physics including:

1. precision measurements of processes predicted by the Standard Model, e.g. soft/high energy QCD interaction, top and bottom quarks physics, tau lepton physics, gauge boson interactions,
2. search for and measurement of the SM Higgs boson,
3. various searches for physics beyond the SM (e.g. SUSY, heavy gauge bosons, extra dimensions),
4. studies of matter at extreme densities using nucleus-nucleus interaction.

To achieve the given goals, the ATLAS detector measures the outgoing particle spectra of proton-proton or nucleus-nucleus collisions over the full azimuthal angle and a wide range of the polar angle. The overall layout of the ATLAS detector can be found in Figure 3.3.

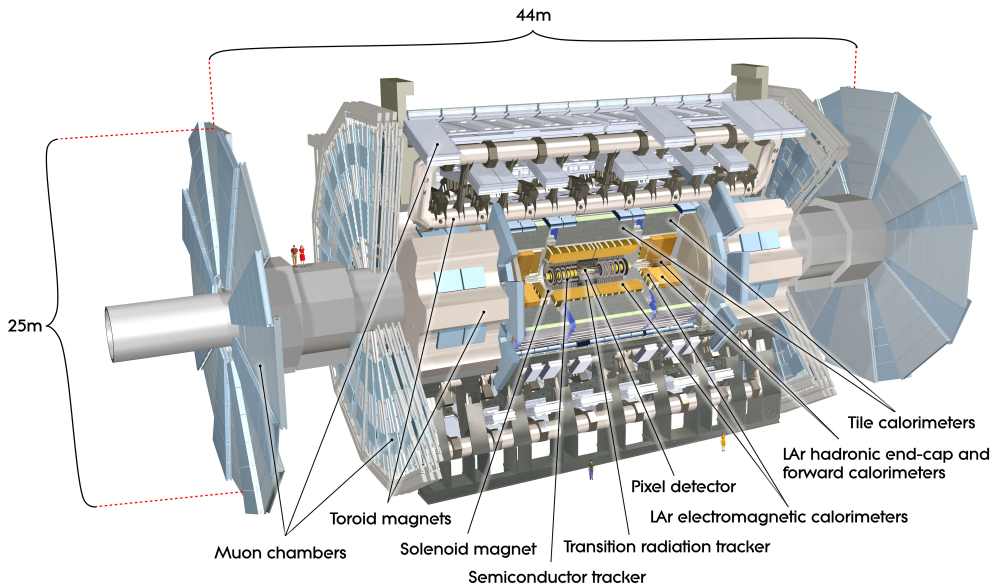


**Figure 3.3:** Schematic overview of the ATLAS detector [89].

The detector itself consists of several subcomponents, each with different specifications, which are build up layer by layer around the beam pipe. The inner most part (close to the beam pipe) is the *Inner Detector* (ID) which allows the reconstructions of charged particle trajectories (*tracking*), the momentum and charge measurement of particles and the reconstruction of decay vertices. A momentum reconstruction of charged particles from the trajectories is only possible if the particles are bent within a magnetic field inside the ID. The ID is therefore enclosed by a

<sup>7</sup>ATLAS is an abbreviation for “**A** **T**oroidal **L**HC **A**pparatu**S**”.

solenoid, which provides a homogenous magnetic field of  $\sim 2$  T.

The inner detector system is enclosed by a calorimeter system which can be separated in two main sub-systems: an electromagnetic calorimeter and a hadronic calorimeter. The majority of charged and neutral particles will be absorbed in the calorimeters, allowing an energy and position measurement of the incoming particles.

Muons, above a certain energy level, and neutrinos are the only SM particles which are expected to pass through the electromagnetic and hadronic calorimeter. Neutrinos only participate in the weak interaction and the probability for an interaction between a neutrino and the detector material is negligible. Most neutrinos will therefore leave the detector unregistered, which results in a missing transverse momentum. Muons, in contrast, can be detected via the muon spectrometer (MS) which surrounds the calorimeter system. The spectrometer consists of tracking chambers installed in a magnetic field of about  $\sim 0.5$  T to  $1.0$  T which is provided by an air-core toroid system.

### 3.2.1 Coordinate System

The nominal interaction point (IP) of the two particle beams defines the origin of the coordinate system of the ATLAS detector. In Cartesian coordinates, the  $z$  axis is defined along the beam axis and the  $x$  and  $y$  axes span the plane transverse to the beam with the  $y$  axis being defined as pointing upwards and the  $x$  axis pointing towards the center of the LHC ring. Consequently, the azimuthal angle,  $\phi$ , describes the position of a particle around the beam axis, while the polar angle,  $\theta$ , defines the angular distance between a particle and the beam axis (see Figure 3.4). It is

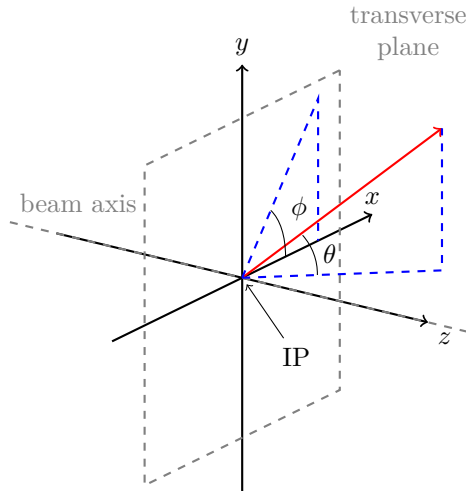


**Figure 3.4:** Schematic overview of the ATLAS coordinate system.

common practice in hadron collider physics to use the rapidity

$$y = \frac{1}{2} \ln \left( \frac{E + p_L}{E - p_L} \right), \quad (3.6)$$

or pseudorapidity

$$\eta = -\ln \left[ \tan \left( \frac{\theta}{2} \right) \right] \quad (3.7)$$

instead of  $\theta$  to parametrize the angular distance of particles to the beam, where  $E$  represents the total energy of the corresponding particle and  $p_L$  its momentum along the beam axis. If the mass of a particle is negligible compared to its momentum, the rapidity converges to the pseudorapidity:

$$\lim_{p \gg m} y(m) \simeq \eta. \quad (3.8)$$

In most cases,  $\eta$  is a reasonable approximation for the rapidity, because the masses of the particles involved (electrons, muons, pions, etc.) are usually small compared to their momenta at the LHC, which ranges from several GeV up to a few TeV. Of course, this approximation is invalid for potential high mass objects like particle jets.

The rapidity difference between two particles,  $\Delta y = y_i - y_j$ , is invariant under a Lorentz boost along the beam axis and therefore independent of the chosen reference frame (same holds for the pseudorapidity in the limit given in Eq. (3.8)). This characteristic is particularly useful at hadron colliders where the incoming partons carry an, a priori, unknown fraction of the protons longitudinal momentum, resulting in an unknown boost between the rest frame of the proton-proton collision and the laboratory frame. The distance,  $\Delta R_{ij}$ , between two points in the  $\eta$ - $\phi$  plane is given by:

$$\Delta R_{ij} = \sqrt{(\Delta \eta)^2 + (\Delta \phi)^2} = \sqrt{(\eta_i - \eta_j)^2 + (\phi_i - \phi_j)^2}. \quad (3.9)$$

Since the longitudinal momentum of the incoming partons is a priori unknown, most physical quantities are expressed by their projections in the transversal plane. The most common quantity is the transverse momentum,  $p_T$ , of a particle, with

$$p_T = \sqrt{p_x^2 + p_y^2}. \quad (3.10)$$

The transverse momentum of the incoming partons is (usually) assumed to be negligible due to the high boost along the beam axis.

### 3.2.2 Inner Detector

The ATLAS inner detector [90, 91] consists of three separate sub-detector elements: (from innermost to outermost element) a *semiconductor pixel detector* [92], a *semiconductor tracker* (SCT) based on silicon microstrips [93] and a drift straw tube [94] based *transition radiation tracker* (TRT) [95, 96].

The pixel detector is the innermost part of the ATLAS detector providing the first active detector material for the incoming particles. Silicon is used as the active material for the high-resolution pixel elements, with an area of about  $50 \times 400(600) \mu\text{m}^2$  per pixel. The modules are mounted on

three cylinders<sup>8</sup>, which are constructed parallel and layer by layer around the beam axis (*barrel*), and on  $2 \times 3$  disks (*end-caps*, with three disks on each detector side), which are assembled perpendicular to the beam pipe.

The SCT detector modules are assembled similarly to the pixel detector: four concentric layers in the barrel and  $2 \times 9$  disks in the end-caps. Instead of single pixels, strips of single sided p-in-n semiconductor sensors are utilized with a pitch of  $\sim 80 \mu\text{m}$ . Both, the pixel and SCT detector, cover a pseudorapidity range up to  $|\eta| = 2.5$  and the full azimuthal space. The intrinsic lateral<sup>9</sup> accuracies for the semiconductors are  $10 \mu\text{m}$  and  $17 \mu\text{m}$ , for pixel and SCT respectively, and  $115 \mu\text{m}$  and  $580 \mu\text{m}$  in the longitudinal<sup>10</sup> direction.

The SCT is followed by the TRT detector, which consists of several layers of drift tubes. Each tube has a diameter of about 4 mm and contains a Xe or Ar based gas mixture. Comparable to the pixel and SCT detector, the TRT tubes are arranged in a cylindrical shape around the beam axis in the barrel region (the tubes are assembled parallel to the beam) and perpendicular to the beam in the end-caps. The TRT covers a pseudorapidity range up to  $|\eta| = 2.0$  (and the full azimuthal space) providing a longitudinal accuracy of  $130 \mu\text{m}$  with an average number of 36 straw tube signals per charged particle trajectory. Transition radiation material in form of polypropylene fibres and foils embeds the tubes in the barrel and end-cap parts. A charged particle at high relativistic  $\gamma$  values will emit transition radiation photons ( $E_\gamma \sim \mathcal{O}(1 - 10) \text{ keV}$ ) when passing two materials with different dielectric constants. The photons are absorbed by the gas mixture resulting in additional energy deposition in the straw tubes, which can be used for particle identification, in particular for the separation between electrons and pions [98]. In total, the whole ID provides approximately  $87 \times 10^6$  readout channels.

### 3.2.3 Calorimeter System

Calorimetry<sup>11</sup> at the ATLAS detector is performed using different sampling calorimeter technologies. The calorimeter systems can be classified into the following main sub-detectors: the electromagnetic liquid-argon (LAr) calorimeter (EM) [99], the electromagnetic end-caps (EMEC) [100], the central hadronic tile calorimeter (tile) [101], the hadronic end-cap calorimeter (HEC) [102] and the forward calorimeter system (FCal) [103]. An overview of the structure can be found in Figure 3.5. All systems are sampling calorimeters consisting of alternating layers of absorber material and active medium.

The innermost calorimeter system is the EM calorimeter, which primarily focuses on the energy measurement of electrons and photons. It is directly mounted behind the ID and consists of a barrel part and two end-caps (one on each detector side), which provide a coverage of  $|\eta| < 1.475$

---

<sup>8</sup>The initial three layer design for the pixel detector had been used for the first data taken periods in the years 2009 - 2012. During the upgrade phase in 2013/14 an additional pixel layer (*B-layer*) [97] was installed, which has been used for the new data taking period in 2015/16.

<sup>9</sup>Which corresponds to the  $R - \phi$  plane (in the spherical coordinate system) for the barrel and end-cap region.

<sup>10</sup>Which corresponds to the  $z$  axis (beam axis) for the barrel region and the  $R$  axis (in the spherical coordinate system) for the end-caps.

<sup>11</sup>The basic concept of calorimetry is the absorption of particles and the subsequent measurement of the deposited energies. Incoming particles will interact with the detector material via the electromagnetic or strong interaction, which will produce shower of secondary particles inside the calorimeter systems. Usually not only the total amount of deposited energy is of interest but also the shape and position of the shower.



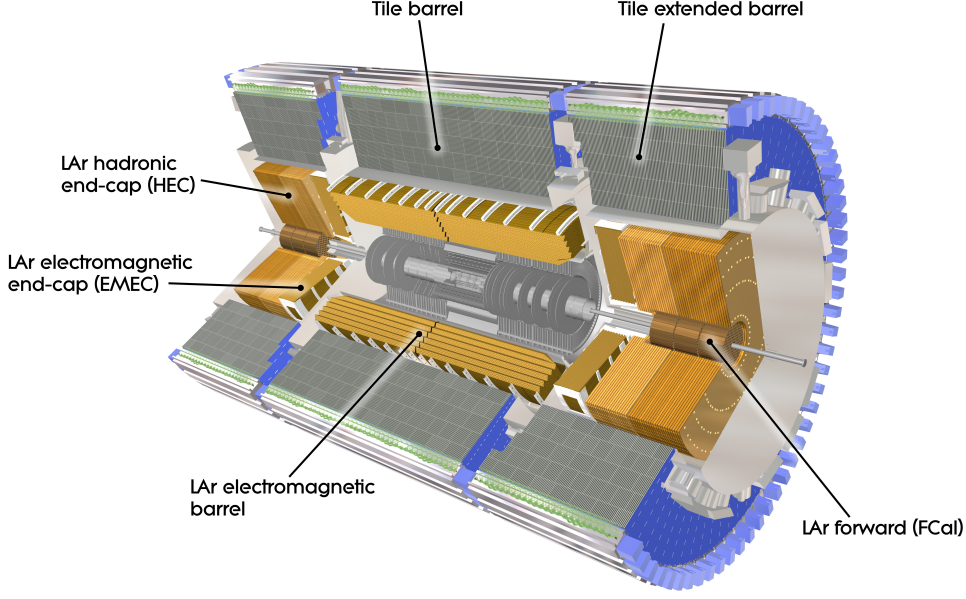


**Figure 3.5:** Schematic overview of the ATLAS calorimeter system [104].

and  $1.375 < |\eta| < 3.2$ , respectively. The barrel part itself is divided into two separate sub-barrels which are mounted around the beam pipe with a small gap of 4 mm around  $z = 0$ . Like the ID components, the end-cap modules of the EM calorimeter are mounted on wheels (two wheels per end-cap), which are assembled in a cryostat system. Planes of lead and LAr, which is filled in gaps in between the lead plates, are arranged in an accordion shape which provides a full coverage in the azimuthal direction and allows a fast signal extraction at the copper electrodes. The lead plates are the absorber material for the incoming particles while the LAr operates as the active material. The modules are segmented into *cells* of readout circuits [105], in which the granularity of the cells varies between the different layers and modules. Typical cell sizes ranges from 0.0031 to 0.1 in  $\Delta\eta$  and 0.025 to 0.1 in  $\Delta\phi$ . The granularity typically decreases with increasing distance to the beam axis [80, cha. 5].

The hadronic tile calorimeter can be divided into a central barrel ( $|\eta| < 1.0$ ), which encloses the barrel part of the EM calorimeter and two extended barrels ( $0.8 < |\eta| < 1.7$ ), one on each side enclosing the corresponding cryostat of the EM calorimeter (see Figure 3.5). An alternating structure of steel plates and scintillator tiles is utilized, with the steel as absorber material for the incoming hadrons and the scintillators as active material. The tiles are arranged around the beam axis with a perpendicular alignment towards the beam pipe, allowing an (almost) full coverage in the azimuthal direction. Particles passing through the scintillator tiles will induce scintillation light (ultraviolet spectrum) [80] which is collected via fibres at the edges of the tile modules. The wavelength of the incoming light is shifted toward higher values and finally detected using photomultiplier tubes. Like the EM calorimeter, the tile calorimeter is segmented into cells (defined by a corresponding group of fibres) with sizes of  $(0.1 - 0.2) \times 0.1$  in  $\Delta\eta \times \Delta\phi$ . The gaps between the central barrel and the extended barrels (*crack-regions*) are necessary to

accommodate services and power supply structures for the ID and the EM calorimeter, but cause a loss in precision of the energy measurement due to the inactive material. This loss is partly recovered using the *Intermediate Tile Calorimeter* (ITC) [101] which is located as an extension of the extended barrel inside the gap.

The hadronic end-cap sampling calorimeters are located behind the EMEC, sharing the same cryostat systems. Each HEC consists of two wheels of copper plates (with a thickness of 25 mm to 50 mm for the front and rear wheel, respectively) with LAr filled gaps (8.5 mm) in between as active medium. The wheels are mounted perpendicular to the beam axis and extend the coverage of the hadronic calorimeter to  $1.5 < |\eta| < 3.2$ . Readout cells of the HEC are of the order of  $0.1 \times 0.1$  in  $\Delta\eta \times \Delta\phi$  for  $|\eta| < 2.5$  and  $0.2 \times 0.2$  for  $|\eta| > 2.5$ , ensuring a higher granularity for regions covered by the ID.

The forward calorimeter is integrated in the cryostat systems of the end-caps and enclosed by the HEC. It covers the very forward region of the detector ( $3.1 < |\eta| < 4.9$ ) which is especially important for the measurement of the missing transverse energy,  $E_T^{\text{miss}}$ , targeting a resolution of  $\Delta E_T^{\text{miss}}/E_T^{\text{miss}} < 10\%$  [103]. The high particle flux in the very forward regions of the detector sets strong requirements to radiation hardness of the materials and the design of the calorimeter. The FCal is a sampling calorimeter which uses liquid argon as active material. Three modules are assembled per end-cap: the first module utilizes copper as absorber material and is designed primarily as electromagnetic calorimeter, while the second and third module are designed as hadronic calorimeter utilizing tungsten as absorber. The absorber materials are formed as a matrix of tubes parallel to the beam pipe. Electrodes in form of rods are centered inside the tubes, while the gap between the rod and the tube is filled with the LAr. This structure allows very small LAr gaps ( $\sim 0.25$  mm) which are necessary to prevent problems with ion accumulation<sup>12</sup>. The readout cell dimensions for the FCal are  $0.1 \times 0.1$  in the front module and  $0.2 \times 0.2$  in the back modules [103].

Overall, the ATLAS calorimeter system provides a (almost) hermetic coverage in the azimuthal direction and up to 4.9 in pseudorapidity with a total number of  $\sim 192\,320$  readout channels. It is built large enough to contain the full sub-particle showers for the vast majority of incoming particles. This ensures a full reconstruction of the particle energies and directions, shields the succeeding muon spectrometer from possible punch-through and provides the input for the calorimeter based trigger systems.

The performance and resolution of the ATLAS calorimeter system during the first years of data taking are discussed in the context of particle reconstruction and calibration in Chapter 4.

---

<sup>12</sup>Ionizing particles passing through the LAr will create free electron and argon ion pairs, in which the ions have a slower drifting velocity inside the LAr compared to the electrons. An increasing rate of incoming particles can cause an accumulation of ions inside the LAr gap and thereby create disturbances of the electric field inside the gap leading to a decrease in performance [106].

### 3.2.4 Muon Spectrometer

The ATLAS muon spectrometer [107] is the outermost component of the full detector system surrounding the tile barrel calorimeter and the cryostats for the EMEC, HEC and FCal. It consists of several layers of tracking chambers and trigger modules in order to perform measurements on muons, with an intended momentum resolution of  $\sim 10\%$  for an energy of 1 TeV. An schematic overview of the muon system is presented in Figure 3.6.

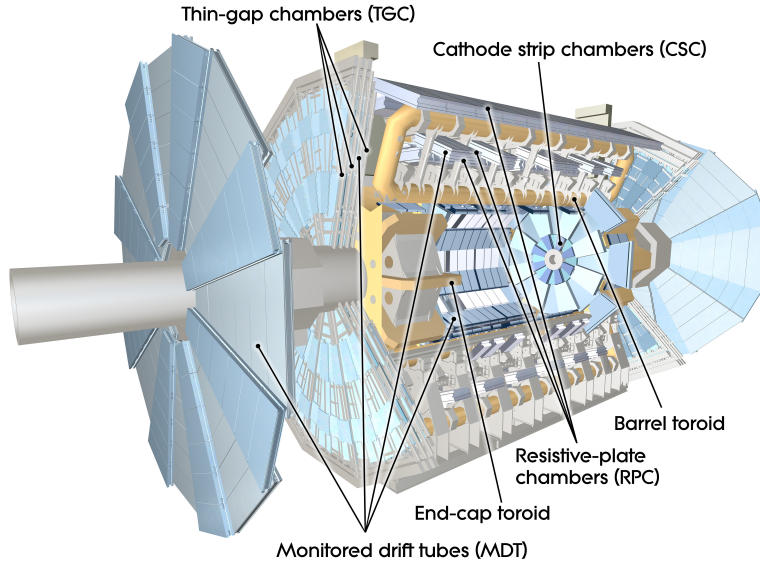


**Figure 3.6:** Schematic overview of the ATLAS muon spectrometer [108].

Like the ID and the calorimeter systems, one differentiates between three sub-elements: one barrel part and two end-caps (one for each detector side). Within the barrel part of the muon systems, the chambers are assembled on three concentric, cylindrical supporting structures around the beam pipe, with a distance of  $\sim 5$  m, 7.5 m and 10 m from the beam axis, respectively. The end-cap chambers are mounted on four wheels per end-cap, which are assembled perpendicular to the beam pipe. The whole muon spectrometer provides a coverage up to  $|\eta| = 2.7$ , except for a gap around  $|\eta| \simeq 0$  which is used for service structures of the ID, the solenoid magnet and the calorimeter system.

Magnetic fields are provided by three air-core toroid systems, with each toroid consisting of eight coils. Using an air-core design reduces to amount of dead material for the traversing particles. The barrel toroid coils are arranged in a symmetric structure around to beam pipe with a separate cryostat system for each coil, while the end-cap toroid systems are arranged between the end-cap chamber wheels using a single cryostat system for each end-cap. The provided *bending power*<sup>13</sup> of the magnetic system is 1.5 T m to 5.5 T m for the barrel toroid and about 1.0 T m to 7.5 T m within the end-cap systems.

<sup>13</sup>The bending power is defined as the integral of the magnetic field over the trajectory of a particle with infinite momentum,  $\int B dl$ . The integration is performed from the innermost to the outermost part the muon system [80].

Four different technologies are deployed for the muon chambers: the tracking is performed using *Monitored Drift Tubes* (MDTs) and *Cathode Strip Chambers* (CSCs) while the trigger system utilizes *Resistive Plate Chamber* (RPCs) in the barrel part and *Thin Gap Chambers* (TGCs) in the end-cap parts.

The MDTs are the main elements within the muon tracking system. Within the innermost layer, the MDTs cover a range up to  $|\eta| = 2.0$  and are replaced with CSCs in the end-caps for the very forward region, while the remaining layer in barrel and end-caps are completely assembled with MDTs. A MDT chamber consist of drift tubes, of about  $\sim 30$  mm in diameter, filled with an Ar/CO<sub>2</sub> gas mixture. The tubes are usually combined in  $2 \times 3(4)$  tube layers (2 layer bundles with 3-4 tube layers per bundle) and are mounted along the azimuthal direction. Each tube provides a resolution of  $80 \mu\text{m}$  which combines to an average resolution of  $30 \mu\text{m}$  to  $35 \mu\text{m}$  per MDT chamber, depending on the number of tube layers.

The CSCs replace the MDT in the very forward region of the innermost end-cap layer, due to the risk of radiation damage in the MDT caused by the increase particle flux<sup>14</sup> compared to the barrel region or the outside layers. Each CSC chambers consist of four planes: each plane works as multiwire proportional chambers using a Ar/CO<sub>2</sub> gas mixture, in which the wires are mounted radially to the beam axis. The cathodes are partitioned into strips of  $\sim 1.5$  mm to  $1.6$  mm (separated by an  $0.25$  mm gap) either perpendicular or parallel to the wire direction, to provide information in both directions. The signal induced by an incoming track is usually distributed along 3 to 5 strips. This setup allows a resolution of  $60 \mu\text{m}$  in the bending plane and about  $5$  mm in the azimuthal direction per CSC chamber.

The trigger chambers are used to provide fast tracking information about muons in the  $\eta$ - $\phi$  plane, which can be used for the hardware level trigger systems. Trigger information is provided for  $|\eta| < 2.4$  and the full azimuthal direction. The measurements in the trigger chambers are also used to complement the measurements in the MDTs, especially the measurement in the azimuthal direction. The barrel trigger system ( $|\eta| < 1.05$ ) consists of RPCs which are mounted below or above the corresponding MDT module on each of the three cylindrical supporting structures of the barrel muon system. Each RPC consists of two independent layers, with each layer consisting of two parallel resistive plates with a gas filled gap of  $2$  mm in between. The readout is performed via strips in  $\eta$  and  $\phi$  with a strip width of about  $25$  mm to  $30$  mm and a separation of  $2$  mm between the strips.

The trigger end-cap systems utilize TGCs, which are mounted on two layers close to the inner layer of the end-cap tracking chambers and on seven layers near the middle layer of the MDT end-caps. In contrast to the RPC, which is designed without wires, the TGCs are multiwire proportional chambers with a gas gap of about  $2.8$  mm and  $1.8$  mm distance between the single wires. While the signal of the wire is used to measure the particle coordinate in the bending plane, radially aligned readout strip with a resolution of  $2$  mrad to  $3$  mrad are utilized to measure the azimuthal coordinate.

---

<sup>14</sup>The MDTs are designed for particles flux densities up to  $150 \text{ Hz cm}^{-2}$  while the CSCs can be safely operated up to  $1000 \text{ Hz cm}^{-2}$  [80].

The entire muon spectrometer provides about 370 000 readout channels for the tracking systems and 677 000 channels for the trigger systems. The performance of the spectrometer in terms of muon reconstruction and identification is discussed in Section 4.4.

### 3.3 LHC and ATLAS performance during Run 1

The concept for the LHC was first introduced during a workshop in Lausanne in 1984 [109], followed by the letter of intent for the ATLAS and CMS detector in 1992. The technical design reports for both experiments were approved in 1997. After more than one decade of deployment, the last LHC magnet was finally mounted in the year 2007. In 2008, the deployment for both the ATLAS and CMS experiment was completed and on September 10 the first proton-proton beam was circulated through the LHC ring. Nine days after the first beam, an incident [110] occurred during a power test, leading to mechanical damage on the LHC ring itself and to a leakage of helium into the LHC tunnel. This incident led to a significant delay (over one year) of the data taking plans. The damaged magnets had been replaced in April 30, 2009 and proton beams have been circulated on November 20. Beginning with December 16 in 2009, the first data taking periods took place with a maximum center-of-mass energy of  $\sqrt{s} = 2.36$  TeV.

After a short technical stop, the ATLAS experiment performed measurements of proton-proton collisions at  $\sqrt{s} = 7$  TeV during the years 2010 and 2011 and continued at a center-of-mass energy of  $\sqrt{s} = 8$  TeV during 2012. These years of the first data taking are commonly referred to as Run 1. The center-of-mass energies during Run 1 are settled significantly below the design energy of  $\sqrt{s} = 14$  TeV, as a consequence of the incident in 2008. Starting February 2013, a long shutdown period started allowing an extensive maintenance of the LHC ring itself and the experiments as well as upgrades to ensure a safe operation of the LHC at higher center-of-mass energies and to improve the performance of the experiments. The new data taking period started on June 2015, using proton-proton collisions at  $\sqrt{s} = 13$  TeV.

Within the context of this thesis, data samples from all three years of operation during Run 1 are utilized: the 2010 samples are used for the underlying event analyses (see Chapter 5), the 2011 samples for MSSM Higgs boson searches (see Chapter 6) and the 2012 measurements for optimization studies on tau identification algorithms (see Chapter 4).

The details of the data taking periods of proton-proton collisions during Run 1 at  $\sqrt{s} = 7$  TeV and  $\sqrt{s} = 8$  TeV are discussed in the following section. Details of the nucleon collision runs as well as special runs at lower center-of-mass energies are omitted and can be found in Ref. [111].

#### 3.3.1 Data taking during the years 2010 to 2012 at the ATLAS experiment

The first injection into the LHC ring took place in February 27, 2010, with the first proton-proton collisions happening under stable beam conditions on March 30 at a center-of-mass energy of  $\sqrt{s} = 7$  TeV (3.5 TeV per proton beam). During 2010, the LHC machine delivered a total integrated luminosity of  $L_{\text{int}} \simeq 45 \text{ pb}^{-1}$  [112] of which roughly  $37 \text{ pb}^{-1}$  are usable for physics analyses. The 2010 period is characterized by a relatively large bunch spacing time of  $t_{\text{bs}} = 150 \text{ ns}$  and low number of pile-up interactions of

$$N_{\text{coll}}^{\text{max}} \sim 5, \quad (3.11)$$

which makes the 2010 dataset preferable for the underlying event analysis (see Section 5.1.3 for details). The data taking period ended on October 25 for the 150 ns bunch spacing configuration. On October 31 a 50 ns bunch spacing operation was tested [111].

After a technical stop during the New Year break, the data taking continued at  $\sqrt{s} = 7$  TeV during 2011 beginning February 19 until October 7. The 2011 data taking is characterized by a reduce bunch spacing time compared to 2010 with a spacing of  $t_{bs} = 50$  ns during the bulk of the year<sup>15</sup> [111]. The instantaneous luminosity was increased by a factor of 18 (in peak luminosity), which results in a total delivered luminosity of  $5.5 \text{ fb}^{-1}$  [112], from which  $4.5 \text{ fb}^{-1}$  are usable for physics analyses. An additional consequence of the increased luminosity is an increased number of pile-up events of up to  $\sim 20$  [112].

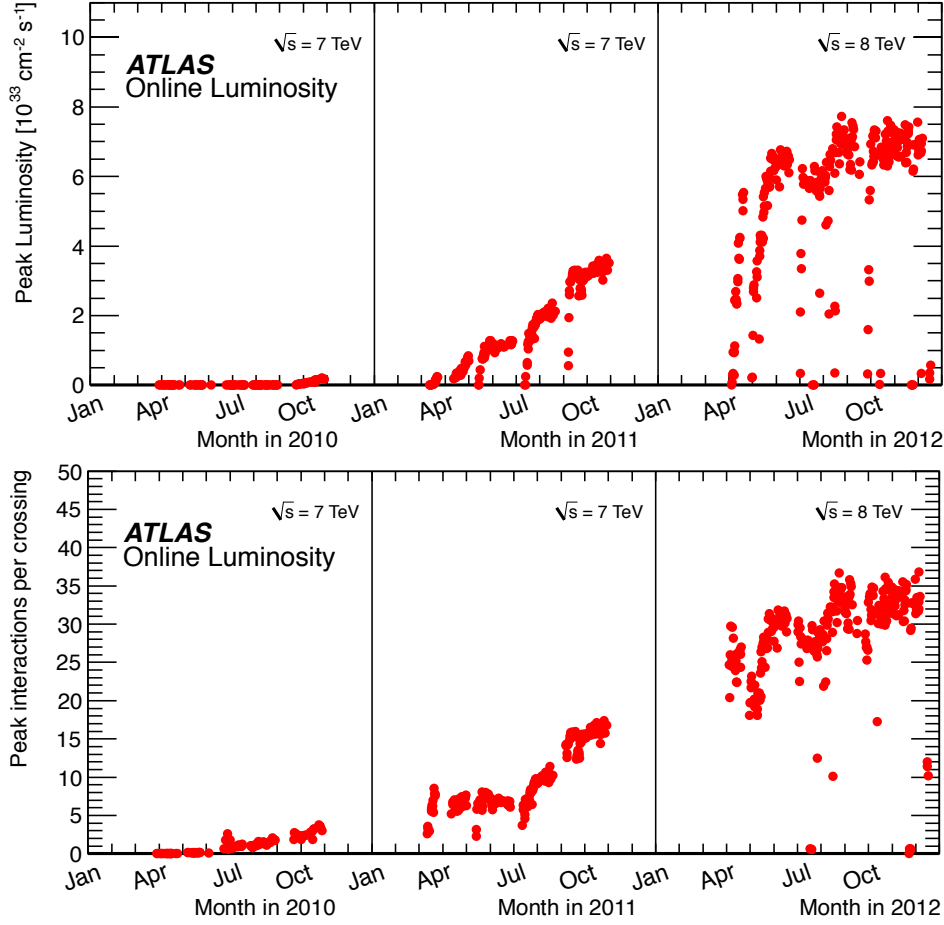


**Figure 3.7:** The top figure presents the peak luminosity for proton-proton interaction and the bottom figure the peak interaction per bunch crossing at the ATLAS experiment, both as a function of time. The distributions are shown for the year 2010 (left), 2011 (middle) and 2012 (right), respectively. Both results are taken from Ref. [113].

In 2012, the center-of-mass energy provided by the LHC has been increased from 7 TeV to 8 TeV (4 TeV per proton beam). The physics program for proton-proton beams in 2012 started on May 4 and ended on December 17, delivering a total luminosity of  $22.8 \text{ fb}^{-1}$ , from which  $20.3 \text{ fb}^{-1}$  are

<sup>15</sup>A few periods had been performed with  $t_{bs} = 75(25)$  ns at the start(end) of the 2011 run.

usable for physics analyses. Similar to the 2011 period, a bunch spacing time of  $t_{\text{bs}} = 50 \text{ ns}$  was utilized for the majority of the data taking period. With the increasing instantaneous luminosity, an increase of pile-up events could be observed with a maximum number of pile-up events of  $\sim 40$ . An overview of the parameters for Run 1 is provided in Table 3.1, separated for all three years. However, for the tau identification studies (see Section 4.6) only a subsample of the 2012 data was utilized, corresponding to an integrated luminosity of  $740 \text{ pb}^{-1}$ .

	2010	2011	2012
Delivered luminosity [ $\text{fb}^{-1}$ ]	0.047	5.5	22.8
Luminosity for physics [ $\text{fb}^{-1}$ ]	37	4.5	20.3
Rel. uncertainty $\delta L/L$ [%]	3.5	1.8	2.8
Peak luminosity [ $10^{33} \text{ cm}^{-2} \text{ s}^{-1}$ ]	0.2	3.5	7.7
Max. number of interactions (pile-up)	$\sim 5$	$\sim 20$	$\sim 40$
Max. number of protons per bunch $\times 10^{11}$	1.2	1.45	1.76
Max. number of bunches per beam	368	1380	1380

**Table 3.1:** Overview of Run 1 data taking parameters for proton-proton collisions in the years 2010, 2011 and 2012. The numbers are taken from Refs. [111, 112].

In summary, the Run 1 proton-proton collision setup is characterized by center-of-mass energies of  $\sqrt{s} = 7 \text{ TeV}$  to  $8 \text{ TeV}$  and a continuous increase in performance during the three years in form of increased instantaneous luminosity, increased number of bunches and reduced bunch spacing time but also in combination with an increased number of additional pile-up interactions, as presented in Figure 3.7.



## 4 Particle Reconstruction and Identification

The foundation for physics analyses in particle collider experiments is the reconstruction and identification of stable particles originating from primary and secondary interactions. For proton-proton collision events, recorded with the ATLAS detector, the reconstruction of particles is performed via a combination of various signal sources of the sub-detector systems.

First, trajectories of charged particles and subsequently vertices are reconstructed from signals in the inner detector and muon spectrometer, while energy deposits in the calorimeter systems are calibrated and clustered to broader structures. The resulting tracks and cell clusters are the baseline for the reconstruction of higher level objects, which are closer related to the physical particles, including: electrons, photons, muons, jets, hadronically decaying tau leptons and the missing transverse momentum.

Once the particles are reconstructed, it is in general necessary to perform an identification process since a significant fraction of the reconstructed particle candidates are usually misclassified. Quality criteria based on the properties of the reconstructed object are applied to increase the purity of a certain particle classification. The identification methods depend on the assumed particle hypotheses and thus are different for the various particles types.

The relevant reconstruction and identification chains used in the ATLAS collaboration are summarized in the Sections 4.1 to 4.7 with a focus on hadronically decaying tau leptons. Following this, a brief overview about the ATLAS trigger system is provided in Section 4.8.

## 4.1 Track and Vertex Reconstruction

The track reconstruction denotes the reconstruction of charged particle trajectories via a mixture of *pattern finding* algorithms and *fitting* procedures of the track candidates [114, 115]. Within this context, a trajectory is defined by five parameters:

$$(d_0, z_0, \phi, \theta, \frac{q}{p})^T, \quad (4.1)$$

where  $d_0$  and  $z_0$  denote the transverse and longitudinal impact parameter, respectively. The parameter  $\phi$  and  $\theta$  represent the azimuthal and polar angles of the track with respect to the laboratory frame, while  $q/p$  represents the charge of the track divided by its associated momentum,  $p$ . Both impact parameters are calculated with respect to a certain vertex position (in general to the primary vertex position). The transverse impact parameter,  $d_0$ , denotes the distance between the considered vertex and the *point of closest approach* (PCA) in the plane perpendicular to the beam axis ( $r \times \phi$  plane in spherical coordinates), while the longitudinal impact parameter,  $z_0$ , represents the distance between the PCA and the vertex position along the beam pipe.

Within this chapter, a brief overview about the track reconstruction in the inner detector system is provided. The reconstruction of muon tracks using information from the muon spectrometer is discussed in Section 4.4.

Two main algorithms are utilized in ATLAS: the *inside-out* and the *outside-in* sequence. The *inside-out* algorithm is used to find primarily trajectories of charged particles originating from a primary interaction within the beam pipe. Recorded *hits*<sup>1</sup> in the silicon based detector elements (pixel or SCT) are extended towards the TRT system based on the Kalman filter algorithm [115]. A weight is associated to each track parametrizing the quality of the track, which depends on track properties like the number of hits, the number of holes<sup>2</sup> and the quality of the track fit. In contrast the *outside-in* sequence focuses on the reconstruction of secondary particles, which are produced from sub-decays of primary particles or from interactions with the detector material, using seeds in the TRT system and extending the track candidates towards the beam pipe. The selection of tracks and the corresponding reconstruction efficiencies are discussed within the context of the underlying event analysis in Section 5.1.

The reconstruction of (primary) vertices [116] is performed using an iterative procedure. Starting with tracks in the region close to the interaction point, a possible vertex position is fitted. Tracks which are (to some degree) incompatible with the fitted vertex position are removed and the fitting procedure is repeated. Once a final vertex position is found, incompatible tracks are removed and used as possible seeds for new vertices. The process is repeated for all tracks in the recorded event. The reconstruction efficiency for vertices is found to be about 90% for a single proton-proton interaction (for common track selection criteria) and decreases with an increasing number of pile-up vertices [114].

---

<sup>1</sup>ID modules which register an energy deposition injected by a charged particle passing through the active material.

<sup>2</sup>A hole is a detector part in which a hit is expected following the current fitted trajectory but not found due to inefficiencies of the detector element.

## 4.2 Reconstruction of Energy Deposits in the Calorimeter

Charged and neutral particles, primarily electrons, photons and hadrons, will interact with the absorber parts of the calorimeter systems, causing electromagnetic showers which result in electric signals in the individual calorimeter cells. Usually an incoming particle shower will deposit its energy across several cells and layers of the electromagnetic and hadronic calorimeter (spread and shape of the shower depends on incoming particle type and energy) and it is necessary to cluster the calorimeter cells in a reasonable way to reconstruct and identify the ingoing particles.

The ATLAS calorimeter has a non-compensating response behavior, which result in the different energy response for electrons (and photons) and hadrons. Two main calibration schemes are utilized for the calorimeter cells: the *electromagnetic* (EM) energy scale [117–125], derived from test beam measurements, which provides the correct response for particles involved in electromagnetic showers and the *local hadron calibration* (LC) [126,127]. The LC scale accounts for the non-compensating response behavior of the calorimeter, for energy deposits out-side of the considered clusters and for inactive material in the detector.

Two main algorithms are used for the clustering: the *sliding-window clustering* and the *topological clustering* [128].

**Sliding-window clustering** The baseline for this particular cluster algorithm is the segmentation of the calorimeter into a grid in the  $\eta$ - $\phi$  plane. Cell energies longitudinal to a corresponding grid element are added up. Local energy maxima above a certain threshold are used as seeds for the clusters. The maxima are found within a fixed size window in  $\eta \times \phi$ . Cells are assigned to the cluster in a rectangular window around an estimated seed position whereby the size of the windows varies depending on the particle hypothesis. This type of clustering algorithm is commonly used of electron and photon reconstruction.

**Topological clustering** For this approach a signal to noise ratio is defined for each cell:

$$t_{\text{cell}} = \frac{|E_{\text{cell}}|}{\sigma_{\text{cell}}^{\text{noise}}} . \quad (4.2)$$

The noise term,  $\sigma_{\text{cell}}^{\text{noise}}$ , is the expected RMS of the considered cell originating from electrical noise plus additional terms from pile-up contributions. Seed cells are defined as having a signal to noise ratio above 4. In an iterative procedure neighboring cells are added with a threshold  $t_{\text{cell}} > 2$  and a final layer of cells with  $t_{\text{cell}} > 0$  is added to form the full topological cluster. The final cluster will combine cells from the EM and hadronic calorimeter. If several local maxima are found within a cluster, the cluster can be split and re-clustered to allow a separation of overlapping shower profiles. This algorithm creates clusters with a variable number of cells assigned (in contrast to the sliding-window algorithm), to resemble the shower profile of the ingoing particle. Typical values for the number of cells per cluster are around 200 - 500, depending on the energy deposited. This kind of cluster algorithm is commonly used for jet finding and the reconstruction of hadronically decaying tau leptons.

## 4.3 Electron Reconstruction and Identification

In this section a brief summary about experimental techniques for the reconstruction, calibration and identification [129, 130] of electrons and positrons<sup>3</sup> at the ATLAS experiment is presented. The techniques presented are optimized using proton-proton collision data at a center-of-mass energy of  $\sqrt{s} = 7 \text{ TeV}$  and an integrated luminosity of  $L_{\text{int}} = 4.7 \text{ fb}^{-1}$  recorded in the year 2011.

### 4.3.1 Reconstruction and Calibration

The electron reconstruction differs for electron candidates in the central region ( $|\eta| < 2.5$ ) and forward region ( $2.5 < |\eta| < 4.9$ ). Within the central region, tracking information provided by the inner detector components allow an association of a track with an energy deposit in the EM calorimeter. Electron candidates above a total transverse energy threshold of  $E_T > 7 \text{ GeV}$  can be reconstructed using this method. In contrast, the forward region relies on calorimeter information only to reconstruct electron candidates, restricting the range of electron candidates to  $E_T > 20 \text{ GeV}$ . In the further context, only electrons reconstructed within the central region are considered.

**Central electron reconstruction** Clusters of energy deposits in the EM calorimeter with  $E_T > 2.5 \text{ GeV}$  are the starting points for the electron reconstruction which are localized using a sliding window algorithm [128]. Tracks with a transverse momentum of  $p_T > 500 \text{ MeV}$  are extrapolated to the middle layer of the EM calorimeter and matched to the center of the clusters. Possible energy losses due to bremsstrahlung are considered for the matching step between a cluster and a track. A preliminary energy estimation is performed for each candidate considering energy deposits in the front of the calorimeter, energy deposits in the various layers of the EM calorimeter as well as possible leakages. In addition, corrections for possible displacements between the inner detector and the calorimeter are applied.

**Central electron calibration** Calibration methods based on the MC simulated detector response are utilized to estimate the true particle energy from detector level observables [130]. Corrections for differences in the calorimeter response and the absolute energy scale between the measurements and the predictions from simulation have been determined using  $Z \rightarrow ee$  measurements. The final results lead to an accuracy in the energy scale of about  $0.3 - 2 \times 10^{-3}$  and to corrections on the resolution of the order of  $\leq 1\%$ . The calibration using the  $Z \rightarrow ee$  events was cross-checked using measurements of  $J/\Psi \rightarrow ee$  events [130].

### 4.3.2 Identification

The electron identification algorithm provides a technique to separate reconstructed electron candidates originating from prompt, mostly isolated electrons against candidates originating from background processes. Possible background processes are hadrons which are misidentified, non-isolated electrons produced in hadron decays and electrons from photon conversion processes due to interactions with the detector material. The identification is based on observables from the calorimeter systems, the tracking systems or a combination of both. A consecutive series of

---

<sup>3</sup>Within the further context only electrons are mentioned but the algorithms are used in the same way for positrons.

selection steps is performed, parametrized in the transverse energy,  $E_T$ , and the pseudorapidity,  $\eta$ , of the corresponding electron candidate. Three reference selection sets (*levels*) of identification criteria are defined: *loose*, *medium* and *tight*. The background rejection increases with tighter selection criteria at the cost of the signal identification efficiency. Details on the selection requirements of each level can be found in Ref. [129].

Measurements in  $Z \rightarrow ee$ ,  $W \rightarrow e\nu$  and  $J/\Psi \rightarrow ee$  events allow a determination of the identification efficiency in data events. Scale factors between the measurements and MC simulations are derived to account for the mis-modeling in the simulation together with the corresponding uncertainties for the scale factors, both parametrized in  $E_T$  and  $\eta$  of the electron candidate.

The combined reconstruction and identification efficiency for electrons as a function of  $E_T$  and an example for the electron scale factors can be found in Figure 4.1.

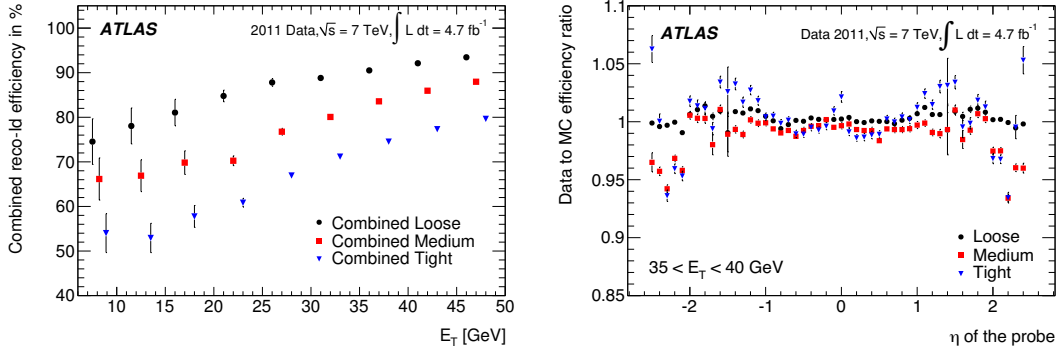


**Figure 4.1:** Combined electron reconstruction and identification efficiency vs.  $E_T$  of the electron candidate (left) and the identification scale factor vs.  $\eta$  of the electron candidate (right), both showing the three reference selection sets *loose*, *medium* and *tight*. Both figures are taken from Ref. [129].

Within the scope of this thesis the *loose* selection level is used, which corresponds to a combined reconstruction and identification efficiency of 75 % to 95 % and scale factors of the order of 1 % to 2 %.

## 4.4 Muon Reconstruction and Identification

The muon is an elementary fermion which is categorized to the second generation of leptons within the SM. Although the properties of a muon are similar to the properties of an electron, the higher mass value of 105.65 MeV [12] and the relatively high mean life time of  $\tau_\mu = 2.2 \times 10^{-6}$  s [12] lead to a quite different signature within the ATLAS detector. The signature of a muon passing through the detector material is characterized by a track in the inner detector system and the muon spectrometer as well as a, relative to its total momentum, small energy deposition in the calorimeter system.

Consequently, the muon reconstruction is dominated by information from the tracking systems (ID and MS) [131]. Depending on the source of the information, it is possible to distinguish between four main types of reconstructed muon:

**Stand-Alone (SA)** Muons reconstructed from MS tracks only;

**Segmented Tagged (ST)** Tracks from the ID which can be extrapolated to at least one track segment in the MS;

**Calorimeter Tagged (CaloTag)** Tracks from ID which match with energy deposits in the calorimeter;

**Combined (CB)** Muons which are constructed from independent measurements in the ID and the MS.

The CB muons provide the highest purity among all types and are used in MSSM Higgs boson search. In ATLAS, two independent approaches (*chains*) are utilized at the time to reconstruct CB muons:

**Chain 1** Based on a statistical combination of the ID and MS tracks. The corresponding covariance matrices of both measurements are considered [131]. This algorithm is also referred to as *Staco* algorithm.

**Chain 2** A global fit is performed simultaneously using the information of the ID and MS [131]. This algorithm is also referred to as *Muid* algorithm.

Within the further context, reconstructed (CB) muons based on the *Staco* algorithm are used.

Tracks in the ID systems are required to pass certain quality criteria to be associated with a given muon candidate. The following list of selection requirements represent the recommendations for the 2011 data set:

1. if a hit inside der *b-layer*<sup>4</sup> is expected from the position of the trajectory, the track need to have at least one *b-layer* hit;
2. the track should provide at least one hit inside the pixel detector and five hits inside the SCT system (inoperative, “dead”, sensor modules which are crossed by the track are counted as hit);

---

<sup>4</sup>Innermost pixel detector layer.

3. the number of holes (detector elements which are expected to show a signal given the considered trajectory) in the pixel and the SCT system should be less than three.

If the trajectory lies within the acceptance of the TRT systems, the following set of selections is performed on top of the pixel and SCT requirements:

1. if  $|\eta^{\text{trk}}| < 1.9$ , then the sum of TRT hits and outliers should be above five and the fraction of outliers should be below 90 %;
2. if  $|\eta^{\text{trk}}| > 1.9$ , the fraction of outliers only need to be below 90 % if the sum of hits and outliers is above five.

An outlier in the TRT system is either defined as a straw tube signal from other tracks or a set of TRT hits for which an extrapolation with the pixel and SCT hits failed. Additional quality criteria for the full muon candidates are defined to ensure certain properties, e.g. a certain level of background rejection or momentum resolution. The relevant criteria depend on the utilized chain and software version and have been provided by the *Muon Combined Performance Group* of the ATLAS experiment in form of three working points: *loose*, *medium* and *tight*.

The performance of the muon reconstruction was studied using measurements of  $Z \rightarrow \mu\mu$ ,  $J/\Psi \rightarrow \mu\mu$  and  $\Upsilon \rightarrow \mu\mu$  processes collected in the years 2011 and 2012 [131]. As an example the muon reconstruction efficiency in  $Z \rightarrow \mu\mu$  events is presented in Figure 4.2 for various muon types using the *staco* reconstruction algorithm. The overall efficiency is largely above 95 %, except for regions close to  $\eta \approx 0$ , where supporting devices for the ID and Calorimeter are located and at  $|\eta| \approx 1.2$ , where some MS Chambers were not installed at the time.

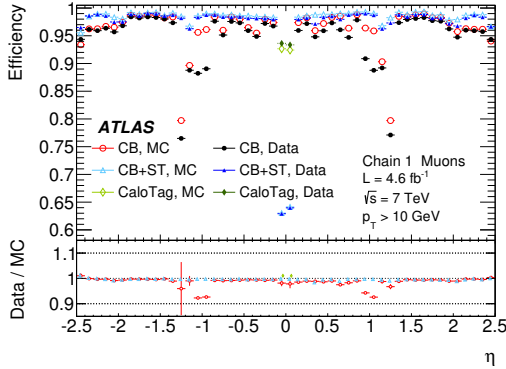


**Figure 4.2:** Muon reconstruction efficiency for different muon types in 2011 [131].

Deviations between the measurements and the simulations are taken into account by correcting the energy scale of the muon momentum predicted by the simulation using measurements of the invariant mass of the  $\mu^-\mu^+$  systems [131]. The corresponding tracks in the ID and MS systems are corrected independently from each other. Systematic uncertainties are found to be around 1 % in the barrel region and about 4 % towards higher  $\eta$  values. The relative momentum resolution is evaluated to be of the order of 1.7 % to 4 % depending on the considered muon momentum and pseudo-rapidity [131].

## 4.5 Jet Reconstruction and Calibration

The nature of the strong interaction prevents the observation of free quarks and gluon and restricts physicists to measurements of QCD bound states like mesons and hadrons. Due to the structure of the strong coupling, quarks and gluon *hadronise* into bundles of particles which share similar directions in  $y \times \phi$  (usually within a certain cone), with  $y$  representing the rapidity of the jet. These particle bundles are referred to as *jets* and the reconstruction and calibration of jets is an important analysis step to understand and analyze collision processes, in particularly at a hadron collider where the majority of scattering processes are pure QCD-based interactions.

The experimental signature of jets are typically bundles of tracks in the ID as well as clusters of energy deposits in the calorimeter systems. Over the past decades different jet clustering algorithms have been developed, each with different proprieties, strengths and weak points. Within the context of this study, jets reconstructed with the anti- $k_t$  algorithm [132] are considered. The following section contains a summary of the anti- $k_t$  algorithm.

**The anti- $k_t$  Algorithm** The starting point for the algorithm are entities which can be associated to particles. Each entity  $i$  should be associated with a position in space defined by the azimuthal angle,  $\phi_i$ , and the polar angle,  $\theta_i$ , as well as a transverse momentum,  $p_{T,i}$ . The clustering of entities is based on the following two distance parameter definitions: the distance between two entities  $i, j$ ,

$$d_{i,j} = \min \left( \frac{1}{p_{T,i}^2}, \frac{1}{p_{T,j}^2} \right) \times \frac{\Delta_{i,j}^2}{R^2} \quad (4.3)$$

and the distance between an entity  $i$  and the beam axis,

$$d_{i,B} = \frac{1}{p_{T,i}^2}, \quad (4.4)$$

where

$$\Delta_{i,j}^2 = (y_i - y_j)^2 + (\phi_i - \phi_j)^2 \quad (4.5)$$

represents the distance of both entities in  $y \times \phi$ . The radius parameter  $R$  of the algorithm allows to control the area considered for the clustering process. Within an iterative process, the smallest distance between all possible entities is calculated: if the smallest distance is  $d_{i,j}$ , both corresponding particles are combined to a new entity and if the distance to the beam,  $d_{i,B}$ , is the smallest the corresponding object is labelled as *jet* and removed from the iteration process. The procedure is repeated until all input objects are combined into jets. Due to the distance definition via the inverse transverse momenta, soft entities (with respect to their transverse momentum) tend to be combined with hard (or high energetic) entities. If no high energetic particles are found within a distance of  $2R$  to another hard particle, the algorithm will combine all soft particles with that hard particle within a (nearly) perfect circle of radius  $R$  around the combined jet axis. The anti- $k_t$  algorithm is found to be infrared and collinear safe providing a robust behavior against additional soft radiations [132].

The input objects for the jet clustering algorithm depend on the considered analysis. Common



objects are tracks from the ID, topological cluster<sup>5</sup> of calorimeter cells or MC particle four vectors obtained from simulations. Within this thesis, topological clusters are used to reconstruct jets in measured data events and for Monte Carlo generated samples including a full detector simulation, while true particle jets are used for acceptance uncertainty studies and unfolding procedures. The FASTJET software package [133, 134] has been utilized for the anti- $k_t$  implementation within the ATLAS software framework.

The anti- $k_t$  algorithm will cluster each input object into a jet (even if a final jet only consists of one object). Subsequently, not only hadronisation products of quarks and gluons will be reconstructed as jets but all incoming particles from proton-proton collisions (which are able to reach the calorimeter) as well as secondary particles, including electrons, muons, photons and hadronically decaying tau leptons. These objects are mostly reconstructed and identified using independent algorithms and jets with an overlap in  $\eta \times \phi$  with one of these objects are removed to avoid double counting. This procedure is usually referred to as *overlap removal*. It should be noted that hadronically decaying tau leptons are treated slightly differently, since anti- $k_t$  jets with  $R = 0.4$  are used as seeds for the tau reconstruction and the overlap removal is performed after a dedicated identification of the tau lepton against QCD jets<sup>6</sup>.

### 4.5.1 Jet Calibration

The starting point for the jet calibration are topological cell clusters in the calorimeter. Initially the calorimeter cells are calibrated to the electromagnetic scale [135], which is the baseline calibration scale for the ATLAS calorimeter. The EM scale correctly retrieves the energy which was deposited by the electromagnetic showers but does not account for the different response behavior for the calorimeter against energy depositions from hadrons. Consequently, the total energy of a jet at this point is derived by the sum over the four momentum vectors of the corresponding components [135].

The jet calibration techniques have been developed during the data taking period, leading to differences in the calibration methods for the data recorded in the years 2010 and 2011. The following section will focus on the techniques deployed for the 2011 data. Details on the jet calibration based on the 2010 data can be found in Ref. [136].

Based on the EM scale, a calibration is applied to correct the *jet energy scale* (JES) from the detector level (energy retrieved from calorimeter information) to the particle level, which correspond to the jet energy one would obtained from clustering directly the stable outgoing particles of the interaction without any detector effects. Four main corrections are applied: a correction for additional energy contributions of pile-up<sup>7</sup>, a correction of the jet direction towards the primary interaction vertex, a calibration to particle level based on MC simulations and residual in situ corrections based on various measurements using the 2011 dataset [135]. The

---

<sup>5</sup>See Section 4.2 for definition of topological clusters.

<sup>6</sup>Details on the tau reconstruction and identification can be found in Section 4.6.

<sup>7</sup>This includes a correction for *in-time* pile-up, which are additional interaction during the same bunch crossing as well as *out-of-time* pile-up, which includes contributions from preceding and succeeding bunch crossings [135].

simulation based corrections aim to provide a scaling factor from the detector level response in the simulation to the particle level response, which is calculated from clustering stable simulated particles into jets. Remaining effects, which not covered by the simulation based correction factor, are targeted using the data driven in situ corrections, which are exploiting a balancing in the transverse momentum of a jet and a calibrated reference object [135]. For central jets, up to  $|\eta| = 1.2$ , either  $Z/\gamma + jets$  events or balancing between high and low  $p_T$  jet systems are used (depending on the considered jet  $p_T$  region), while forward jets are calibrated using di-jet systems. More details on the various studies can be found in Ref. [135].

The combined systematic uncertainty for the JES extracted from the 2011 dataset has been estimated to be around 1 % to 3 % for jets within the central region of the detector which increase up to 6 % for very forward jets ( $|\eta| = 4.5$ ) [135]. For the 2010 dataset, the total JES uncertainty has been estimated to be about 2.5 %, for central jets ( $|\eta| < 0.8$ ) and a transverse momentum of  $60 \leq p_T < 800$  GeV, up to 14 % for jets with  $p_T < 30$  GeV in the very forward region.

### 4.5.2 Jet Resolution

The jet energy resolution for anti- $k_t$  jets has been measured within the ATLAS collaboration using datasets recorded in 2010 and 2011. Two different methods have been deployed for the in situ resolution measurement: a method based on a Gauss fit of the  $p_T$  asymmetry in di-jet events and a bisector method [137]. The bisector method makes use of the projection of the transversal vector sum of a di-jet system into a coordinate system which bisects the  $\Delta\phi$  angle between both jets. For the 2010 dataset, the jet resolution,  $\sigma(p_T)/p_T$ , has been estimated to be about 7 % to 18 %, parametrized in the transverse momentum and the rapidity value of the corresponding jet [137]. A reasonable agreement within 10 % has been evaluated for the relative jet resolution between the data and the simulations. In 2011, the same estimation methods have been utilized resulting in a jet energy resolution of about 5 % to 19 % with a similar agreement between data and simulation compared to 2010. An example for the jet energy resolution as a function of the average transverse jet momenta for the 2011 data is shown in Figure 4.3.

### 4.5.3 Jet Vertex Fraction

The jet vertex fraction (JVF) allows to estimate the amount of contribution originating from the primary interaction vertex to a considered jet using tracking information [135, 136] and thus allows to suppress jets which are likely to arise from pile-up interactions. Tracks are associated with a certain jet if they are located within a distance of  $\Delta R = 0.4$  in  $\eta \times \phi$  to the jet axis. The JVF,

$$f_{\text{JVF}}(\text{jet}|\text{vtx}) = \frac{\sum p_T^{\text{trk}|\text{vtx}}}{\sum p_T^{\text{trk}}} , \quad (4.6)$$

is now defined as the scalar transverse momentum sum of tracks associated to the considered jet and vertex divided by the scalar transverse momentum sum of all tracks associated to the jet.

Since the JVF relies on tracking information, it is only usable for jets located within the ID acceptance. For this thesis, the JVF selection is only applied on jets with  $|\eta^{\text{jet}}| < 2.4$  and  $p_T^{\text{jet}} < 50$  GeV ( $\sim 99$  % of pile-up are below the given  $p_T$  threshold).

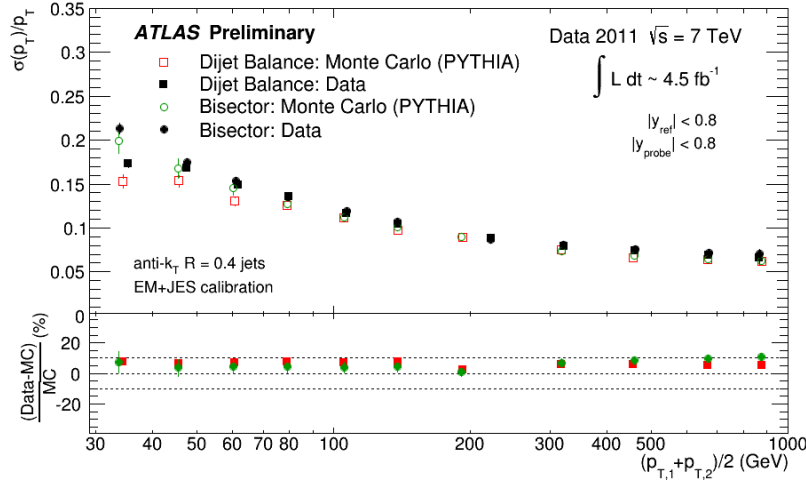


**Figure 4.3:** Relative jet resolution as a function of the average transverse jet momenta for anti- $k_t$  jets with  $R = 0.4$  is shown for data (2011) and simulation, for both estimation methods [138].

#### 4.5.4 Jet cleaning

This section will summarize experimental techniques for data cleaning to ensure a good quality for the jet and  $E_T^{\text{miss}}$  reconstruction algorithms within the ATLAS collaboration, collectively referred to as *jet cleaning*. The intention is to identify mis-reconstructed (“fake”) jets or jets reconstructed within problematic detector regions. The full details for the jet cleaning can be found in Refs. [136,139]. Within the context of this thesis, the techniques described in the papers are used, although the selection criteria can slightly differ, following the recommendation of the jet performance group at the time.

The majority of mis-reconstructed jets originate from sporadic, localized noise bursts<sup>8</sup> mostly within the end-caps of the hadronic calorimeter (HEC). Jets reconstructed from noise bursts in the HEC are characterized by a large energy fraction within the hadronic end-caps,  $f_{\text{HEC}}$ , compared to the total jet energy and the energy deposits are typically distributed over a small number of cells. The quality of the energy reconstruction within the noisy cells is typically bad, which is quantified by comparing the measured pulse shape to the reference shape. A large discrepancy is expressed in a low quality for a given cell. In general, a cell can provide positive or negative signals. Negative signals (resulting in a negative energy) can appear in noisy cells or cells containing energy depositions of several proton-proton interactions, due to the way the energy is extracted from the pulse shape. Subsequently, noise burst jets usually show a large fraction of cells with bad quality in the HEC,  $f_{\text{HEC-Quality}}$ , and a quite high negative energy,  $E_{\text{neg}}$  [136,139].

Noise bursts can also affect cells within the EM calorimeter leading to coherent noise. Jets reconstructed from those cells are identified similar to the HEC case: the jets usually show a large fraction of energy within the EM calorimeter,  $f_{\text{EM}}$ , and a large fraction of bad quality cells,

<sup>8</sup>A *noise bursts* is characterized by a group of calorimeter cells which are affected by noise at the same time, see Ref. [140] Chapter 5.3.

$f_{\text{EM-Quality}}$  [136, 139].

A second source for fake jets are jets which are reconstructed from energy deposits of interactions not related to the proton-proton collision(s), collectively referred to as *non-collision background*. Possible interactions are e.g. collisions with the remaining gas in the beam pipe or bremsstrahlung from cosmic muons. These kinds of fake jets are characterized by unusual timings of the energy deposits or unexpected characteristics in distributions of the energy deposits within the different parts of the calorimeter [136, 139]. The mean signal time for each cell with respect to the event time (the time of the primary proton-proton interaction) is expected to be small. For fake jet identification a *jet time*,  $t_{\text{jet}}$ , is calculated using the mean time of all cell associated with the jet weighted by the cell energy squared. Each jet with  $t_{\text{jet}}$  above 10 ns is defined as fake jet. In addition, jets with a large or small fraction of energy in the electromagnetic calorimeter and low fraction of energy coming from charged particles are classified as fake jets. The fraction of energy from charged particles, denoted  $f_{\text{Ch}}$ , is the transverse momentum sum of all tracks associated with the jet divided by the total calibrated transverse momentum of the jet. Jets with more than 99% of their energy deposit in one single calorimeter layer (measured in  $f_{\text{Max}}$ , the maximum energy fraction found in one layer) are also considered as fake jets candidates [136, 139]. The selection criteria can vary for different regions in  $\eta^{\text{jet}}$ .

The full list of selection criteria used for the analyses in the years 2010 and 2011 can be found in Table 4.1 and Table 4.2.

Another source for inaccurate jet reconstruction are jets which are reconstructed within

Source	Selection Criteria
HEC noise	$f_{\text{HEC}} > 0.5$ and $f_{\text{HEC-Quality}} > 0.5$ $f_{\text{HEC}} > 1 - f_{\text{HEC-Quality}}$ $E_{\text{neg}} > 60 \text{ GeV}$
EM noise	$f_{\text{EM}} > 0.9$ and $f_{\text{EM-Quality}} > 0.8$ for $ \eta^{\text{jet}}  < 2.8$
Non-collisions backgrounds	$ t_{\text{jet}}  > 10 \text{ ns}$ $f_{\text{EM}} < 0.05$ and $f_{\text{Ch}} < 0.1$ $f_{\text{EM}} > 0.95$ and $f_{\text{Ch}} < 0.05$ $f_{\text{Max}} > 0.99$ $f_{\text{EM}} < 0.05$ for $ \eta^{\text{jet}}  \geq 2.0$

**Table 4.1:** Selection criteria for fake jets in 2010 data.

problematic regions of the ATLAS detector. This type of jets can be a real jets originating from the primary proton-proton collision but the energy calculation can be faulty [136, 139]. Two main types are considered.

1. Jets with a fraction of inactive cells above 50%. The energy fraction deposited within an inactive cell is estimated using the depositions in the surrounding cells. It is not possible to ensure a good jet energy reconstruction if the number of inactive cells associated with the jets grows to large.
2. Between the barrel and the end-cap component of the hadronic tile calorimeter additional scintillators are mounted. The calibration of the scintillators was not fully understood at

Source	Selection Criteria
HEC noise	$f_{\text{HEC}} > 0.5$ and $f_{\text{HEC-Quality}} > 0.5$ $E_{\text{neg}} > 60 \text{ GeV}$
EM noise	$f_{\text{EM}} > 0.95$ and $f_{\text{EM-Quality}} > 0.8$ for $ \eta^{\text{jet}}  < 2.8$
Non-collisions backgrounds	$ t_{\text{jet}}  > 25 \text{ ns}$ $\left. \begin{array}{l} f_{\text{EM}} < 0.05 \text{ and } f_{\text{Ch}} < 0.05 \\ f_{\text{Max}} > 0.99 \end{array} \right\} \text{ for }  \eta^{\text{jet}}  < 2.0$ $f_{\text{EM}} < 0.05 \text{ for }  \eta^{\text{jet}}  \geq 2.0$

**Table 4.2:** Selection criteria for fake jets in 2011 data.

the time which could affect the jet energy reconstruction. Jets with an energy fraction above 50 % in the scintillators are considered as problematic.

The treatment for these kinds of jets is analysis dependent and is discussed in the corresponding analysis chapters.

## 4.6 Tau Reconstruction and Identification

The tau lepton is the heaviest known elementary lepton within the Standard Model of particle physics. It is a fermionic particle, classified to the third generation, with a spin of  $1/2$  and a mass value of  $m_\tau = 1776.82(16)$  MeV [12] and can be seen as a heavier version of an electron or muon. The mean lifetime of a tau lepton is around  $\tau = 290.3(5) \times 10^{-15}$  s [12] which results in a proper decay length of  $c\tau = 87.03 \mu\text{m}$ .

Due to the relative short mean life time, the majority of tau leptons produced in proton-proton collisions at the LHC will decay within the beam pipe of the LHC ring<sup>9</sup> and thus be unable to reach active detector material. Only a small fraction of highly boosted tau leptons will be able to pass through the first layers of the inner detector. This property has an important consequence from an experimental point of view: in contrast to electron and muon particles the tau leptons can not be reconstructed directly but rather need to be reconstructed from their decay products.

Tau leptons decay via the weak interaction mediated by a W boson to a tau neutrino<sup>10</sup> and lighter leptons (electrons or muons) and the corresponding neutrinos or into a quark pair which immediately hadronizes. An example for a leading order Feynman diagram is shown in Figure 4.4. About one third of the tau leptons will decay either into electrons or muons with a branching fraction of  $\mathcal{B}(\tau \rightarrow e\nu) = 17.8\%$  and  $\mathcal{B}(\tau \rightarrow \mu\nu) = 17.4\%$  [12], respectively. Both decay channels are referred to as *leptonic decay* within the further context. The remaining tau leptons will decay

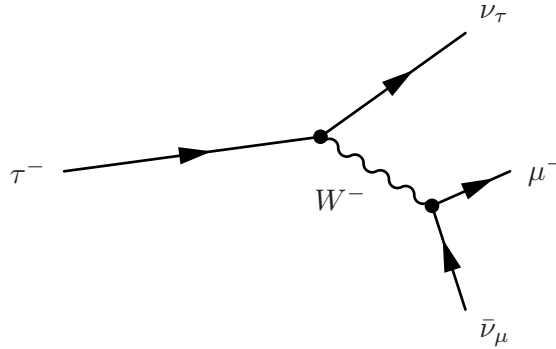


**Figure 4.4:** Feynman diagram for a tau decay into  $\mu^-$ ,  $\bar{\nu}_\mu$  and  $\nu_\tau$  at leading order in perturbation theory.

with a branching fraction of about 64.8% into a quark pair (*hadronic decay*) which will hadronise mostly into one or three charged pions and a variable number of additional neutral pions [12]. A small fraction of decays (around 2.9%) will include contributions from kaons. Hadronically decaying tau leptons,  $\tau_{\text{had}}$ , are categorized in the number of charged particles produced during the tau decay: one prong tau leptons<sup>11</sup>,  $\tau_{1\text{-prong}}$ , with a branching ratio of  $\mathcal{B}(\tau_{1\text{-prong}}) = 49.5\%$  and three prong tau leptons,  $\tau_{3\text{-prong}}$ , with a branching ratio of  $\mathcal{B}(\tau_{3\text{-prong}}) = 15.2\%$ . Decays with higher prong numbers are possible (but only odd numbers are allowed due to charge

<sup>9</sup>The radius of the beam pipe is around 36 mm [80].

<sup>10</sup>The term neutrino in this context is used for both: the neutrino and its anti-particle, depending whether a tau or anti-tau is decaying.

<sup>11</sup>In literature one can find that leptonically decaying tau leptons are sometimes included in the one prong definition. Within the context of this thesis, the term one prong tau will be only used for hadronically decaying tau leptons.

conservation) but not further considered, because the branching ratio for five prong tau leptons is already at the order of  $10^{-3}$ , and with an increasing number of particles produced in the tau decay the separation of tau lepton decays against QCD induced jets becomes more difficult.

To perform a physics analysis with tau leptons it is necessary to reconstruct and identify tau leptons based on their decay products. A direct identification of leptonically decaying tau leptons is not performed and instead electrons or muons from tau decays are reconstructed using the proper reconstruction algorithms<sup>12</sup>. The tau reconstruction and identification is therefore restricted to hadronically decaying tau leptons. A typical signature in the detector is characterized by one or three tracks in the ID, which are located within a relative small cone in  $\eta \times \phi$ , and a corresponding cluster of energy deposits in the calorimeter. The details on the reconstruction of possible tau candidates from the energy clusters and tracking information is discussed on Section 4.6.1. After the reconstruction, a calibration is performed to estimate the visible (without the momentum removed by the neutrinos) part of the original tau momentum/energy scale by taking the response of the calorimeter into account. Details on the tau energy scale calibration are presented in Section 4.6.2.

The identification of tau leptons terms the process of differentiation between tau lepton candidates originating from real hadronic tau decays and candidates originating from other physical particles which can mimic a tau decay, predominantly QCD-induced jets but also electrons and, to a lesser extent, muons [141].

The fraction of misidentified tau leptons from electrons or muons can be significantly reduced by removing tau candidates which overlap with a reconstructed electron or muon candidate with a certain distance in  $\eta \times \phi$ . Within the context of the MSSM Higgs search, events containing an electron or muon candidate above a certain momentum threshold are completely removed, which accomplishes a similar result in terms of leptonic misidentification. A small fraction of remaining misidentified tau candidates from electrons, which do not pass the electron identification, is further suppressed by applying a dedicated electron-veto for each tau candidate. The details on the tau identification against electrons are summarized in Section 4.6.3.

The separation against QCD-induced jets employs differences in the energy distribution between jets and real tau lepton decays as well as differences in the tracking spectra. The corresponding algorithms have been developed and improved during the data taking (and are still under regular development) and only a few dedicate stages during the development process are presented in this thesis. In particular, two main versions of the tau identification algorithm are discussed: the tau identification using the early 2012 data set and the tau identification algorithm used for the 2011 data set. The identification using the early 2012 data is part of the thesis work and will be explained in detail in Section 4.6.4. The basic concepts and methods for the tau identification are explained, exemplary for the rest of the tau identification versions, as well as the concrete results at the time. A description of the final tau identification in the 2012 dataset can be found in Ref. [141]. Afterwards, the tau identification in 2011 [142] will be briefly discussed in Section 4.6.5, which is used for the MSSM Higgs boson search.

---

<sup>12</sup>See Section 4.3 and Section 4.4 for details.

### 4.6.1 Reconstruction of hadronically decaying tau leptons

This section will give a brief overview about the tau reconstruction [141] used at the ATLAS experiment. The baseline for the tau reconstruction are anti- $k_t$  jets constructed from topological cell clusters using a radius parameter  $R = 0.4$ . Only jets with a transverse momentum  $p_T > 10 \text{ GeV}$  and  $|\eta| < 2.5$  are considered as possible tau candidates.

In a second step, the production vertex of the tau lepton is identified by matching tracks corresponding to a certain vertex with the direction of the tau candidate, within an radius of  $\Delta R < 0.2$  around the jet axis. Subsequently, corrections to the tau candidate axis are applied based on the vertex position. Once the final direction is determined two cones around the axis are defined: the *core* region with a distance of  $\Delta R < 0.2$  in  $\eta \times \phi$  and the *isolation* region with  $0.2 < \Delta R < 0.4$ , both distances defined with respect to the tau axis. Since the tau decay products are usually bundled within a narrow cone in the direction of the original tau lepton, the core region will primarily contain tracks and energy deposits (bundled in topological clusters) of the tau decay. The momentum vector  $\vec{p}_\tau$  is therefore calculated using the topological clusters within the core region.

All tracks in the core region, above a transverse momentum threshold of  $p_T^{\text{trk}} > 1 \text{ GeV}$ , are associated with the tau lepton candidate if the tracks fulfill certain quality criteria, including a minimal number of hits in certain layers of the inner detector and impact parameter cuts with respect the tau production vertex [141].

The isolation region is not used for the tau reconstruction itself, but rather for the definition of certain variables to discriminate against QCD-induced jets, employing the fact that QCD-jets usually deposit more activity in the isolation region compared to hadronically decaying tau leptons.

For a certain fraction of tau candidates, the number of reconstructed tracks will differ from the true number of charged particles due to inefficiencies or resolution effects of the detector or the rejection of tracks due to the selection requirements. Hadronic tau decays with three charged particles can be reconstructed as a 2-prong tau if, for example, two tracks are too close to each other to be separated during the track reconstruction. This effect increases with increasing transverse momentum of the tau candidate and results in a significant loss during the tau reconstruction for high  $p_T$  tau leptons. To avoid this effect, the calibration and identification of tau leptons is defined for 1-prong and *multi-prong* tau candidates, which includes the 2-prong as well as the 3-prong candidates.

### 4.6.2 Energy calibration of hadronically decaying tau leptons

The calibration of hadronically decaying tau leptons tries to recover the correct energy scale of the visible tau decay products [141, 143], referred to as *tau energy scale* (TES). Baseline for the calibration are topological cell cluster in the calorimeter, which are calibrated to the local hadron scale. A calibration constant,

$$R_{\text{cal}} = \frac{\langle E_{\text{LC}}^\tau \rangle}{E_{\text{true-vis}}^\tau}, \quad (4.7)$$



is used to parameterize the transition between the underlying true energy of the visible tau decay products,  $E_{\text{true-vis}}^\tau$  to the mean energy,  $\langle E_{\text{LC}}^\tau \rangle$ , measured in the calorimeter at local hadron calibration scale [143]. The constant is estimated using simulations of tau decays and the interaction of the decay products with the ATLAS calorimeter, parametrized in the energy,  $E_{\text{LC}}^\tau$ , associated to the tau candidate at LC scale, the pseudorapidity of the tau candidate and the number of prongs (1-prong or multi-prong). In addition, corrections for the  $\eta$  position of the tau candidate and for the energy contribution due to pile-up interactions are applied. The first correction takes differences between the  $\eta$  value of the combined real tau decay products and the estimated tau axis from the calorimeter cluster into account, while the pile-up contribution is considered by subtracting the estimated energy deposits from additional proton-proton interactions from the measured tau candidate energy [143]. The resulting resolution in the transverse momentum of the tau candidate (for the central region) is shown in Figure 4.5. Systematic uncertainties related to the TES arise from uncertainties in the calorimeter response,

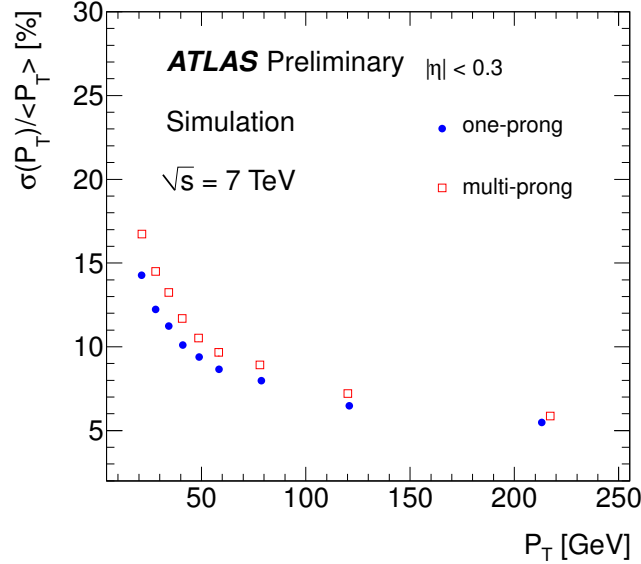


**Figure 4.5:** Resolution in the transverse momentum of 1-prong and multi-prong tau candidates for  $|\eta| < 0.3$ . Results are taken from Ref. [143].

uncertainties in the modeling of the simulation (underlying event model and detector simulation) as well as uncertainties related to non-closure effects of the method itself. A mixture of simulations, combined test beam results and in-situ measurements [143] are utilized to estimate the total uncertainty on the TES, resulting in an uncertainty of 2.4 % to 3.5 % for 1-prong tau candidates and 2.4 % to 5 % for multi-prong candidates, respectively. The uncertainties are estimated for different regions in the transverse momentum and the pseudorapidity of the considered tau candidate.

### 4.6.3 Distinguishing Tau Leptons and Electrons

Incoming electrons can be misidentified as hadronically decaying tau leptons with one charged track, since they also provide a cluster of energy deposits in the calorimeter systems due the induced electromagnetic showers. The discrimination between electrons and tau leptons is

performed either using a cut based or *boosted decision tree* (BDT) [144,145] based approach using various observables which parametrize the difference in the shower shapes. Both approaches are optimized for four different regions in pseudorapidity, providing three working points, *loose*, *medium* and *tight*, for each region. The working points correspond to tau identification efficiencies of 95 %, 85 % and 75 %, respectively. Simulated  $Z \rightarrow \tau^+ \tau^-$  samples are used as model for the optimizations while the background is either modelled using simulated  $Z \rightarrow ee$  samples for the BDT approach and early 2011  $Z \rightarrow ee$  measurements for the cut based approach. A detailed reference for the electron discrimination in 2011 can be found in Refs. [142,146].

The final performance for two of the four considered  $\eta$  regions are presented in Figure 4.6, showing the cut based as well as the BDT based approach. The maximal signal efficiencies are below the specified value above, because the tau reconstruction efficiency has been included.

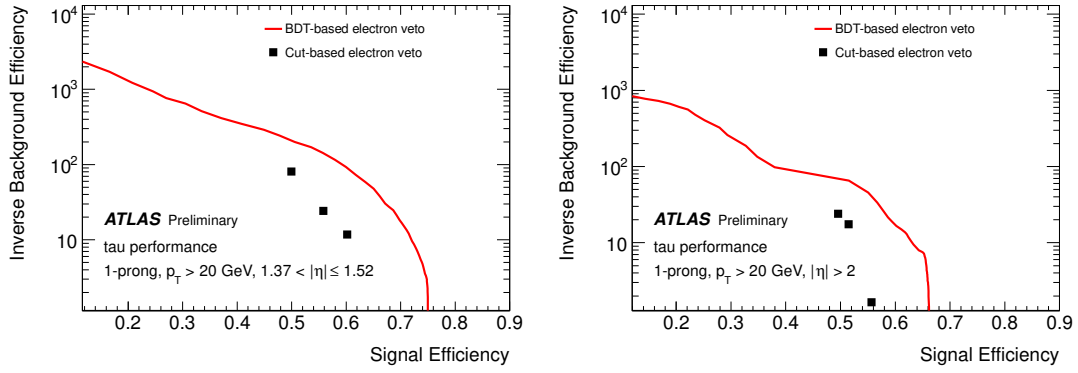


**Figure 4.6:** The background rejection as a function of the signal efficiency for the discrimination between electrons and tau leptons is shown for two different regions in  $\eta$ . The results are taken from Ref. [146].

#### 4.6.4 Tau discrimination against QCD-induced jets using early 2012 data

In this section, the tau identification against QCD jets is discussed using the early 2012 data samples, with an emphasis on the *log-likelihood* (LLH) method which was part of the thesis work. The full details and results have been published by the ATLAS collaboration and can be found in Ref. [147].

QCD-induced jets are the most likely objects to be misidentified as a hadronically decaying tau lepton and the separation between jets and real tau decays is a key ingredient for physics analyses including tau leptons. A major part of the QCD background for tau leptons is already removed by requiring 1 or 3 tracks within the tau candidate core region. It is expected that tracks and energy deposits of the decay products are bundled in a narrow region around the tau axis for real tau decays, while QCD induced jets tend to have a wider spread of particles due to additional QCD radiation processes. For real tau lepton decays close to no activity is expected in the isolation region (apart from contributions of additional scattering processes like underlying event and pile-up), in contrast to QCD-induced jets.

It should be mentioned that the differences between the decay structure of tau leptons and the substructures of QCD induced jets are more prominent for gluon than for quark induced jets. QCD jets originating from quarks tend to be more “tau-like” in their substructure and thus more likely to mimic a  $\tau_{\text{had}}$  decay. Within the context of the tau identification, no differentiation between quark and gluon induced jets is performed, treating both types equally. However, the effect is considered for studies of the tau identification efficiency in simulated background events and is discussed in detail in Section 6.2.

The following studies are based on simulated samples including real tau leptons, denoted as signal samples, and data taken during the year 2011 and early 2012 at the ATLAS detector for the QCD background, denoted as background samples. Real tau decays are taken from  $Z \rightarrow \tau\tau$ ,  $W \rightarrow \tau\nu$  and  $Z' \rightarrow \tau\tau$  processes, which were simulated using the PYTHIA 8 [148] Monte Carlo event generator in combination with the GEANT4 software for the ATLAS detector simulation. The  $Z'$  samples are simulations of models including an additional neutral heavy gauge boson [149–154] with a mass of 250, 500, 750, 1000 or 1250 GeV. These samples allow the population of the high  $p_T$  phase-space. The background samples are di-jet events recorded with the ATLAS detector in the first months of data taking in 2012. Using measured data samples ensures a correct description of the QCD jet substructure, avoiding uncertainties arising from the modeling of the hadronisation process within the Monte Carlo event generator.

### Observables

The substructure of tau candidates, in particular the track spectrum and the shower profile within the calorimeter, is characterized using a set of observables, which are sensitive to the differences between hadronic tau decays and QCD-induced jets. The considered set of observables has been improved during the Run 1 data taking. For the 2011 and early 2012 datasets, observables describing the average energy and track spread in the core region are used as well as the number of tracks in the isolation region and the distance of the tau decay vertex to the primary vertex of the interaction (normalized to the expected error) [142,147]. For the full 2012 dataset, additional observables have been considered characterizing the contribution of neutral pions in the tau decay structure [141].

The observables are partly different for 1-prong and multi-prong tau candidates. Some observables provide a significant separation power only for a certain prong type while other observables are only defined for multi-prong candidates, for example the distance between the tau decay vertex and the primary vertex, since at least two tracks are required to reconstruct the tau decay vertex. Three observables are utilized for 1-prong and multi-prong candidates: the pile-up corrected *energy and leading track momentum fraction* in the core region and the *weighted track radius*. The exact definitions can be found in Table 4.3 and the corresponding distributions are presented in Figure 4.7, comparing the predictions from real hadronic tau lepton decays with QCD jet measurements. A pile-up correction factor has been introduced to ensure that the mean value of the corrected observable is independent of the number of reconstructed vertices per bunch crossing and by thus reducing the dependency of the identification efficiency against pile-up.

Two additional observables are considered for 1-prong candidates only: the *impact parameter*

significance of the leading track and the number of tracks within the isolation region. For multi-prong candidates the following three observables are added: the *maximum track distance*, the *transverse flight path significance* and the *mass of the combined track system*. The exact definitions and corresponding distributions for the prong specific observables can be found in Section A.2.1.

Observable	Symbol	Description
Pile-up corrected energy fraction	$f_{\text{core}}^{\text{corr}}$	<p>Sum over cell energy deposits projected in the transversal plane, <math>E_{T,i}</math>, within a radius <math>R &lt; 0.1</math> in <math>\eta \times \phi</math> around the tau candidate axis divided by the same sum within a radius of <math>R &lt; 0.2</math> with</p> $f_{\text{core}} = \frac{\sum_i^{R<0.1} E_{T,i}}{\sum_j^{R<0.2} E_{T,j}}$ <p>and</p> $f_{\text{core}}^{\text{corr}} = f_{\text{core}} + 0.003 \times N_{\text{vtx}}$ <p>where <math>N_{\text{vtx}}</math> represents the number of reconstructed primary vertices. The correction is performed for tau candidates with <math>p_T &lt; 80</math> GeV.</p>
Pile-up corrected leading track momentum fraction	$f_{\text{trk}}^{\text{corr}}$	<p>Fraction between the transverse momentum of the leading core track, <math>p_T^{\text{lead-trk}}</math>, and the energy sum of calorimeter cells within a radius of <math>R &lt; 0.2</math> around the tau candidate axis:</p> $f_{\text{trk}} = \frac{p_T^{\text{lead-trk}}}{\sum_j^{R<0.2} E_{T,j}}.$ <p>The pile-up correction to obtain <math>f_{\text{trk}}^{\text{corr}}</math> is performed in the same way as for <math>f_{\text{core}}^{\text{corr}}</math>.</p>
Weighted track radius	$R_{\text{trk}}$	<p>Scalar sum of the transverse track momenta, <math>p_{T,i}</math>, weighted with the distance <math>\Delta R_i</math> of each track to the tau axis divided by the unweighted scalar transverse momentum sum of the tracks:</p> $R_{\text{trk}} = \frac{\sum_i^{R<0.4} p_{T,i} \times \Delta R_i}{\sum_i^{R<0.4} p_{T,i}}.$ <p>The tracks are associated to the tau candidate within a radius of <math>R &lt; 0.4</math> around the tau candidate axis.</p>

**Table 4.3:** Definition of observables used for the tau identification against QCD-induced jets [147]. The given observables are used for 1-prong and multi-prong tau candidates.

Two main identification methods have been utilized for the identification process: a projective log-likelihood method and a boosted decision tree. Both algorithms are based on the same input observables mentioned above. The optimization of the LLH method using the early 2012 data was part of the thesis work and will therefore be illustrated in more detail.

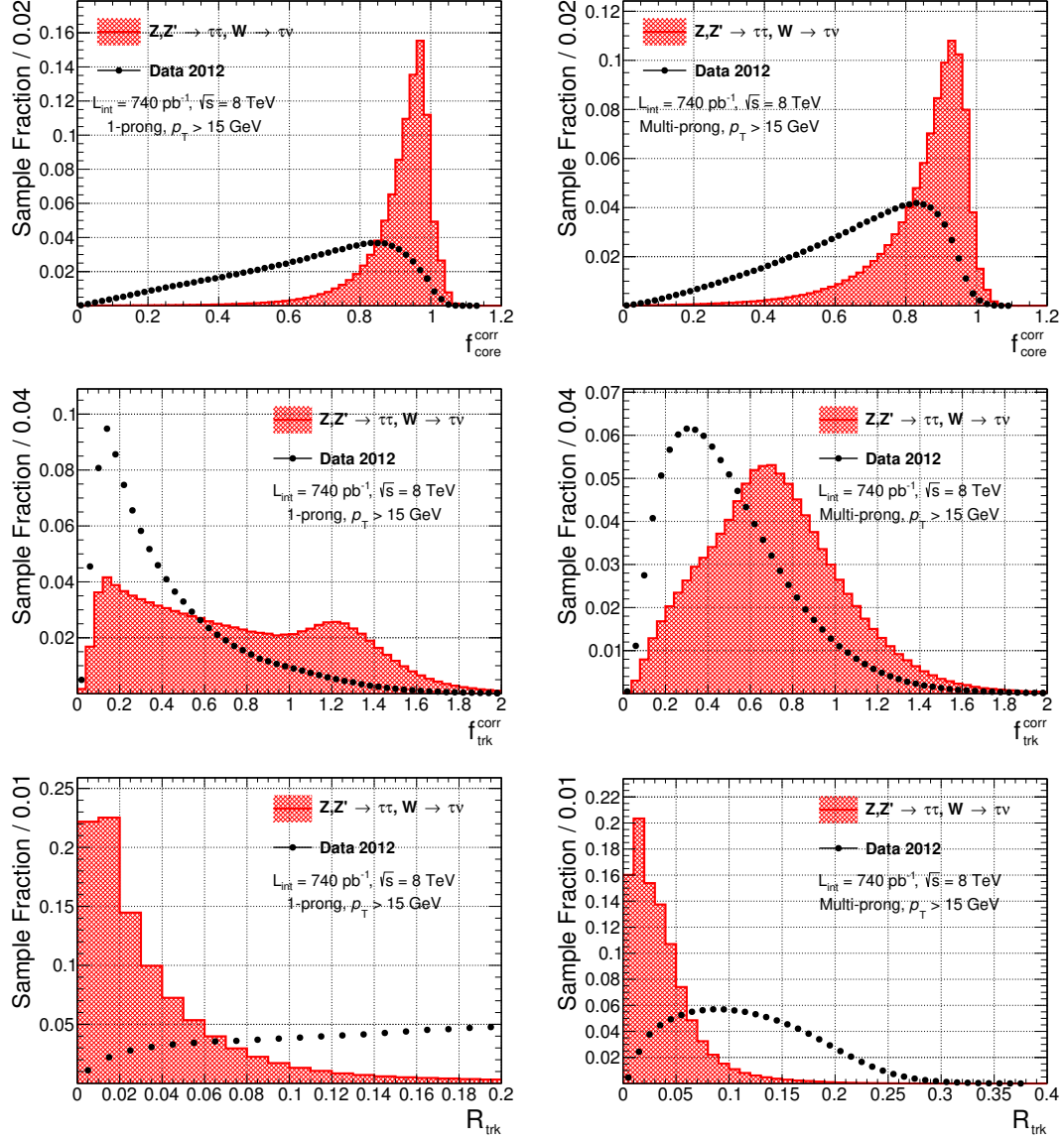


**Figure 4.7:** Distributions for the pile-up corrected energy fraction (top), the pile-up corrected leading track momentum fraction (middle) and the track radius (bottom) for 1-prong (left) and multi-prong (right) tau leptons are shown. Predictions for real tau leptons, which are taken from simulations of  $Z \rightarrow \tau^+\tau^-$ ,  $Z' \rightarrow \tau\tau$  and  $W \rightarrow \tau\nu$  processes, are compared with distributions from QCD-induced jets, which are measured using early 2012 data recorded with the ATLAS detector.

### Projective Log Likelihood

Precondition for the LLH method is the calculation of probability density functions (PDFs),  $P_i^{S,B}$ , for each observable  $i$ . The PDFs are calculated for signal (S) and background (B) samples, using tau candidates either from real tau decays or QCD jets, respectively. The PDFs are parametrized in the number of charged particles of the tau candidate and in the transverse momentum,  $p_{T,\text{vis}}^{\tau_{\text{had}}} := p_T$ , of the visible part of the hadronically decaying tau lepton<sup>13</sup>, using the following three regions:  $p_T \in [0, 45]$  GeV,  $p_T \in [45, 100]$  GeV and  $p_T > 100$  GeV. Using a parametrization in  $p_T$  allows to account for the dependence of the tau decay substructure from the incoming tau momentum. A possible dependence with respect to pile-up is covered by using the corrected observables mentioned above and no additional parametrization of the PDFs in the number of reconstructed vertices is performed.

The likelihood function  $L_{S,B}(a)$  for a given tau candidate  $a$  is defined by

$$L_S(a) = \prod_{i=1}^N P_i^S(x_i^a) \quad \text{and} \quad L_B(a) = \prod_{i=1}^N P_i^B(x_i^a), \quad (4.8)$$

where  $x_i^a$  is the value of the observable  $i$  for the given tau candidate  $a$ . For  $p_T$  values close to the borders defined above, a linear interpolation within certain  $p_T$  windows is performed. The LLH score, denoted  $\lambda(a)$ , is defined as the natural logarithm of the ratio between the signal and the background likelihood function:

$$\lambda(a) = \ln \left( \frac{L_S(a)}{L_B(a)} \right) = \sum_{i=1}^N \ln \left( \frac{P_i^S(x_i^a)}{P_i^B(x_i^a)} \right), \quad (4.9)$$

for a given tau candidate  $a$ . The normalized<sup>14</sup> distribution for the LLH score, sampled over a large number of tau candidates<sup>15</sup>, is shown in Figure 4.8. Tau candidates originating from real tau decays will obtain on average a higher LLH score value than candidates originating from QCD jets. The double peak structure for the signal samples is a results of the mixture between samples close the electroweak breaking scale (primary  $Z \rightarrow \tau\tau$  and  $W \rightarrow \tau\nu$ ) and the  $Z' \rightarrow \tau\tau$  samples including masses above 1 TeV. Tau lepton decays from  $Z'$  resonances will have on average a higher transverse momentum when compared to Z decays, resulting in more collimated tau decay substructures and an increased value in the LLH score. The double peak does not introduce a bias to the tau identification, since the final working points are defined with a  $p_T$  dependent LLH score threshold as explained below. Nevertheless, in a later version of the LLH, the double peak structure has been removed by proper reweighing of the tau candidates  $p_T$  distribution.

The performance of the LLH method can be expressed in terms of a signal efficiency,  $\epsilon_{\text{sig}}$ , and a background efficiency,  $\epsilon_{\text{bkg}}$ . Given the LLH score above, the signal efficiency is defined as the number of real tau decays which are reconstructed and pass a certain identification level divided by the number of real tau decays in the Monte Carlo simulation. Passing an identification

<sup>13</sup>This is the part the transverse momentum which can be reconstructed from calorimeter clusters.

<sup>14</sup>The integral from  $-\infty$  to  $+\infty$  is normalized to one.

<sup>15</sup>A technical detail: the events used for the calculation of the PDFs are orthogonal to the one used for the LLH score calculation to avoid a possible bias.

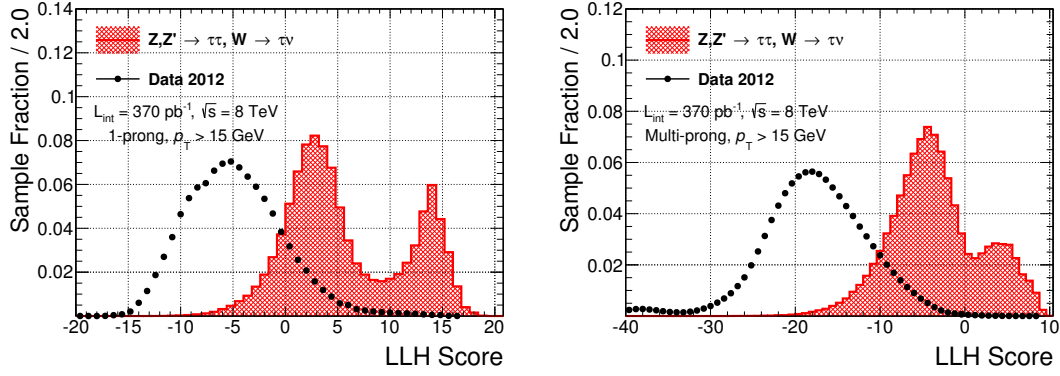


**Figure 4.8:** Normalized LLH score distribution for 1-prong (left) and multi-prong (right) tau candidates. The red shaded area represents the distributions for the combined signal samples and the black dots represent the combined background samples.

level means that the LLH score for the considered candidate  $a$  is above a certain threshold  $\lambda_t$ . The background efficiency is defined as the number of tau candidates (QCD jets) passing the identification threshold, divided by the number of reconstructed tau candidates,

$$\epsilon_{\text{sig}} = \frac{N_{\tau\text{-cand.}}^{\text{recon.}} (\lambda > \lambda_t)}{N_{\tau}^{\text{true}}} \quad (4.10)$$

$$\epsilon_{\text{bkg}} = \frac{N_{\text{jets}}^{\text{recon.}} (\lambda > \lambda_t)}{N_{\text{jets}}^{\text{recon.}}} \quad (4.11)$$

The efficiency is therefore a function of the identification threshold  $\lambda_t$ . This allows the definition of three working points *loose*, *medium* and *tight* which correspond to a signal efficiency of 70 %, 60 % and 40 % for 1-prong tau candidates and 65 %, 50 % and 35 % for multi-prong candidates, respectively. The threshold  $\lambda_t$  itself is parametrized in the energy scale,  $Q^2$ , of the considered tau candidate. Usually the scale is set to the reconstructed transverse momentum,  $p_T$ , of the tau candidate:

$$\lambda_t = \lambda_t (Q^2 := p_T) \quad (4.12)$$

The thresholds are defined with respect to a constant behavior of the signal efficiency against the visible part<sup>16</sup> of the true transverse momentum,  $p_{T,\text{vis}}^{\text{true-}\tau} := \hat{p}_T$ , of the original tau particle. Since  $\hat{p}_T$  is only accessible in simulation, it is necessary to replace it with a corresponding reconstructed quantity, accessible from measurements. For a given interval,  $[\hat{p}_T^i, \hat{p}_T^j]$ , the expected reconstructed transverse momentum,

$$E[p_T] \Big|_{\hat{p}_T^i}^{\hat{p}_T^j} = \langle p_T \rangle \Big|_{\hat{p}_T^i}^{\hat{p}_T^j}, \quad (4.13)$$

is estimated from Monte Carlo simulations. The LLH threshold  $\lambda_t$  for a given  $\hat{p}_T$  interval is subsequently replaced by the LLH threshold for the expected reconstructed  $p_T$ :

$$\lambda_t \left( \hat{p}_T \in [\hat{p}_T^i, \hat{p}_T^j] \right) = \lambda_t \left( \langle p_T \rangle \Big|_{\hat{p}_T^i}^{\hat{p}_T^j} \right) \quad (4.14)$$

<sup>16</sup>Visible part is defined as the transverse vector sum of all stable particle emerging from the tau decay excluding neutrinos.

Distributions of  $\lambda_t$  as a function of  $\langle p_T \rangle$  for all three working points are shown in Figure 4.9. The behavior of  $\lambda_t$  is within the fluctuations similar between the three working points, except for a constant offset. Final results for the signal and background efficiencies as a function of the true

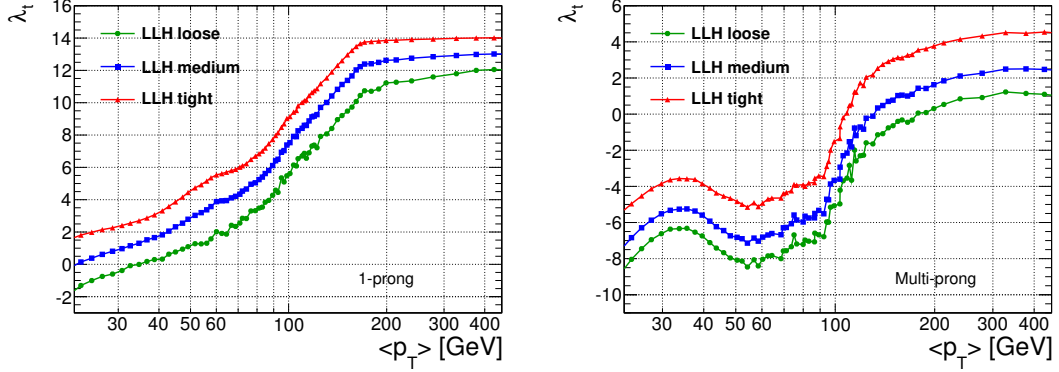


**Figure 4.9:** The LLH score threshold  $\lambda_t$  as a function of expected reconstructed transverse momentum  $p_T$  is presented for 1-prong (left) and multi-prong (right) tau candidates. Three working points are shown: *loose* (green circles), *medium* (blue squares) and *tight* (red triangle).

visible part of the transverse momentum and the number of reconstructed vertices per bunch crossing are presented in Figure 4.10 and Figure 4.11, respectively. In both cases the behavior of the signal efficiency is (at least approximately) constant against the observable considered, except for a turn on effect at low  $p_{T,\text{vis}}^{\text{true-}\tau}$ . The background efficiency also shows a quite constant behavior (for multi-prong at  $p_{T,\text{vis}}^{\text{true-}\tau} > 60$  GeV), although the LLH thresholds are not trained with respect to the background samples.

### Boosted decision tree

The tau identification using a boosted decision tree was not part of the thesis work and is summarized briefly. The full details can be found in Refs. [141, 147].

Two independent BDTs are trained for 1-prong and multi-prong tau decays using the BDT implementation of the TMVA [155] package within the ROOT [156] framework. The same observables as for the LLH method are used to ensure a comparability between both methods. Like in the LLH case, the result of the BDT training is expressed in a final discrimination variable, the *BDT score*. The BDT score distribution sampled over a large amount of tau candidates can be found in Figure 4.12, using the same signal and background composition as for the LLH method. The BDT scores are arranged between  $[0, 1]$ , whereat zero denotes a very “jet-like” and one a very “tau-like” candidate.

The same working points for *loose*, *medium* and *tight* are defined like for the LLH method, also ensuring a constant behavior in  $p_{T,\text{vis}}^{\text{true-}\tau}$  and  $N_{\text{Vtx}}$ . The BDT results are similar to the results of the LLH method and two example distributions are shown in Figure 4.13.

### Performance

The performance of the identification methods can be expressed by the fraction of tau candidates originating from QCD jets which are rejected by the algorithm for a given signal efficiency. The



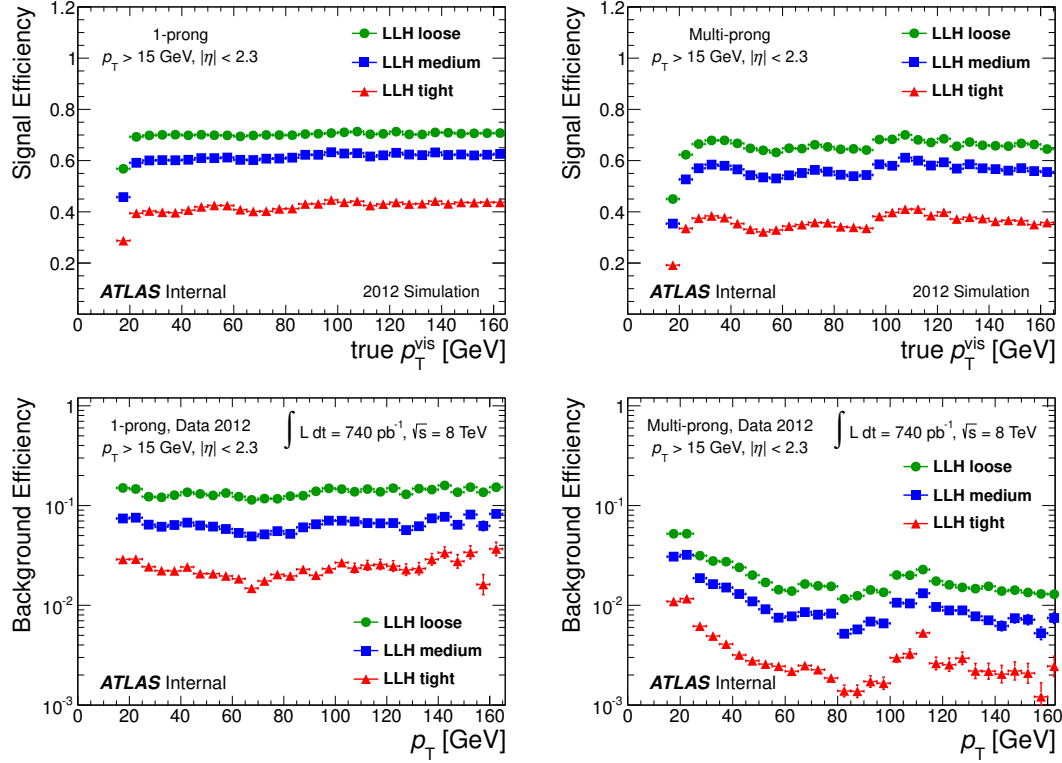


**Figure 4.10:** Tau identification efficiency for signal (top) and background (bottom) events using the LLH method are presented as a function of transverse momentum for 1-prong (left) and multi-prong (right) candidates. The efficiencies are shown for three working points: *loose* (green circles), *medium* (blue squares) and *tight* (red triangle). The results have been published in Ref. [147].

rejection rate, denoted  $r_{\text{bkg}}$ , is defined as the inverse of the background efficiency:

$$r_{\text{bkg}} = \frac{1}{\epsilon_{\text{bkg}}} , \quad (4.15)$$

thus representing the fraction of QCD jets being misidentified. For example a rejection rate of  $r_{\text{bkg}} = 1/1000$  for a given signal efficiency means that on average one out of 1000 QCD jets will pass the tau identification and thus be misidentified as a hadronically decaying tau lepton. Rejection rates as a function of the signal efficiency are presented in Figure 4.14 for one-prong and multi-prong tau candidates, split into two different phase space regions in  $p_T$ . The maximum signal efficiency is limited below 100%, due to inefficiencies in the tau reconstruction step. The BDT algorithms show in most cases a better performance (except for small  $\epsilon_{\text{sig}}$  in high  $p_T$  regions) compared to the LLH method, which was already observed in the 2011 dataset. The BDT algorithm is therefore used as the default tau identification algorithm, while the LLH method is mostly used for crosschecks.

#### 4.6.5 Tau discrimination against QCD-induced jets in 2011

The general concepts for the tau identification in 2011 [142, 146] are similar to the methods utilized for the early 2012 study, discussed in Section 4.6.4. The main improvements in the early

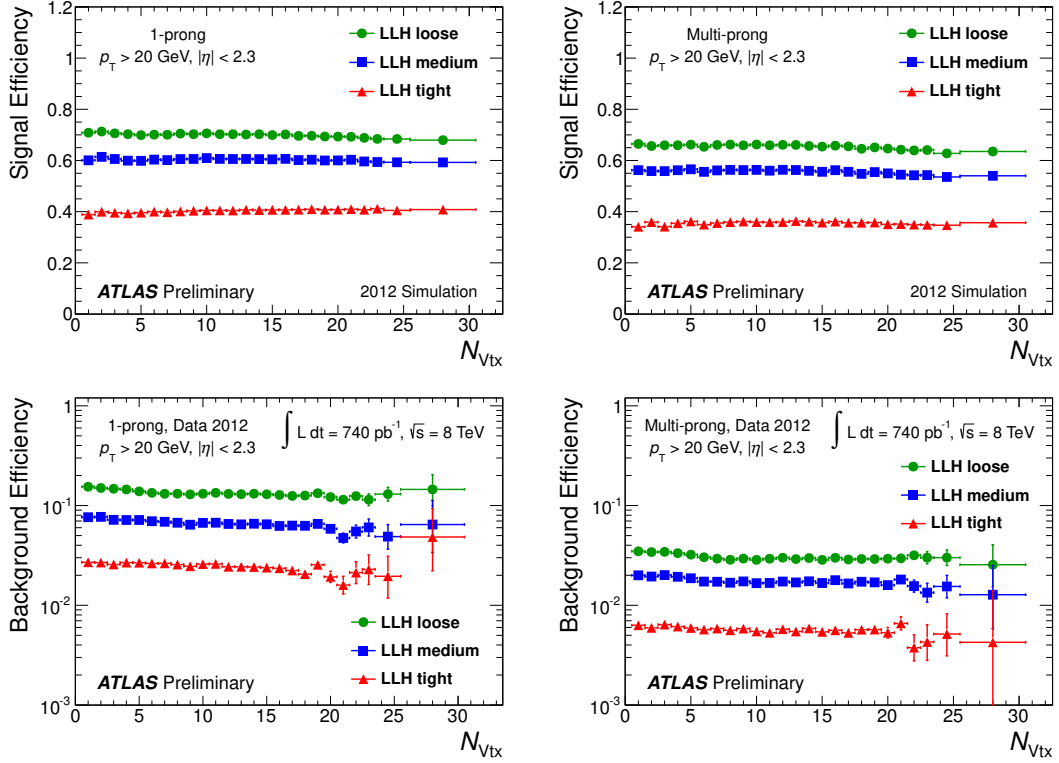


**Figure 4.11:** Tau identification efficiency for signal (top) and background (bottom) events using the LLH method are presented as a function of the number of reconstructed primary vertices during the same bunch crossing for 1-prong (left) and multi-prong (right) candidates. The efficiencies are shown for three working points: *loose* (green circles), *medium* (blue squares) and *tight* (red triangle). The results have been published in Ref. [147].

2012 study compared to the 2011 identification arise from the pile-up corrections of the energy and leading track momentum fraction and from an optimization of the utilized set of observables. In 2011, the PDFs have been parametrized in the number of vertices, in addition to the parametrization in  $p_T$ , which has been removed in 2012, in favor of the observable based pile-up correction. The performance of the tau identification expressed in terms of signal efficiencies vs. background rejection is presented in Figure 4.15. The general behavior for both algorithms is comparable with the 2012 results, although the overall background rejection is weaker in relation to the results shown in Figure 4.14.

The training of the tau identification algorithms has been performed based in simulated hadronic tau decays. In order to quantify possible deviations in performance when used in data, tau identification *scale factor* are derived from measurements in  $Z \rightarrow \tau\tau$  and  $W \rightarrow \tau\nu$  events, parameterizing possible variations in the signal efficiency. The scale factor measurements are based on *tag-and-probe* methods selecting a tau decay into a muon as tag for the  $Z \rightarrow \tau\tau$  process and a high value of  $E_T^{miss}$  as tag for the  $W \rightarrow \tau\nu$  process [146]. The probe tau candidate is the remaining hadronically decaying tau lepton, which is used to estimate the scale factor defined as the fraction of probe candidates passing a certain ID working point compared to the prediction derived from simulations. Overall, no significant deviations between the measurements

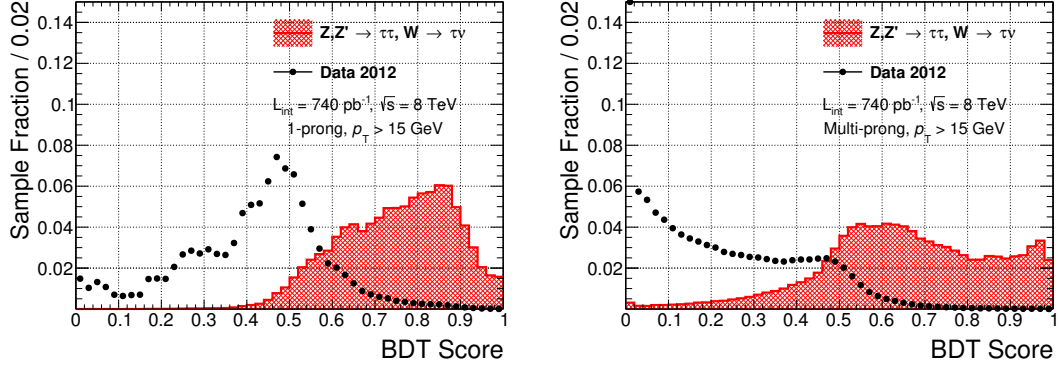


**Figure 4.12:** Normalized BDT score distribution for 1-prong (left) and multi-prong (right) tau candidates. The red shaded area represents the distributions for the combined signal samples and the black dots represent the combined background samples. The results are taken from Ref. [147].

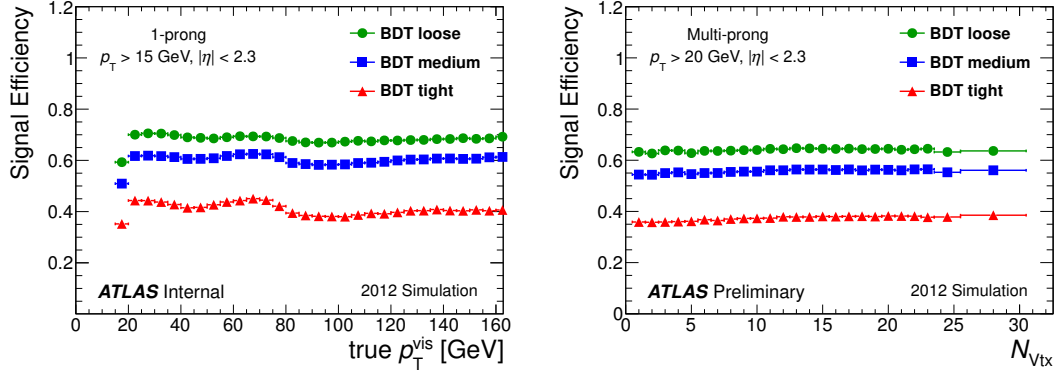


**Figure 4.13:** Tau identification efficiency for signal events using BDT method are presented as a function of transverse momentum for 1-prong (left) and as a function of  $N_{\text{Vtx}}$  for multi-prong (right). The efficiencies are shown for three working points: *loose* (green circles), *medium* (blue squares) and *tight* (red triangle). The results are taken from Ref. [147].

and the predictions have been found and the scale factors are set to unity. The corresponding systematic uncertainty have been estimated to be of the order of 4% to 8% for the loose and medium BDT working point, calculated individually for 1-prong and 3-prong tau candidates with  $p_T > 22 \text{ GeV}$  [146].

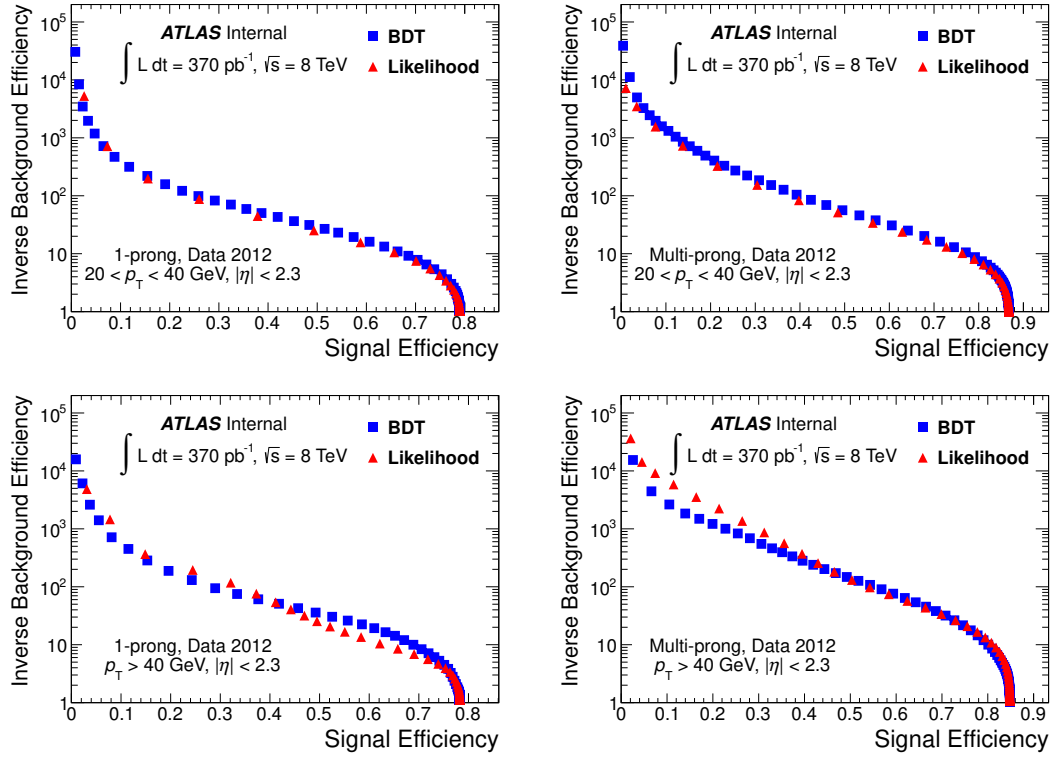


**Figure 4.14:** Signal efficiencies vs. background rejection using early 2012 data is shown for 1-prong (left) and multi-prong (right) tau candidates in two independent  $p_T$  region: low- $p_T$  (top) and high- $p_T$  (bottom). The BDT performance curve is shown in blue squares and the LLH in red triangles. The results have been published in Ref. [147].

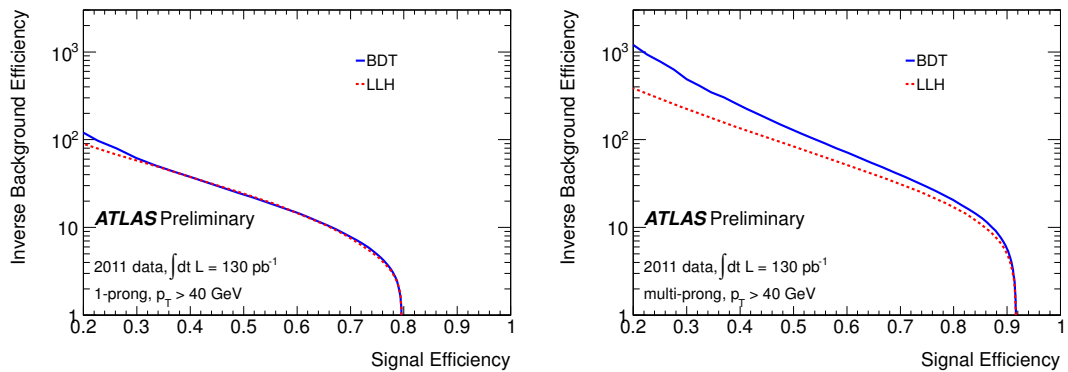


**Figure 4.15:** Signal efficiencies vs. background rejection using the 2011 data is shown for 1-prong (left) and multi-prong (right) tau candidates for  $p_T$  > 40 GeV. The results are taken from Ref. [146].

## 4.7 Missing Transverse Momentum and $\Sigma E_T$

The missing momentum, originating from undetected particles like neutrinos or weakly interacting particles predicted from BSM models, is an important observable for a considerable amount of analyses in high energy physics. In a hadron collider like the LHC, the longitudinal momentum of the interacting partons is a priori unknown<sup>17</sup> and therefore the *missing transverse momentum* is utilized. The transverse momentum of the incoming partons is assumed to be close to zero (due to the heavy boost of the partons along the beam pipe), so that each imbalance (deviation from zero) in the vector sum of transverse momenta of all particles indicates the presence of undetected particles within the given proton-proton interaction. The missing transverse momentum vector,

$$\vec{E}_T^{\text{miss}} = \begin{pmatrix} E_x^{\text{miss}} \\ E_y^{\text{miss}} \end{pmatrix}, \quad (4.16)$$

is defined as the negative vector sum over all detected particles and its magnitude,

$$E_T^{\text{miss}} = \sqrt{(E_x^{\text{miss}})^2 + (E_y^{\text{miss}})^2}, \quad (4.17)$$

is the missing transverse momentum also often referred to as *missing transverse energy*<sup>18</sup>. Thus, the direction within the azimuthal space is defined by the following equation:

$$\phi^{\text{miss}} = \arctan \left( \frac{E_y^{\text{miss}}}{E_x^{\text{miss}}} \right). \quad (4.18)$$

It should be noted that the direction of the missing momentum is not necessary the same as the direction of the undetected particles, in the case that more than one particle is emitted.

At reconstruction level,  $E_T^{\text{miss}}$  is calculated from several sources: objects reconstructed from energy deposits in the calorimeter (electrons, photons, hadronically decaying tau leptons, jets and deposits from muons passing through the calorimeter), calorimeter cells which are unassociated to any object and reconstructed muons from the muon spectrometer [157]. Tracking information from the ID are used to account for soft particles which are unable to reach the calorimeter and to supplement the muon information.

Each of the calorimeter related terms,  $T_j$ , is defined as the negative sum of cell energies,  $E_i$ , for cells associated to the corresponding object, projected in the transversal plane using the azimuthal angle,  $\phi_i$ , and polar angle,  $\theta_i$ , of the cells [157],

$$E_x^{\text{miss}, T_j} = - \sum_{i=1}^{N_{\text{cells}}} E_i \sin \theta_i \cos \phi_i \quad (4.19)$$

$$E_y^{\text{miss}, T_j} = - \sum_{i=1}^{N_{\text{cells}}} E_i \sin \theta_i \sin \phi_i, \quad (4.20)$$

while the muon related terms are calculated from the negative sum of transverse momenta from

<sup>17</sup>In general a parton will carry an a priori unknown fraction  $x$  of the total proton momentum.

<sup>18</sup>Hence the symbol  $E$ . Usually one assumes  $E = |\vec{p}|$  for the involved particles, since the particle masses, which contribute to the missing energy (SM particle which are stable enough to reach the detector elements), are usually small against the corresponding particle momenta at LHC energies.

muon tracks,

$$\vec{E}_T^{\text{miss, muon}} = - \sum_{i=1}^{N_\mu} \vec{p}_{T,i}^\mu. \quad (4.21)$$

Within this context, it is useful to define a related observable: the *total transverse energy* defined by

$$\sum E_T = \sum_{i=1}^{N_{\text{cells}}} E_i \sin \theta_i. \quad (4.22)$$

For both observables, only cells combined to a topological cluster are used<sup>19</sup> to reduce the impact of noise in the calorimeter cells [157]. Each term is calibrated independently, according to the associated objects<sup>20</sup>.

The performance of the missing energy reconstruction has been tested in measurements of minimum bias, di-jet,  $Z \rightarrow ll$  and  $W \rightarrow l\nu$  processes, showing a resolution of 2 GeV to 12 GeV for total transverse energies up to  $\sim 600$  GeV [157]. Systematic uncertainties related to the reconstructed particles (e.g. uncertainties on the energy scale of electrons, photons, jets, taus, ...) are propagated to the missing transverse energy by re-calculating  $E_T^{\text{miss}}$  after applying the uncertainty shifts to the reconstructed objects. The same procedure is used to estimate the systematic uncertainties of the  $\sum E_T$  observable. In addition, systematic uncertainties for cells outside of reconstructed objects and from soft jets ( $7 \text{ GeV} < p_T^{\text{jet}} < 20 \text{ GeV}$ ) are evaluated to 13% and 10%, taking contributions from the calorimeter as well as modeling uncertainties from the simulations into account [157]. An example for the fractional uncertainties as well as the total systematic uncertainty on  $E_T^{\text{miss}}$  as a function of  $\sum E_T$  is shown in Figure 4.16, measured in  $W \rightarrow \mu\nu$  events.

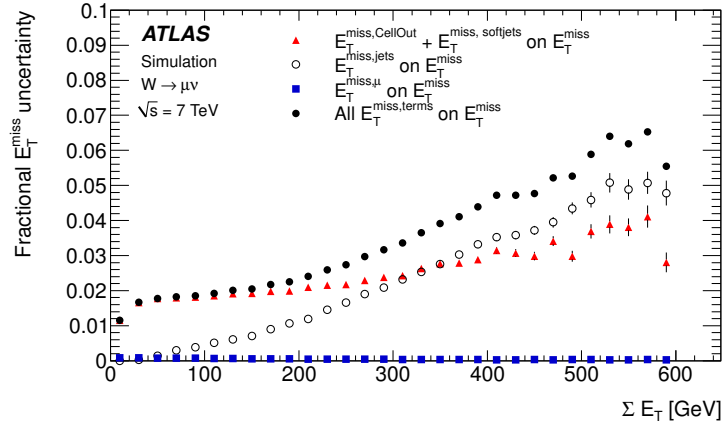


**Figure 4.16:** Systematic uncertainty on the missing transverse momentum measured in  $W \rightarrow \mu\nu$  events [157].

<sup>19</sup>Except for electrons and photons.

<sup>20</sup>For example, contributions of cells, which are associated to electrons, are calibrated based in this particle assumption.

## 4.8 Trigger

In order to search for rare events in high energy particle physics using collider experiments like LHC, it is unavoidable to work with an enormous number of collisions per time interval due to the random nature of quantum physics. It is not possible to force a certain final state as result of a proton-proton collision, instead the frequency of a certain final state to occur is connected to a probability usually expressed in terms of a cross section. The hierarchy of cross sections for different processes enfolds several orders of magnitude between the total inelastic cross section and rare processes like W,Z boson production, Vector boson scattering, Higgs boson production, production of possible new particles predicted in various beyond SM theories, etc. To give an example: the production cross section of the SM Higgs-boson is about 10 magnitudes lower compared to the total proton-proton cross section as shown in Figure 4.17.

The rate at which a final state  $\mathcal{X}$  is observed, relates to the cross section of the considered process and the luminosity  $\mathcal{L}$  of the experimental arrangement,

$$R(\mathcal{X}) = \frac{dN(\mathcal{X})}{dt} = \sigma(pp \rightarrow \mathcal{X}) \times \mathcal{L}. \quad (4.23)$$

To accumulate enough statistics for the measurements it is therefore necessary to work with high instantaneous luminosities. At the LHC design luminosity of  $\mathcal{L}_{\text{design}} = 10^{34} \text{ cm}^{-2} \text{ s}^{-1}$  one expects of the order of 850 million proton-proton collisions per second. A time interval of 25 ns between two bunches will lead to a bunch crossing rate of about 40 MHz. With a typical event size<sup>21</sup> of about 1.5 MB one would need a readout system powerful enough to store several TB of data per second. Such high rates are beyond the technical and processable capabilities and it is necessary to filter the incoming events based on signatures of rare physics processes before the events are finally written on a permanent storage element. The filtering is performed using a complex trigger system which reduces the incoming proton-proton collision rate by an order of  $10^6$ .

The ATLAS trigger system [80] is divided in into three subsystem: *level one* (L1), *level two* (L2) and *event filter* (EF). L2 and EF are collectively denoted as *High-Level Trigger* (HLT). Each level will subsequently perform additional selection steps on collision events which pass the preceding level to reduce the incoming event rate.

The L1 triggers are designed to perform a first and rough search for interesting physics signatures in the muon or calorimeter system. Two basic types of L1 triggers are used: L1 muon triggers, which use information from the RPCs in the barrel region and the TGCs in the end-caps, and the L1 calorimeter triggers. In order to analyze an event within a very narrow time interval the L1 calorimeter triggers are using a reduced granularity: the cells of the calorimeter are combined within the  $\eta$ - $\phi$  plane to “trigger towers”. The size of the towers is different depending on the region of the calorimeter considered, but for the most parts a size of  $\eta \times \phi = 0.1 \times 0.1$  is used. The trigger performs searches for energy accumulations based on the towers to spot interesting regions in the  $\eta$ - $\phi$  plane which could contain signatures of various physic processes, denoted as “regions of interest” (RoI). The information within the RoIs are passed to the L2 trigger for a detailed analysis at full granularity. The L1 triggers reduce the incoming event rate to

<sup>21</sup>The number of readout channel at the ATLAS detector is about 140 millions.

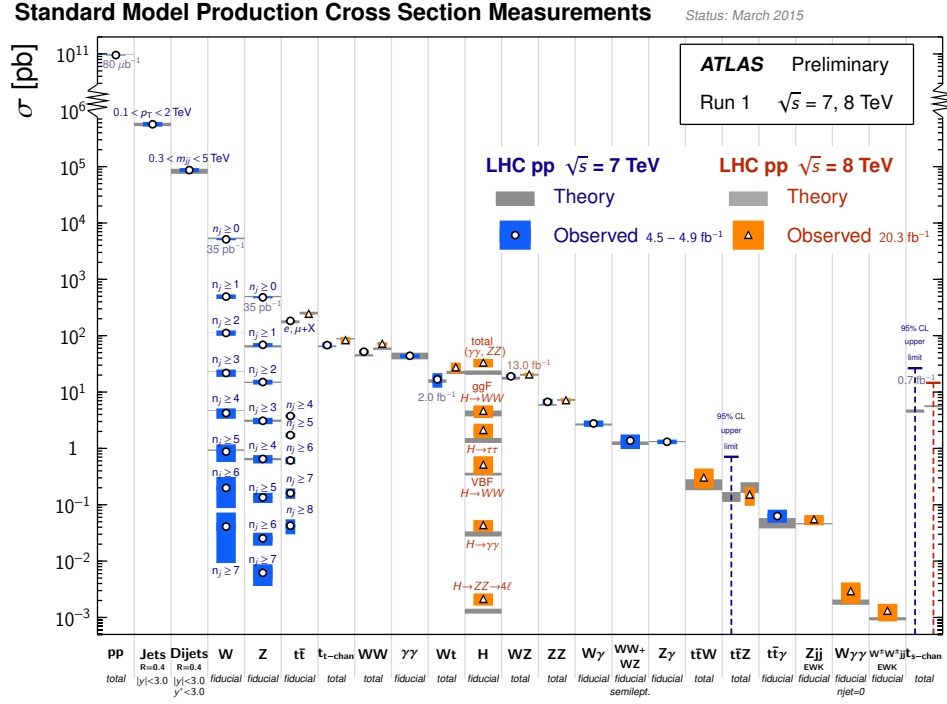


**Figure 4.17:** Summary of cross section measurements of SM processes at the ATLAS detector using proton-proton collision events at a center of mass energy of  $\sqrt{s} = 7$  TeV and  $\sqrt{s} = 8$  TeV [158]. The measurements are compared to SM predictions.

approximately 75 kHz with an average processing time of 2.5  $\mu$ s per event.

Events passing the L1 trigger are forwarded to L2 which reduces the rate to approximately 3.5 kHz with an average processing time per event of 40 ms. The L2 triggers make use of the full granularity of the detector and can combine information of all detector subsystems including track information of the inner detector. To speed up the trigger decision process, only small parts<sup>22</sup> in the  $\eta$ - $\phi$  plane of the full event record are considered based on the RoIs found by L1.

The final selection is performed on EF level to ensure a maximum event rate of 200 Hz with an average processing time of 4 s per event. Like the L2 triggers the full granularity of all sub-detector systems can be used on EF level but now considering the full event information. The EF algorithms for reconstructing and identifying physical objects are often close to their offline counterparts but the selection is normally looser compared to offline analyses.

A certain combination of the different levels is denoted as *trigger chain*. It should be noticed that not always all three levels are actively used for the event selection. Depending on the analysis also L1 or L2 trigger decision can already provide enough separation power between an interesting signal and background.

Different types of trigger items and trigger chains are used in ATLAS when searching for specific

<sup>22</sup>On average  $\sim 2\%$  of the event size is used.



signatures in the detector. In the context of this thesis only the trigger setup used for the Run 1 data taking will be discussed. The triggers in use search for one or more signatures of physical objects like electrons or muons above a certain threshold in transverse energy or transverse momentum<sup>23</sup>. Commonly used triggers are triggers for photons or leptons (electrons, muons and hadronically decaying tau leptons), triggers for jets from QCD interactions and triggers for missing transverse energy to be sensitive to particles which leave the experiment undetected like neutrinos. Each trigger makes use of different sub-detector parts depending on the required signature. An individual pre-scaling of each trigger is possible, allowing only a certain fraction of acceptable events to pass the trigger. The pre-scales help to ensure a manageable event rate and are adjusted during the data taking.

### 4.8.1 Minimum Bias Trigger

The *Minimum Bias Trigger* (MBT) systems allow to trigger on inelastic proton-proton collisions with a minimal set of requirements. Two main MBTs are used in the ATLAS experiment: a MBT based on *Minimum Bias Trigger Scintillators* (MBTS) and a MBT based on signals in the inner detector systems. This section will give a brief overview of Minimum Bias Triggers using the MBTS which is the main Minimum Bias Trigger used in the ATLAS experiment. The main references for the MBT in measurements at  $\sqrt{s} = 900 \text{ GeV}$  and  $\sqrt{s} = 7 \text{ TeV}$  can be found in Refs. [159, 160].

The MBTS [161] consist of 2 disks of scintillator counters, one on each detector side. Each disk is mounted orthogonal to the beam axis and installed on the cryostat of the calorimeter. This setup allows a coverage of  $|\eta| \in [2.09, 3.84]$ . A charged particle passing through the MBTS will induce a light emission within the scintillator material which is detected using photomultipliers. A “hit” in the MBTS is now defined as a signal above a certain threshold. Several MBT configurations are used in ATLAS, requiring one or more hits at one or both sides of the detector.

The efficiency<sup>24</sup> of the MBT versus the number of tracks with a  $p_T > 100 \text{ MeV}$  from the same proton-proton collision is shown in Figure 4.18. The trigger efficiency is close to 100 % except for very low charged particle multiplicities. Effects of the trigger inefficiency are considered in the relevant analyses.

### 4.8.2 Jet Trigger

A jet trigger algorithm is designed to search for jets with a transverse energy,  $E_T$ , above a certain threshold [162].

At L1 the trigger will search for energy deposits in the calorimeter using trigger towers scanning the accessible phase-space in  $\eta$  and  $\phi$ . Different window sizes are used, ranging from  $0.4 \times 0.4$ ,  $0.6 \times 0.6$  to  $0.8 \times 0.8$ . Once the L1 trigger finds an energy deposit above a certain energy threshold

<sup>23</sup>For the majority physics signatures (e.g. electrons or muons) the transverse energy can be seen as equivalent to the transverse momentum, since the common energies of the considered particles are large compared to their masses.

<sup>24</sup>The efficiency is defined against a control sample taken by minimum bias trigger based on inner detector information [160].

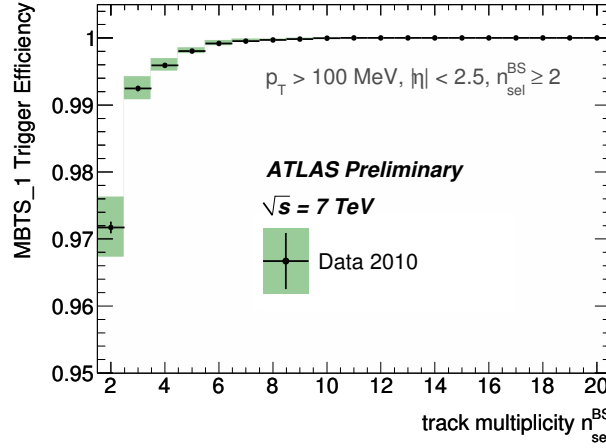


**Figure 4.18:** Efficiency of the MBTS as a function of reconstructed tracks with  $p_T > 100$  MeV for a center-of-mass energy of  $\sqrt{s} = 7$  TeV. The green shaded area shows the combined statistical and systematical uncertainty. The result is taken from Ref. [160].

a region of interest (RoI) around the direction of the deposit is defined. The L2 and EF filter trigger will then use the calorimeter cluster found in the RoI to perform further steps. On L2 a simple cone clustering algorithm is used to reconstruct the jet while on EF the full offline jet reconstruction is performed. The reconstruction on the EF level is the same as described in Section 4.5, except for a different energy calibration and only clusters in the RoI are considered.

The jet triggers are denoted with L1\_J50, L2\_J70 and EF\_J75 in which L1, L2 and EF denote the corresponding trigger level and the number denotes the  $E_T$  trigger threshold in GeV. An example for the jet trigger efficiencies is shown in Figure 4.19 for the given L1, L2 and EF triggers.

Most jet triggers are prescaled to deal with the high QCD cross section at the LHC. The pre-scale factor anti-correlates with the energy threshold of the given trigger. Consequently, the pre-scale factor decrease with increasing trigger threshold. The lowest un-prescaled trigger thresholds for the 2010 dataset ranges from 15 GeV to 195 GeV during the data taking, due to the changes in the run conditions. For 2011 the lowest un-prescaled jet trigger threshold was 240 GeV.

### 4.8.3 Muon Trigger

At L1 the muon trigger algorithms search for two to three hits in either the resistive plate chamber (RPC) or the thin gas chambers (TGC) for the barrel and end-cap region, respectively [165]. A first estimate of the muon candidates transverse momentum is performed and the region of interest (RoI) is defined as input for the HLT. On L2 a simple and fast muon reconstruction is performed within the RoI provided by the L1 trigger using information from the MDTs. Also a combination with tracks from the inner detector and isolation requirements are possible on L2. The EF performs the full muon reconstruction as described in Section 4.4 and finally requires one or two muon candidates above a certain  $p_T$  threshold.

Within the context of this thesis two un-prescaled single-muon trigger are used: the EF\_mu18\_MG

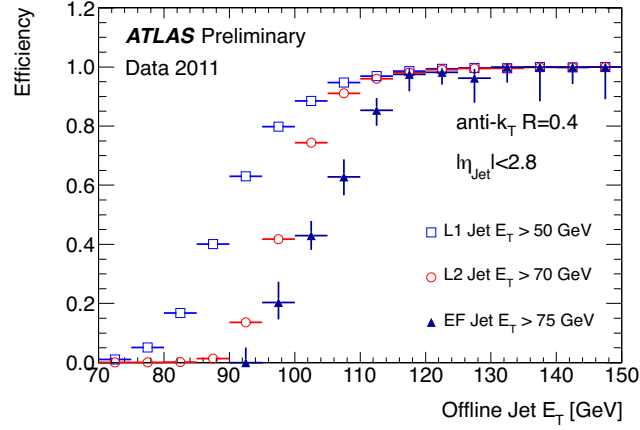


**Figure 4.19:** Jet trigger efficiency at L1, L2 and EF for anti- $k_t$  jets with a radius parameter  $R = 0.4$  in the barrel part of the calorimeter. The efficiency is shown as a function of the transverse jet energy [163, 164].

and EF\_mu18\_MG\_medium. Both require a muon candidate with  $p_T > 18$  GeV but the underlying L1 trigger items are different. The L1 trigger for EF\_mu18\_MG\_medium has a slightly higher  $p_T$  threshold and was used starting in August 2011 to account for the increased luminosity.

The efficiencies of the muon triggers are measured using tag-and-probe methods in  $Z \rightarrow \mu\mu$  events, by selecting di-muon events with an invariant mass close to the mass of the Z boson. One of the muons (the *probe* muon) is subsequently used for the efficiency measurements [165]. Some example results are shown in Figure 4.20. The turn-on curve is very steep for the muon trigger and converges at  $p_T > 20$  GeV to a constant value. Scale factors are derived to account for the differences between the measurement and the MC predictions, parametrized in  $\eta$  and  $\phi$  of the muon candidate to resemble the structure of the muon trigger systems. The total uncertainty on the scale factors is of the order of 1 % [165].

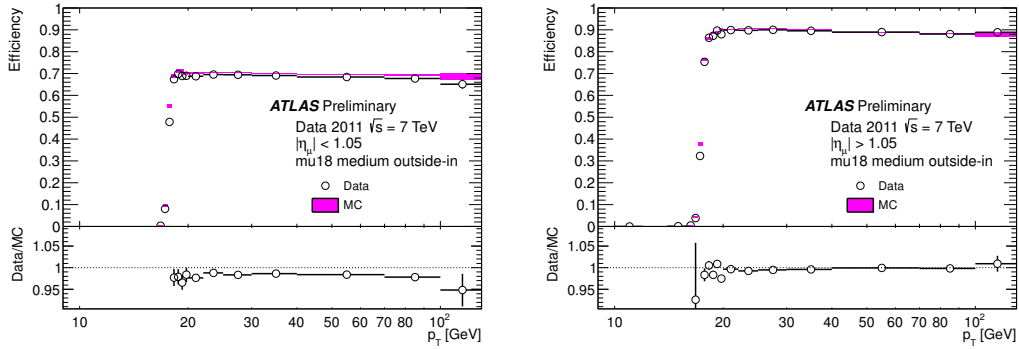


**Figure 4.20:** Muon trigger efficiencies are shown as function of  $p_T$  for two different regions in the pseudorapidity  $\eta$ . The efficiency is measured in  $Z \rightarrow \mu\mu$  events and compared with MC predictions. The results are taken from Ref. [165].

#### 4.8.4 Tau Trigger

Similar to the tau reconstruction and identification discussed in Section 4.6 the tau trigger tries to identify hadronically decaying tau leptons [141, 166], but in contrast to the offline identification restricting the resources and time for the trigger decision. The goal is to filter a set of collision events which are likely to include signatures of one or more hadronic tau lepton decays.

The L1 tau trigger makes use of trigger towers in the calorimeter (using electromagnetic as well as hadronic calorimeter cells) with a tower size of  $0.1 \times 0.1$  in  $\eta \times \phi$ . Squares of  $4 \times 4$  trigger towers are used to find regions of interest containing a possible tau trigger candidate. Like the full tau reconstruction, the inner part of the region (a  $2 \times 2$  square of towers) is defined as the *core* region and the outer part as the *isolation* region. The splitting follows the assumption that the majority of the particle flow originating from a real tau decay will end up in the core region, due to the Lorentz boost of the tau decay system. Several L1 tau trigger items are used in the ATLAS trigger system, triggering on candidates with a transverse energy in the core region,  $E_T^{\text{core}}$ , above a certain threshold. In addition an isolation requirement can be applied, requiring a transverse energy in the isolation cone,  $E_T^{\text{iso}}$ , to be below a certain threshold.

So far, the selection of tau trigger candidates is only based on calorimeter information. On L2, tracking measurements are added by matching tracks (passing certain quality criteria) within an area around the candidate found by the L1 trigger. In addition, observables are calculated using calorimeter information to describe the shower shape of the candidate within the calorimeter. A candidate is accepted on L2 if one to four tracks could be matched and if the candidate passed a sequence of criteria based on the shower shape observables.

The final selection is performed on event filter level, by requiring that one or two tau trigger candidates pass a final tau identification with one to three associated tracks. The identification algorithm on trigger level is similar to the offline tau identification using track and cluster based observables as input for a boosted decision tree algorithm. Like the offline tau identification, different working points for the identification level are defined. Within the context of this thesis the *medium* working point was utilized, which corresponds to a signal efficiency of about 85 % and 80 %, for 1-prong and multi-prong tau candidates, respectively. These efficiencies are in general looser than the corresponding offline working points to ensure that the trigger will not cut into the phase space available in the offline identification. Within the context of this thesis two tau related triggers are used: a di-tau trigger with relatively low energy thresholds, `EF_tau20(T)_medium1_tau29(T)_medium1`, and a single tau trigger with a high-energy threshold, `EF_tau125_medium1`.

**EF\_tau20(T)\_medium1\_tau29(T)\_medium1** Requires two tau trigger candidates in the event with transverse energy of  $E_T > 20$  GeV and  $E_T > 29$  GeV, respectively, both passing the medium BDT [144, 145] working point on trigger level. The underlying L1 thresholds are  $E_T = 8$  GeV and 11 GeV, which were raised<sup>25</sup> during the 2011 data taking to 11 GeV and 15 GeV to account for the increasing luminosity and the accompanying increase of the trigger rates. The ditau trigger was un-prescaled during the full 2011 data taking period.

---

<sup>25</sup>Denoted with the **T** in the trigger name.

**EF\_tau125\_medium1** Requires one tau trigger candidate in the event with  $E_T > 125$  GeV passing the medium BDT working point on trigger level. The underlying L1 trigger threshold was 50 GeV. The single tau trigger was un-prescaled during the full 2011 data taking period.

**Performance** Efficiencies of the tau triggers are measured in  $Z \rightarrow \tau\tau$  and  $W \rightarrow \tau\nu$  events using tag-and-probe methods [141, 166]. The efficiency of a tau trigger is defined as the number of tau trigger candidates passing a certain identification level divided by the number of tau candidates identified with the offline tau identification at the *tight* working point. Only trigger candidates are considered which match within an angular distance  $\Delta R < 0.2$  with the offline tau candidate. The efficiency as a function of the transverse momentum is shown in Figure 4.21 (left) for the **EF\_tau29\_medium1** trigger. The efficiency shows a turn on behavior up to  $p_T \approx 45$  GeV and then saturates into a plateau around 80 %. The comparison of trigger efficiencies measured in real  $Z \rightarrow \tau\tau$  events (the effect is similar for  $W \rightarrow \tau\nu$  events) with the MC predictions shows a deviation up to 5 %. Scale factors as a function of the tau candidate  $p_T$  are derived to correct the MC simulations: an example for a trigger scale factor is shown in Figure 4.21 (right). The combined statistical and systematic uncertainties for the scale factors are of the order of 2 % to 4 %.

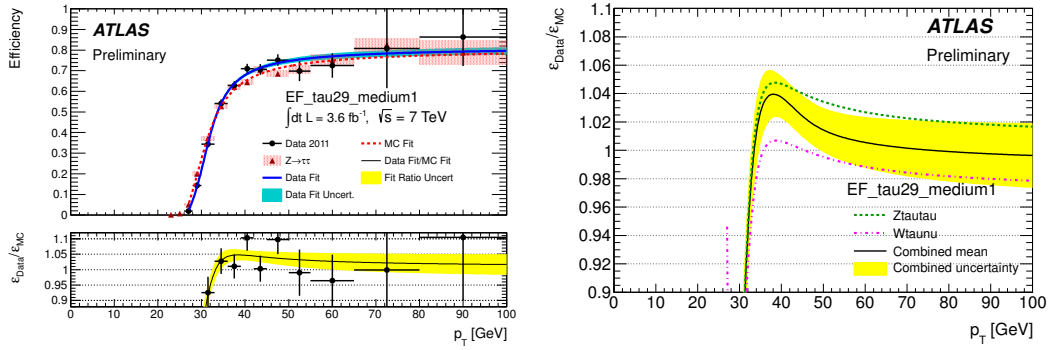


**Figure 4.21:** The efficiency (left) and the scale factor (right) for the **EF\_tau29\_medium1** is shown as function the  $p_T$  of the tau candidate. The efficiencies are measured in  $Z \rightarrow \tau\tau$  events and compared with MC predictions (red triangles). The results are taken from Ref. [166].



## 5 Measurement of the Underlying Event

Searches for new particles, for example the search for the Higgs boson, are performed using data collected in proton-proton collisions at the LHC. Protons have advantageous properties: they are relatively easy to produce (compared to for examples anti-protons which were used in proton anti-proton collision at the Tevatron accelerator [87]) even in high densities, protons are stable<sup>1</sup> and have a heavily suppressed synchrotron radiation, which allows an efficient acceleration using a circular collider compared to the acceleration of lighter particles like electrons.

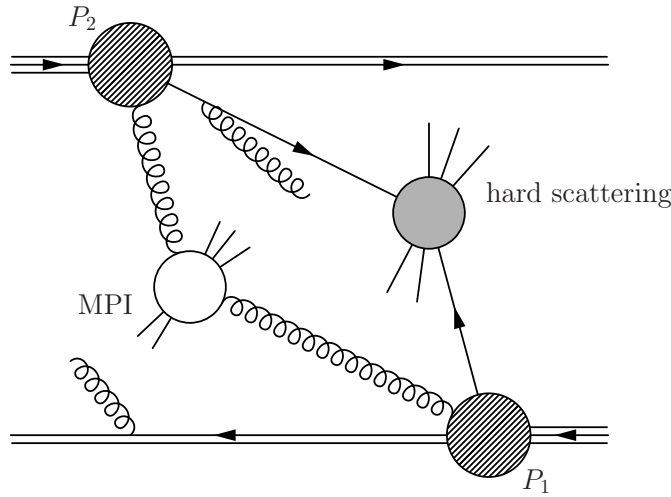


**Figure 5.1:** Illustration of a proton-proton collision including a hard scattering process (grey circle), one additional parton-parton scattering (MPI, white circle) as well as additional initial and final state radiation.

But the downside, protons are not elementary particles and built out of quarks and gluons, collectively termed *partons*<sup>2</sup>. The quarks are differentiated in three *valence* quarks (two up and one down quark) and “an infinite sea of light  $q\bar{q}$  pairs” [168]. The latter ones are denoted as *sea quarks* and can be described by higher order corrections in perturbation theory. The probability to find a certain quark flavor within the proton at an energy scale  $Q^2$ , carrying a momentum fraction  $x$  of the total proton momentum, is described by a *parton distribution function* (PDF),  $f(x, Q^2)$ , illustrated in Figure 5.2.

The complex proton structure leads to a complicated collision landscape between two protons, consisting of several sub-reactions between the partons. The majority of interactions are strong

<sup>1</sup>So far a proton decay has not been observed (which would lead to implications for theories beyond the SM) yet and the lower limits of the proton mean life time are of the order of  $2.1 \times 10^{29}$  years [12].

<sup>2</sup>The term *parton* was introduced by R. Feynman in 1969 [167]. The parton model was utilized by J. D. Bjorken and E. A. Paschos to explain measurements of deep inelastic lepton-nucleon scattering experiments [37].

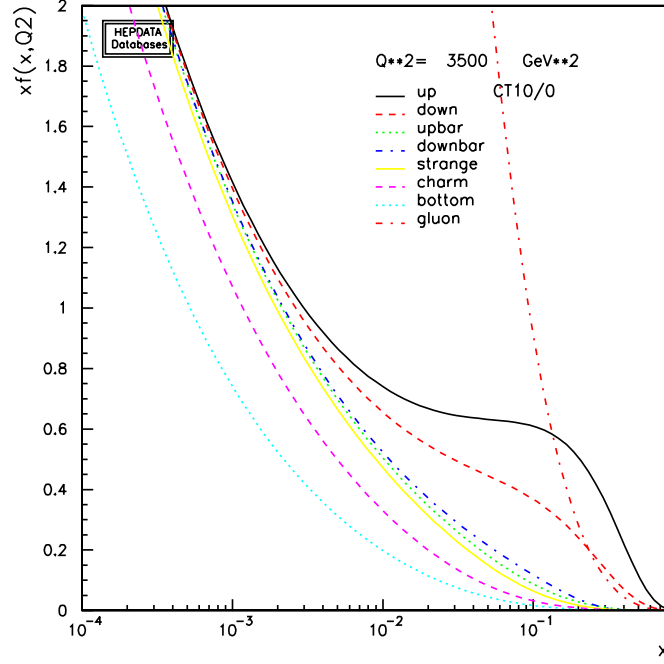


**Figure 5.2:** Parton distribution functions  $x \cdot f(x, Q^2)$  vs.  $x$  for a momentum scale  $Q^2 \sim (60 \text{ GeV})^2$  using the CT10 set [169]. The plot was created using the PDF plotting tool provided by the HepData project: <http://hepdata.cedar.ac.uk/pdf/pdf3.html> (28.09.2015).

interactions, normally with a quite low momentum transfer between the interacting partons. Only a fraction of collisions involves high momentum transfers, denoted as *hard scattering*. The hard scattering processes are usually the processes involving the “interesting” physics, including the production of resonances at high masses like Z,W or Higgs bosons but also high energy jet production. The final state signatures of the hard scattering can be used to trigger and classify the event by searching for particles with high transverse momentum within the fiducial region of the detector. Additional interactions are accompanying the hard scattering including additional parton-parton interactions, denoted as multiple parton interaction (MPI), interaction with remnants of the proton scattering as well as initial and final state radiations of all sub-processes, illustrated in Figure 5.1. These interactions are collectively denoted as “underlying event” (UE).

The underlying event contribution is dominated by QCD processes at low energy scales. Since these processes cannot be deduced from first principles via perturbation theory, they are modeled in Monte Carlo event generators using phenomenological concepts and algorithms. These models introduce additional parameters which are a priori unknown and need to be fitted to measurements. The fitting process of MC models is usually referred to as *tuning* and depends in general on the center-of-mass energy and the impact parameter of the proton-proton collision. If the collision is nearly central, and therefore the impact parameter close to zero, one expects that the mean UE contribution is constant against the hard scattering energy scale. To account for the dependencies within the tuning processes, it is important to provide measurements sensitive to the UE contribution at the considered center-of-mass energy and, if possible, over a large range of hard scattering energy scales, since a bulk of analyses at the LHC are operating at



processes with high energy momentum transfer between the protons.

So far, underlying event contributions were measured using collision data from experiments at the Tevatron and the LHC. The CDF collaboration published several UE measurements in inclusive jet events and Drell-Yan events at a center-of-mass energy of 1.8 TeV [170] and 1.96 TeV [171] using proton-antiproton collision data at Tevatron. UE measurements using proton-proton collision data at center-of-mass energies of 900 GeV, 2.76 TeV and 7 TeV at the LHC were published by the ATLAS [172–175], ALICE [176] and CMS [177–182] collaborations using minimum bias, track-jets and Z boson events.

In this chapter, the underlying event analysis in dijet events using data at  $\sqrt{s} = 7$  TeV recorded with the ATLAS detector at LHC is presented, which has been published by the ATLAS collaboration in 2014 [183]. The measurements cover the underlying event contribution over a large energy range and are already used for tuning efforts within the ATLAS collaboration [184].

## 5.1 Underlying Event Analysis

The term underlying event incorporates particle and energy flow contributions from different parts of the proton-proton interaction, which are not classified as the hard scattering. It is not possible to separate the UE contribution from particles originating from the hard scattering process on a single event basis. Instead particle multiplicity densities as well as momentum and energy flow densities are measured in geometrical regions sensitive to contributions of the UE.

Within the scope of this thesis, the underlying event is measured in dijet events containing at least one jet above a certain transverse momentum threshold. The dominant contributions arise from  $2 \rightarrow 2$  parton scattering processes with two quarks or gluons in the final state, which are observed as jets, illustrated in Figure 5.3. To preserve the total transverse momentum it is necessary that both jets balance each other: both jets should carry roughly the same amount of transverse momentum and should be separated by  $180^\circ$  in the azimuthal plane. The longitudinal momentum of the outgoing particles is not fixed, because the initial longitudinal momentum fraction of the interacting partons is unknown, while the transverse momentum component of the incoming partons is assumed to be zero<sup>3</sup>. Initial and final state radiation can lead to higher jet multiplicities which degrades the balance between the two hard scattered particles.

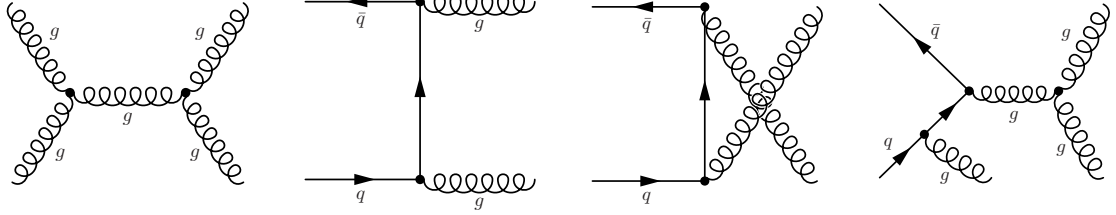


**Figure 5.3:** Example Feynman diagrams for dijet productions with quarks and gluons in the initial and final state.

The cross section for the inclusive dijet production with two initial partons (i,j) and to two final partons (k,l) can be expressed at lowest order of perturbation theory in the following formula [168, ch. 7]:

$$\frac{d^3\sigma}{dy_3 dy_4 dp_T^2} = \frac{1}{16\pi s^2} \sum_{i,j,k,l} \frac{f_i(x_1, \mu^2)}{x_1} \frac{f_j(x_2, \mu^2)}{x_2} \times \overline{\sum} |\mathcal{M}(ij \rightarrow kl)|^2 \frac{1}{1 + \delta_{kl}} \quad (5.1)$$

where  $f_{i,j}(x_{1,2}, \mu^2)$  represents the parton density distribution for the corresponding incoming partons at the momentum fractions  $x_{1,2}$  of the two incoming protons. The sum over all involved matrix elements is represented by  $\overline{\sum} |\mathcal{M}|^2$ . The equation is evaluated at a certain momentum scale  $\mu$  with  $y_{3,4}$  representing the rapidities of the two outgoing particles in the laboratory frame.

Measurements for the inclusive jet and dijet production have been performed within the ATLAS collaboration [185, 186]. The cross sections for the jet production are strongly dependent on the transverse momentum of the produced jets as well as the considered region in rapidity. For the fiducial region considered within the context of this analysis, the total jet production cross

<sup>3</sup> To be more precise, this assumptions only holds in the “infinite momentum frame”, in which the momentum vector of the proton can be approximated with  $p^\mu = (E, 0, 0, E)^T$  for  $E \gg m_{\text{proton}}$ , which is a reasonable assumption for proton energies at the LHC.

section is of the order of  $10^6$  pb and, except for soft QCD scattering processes, it is the dominant interaction in proton-proton collisions at the LHC.

### 5.1.1 General Analysis Strategy

The central idea is the splitting of the azimuthal space in regions which are sensitive to the hard scattering component and regions sensitive to the underlying event contribution. Observables measured within these regions are unfolded afterwards to remove resolution and migration effects caused by interactions with the detector. Hence two level of particle definitions are used for Monte Carlo simulation samples: the *detector level* including a detector simulation and a *particle level* resembling the expected observable distributions without any detector simulation. On detector level, every observable is defined using either topological calorimeter clusters built from energy deposits in electromagnetic and hadronic calorimeter or tracks of charged particles measured within the inner detector. The corresponding observables on particle level are expressed using charged and neutral particles with a mean lifetime of  $\tau > 0.3 \times 10^{-10}$  s.

UE measurements using this kind of analysis technique were already performed at Tevatron in  $p\bar{p}$  collisions at a centre-of-mass energies of  $\sqrt{s} = 1.8$  TeV and 1.96 TeV but are also heavily used within UE measurements at ATLAS, ALICE and CMS.

The baseline is the identification and parametrization of the hard scattering interaction. For the dijet topologies, the jet with the highest transverse momentum among all jets within the event (“leading jet”) is used to parametrize the energy scale and direction of the hard scattering in the azimuthal phase space. The scale is defined by the transverse momentum of the leading jet,  $p_T^{\text{lead}}$ , and the direction by the  $\phi$  coordinate,  $\phi_{\text{lead}}$ .

Jets in data and in detector level simulation are reconstructed from topological calorimeter clusters using the anti- $k_t$  jet cluster algorithm with a radius parameter of  $R = 0.4$ . For particle level simulations, the same jet clustering algorithm is deployed but, instead of topological calorimeter cluster, stable neutral and charged particles, except neutrinos, are used. In both cases the jets are required to provide a minimal transverse momentum of  $p_T > 20$  GeV and maximal rapidity  $|y| < 2.8$  to ensure that the jets are well located within the barrel region of the calorimeter. For detector level jets the EM+JES calibration scale is applied.

The azimuthal space is subsequently portioned into four main regions depending on the azimuthal distance  $\Delta\phi = |\phi - \phi_{\text{lead}}|$  of the leading jet against the object of interest<sup>4</sup>: the *toward* region with  $\Delta\phi < 60^\circ$ , two *transverse* regions with  $60^\circ < \Delta\phi < 120^\circ$  and an *away* region with  $\Delta\phi > 120^\circ$ , which are illustrated in Figure 5.4. Observables in the toward and away region are dominated by particle interactions originating from the hard scattering process. The toward region contains by construction the leading jet and the away region is covering particles from the balancing jet.

The underlying event contributions are assumed to be uncorrelated from the hard scattering and therefore on average equally distributed against  $\phi_{\text{lead}}$ . Within the toward and away region the UE contribution is concealed by the hard scattering but not within in the transverse regions

<sup>4</sup>Either topological clusters or tracks (on particle level the corresponding counterpart is used) which are used to construct the final observables.

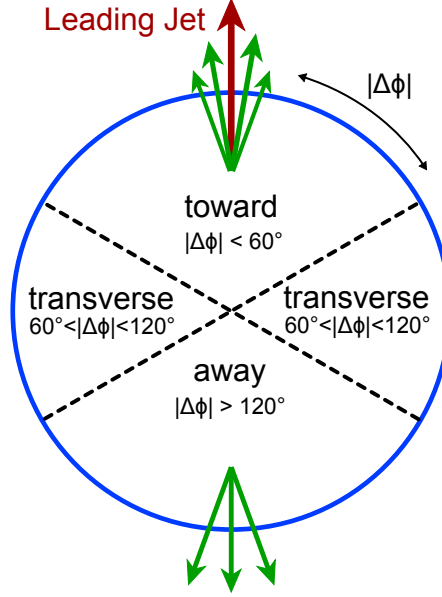


**Figure 5.4:** Illustration of the azimuthal plane split for a single event. All regions are defined by the angular distances  $\Delta\phi$  to the central axis of the leading jet: the toward region is defined around the leading jet with  $|\Delta\phi| < 60^\circ$ , both transverse region with  $60^\circ < |\Delta\phi| < 120^\circ$  and the away region with  $|\Delta\phi| > 120^\circ$ . The toward and away regions are dominated by contributions of the hard scattering while the transverse regions are sensitive to the underlying event.

which are perpendicular to the plane of hard scattering. The transverse region is consequently sensitive to the underlying event contribution. The sensitivity can be spoiled by additional initial and final state emissions of the hard scattering. Especially wide range emissions are problematic because they can directly contribute to the particle flow within transverse region and disturb the balance of the assumed dijet system. The resulting balancing jet(s) may no longer be covered by the away region and at least partially migrated into the transverse region, illustrated in Figure 5.5.

To allow a more distinct separation between the pure UE contribution and the hard scattering two additional analysis steps are performed. In a first step, both transverse regions are categorized in a *trans-max* and *trans-min* region which are defined as the transverse region with more/less activity for the considered observable, respectively. The trans-max region is more likely to be affected by contributions from the hard scattering and consequently the trans-min region is more sensitive to the UE contribution. The difference between the trans-max and trans-min region, denoted as *trans-diff*, is sensitive to the initial and final state radiation of the hard scattering, because the average contribution of the underlying event is subtracted from the trans-max region. In a second step, the separation of the event selection in an inclusive and an exclusive dijet topology is performed. Additional selection requirements for the exclusive dijet selection ensure a clean and balanced dijet topology, minimizing the contributions from radiations.

### 5.1.2 Observables

To quantify the underlying event contribution, multiplicity distributions and momentum (or energy) sums of track or clusters within the transverse regions are used. But the underlying

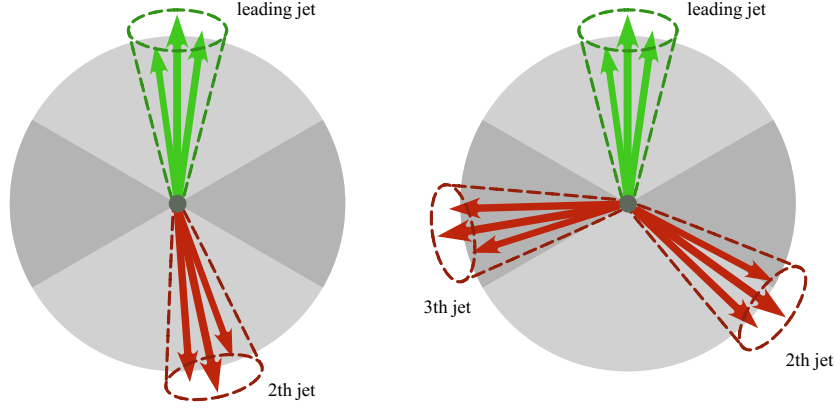


**Figure 5.5:** Illustration of a two and three jet topology projected in the azimuthal plane. The left side shows a dijet topology with both jets located within the toward/away region. The right side illustrates the effect of an additional 3th jet originating from a wide angle emission in the hard scattering process contributing to the energy and particle flow in the transverse regions. The lighter grey area represents the toward/away region and the darker grey areas both transverse regions.

event contributions cannot be reliably separated from the hard scattering on an event-by-event basis and instead the mean values of the densities are considered.

The observables are presented on two different ways: *one dimensional distributions* and *profile distributions*. The one-dimensional distributions are histograms of the charged particle multiplicity or the sum of transverse momenta of charged particles for a given range in  $p_T^{\text{lead}}$ . All histograms are normalized to unity.

The mean values of the observables are presented using profile histograms, which show for each bin in  $p_T^{\text{lead}}$  the corresponding mean value of an observable  $\mathcal{O}$  and its standard deviation as uncertainty using the arithmetic mean estimator. For a given bin  $i$  in  $p_T^{\text{lead}}$  the mean value of  $\mathcal{O}$  is defined by

$$\langle \mathcal{O} \rangle_i = \frac{\sum_{j=1}^{N_i} \mathcal{O}_j(p_{T,i}^{\text{lead}})}{N_i}, \quad (5.2)$$

with a standard deviation of

$$\sigma(\mathcal{O})_i = \sqrt{\frac{1}{N_i} \sum_{j=1}^{N_i} \left( \mathcal{O}_j(p_{T,i}^{\text{lead}}) - \langle \mathcal{O} \rangle_i \right)^2}, \quad (5.3)$$

where  $N_i$  is the number of events and  $\mathcal{O}_j(p_{T,i}^{\text{lead}})$  the value of the considered observable. Most observables are normalized to the area  $\delta\eta\delta\phi$  covered by the considered region in the  $\eta$ - $\phi$  plane.

**Track Based Observables** Track based observables are the mean number of tracks,  $\langle N_{\text{ch}}/\delta\eta\delta\phi \rangle$ , and the mean scalar sum of the tracks transverse momenta,  $\langle \sum p_T/\delta\eta\delta\phi \rangle$ , per unit in  $\eta$ - $\phi$ . In addition the mean value of the average transverse momentum<sup>5</sup> in each event,  $\langle p_T \rangle = N_{\text{ch}}/\sum p_T$ , is considered. Tracks are required to pass the following set of requirements:

<sup>5</sup>Please note that this observable combines two averaging processes: first the mean transverse momentum for a specific event and second the mean value of the first average over all events.

1. The transverse momentum of the tracks should be  $p_T^{\text{trk}} > 500 \text{ MeV}$  with a pseudorapidity value of  $|\eta^{\text{trk}}| < 2.5$ .
2. Each track should be reconstructed with at least one hit in the pixel layers and at least six hits in the SCT layers.
3. At least one hit in the innermost pixel layer (*B-layer*) is mandatory (only if the pixel module was active during the data taking).
4. Track impact parameters with respect to primary vertex (PV) are required to be below 1.5 mm to reduce the impact from tracks not originating from the PV (e.g. tracks from pile-up interactions):

$$d_0^{\text{PV}} < 1.5 \text{ mm} \quad \text{and} \quad z_0^{\text{PV}} \cdot \sin(\theta^{\text{trk}}) < 1.5 \text{ mm}.$$

5. The probability to obtain a  $\chi^2$  fit value equal or greater than the observed  $\chi_{\text{obs}}^2$  value<sup>6</sup> should be  $> 0.01$  for tracks with  $p_T^{\text{trk}} > 10 \text{ GeV}$  in order to reduce the amount of tracks with a mis-reconstructed  $p_T^{\text{trk}}$  [187].

The corresponding simulated particle level distributions are defined using charged and stable particles with  $p_T > 500 \text{ MeV}$  and  $|\eta| < 2.5$ . Only primary particles produced in the simulated proton-proton collision and their successor are considered, secondary particle due to detector simulation using GEANT4 [40] (e.g. interaction with the detector material) are not considered.

**Cluster Based Observables** So far, only observables measuring the underlying event contributions of charged particles are defined. To measure also the neutral particle flow, the mean scalar sum of transverse energy per unit in  $\eta \times \phi$ , denoted  $\langle \sum E_T / \delta\eta \delta\phi \rangle$ , build from topological clusters in the calorimeter is considered, containing energy depositions from both neutral and charged particles. No additional energy threshold is applied and the clusters are collected within two regions in  $\eta$ :  $|\eta^{\text{clus}}| < 2.5$  to match the phase space covered by the inner detector and  $|\eta^{\text{clus}}| < 4.8$  to use (nearly) the full coverage of the calorimeter. Within  $1.3 < |\eta^{\text{clus}}| < 1.32$  only clusters with an energy fraction in the hadronic calorimeter below 40 % are considered (in order to avoid anomalies in clusters with high  $f_{\text{had}}$  within this region):

$$f_{\text{had}}(\text{cluster}) < 0.4. \quad (5.4)$$

The corresponding particle level distributions are defined as the mean scalar sum of transverse energy per unit in  $\eta \times \phi$  for charged and neutral, stable particles (excluding again secondary particles from the detector simulation). The particles are selected within the same pseudorapidity regions,  $\eta < 2.5$  and 4.8, and are required to provide a minimal scalar momentum of  $p > 200 \text{ MeV}$  and 500 MeV for neutral and charged particles, respectively. Particles with lower momentum are most likely stopped and absorbed before reaching the calorimeter and will therefore not contribute to the energy depositions [175].

---

<sup>6</sup>Technically one requires that the complementary cumulative distribution function,  $S(\chi^2)$ , of the  $\chi^2$  distribution for the considered degrees of freedom to be greater than 0.01 for the observed  $\chi_{\text{obs}}^2$  value:  $S(\chi_{\text{obs}}^2) > 0.01$ .

In general it is not possible to reliably associate every track to a particular energy deposition in the calorimeter<sup>7</sup>. A clear separation between the contribution of charged and neutral particles to the UE is therefore not possible. Instead the mean fraction of energy carried by the charged particles is considered by measuring the ratio between  $\sum p_T$  and  $\sum E_T$ , denoted as *mean charged fraction*  $\langle \sum p_T / \sum E_T \rangle$ . A summary of the observables can be found in Table 5.1.

Formula symbol	Detector Level	Particle Level
$\left\langle \frac{N_{\text{ch}}}{\delta\eta\delta\phi} \right\rangle$	Mean number of tracks per unit in $\eta \times \phi$	Mean number of charge, stable particles per unit in $\eta \times \phi$
$\left\langle \frac{\sum p_T}{\delta\eta\delta\phi} \right\rangle$	Mean scalar transverse momentum sum of tracks per unit in $\eta \times \phi$	Mean scalar transverse momentum sum of charge, stable particles per unit in $\eta \times \phi$
$\langle p_T \rangle$	Mean value of the average transverse track momentum per event	Mean value of the average transverse momentum of charge, stable particles
$\left\langle \frac{\sum E_T}{\delta\eta\delta\phi} \right\rangle$	Mean scalar transverse energy sum of topological cluster in the calorimeter per unit in $\eta \times \phi$	Mean scalar energy sum of stable neutral and charged particles
$\langle \sum p_T / \sum E_T \rangle$	Mean ratio of the scalar transverse momentum sum of tracks over the scalar transverse energy sum of calorimeter cluster	Mean ratio of the scalar transverse momentum sum of charged particles over the scalar energy sum of charged and neutral particles

**Table 5.1:** Observables for the underlying event analysis on detector and particle level.

<sup>7</sup>For some certain physical processes and particles, one can perform an association between tracks and calorimeter clusters, e.g. for the identification of high energetic (isolated) electrons.

### 5.1.3 Data & Monte Carlo Event Samples

**Data** The underlying event measurement is performed using proton-proton collision data at a center-of-mass energy of  $\sqrt{s} = 7\text{ TeV}$  recorded with the ATLAS Experiment at LHC. The measurements took place during the Run 1 phase of the ATLAS experiment in the year 2010 over a time interval of almost seven months. The recordings are staggered in periods, which range from period A – I. A total luminosity of  $\sim 47\text{ pb}^{-1}$  was recorded with a peak instantaneous luminosity of the order of  $0.2 \times 10^{32}\text{ cm}^{-2}\text{ s}^{-1}$  [112]. After additional requirements for stable beam conditions and data quality (ensuring that all relevant sub-detector systems are working properly) a total integrated luminosity of  $\mathcal{L}_{\text{int}}^{2010} = 37.0(13)\text{ pb}^{-1}$  has been used for the underlying event analysis.

Details on the run setup can be found in Section 3.3. For the underlying event analysis, the relative low number of pile-up interactions during the 2010 data taking period (up to  $\sim 5$  collisions on average) is an advantage because pile-up interactions are a possible background. In addition, the relative low trigger thresholds and pre-scales in 2010, compared to the data taking in 2011 and 2012, allow to accumulate a reasonable amount of statistics of interactions at low energy scales.

**Simulations** Simulations of proton-proton collisions including interactions which are typically associated to the underlying event (MPIs, initial and final state radiations and beam remnants interactions) are utilized for correction and unfolding procedures of the measurements and for subsequent comparisons of the corrected data with predictions at particle level.

QCD interactions with multi-jet final states are simulated using the leading order Monte Carlo generators PYTHIA 6 [188], PYTHIA 8 [148], HERWIG++ [189], HERWIG+JIMMY [190, 191] and ALPGEN+HERWIG+JIMMY [192] as well as the next-to-leading order generator POWHEG [193–195] interfaced with PYTHIA 6. All samples are generated at a center-of-mass energy of  $\sqrt{s} = 7\text{ TeV}$  but with different parton shower, MPI and hadronisation models as well as different parton distribution functions for the incoming protons. The underlying event measurements are sensitive to the properties of these models and allow to test and tune the different model parameter.

Two different sets of simulated samples are employed:

1. The first set contains two samples used within the unfolding procedure to compare the measurements directly with particle level predictions without the necessity of an additional detector simulation. The unfolding is performed using a PYTHIA 6 sample with MRST LO\* [196] as PDF and the AMBT1 [197] tune. Possible systematic effects due to the unfolding procedure are evaluated using a HERWIG++ samples with a MRST LO\* PDF and a LO\*\_JETS<sup>8</sup> tune [198]. Both samples are generated on detector level using a GEANT4 based simulation of the ATLAS detector.

---

<sup>8</sup>The LO\*\_JETS parameter configuration is an old tune compared to the HERWIG++ tunes used for the comparison with the unfolded measurements. This is acceptable for the unfolding procedure, because the unfolding process is sensitive to the transition between particle and detector level rather than to the details of the tuning.



2. The second set contains particle level samples from various MC generators. The full list of samples can be found in Table 5.2.

MC Event Generator	Version	PDF(s)	Tune
Samples for data correction & unfolding			
PYTHIA 6	6.425	MRST LO*	AMBT1
HERWIG++	2.5.0	MRST LO*	LO*_JETS
Samples for comparisons between measurements and MC predictions			
PYTHIA 8	8.157	CT10 [169]	AU2 [199]
PYTHIA 6	6.425	CTEQ5L [200]	Perugia 2011 [201]
PYTHIA 6	6.421	CTEQ5L	DW [202]
HERWIG++	2.5.1	MRST LO** [203]	UE7-2 [204]
HERWIG+JIMMY	6.510	MRST LO**	AUET2 [205]
ALPGEN+HERWIG+JIMMY	2.13 + 6.510	CTEQ6L1 [206]	AUET1 [205]
POWHEG+PYTHIA 6	r2169 + 6.425	CT10 + CTEQ5L	Perugia 2011

**Table 5.2:** Monte Carlo event generator used within the context of the underlying event analysis on dijet topologies. For POWHEG+PYTHIA 6 two separated PDF sets are applied: CT10 for the matrix element calculation using POWHEG and CTEQ5L for the parton shower and MPI simulation within PYTHIA 6.

For the PYTHIA 6 generator, three different tunes are tested: AMBT1, Perugia 2011 [201] and DW [202]. The AMBT1 is the first tune performed by the ATLAS collaboration using the first minimum bias measurements at the LHC. Perugia 2011 is the latest tune of the Perugia series and based on early LHC minimum bias measurements using the  $p_T$ -ordered parton shower model of PYTHIA [183]. In contrast, the PYTHIA 6 DW tune has been derived using measurements from CDF during Run II using a virtually-ordered parton shower model.

The PYTHIA 8 Monte Carlo generator allows to interleave the MPI scattering model with the initial state and final state radiation process. The AU2 [199] tune is primarily based on UE measurement using tracks performed by the ATLAS collaboration at  $\sqrt{s} = 7$  TeV.

For HERWIG+JIMMY and ALPGEN+HERWIG+JIMMY two ATLAS tunes are used: the AUET2 [205] and the older version AUET1 [205], respectively, both using data from underlying event measurements at ATLAS and CDF. With the HERWIG++ generator, a color reconnection model has been introduced and the UE7-2 [204] tune allows a reasonable description of the ATLAS minimum bias and underlying events measurements using tracks [183].

#### 5.1.4 Event Selection

The event selection is performed to accumulate a sample for proton-proton interactions with dijet topologies in the final state, originating (largely) from QCD interactions. The selection also reduces the contamination from possible background interactions. The most dominant background sources are cosmic muons, non-collision background and pile-up interactions.

The first selection step is the requirement for stable beams and well operating detector elements,

which are necessary for the measurements. This includes the L1 trigger processor, the high-level trigger processor (for events where the high-level trigger is required), the ID systems (Pixel and SCT layers as well as the TRT) with the solenoid, the full electromagnetic and hadronic calorimeter (barrel and end-cap parts) and the detector elements for luminosity measurements. In addition, a good reconstruction quality for tracks and jets is mandatory.

Two main analysis topologies are extracted from collision events passing the general requirements above. The first topology is denoted as *inclusive* jet topology and is designed to select dijet events with the least possible bias (including dijet events in which one jet does not pass the jet selection requirements). This topology is the baseline for the underlying event analysis and allows a good comparison with previous UE measurements at Tevatron and the LHC experiments. The second topology is denoted as *exclusive* dijet topology and is performed on top of the inclusive selection. Additional requirements for a dijet topology are forced, which allow a cleaner measurement of the underlying event contribution at the price of a possible selection bias due to the restrictions in the jet spectrum.

**Inclusive jet topology** At least one jet needs to be reconstructed with a transverse momentum of  $p_T^{\text{jet}} > 20 \text{ GeV}$  and rapidity of  $|y^{\text{jet}}| < 2.8$ , to ensure that the jet is well located within the barrel region of the calorimeter. If more than one jet above 20 GeV has been reconstructed, the *leading* jet is required to be within the barrel region:

$$|y^{\text{lead jet}}| < 2.8 . \quad (5.5)$$

A jet cleaning is performed by rejecting events with at least one fake or problematic jet. Details for jet cleaning definitions can be found in Section 4.5.4. Fake jets or jets with mis-reconstructed energy can lead to a false classification of the leading jet which would result in a re-orientation of the  $\phi$  splitting and a wrong association of the underlying event contribution.

The trigger requirements are following the recommendations for the jet cross section measurements to ensure the minimal possible bias for the dijet event selection. Trigger chains including minimum bias and central jet trigger are applied, in which the specific trigger choice depends on the period of data taking and the transverse momentum of the leading jet. Two main trigger systems are utilized:

1. A one sided L1 minimum bias trigger based on MBTS, L1\_MBTS\_1. Charged particles above a certain energy threshold passing at least one of the two MBTS disks (therefore one sided) are enough to invoke the trigger. For the very early part of data taking (the first runs of period A) the L1\_MBTS\_1 was used to trigger all dijet events, due to a mis-timing problem within the L1 jet trigger system. For periods afterwards (the rest of period A is denoted as A\*) the minimum bias trigger is used for events with a  $p_T^{\text{lead}} < 60 \text{ GeV}$ .
2. Jet trigger with different energy thresholds are applied. For the central region eight L1 jet trigger items were available: L1\_J5/10/15/30/55/75/95/115 which are applied for Period A\* - F, since the high-level trigger were only used for validation purpose up to this point and only the L1 trigger were actively rejecting events. Beginning with Period G also

the high-level trigger system was active and the trigger EF\_J20/35/50/75/95\_jetNoEF have been used for the event selection. The energy scale on the trigger thresholds is an uncalibrated scale (energy sum of the calorimeter cell associated with the jet without any further calibration scale factors applied). The final calibrated scale is usually higher, due to the compensation for hadronic components within the electromagnetic calorimeter.

The trigger choice is a balancing act between the trigger efficiency and the pre-scale applied to the trigger. For a considered range in  $p_T^{\text{lead}}$ , the trigger with the lowest pre-scale but still with an efficiency above 99 % is chosen to ensure a maximum amount of data but also ensure that the trigger is operating within the efficiency plateau and not in the turn-on curve. The full list of triggers with their corresponding  $p_T^{\text{lead}}$  intervals is shown in Table 5.3.

$p_T^{\text{lead}}$ [GeV]	Period A* - F	Period G - I
20 - 60	L1_MBTS_1	L1_MBTS_1
60 - 80	L1_J5	EF_J20_jetNoEF
80 - 110	L1_J5	EF_J20_jetNoEF
110 - 160	L1_J15	EF_J35_jetNoEF
160 - 210	L1_J30	EF_J50_jetNoEF
210 - 260	L1_J55	EF_J75_jetNoEF
260 - 310	L1_J75	EF_J95_jetNoEF
310 - 400	L1_J95	L1_J95
> 400	L1_J95	L1_J115

**Table 5.3:** Trigger chains applied for the underlying event analysis. For the early part of Period A all events are triggered using the minimum bias trigger. Beginning with Period A\* the required trigger depends on the transverse momentum of the leading jet.

At least one primary vertex is required to reject background events originating from cosmic muons and non-collision background within the beam pipe. The position of the primary vertex in the beam pipe should be consistent with the position of the beam crossing area and at least five tracks should be associated with the vertex. The previous requirement to have at least one jet above 20 GeV already selects events with some activity and consequently above 99 % of the events are passing the vertex criteria. A possible bias due to requirement of five tracks has been studied and found to be negligible (see Section 5.2.3).

To reduce the influence of pile-up interactions all events with more than one reconstructed primary vertex (vertices located within the beam crossing area) with two or more associated tracks are removed. This requirement is particularly important for the later data taking periods in which the average interactions per bunch crossing increase up to three. The pile-up rejection is crucial for cluster based observables. For track-based observables one can reduce the pile-up contamination by rejecting tracks associated with pile-up vertices but it is not possible to associated individual components within the energy depositions of a calorimeter cell with a certain vertex. Without a pile-up rejection, the corrections for the pile-up contributions would have be performed entirely during the unfolding step, relying on a sufficiently modeled pile-up contribution in the Monte Carlo generators. Even with the rejection, a small pile-up contribution

remains due to the finite resolution of the inner detector. If the primary and a pile-up vertex are too close together to be separated as two independent objects, one will end up with a merged vertex in which the pile-up contribution will act like a multiple parton interaction. The expected fraction of merged vertices is estimated to be at the order of a few percent and the effect on the observables is considered as systematic uncertainty. The details of the merged vertex study are shown in Section 5.2.3.

**Exclusive dijet topology** The selection for the exclusive dijet topology is performed on top of the inclusive selection. In addition to the leading jet in the inclusive selection exactly one additional jet with the same selection criteria is required (events with three or more jets are rejected). The additional jet is denoted as *sub-leading* jet.

To suppress possible radiations below the 20 GeV momentum threshold or above 2.8 in rapidity, additional angular and momentum balancing criteria between the leading and sub-leading jet are enforced. The angular separation between the two jets,  $\Delta\phi_{\text{lead,sub}} = |\phi_{\text{lead}} - \phi_{\text{sub}}|$ , should be greater than 2.5 (to ensure that the sub-leading jet is located within the away region) and the transverse momentum ratio between the sub-leading and the leading jet,  $p_{\text{T}}^{\text{sub}}/p_{\text{T}}^{\text{lead}}$ , should be greater than 50%.

ID	Selection Criterion	Description
<i>Inclusive Jet Topology</i>		
1	Data quality	Stable beam, optimal detector/reconstruction performance
2	Jet selection	Classification of the leading jet to define direction and energy scale of hard scattering
3	Jet cleaning	Remove events with at least one fake or problematic jet
4	One primary vertex	Remove background events from cosmic muons and non-collision background
5	Pile-Up Veto	Reject events with more than one reconstructed primary vertex
<i>Exclusive Dijet Topology</i>		
6	Third jet veto	Reject events with more than two jets with $p_{\text{T}} > 20 \text{ GeV}$
7	$p_{\text{T}}$ balancing	Balancing requirement for the transverse momentum of the leading and sub-leading jet: $p_{\text{T}}^{\text{sub}}/p_{\text{T}}^{\text{lead}} > 0.5$
8	$\phi$ balancing	Balancing within the azimuthal space between the leading and sub-leading jet: $\Delta\phi_{\text{lead,sub}} > 2.5$

**Table 5.4:** Summary of the selection criteria for the *inclusive* jet and *exclusive* dijet topology.

In total 429,049 proton-proton collision events have passed the inclusive jet selection with 50 % of the events being selected by the minimum bias trigger and the rest using the jet triggers. After the exclusive selection 98,838 event are left with 32 % of the events being triggered by the minimum bias trigger systems. A summary of the event selection can be found in Tables 5.4 and 5.5.

	Total	Minimum Bias Trigger	Jet Trigger
Inclusive	429,049	215,742 (50.3 %)	213,307 (49.7 %)
Exclusive	98,838	31,995 (32.4 %)	66,843 (67.6 %)

**Table 5.5:** Number of events after the inclusive and exclusive selection.

## 5.2 Correction & Unfolding

To compare the results obtained from data with MC particle level predictions, it is necessary to perform a correction and unfolding procedure to the measured observables. The unfolding process should be able to remove various smearing and migration effects due the finite resolution of the detector and possible interaction of the outgoing particles with the detector material. Reconstruction and identification algorithms, which process the raw signals if the ATLAS detector, can also add smearing effects to the final observables. In case of a perfect unfolding algorithm, the resulting (unfolded) observable distributions would resemble the particle spectra as they would be observed with an ideal detector. The main effects which could spoil the observable distributions are summarized in the following list.

1. In-efficiencies in the reconstruction of objects related to physical particles. The dominant effect arises from in-efficiencies in the reconstruction of inner detector tracks.
2. Mis-reconstruction and misidentification of objects, in particular tracks from secondary interactions with the detector material can be falsely classified as tracks originating from the primary interaction.
3. Uncertainties in the reconstruction of the track momentum vectors and the jet/cluster energy scales. Possible uncertainties in the jet energy scale reconstruction can lead to a mis-classification of the leading jet and, hence, to a reorientation of the division in azimuthal space. Subsequently the contribution of the hard scattering can be assigned to the underlying event observables.
4. Related to the point above, small uncertainties in the direction of the tracks can cause migration effects in track based observables. The uncertainties in the direction arise from the finite resolution of the detector and multiple scattering processes of a charged particle with the inner detector material, which will lead to small modification of the particle trajectory. This kind of effect is usually small compared to others and is only relevant at the borders of the considered fiducial phase space ( $|\eta^{\text{trk}}| \sim 2.5$ ) and at the edges of both transverse regions.
5. Although a pile-up veto is applied, it is still possible that a pile-up vertex is too close to the considered primary vertex to be identified as separated vertex. In this case both vertices will be reconstructed as one “merged” vertex and the pile-up interactions can add contributions to the underlying event.
6. Possible particle flow originating from non-collision background interactions can be falsely interpreted as contribution to the underlying event.

The full unfolding procedure is performed in two separated steps. First, corrections for the track reconstruction and misidentification efficiencies are applied for track based observables. In a second step, a general unfolding procedure based on an iterative Bayesian unfolding method is utilized for all observables to handle the remaining smearing effects.

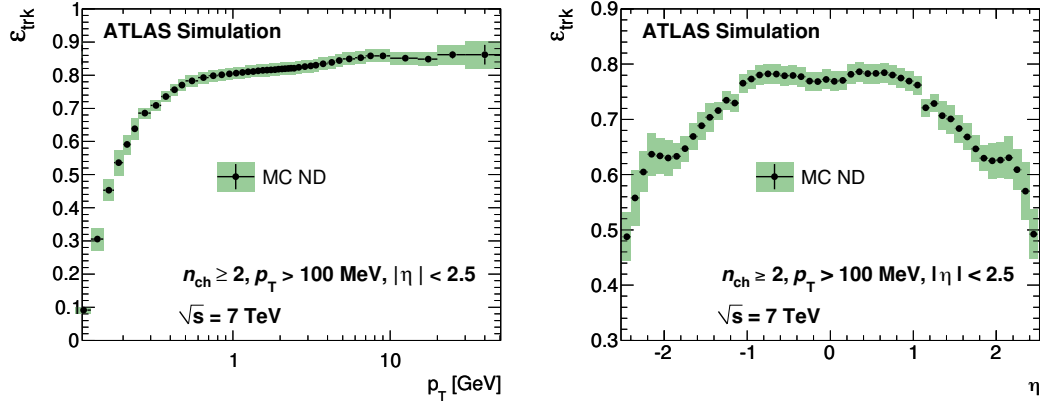


**Figure 5.6:** Track reconstruction efficiency parametrized in the transverse momentum  $p_T$  and the pseudorapidity  $\eta$  of the considered track. The efficiencies are derived using the PYTHIA 6 Monte Carlo event generator. The green shaded area represents the combined statistical and systematic uncertainty, while the black bars represent the statistical uncertainty only. Both results are taken from Ref. [187].

### 5.2.1 Track Observable Corrections

Track based observables are corrected utilizing studies of the ATLAS minimum bias group [187] to remove effects from reconstruction inefficiencies and the detector resolution. The following corrections are considered:

**Track reconstruction efficiency** The efficiency to reconstruct a charged particle as a track was studied in detail by the minimum bias group within the ATLAS experiment. The evaluation of the reconstruction efficiency,  $\epsilon_{\text{trk}}(p_T, \eta)$ , was performed using simulations of non-diffractive proton-proton collisions, generated with the PYTHIA 6 Monte Carlo event generator, parametrized in  $p_T$  and  $\eta$  of the original truth particle (see Figure 5.6). Requirements on the minimal number of hits in the silicon layers are responsible for the decrease in the reconstruction efficiency for particles with low transverse momentum, because on average the particles need a certain transverse momentum to pass through the minimal number of required layers. The efficiency also decreases for increasing pseudorapidity, because the particles need to pass through a larger amount of material.

The track inefficiency is considered by weighting each track with:

$$w_{\text{trk}}(p_T, \eta) = \frac{1}{\epsilon_{\text{trk}}(p_T, \eta)} . \quad (5.6)$$

**Secondary particles** Secondary particles are particles which are not originating directly from the primary interaction. This includes decay products, interactions of particles with the detector material and photon conversions. A small number of tracks are fake tracks which are not correlated to true physical particles. The fraction of secondary particles,  $f_{\text{sec}}$ , was estimated

using simulations [187] and considered by applying the following weight for each track:

$$w_{\text{sec}}(p_{\text{T}}, \eta) = 1 - f_{\text{sec}}(p_{\text{T}}, \eta) . \quad (5.7)$$

The impact of fake particles above  $p_{\text{T}} > 500 \text{ GeV}$  was found to be negligible.

**Particle outside the kinematic range** Particles outside the considered phase space can migrate into the considered kinematic region due to resolution effects. Similar to the secondary particles, the fraction of particle migrated in from outside the kinematic range,  $f_{\text{OKR}}$ , was estimated using Monte Carlo simulation [187] and is incorporated utilizing the following weight for each track:

$$w_{\text{OKR}}(p_{\text{T}}, \eta) = 1 - f_{\text{OKR}}(p_{\text{T}}, \eta) . \quad (5.8)$$

In the full correction procedure a product of all three weights is applied for each track:

$$w_{\text{tot}}(p_{\text{T}}, \eta) = w_{\text{trk}} \cdot w_{\text{sec}} \cdot w_{\text{OKR}} = \frac{(1 - f_{\text{sec}}(p_{\text{T}}, \eta)) \cdot (1 - f_{\text{OKR}}(p_{\text{T}}, \eta))}{\epsilon_{\text{trk}}(p_{\text{T}}, \eta)} \quad (5.9)$$

resulting in the following equations for the corrected track multiplicity,  $N_{\text{trk}}^{\text{corr}}$ , and the corrected transverse momentum sum,  $\sum p_{\text{T}}^{\text{corr}}$ :

$$N_{\text{trk}}^{\text{corr}} = \sum_{i=1}^N w_{\text{tot}}(p_{\text{T}}^i, \eta^i) \quad (5.10)$$

$$\sum p_{\text{T}}^{\text{corr}} = \sum_{i=1}^N w_{\text{tot}}(p_{\text{T}}^i, \eta^i) \cdot p_{\text{T}}^i \quad (5.11)$$

where  $i$  is the index of the considered track and  $N$  the total number of tracks in the considered analysis region. On average the corrected track multiplicity and the corrected transverse momentum sum should resemble their particle level counterparts.

The track efficiency has the largest impact on the correction, followed by the correction for secondary particles. Particles from outside the kinematic range only have an impact around  $|\eta^{\text{trk}}| \sim 2.5$  and the overall contribution to the underlying event observables is found to be negligible.

### 5.2.2 Iterative Bayesian Unfolding

The primary idea of unfolding an experimental distribution is based on the relationship between the underlying *true*<sup>9</sup> distribution, which would be observed with an ideal detector, and the *measured* or *reconstructed* distribution, which is the result of a non-perfect (and therefore realistic) detector. Possible smearing effects include: migration effects due to systematic uncertainties, a non-linear response behavior of the considered detector elements as well as a limited acceptance of the experimental setup.

---

<sup>9</sup>Also denoted with *particle*, *hadron* or *truth* level distribution.



The number of reconstructed events,  $n(\mathcal{R}_j)$ , in the bin<sup>10</sup>  $j$  is connected to the number of true events,  $n(\mathcal{T}_i)$ , in the bin  $i$  by:

$$n(\mathcal{R}_j) = \sum_{i=1}^M P(\mathcal{R}_j | \mathcal{T}_i) n(\mathcal{T}_i), \quad (5.12)$$

where  $M$  is the number of bins and  $P(\mathcal{R}_j | \mathcal{T}_i)$  represents the conditional probability for a given event with the true value  $\mathcal{T}_i$  to be reconstructed as value  $\mathcal{R}_j$ . It is convenient to construct a *smearing*<sup>11</sup> matrix  $S$  where each element  $S_{ij}$  contains the conditional probability:

$$S_{ij} := P(\mathcal{R}_j | \mathcal{T}_i) \quad i, j \in [1, M]. \quad (5.13)$$

Inverting the smearing matrix would allow to obtain the true distribution from the measured distribution. Unfortunately, this method can lead to problems if the matrix is singular or if the entries of the matrix suffer from large statistical fluctuations. These properties can cause *ill-posed* problems which results in unphysical solutions [207, 208].

Several solutions have been developed to address the unfolding problems. A simplistic, but common, approach is the *bin-by-bin unfolding*. Within this method a simple correction factor,  $\mathcal{C}_i$ , for each bin  $i$  is defined as the ratio of the true number of events over the reconstructed number of events:

$$\mathcal{C}_i = \frac{n(\mathcal{T}_i^{\text{MC}})}{n(\mathcal{R}_i^{\text{MC}})}, \quad (5.14)$$

where *MC* indicates that the distributions are derived from simulations, usually using Monte Carlo methods. The unfolded number of events,  $n(\mathcal{U}_i^{\text{Data}})$ , for bin  $i$  is then estimated by multiplying the correction factor with measured (reconstructed) number of events,  $n(\mathcal{R}_i^{\text{Data}})$ :

$$n(\mathcal{U}_i^{\text{Data}}) = \mathcal{C}_i \cdot n(\mathcal{R}_i^{\text{Data}}). \quad (5.15)$$

The major drawback of the bin-by-bin unfolding method is the missing treatment of migration and correlation effects between the different bins. More sophisticated methods allow a handle on this problem; for example, the HBOM method [209] or matrix inversion methods with regularization procedures like the SVD approach [210].

**Bayesian Iterative Unfolding** For the underlying event analysis an iterative unfolding method based on the Bayes' theorem developed by G. D'Agostini in 1994 [211] has been applied. The conditional probability  $P(\mathcal{T}_i | \mathcal{R}_j)$  can be related to the smearing matrix in eq. (5.13) using the Bayes' formula:

$$P(\mathcal{T}_i^{\text{MC}} | \mathcal{R}_j^{\text{MC}}) = \frac{P(\mathcal{R}_j^{\text{MC}} | \mathcal{T}_i^{\text{MC}}) P(\mathcal{T}_i)}{P(\mathcal{R}_j^{\text{MC}})} \quad (5.16)$$

$$= \frac{P(\mathcal{R}_j^{\text{MC}} | \mathcal{T}_i^{\text{MC}}) P(\mathcal{T}_i)}{\sum_i P(\mathcal{R}_j^{\text{MC}} | \mathcal{T}_i^{\text{MC}}) P(\mathcal{T}_i)}, \quad (5.17)$$

<sup>10</sup>Within the context of this thesis, the unfolding of binned distributions (histograms) is discussed in which the number of bins is the same for the reconstructed and the true distribution.

<sup>11</sup>Please note that the term *smearing* matrix is not consistently used within the literature.

where  $P(\mathcal{T}_i)$  is the unknown, prior probability distribution for the true value in bin  $i$ . The smearing matrix  $P(\mathcal{R}_j^{\text{MC}} | \mathcal{T}_i^{\text{MC}})$  is estimated using simulation based on Monte Carlo methods. Subsequently the number of unfolded events,  $n(\mathcal{U}_i^{\text{Data}})$ , can be estimated from the measured data values,  $n(\mathcal{R}_i^{\text{Data}})$ , using:

$$n(\mathcal{U}_i^{\text{Data}}) = \sum_{j=1}^M P(\mathcal{T}_i^{\text{MC}} | \mathcal{R}_j^{\text{MC}}) n(\mathcal{R}_i^{\text{Data}}) . \quad (5.18)$$

Eq. (5.18) does not account for true events with no corresponding reconstructed counterpart. These kinds of events are classified as *missed* and can occur due to the kinematic selection requirements in the event reconstruction. The missing effects are considered by modifying Eq. (5.18):

$$n(\mathcal{U}_i^{\text{Data}}) = \frac{1}{\epsilon_i} \sum_{j=1}^M P(\mathcal{T}_i^{\text{MC}} | \mathcal{R}_j^{\text{MC}}) n(\mathcal{R}_i^{\text{Data}}) , \quad (5.19)$$

where  $\epsilon_i$  represents the probability that an event in bin  $i$  of the true distribution has no counterpart in the reconstructed distribution. In addition, *fake* events are observed, which are events found in the reconstruction with no counterpart in the true distribution, e.g. jet or tracks reconstructed from detector noise. The contribution of *fake* events is small and considered by adding an additional bin to the smearing matrix, which is representing the prior probability that a bin  $i$  contains fake events. The fake probability is estimated using Monte Carlo simulations.

The unfolded number of events,  $n(\mathcal{U}_i^{\text{Data}})$ , will depend on the prior probability distribution  $P(\mathcal{T}_i)$ , which results in a possible model dependency of the final unfolded distributions. In order to remove the dependency, an iterative procedure [211] is utilized by replacing the prior for each iteration with the unfolded distribution of the preceding one, using the following algorithm for bins  $i \in [1, N]$ :

1. The initial prior,  $P_0(\mathcal{T}_i)$ , for the first iteration is estimated from Monte Carlo simulation using the particle level distribution normalized to unity:

$$P_0(\mathcal{T}_i) = P_0(\mathcal{T}_i^{\text{MC}}) := \frac{n(\mathcal{T}_i^{\text{MC}})}{\sum_i n(\mathcal{T}_i^{\text{MC}})} . \quad (5.20)$$

2. The initial number of expected event,  $n_0(\mathcal{U}_i^{\text{Exp}})$ , is estimated by scaling the initial prior with the number of observed events,  $N_{\text{obs}}$ :

$$n_0(\mathcal{U}_i^{\text{Exp}}) := P_0(\mathcal{T}_i^{\text{MC}}) N_{\text{obs}} . \quad (5.21)$$

3. The corrected distribution for the  $k^{\text{th}}$  iteration step,  $n_k(\mathcal{U}_i^{\text{Data}})$  with  $k = 1, \dots, k_{\text{max}}$ , is calculated according to Eq. (5.19) using the prior estimated in the  $(k-1)$  iteration step,  $P_{k-1}(\mathcal{T}_i^{\text{MC}})$ .
4. The new prior,  $P_k(\mathcal{T}_i^{\text{MC}})$ , and the new expected number of events,  $n_k(\mathcal{U}_i^{\text{Exp}})$ , for the  $k^{\text{th}}$  iteration step, is estimated using the normalized and unfolded distribution  $n_k(\mathcal{U}_i^{\text{Data}})$

obtained in step 3:

$$P_k(\mathcal{T}_i^{\text{MC}}) = \frac{n_k(\mathcal{U}_i^{\text{Data}})}{\sum_i^N n_k(\mathcal{U}_i^{\text{Data}})} \quad (5.22)$$

$$n_k(\mathcal{U}_i^{\text{Exp}}) = n_k(\mathcal{U}_i^{\text{Data}}) \quad (5.23)$$

5. A  $\chi^2_{k,k-1}$  comparison between the estimated number of event obtained in  $k^{\text{th}}$  iteration step,  $n_k(\mathcal{U}_i^{\text{Exp}})$ , and the estimated number of events obtained in the  $(k-1)^{\text{th}}$  iteration step,  $n_{k-1}(\mathcal{U}_i^{\text{Exp}})$ , is performed.
6. The iteration stops if the  $\chi^2$  distribution reaches an optimal iteration point,  $k_{\text{opt}}$ , otherwise the iteration process continues starting with step 3.

The unfolded distribution for each iteration step will converge against the estimated distribution with an increasing number of iterations, removing the dependence on the initial prior distribution. However, statistical fluctuation in the smearing matrix can cause a divergent behavior for a large number of iterations and effect the unfolded distribution [211], illustrated in Figure 5.7. Therefore, an optimal number of iterations is a compromise between achieving a prior independence and preventing an amplification of the statistical fluctuations.

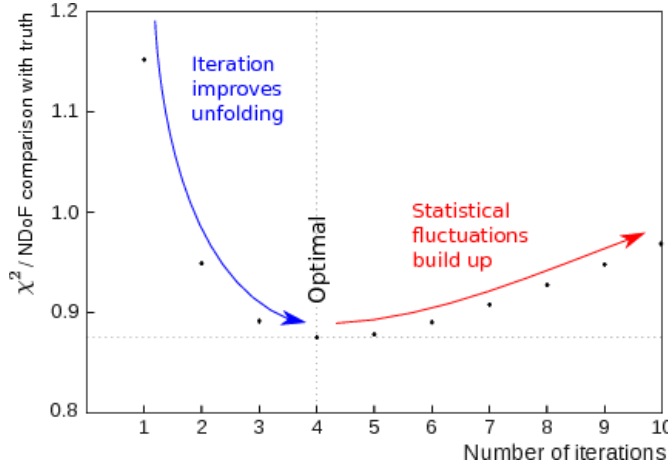


**Figure 5.7:** Example for the convergence behavior using the iterative Bayesian unfolding method. The example is taken from the Imagiros framework reference [212].

The unfolding procedure has been performed using an implementation within the Imagiros framework developed by B. Wynne [212]. For all observables an optimal iteration point  $k_{\text{opt}} = 2$  has been determined.

**Smearing Matrices for Single Observables** The smearing matrices for the Bayesian unfolding procedure are estimated using the PYTHIA 6 Monte Carlo generator with the MRST LO\* PDF and the AMBT1 tune. Matrices for the charged particle multiplicity, the transverse momentum sum of charged particles, the mean transverse momentum of charged particles and the transverse energy sum of charged and neutral particles (compared to the transverse energy sum of clusters in detector level) are shown in Figure 5.8. The first three observables (Figures 5.8a to 5.8c) are

derived from tracking information and the corresponding matrices are calculated after the tracks based corrections, described in Section 5.2.1. The remaining smearing effects are subsequently reduced, resulting in mainly diagonal smearing matrices in contrast to the cluster based matrix (Figure 5.8d).

**Smearing Matrices for Correlated Observables** To unfold distributions containing two (or in general more) correlated observables it is not possible to unfold the observables independently from each other and preserve the correlation. Instead the unfolding process is used on a combination of both input observables [212].

For two binned distributions  $\mathbf{x} = (x_1, x_2, \dots, x_M)$  and  $\mathbf{y} = (y_1, y_2, \dots, y_N)$  a combined observable  $\mathbf{g}$  is constructed with

$$g_{ij} = x_i y_j \quad i \in [1, M], j \in [1, N] \quad (5.24)$$

for each combination between the bins in  $\mathbf{x}$  and  $\mathbf{y}$ . Unfolding the combined observable will preserve possible correlations. The method is applied to profile histograms containing density observables as a function of the leading-jet  $p_T$  and the charged particle multiplicity,  $N_{\text{ch}}$ . Smearing matrices for the profile histograms as a function of  $p_T^{\text{lead}}$  are shown in Figure 5.9 and as a function of  $N_{\text{ch}}$  in Figure 5.10, respectively.

Comparing the smearing matrices for correlated observables in Figure 5.9 with their counterparts in Figure 5.8 allows a graphical interpretation. The following example will focus on the matrix for  $N_{\text{ch}}$  in Figure 5.8a and the matrix for  $N_{\text{ch}}$  vs.  $p_T^{\text{lead}}$  in Figure 5.9a, but similar interpretations hold for all combined smearing matrices in Figure 5.9. The overall structure of the correlated matrix in Figure 5.9a follows the form of the matrix for  $N_{\text{ch}}$  only, but with each bin in Figure 5.8a being replaced by a “little” smearing matrix for  $p_T^{\text{lead}}$  in the given *Reco/Truth* bin in  $N_{\text{ch}}$ . Likewise the matrix in Figure 5.10 follows the structure of the  $\langle p_T \rangle$  smearing matrix with a smearing sub-matrix for  $N_{\text{ch}}$  in each *Reco/Truth* bin in  $\langle p_T \rangle$ .

The method drastically increases the number of bins for the smearing matrices compared to smearing matrices for one observable: for two distributions  $\mathbf{x}$  and  $\mathbf{y}$ , with  $M$  and  $N$  number of total bins respectively, in total  $(M \times N)^2$  bins for a smearing matrix are necessary.

**Statistical Uncertainties** The statistical uncertainties of the unfolded distributions are a composition of statistical fluctuations in the original distributions, the smearing matrices and the prior distributions. After each iteration, the uncertainties are recalculated due to the continuous change of the prior in each iteration step. The correct uncertainties are obtained by calculating the covariance matrix taking the effect of the iteration process into account [213].

### 5.2.3 Non-collision Background and Merged Vertices

**Merged vertices** If the distance  $\Delta Z$  between two vertices along the beam-axis becomes too small, the vertex reconstruction algorithm may merge both vertices into one primary vertex. The merging effect occurs for distances below 10 mm and becomes dominant for  $\Delta Z < 5$  mm. In Figure 5.11 the  $\Delta Z_{\text{PV,PU}}$  distribution for the distance between the primary vertex and pile-up

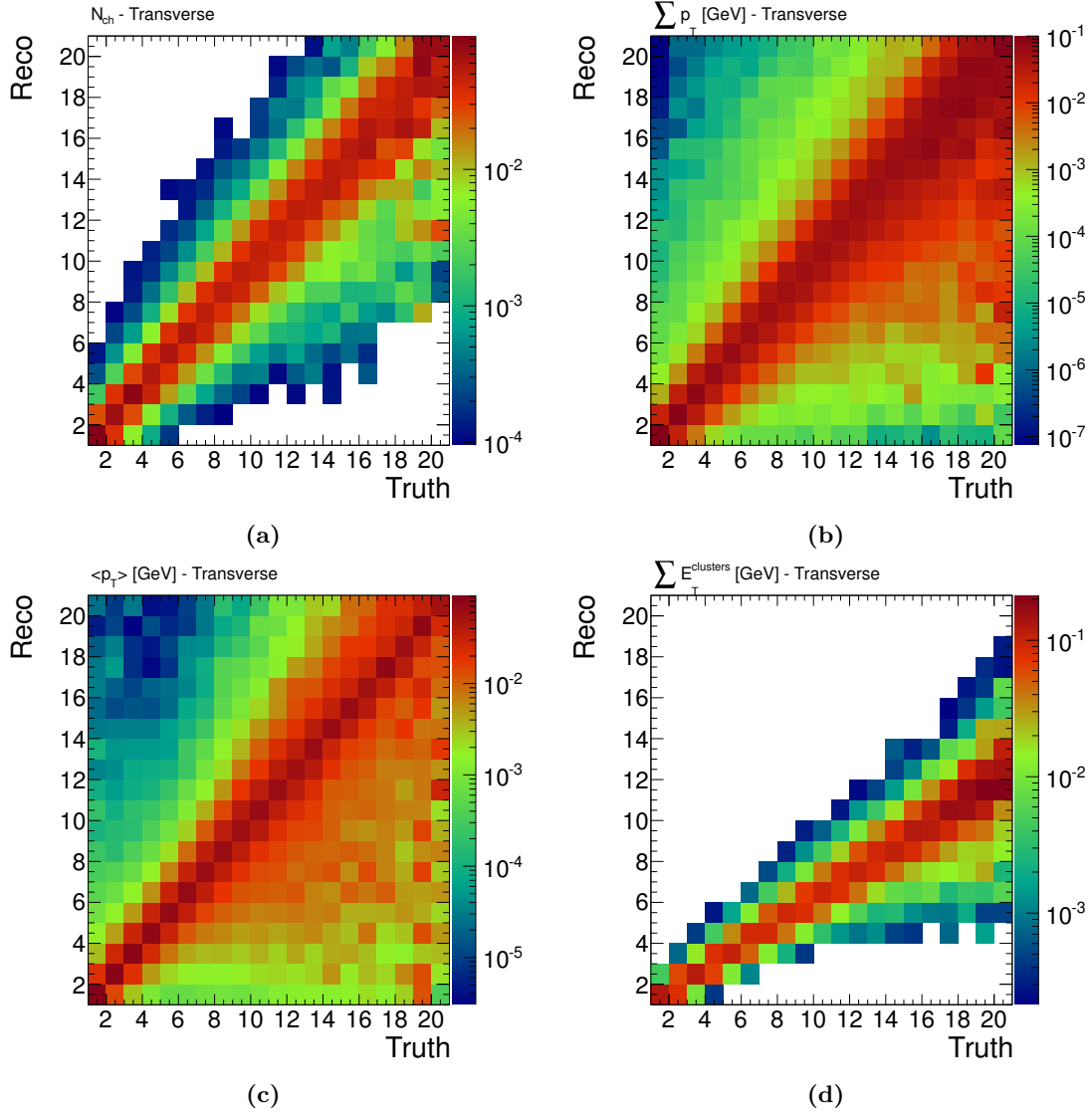


**Figure 5.8:** Smearing matrices for the charged particle multiplicity (top left), the charged particle transverse momentum sum (top right), the mean transverse momentum of charged particles (bottom left) and the transverse energy sum of charged and neutral particles (bottom right), calculated for the inclusive topology in the transverse region. The matrices have been estimated using the PYTHIA 6 MC generator with the AMBT1 tune. The true values, denoted *Truth*, are shown on the x axis and the reconstructed values, denoted *Reco*, are shown on the y axis.

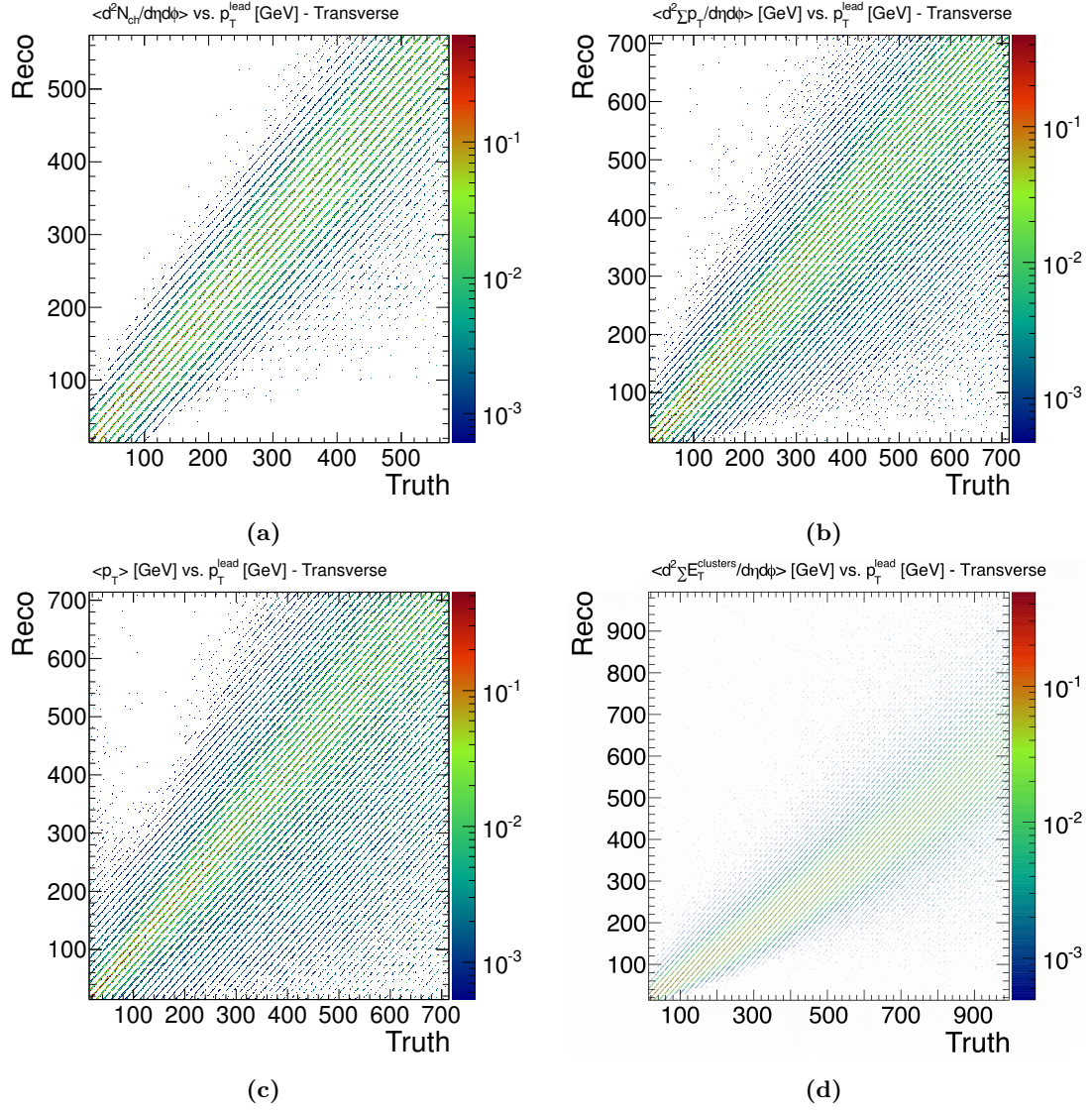


**Figure 5.9:** Smearing matrices for the charged particle multiplicity density (top left), the charged particle transverse momentum sum density (top right), the mean transverse momentum of charged particles (bottom left) and the transverse energy sum density of charged and neutral particles (bottom right), all against the leading-jet  $p_T$ , calculated for the inclusive topology in the transverse region. The matrices have been estimated using the PYTHIA 6 MC generator with the AMBT1 tune. The true values, denoted *Truth*, are shown on the x axis and the reconstructed values, denoted *Reco*, are shown on the y axis.

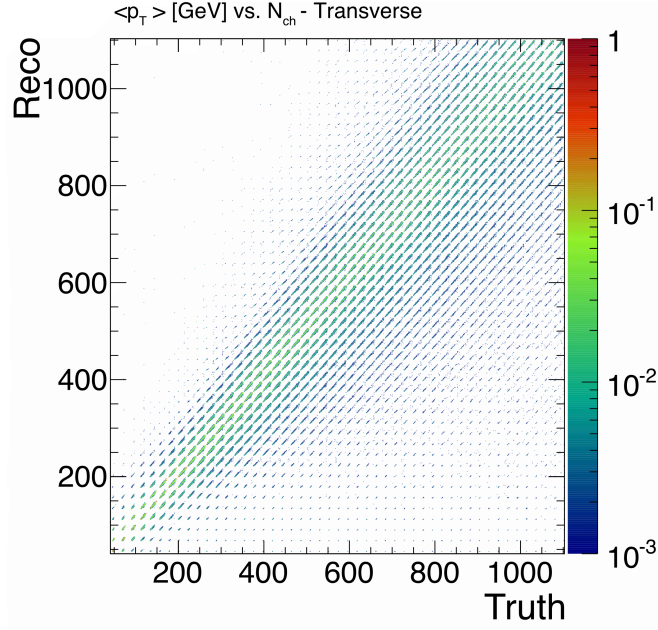


**Figure 5.10:** Smearing matrix for the mean transverse momentum of charged particles against the charged particle multiplicity, calculated for the inclusive topology in the transverse region. The matrix has been estimated using the PYTHIA 6 MC generator with the AMBT1 tune. The true values, denoted *Truth*, are shown on the x axis and the reconstructed values, denoted *Reco*, are shown on the y axis.

vertices in the 2010 data is shown. The merging effect is responsible for the central dip. Particles emerging from the additional merged pile-up vertices will contribute to the underlying event as a new source of multiple scattering. The effect on the underlying event observables is estimated using a simulation with an adequate modeling of the pile-up conditions for the 2010 data taking period and comparing the results to a simulation without pile-up. Both samples were generated using the PYTHIA 6 Monte Carlo event generator with the MRST LO\* PDF and the AMBT1 tune. A maximum deviation of the order of 1% is observed which is passed through the Bayesian unfolding framework. The systematic uncertainty of the merged vertex effect is found to be of the order of 2% to 5% depending on  $p_T^{\text{lead}}$ .

To ensure a sufficient modeling of the merged vertex effect during the simulation, the fraction of expected merged vertices is measured in data and compared to the MC predictions. A fit to the  $\Delta Z_{\text{PV,PU}}$  spectrum is performed for data and simulations using a Gaussian distribution with a gap around  $\Delta Z = 0$  and a width of  $\Delta Z_{\text{gap}} = 10$  mm:

$$f_{\text{model}}(\Delta Z) = \begin{cases} \mathcal{C} \cdot e^{-\frac{(\Delta Z - \mu)^2}{2\sigma^2}}, & \Delta Z \geq \Delta Z_{\text{gap}} \\ 0, & \Delta Z < \Delta Z_{\text{gap}} \end{cases} \quad (5.25)$$

where  $\mathcal{C}$ ,  $\mu$  and  $\sigma$  are the free fit parameter representing the overall normalization, the mean and the width of the Gaussian distribution, respectively. The fitted parameters are utilized to construct a full Gaussian distribution without a gap which allows an estimation of the vertex placement along the beam pipe without any merging effects. The fraction of merged vertices,  $f_m$ ,

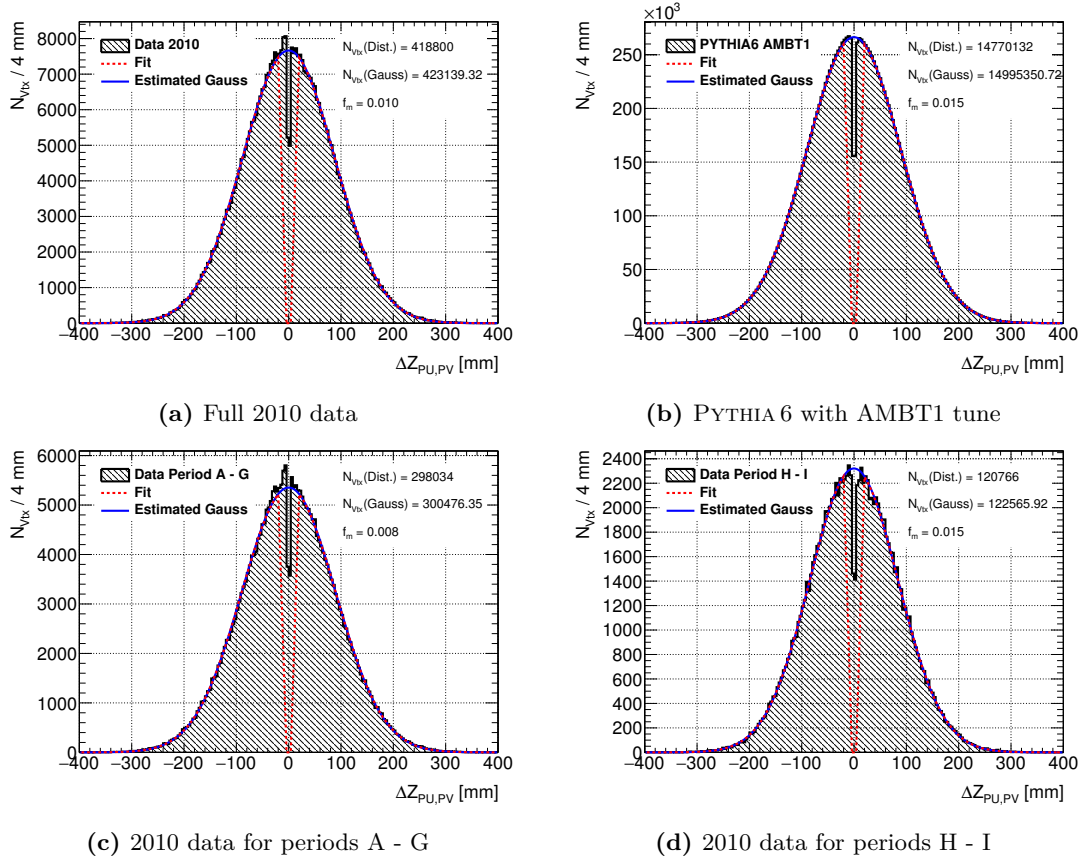


**Figure 5.11:**  $\Delta Z_{PV,PU}$  distribution shown for the full 2010 data set (a), the PYTHIA6 simulation sample (b), data periods A-G (c) and the data periods H-I (d). The red lines represents the fit results for a Gaussian distribution with a gap around  $\Delta Z = 0$  and the blue line represents the estimation for a full Gaussian without merged vertices.



is defined as

$$f_m = 1 - \frac{N_{Vtx}(\text{Dist.})}{N_{Vtx}(\text{Gauss})}, \quad (5.26)$$

where  $N_{Vtx}(\text{Dist.})$  is integral over the  $\Delta Z_{PV,PU}$  distribution in data or MC, respectively, and  $N_{Vtx}(\text{Gauss})$  is the integral over the corresponding, estimated Gaussian distribution. Both results are shown in Figure 5.11a and Figure 5.11b, respectively. For the combined data set a total fraction of  $f_m = 1\%$  is measured compared to the simulated fraction of  $1.5\%$ . The slightly higher fraction in the simulation will lead to a slight overestimation of the systematic uncertainty. The deviation in the fractions is a result of the frequent changes in the run conditions for the earlier periods of data taking, resulting in the not quite Gaussian distribution for  $\Delta Z_{PV,PU}$  in these periods. However, the statistical impact of the early periods on the merged vertex effect is small and the overall fraction is dominated by the later periods H and I, which include a much larger fraction of the luminosity and, thus, an increased pile-up contribution. The  $\Delta Z_{PV,PU}$  distribution separated for the earlier periods A-G and the later periods H-I are shown in Figure 5.11c and Figure 5.11d, respectively, showing a reasonable agreement between the simulation and the later periods. The distributions for each period independently are shown in Figure A.4 in Section A.3.1.

**Primary vertex position** Possible systematic uncertainties due to incorrect modeling of the primary vertex position along the beam axis are studied by comparing the jet spectra for different primary vertex positions. The overall effect is found to be negligible.

**Primary vertex track requirement** A reconstructed vertex is considered as primary interaction vertex only if at least five tracks are associated with the vertex to ensure a high reconstruction efficiency. This requirement can introduce a possible bias to the underlying event contribution, because it requires a certain amount of activity within the collision event and, hence, introduces a possible rejection of the soft QCD spectrum. The effect is studied in data by relaxing the track requirement to two tracks per vertex. Only  $0.025\%$  of the events are effected, because the requirement to find at least one jet above  $20\text{ GeV}$  implies already a reasonable activity within the proton-proton interaction. The overall effect on the underlying event observables is of the order of a few per-mille and considered to be negligible.

**Non-collision background** Contributions from non-collision interactions, e.g. interactions from cosmic muons or interactions with the remaining gas in the beam pipe, can spoil observables for the underlying event measurements. To evaluate possible effects, data samples where no real proton-proton collision candidate is expected are investigated. The events are collected using cosmic muon triggers and either minimum bias or jet triggers with a low energy threshold triggered in timing intervals outside a proton bunch crossing. In total a sample corresponding to an integrated luminosity of  $2\text{ pb}^{-1}$  is selected. No events passing the event and jet selection criteria (particularly the jet cleaning criteria) are found within the sample. Therefore, the contribution is considered to negligible.

### 5.2.4 Systematic Uncertainties

In this section, the estimation of the systematic uncertainties through the unfolding process is presented. Two main sources of systematic uncertainties are considered: uncertainties due to the remaining model dependence of the unfolding process itself and systematic uncertainties associated with the measurement, which are propagated through the unfolding process.

**Model Dependence Systematics** In general, the unfolded results are depended on the utilized particle level model represented by the given prior. The iterative procedure reduces the dependence on the prior and the possible remaining dependencies are considered in the systematic *unfolding uncertainty*.

The systematics are estimated by using different Monte Carlo generators and different starting priors for each utilized generator. In case of multiple starting prior distributions, the mean unfolded value for bin  $i$  is constructed as average over the unfolded results for all possible starting prior distributions:

$$n(\mathcal{U}_i^{\text{Data}}) = \frac{1}{N_{\text{prior}}} \sum_{d=1}^{N_{\text{prior}}} n(\mathcal{U}_{i,d}^{\text{Data}}) , \quad (5.27)$$

where  $n(\mathcal{U}_{i,d}^{\text{Data}})$  represents the unfolded value for bin  $i$  and the starting prior  $d$  and  $N_{\text{prior}}$  represents the total number of starting prior distributions.

The unfolding process was performed using two different Monte Carlo event generators: PYTHIA 6 and HERWIG++. The details for the generated samples are presented in Section 5.1.3. For both samples two different starting priors are utilized: the particle-level distribution of the corresponding generator for the considered observable and a weighted version of the same distribution in which the weights ensure that the reconstructed distribution of the generator matches with the non-unfolded measured distribution. Unfolded distributions for both generators have been calculated according to Eq. (5.27). The mean value of the PYTHIA 6 results is considered as mean value for the final unfolded results. Deviations of the unfolded distributions between PYTHIA 6 and the HERWIG++ samples are used to construct a symmetric error band:

$$\sigma(\mathcal{U}_i^{\text{Data}}) := |n(\mathcal{U}_{i,\text{PYTHIA 6}}^{\text{Data}}) - n(\mathcal{U}_{i,\text{HERWIG}}^{\text{Data}})| \quad (5.28)$$

where  $\sigma(\mathcal{U}_i^{\text{Data}})$  is the systematic uncertainty in the bin  $i$  and  $n(\mathcal{U}_{i,\text{PYTHIA 6}}^{\text{Data}})$  and  $n(\mathcal{U}_{i,\text{HERWIG}}^{\text{Data}})$  are the corresponding unfolded values using PYTHIA 6 or HERWIG++ as particle-level model, respectively.

The major differences between both MC generators are the result of the different modeling of soft QCD processes, especially QCD radiation at low energies. The uncertainties are usually of the order of 1 % but the uncertainties can grow up to 22 % at the edges of the considered fiducial phase space. Comparisons between the weighted and unweighted priors for both MC generator lead to an overall systematic uncertainty of 1 %.

**Experimental Systematic Uncertainties** To evaluate the influence of experimental systematic uncertainties, associated with the measured distribution, on the unfolded results, it is necessary to process the uncertainties through the unfolding algorithm. For each uncertainty, a pseudo-experiment is performed by applying the corresponding variation to the input data and calculate a new measured distribution for each observable. The input data are scaled with  $\pm 1\sigma$  for the considered uncertainty.

The scaled distributions of each pseudo-experiment are unfolded with each prior resulting in total number of unfolded distributions,  $N_{\text{tot}}$ , per observable:

$$N_{\text{tot}} = N_{\text{prior}} \times (N_{\text{sys}} + 1) , \quad (5.29)$$

where  $N_{\text{sys}}$  is the total number of considered systematic variations. The final mean value of the unfolded distribution is now constructed as average over all systematic uncertainties and priors, modifying eq. (5.27) to

$$n(\mathcal{U}_i^{\text{Data}}) = \frac{1}{N_{\text{tot}}} \sum_{d=1}^{N_{\text{tot}}} n(\mathcal{U}_{i,d}^{\text{Data}}) . \quad (5.30)$$

The systematic variations are assumed to be distributed around the central value following the Gaussian formula for each bin  $i$ . The final upper and lower systematic bounds,  $\sigma_+^{\text{tot}}$  and  $\sigma_-^{\text{tot}}$ , are defined as the interval around the central value that contain 68 % of all systematic variation which are above or below the central value.

The following list of systematic uncertainties is considered:

**Jet related uncertainties** Uncertainties on the jet energy scale, jet energy resolution as well as uncertainties on jet reconstruction efficiency are considered. Details are presented in Section 4.5. For the underlying event observables, the combined jet related uncertainties are of the order of 1 % to 3 %.

**Track related uncertainties** The dominant uncertainty associated with tracks is the uncertainty on the track reconstruction efficiency. The reconstruction efficiency is applied within the correction procedure as explained in Section 5.2.1 and the corresponding systematic variations in the weights are propagated through the full unfolding framework. The dominant effects arise from two sources: uncertainties on the material budget in the inner detector and the uncertainties related the  $\chi^2$  probability cut on tracks [187]. The reconstruction uncertainty depends strongly on the pseudorapidity  $\eta$  of the considered track and is of the order of 2 % to 7 % (for tracks with  $p_{\text{T}}^{\text{trk}} > 500 \text{ MeV}$ ). For the  $\chi^2$  probability an uncertainty value of 10 % is applied for tracks with  $p_{\text{T}}^{\text{trk}} > 10 \text{ GeV}$ , parametrizing the difference in the fraction of tracks passing the  $\chi^2$  requirement in data and Monte Carlo simulations.

**Cluster Energy Scale Uncertainty** The energy measured in calorimeter cells is scaled to take the response behavior of the calorimeter for different particles into account. For electromagnetic particles (mainly electrons and photons) the energy scale factors are derived via measurements of  $\pi^0 \rightarrow \gamma\gamma$  decays and a fit to the invariant mass spectrum,  $M_{\gamma\gamma}$ , of both

photons. The uncertainties for the energy scale are  $\eta$  dependent and of the order of 2 % to 15 % [214]. The energy scale for hadronic particles was estimated by comparing the energy deposit of an isolated charged particle with the transverse momentum of an associated track in the inner detector. The uncertainty for the energy scale was found to be of the order of a few percent [136].

**Merged Vertices** The uncertainties for the effects of merged vertices are discussed in detail in Section 5.2.3. In total an uncertainty of 1 % on the underlying event observables is assigned to the merged vertex effect and passed to through the unfolding framework.

The influence of remaining sources of uncertainties, like the non-collision background contributions, is found to be negligible as discussed in Section 5.2.3.

An example for the influence of systematic uncertainties is presented in Figure 5.12 for the  $\sum p_T$  density distribution against  $p_T^{\text{lead}}$ , showing the systematic variations of the jet energy scale, jet energy resolution, track reconstruction efficiency and the effect of merged vertices. All distributions are presented for the transverse region after the inclusive event selection.

Summaries for the uncertainty values after the unfolding procedure, separated for the different sources, are shown in Table 5.6 and Table 5.7 for the inclusive and exclusive analysis topology, respectively. Similar tables have been presented in Ref. [183].

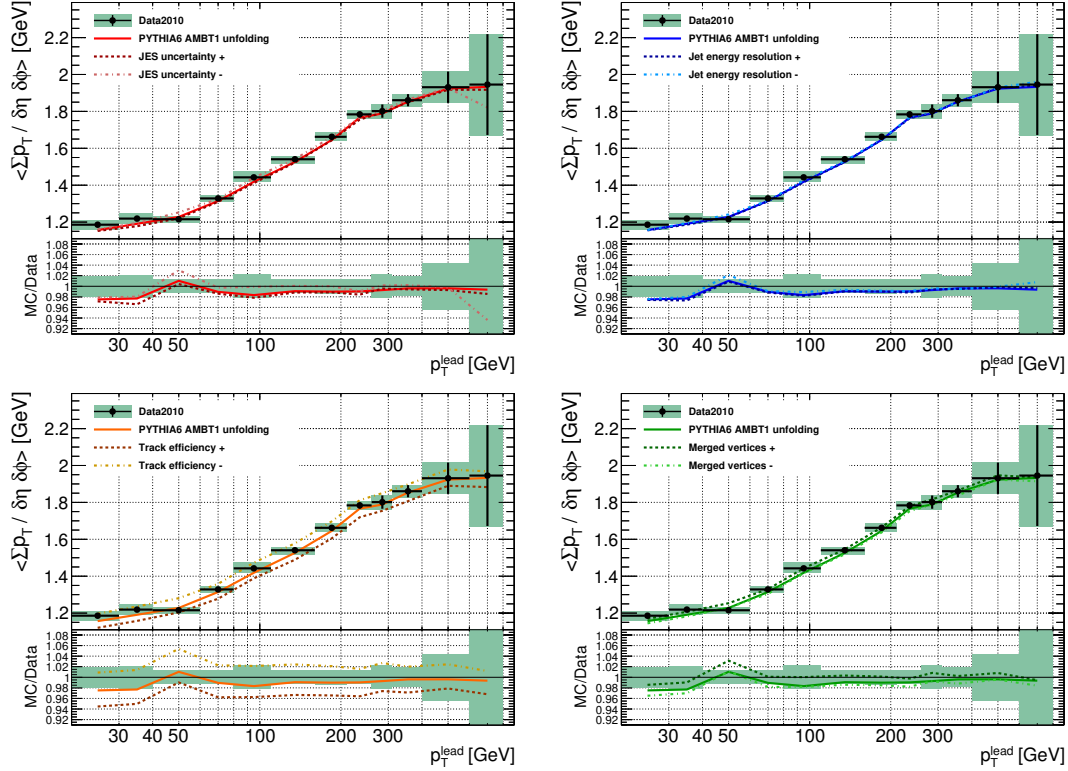


**Figure 5.12:** Distributions for the transverse momentum sum density for different sources of systematic uncertainties: jet energy scale (JES), jet energy resolution, track reconstruction efficiency and the effect of merged vertices. All distributions of presented in the transverse region after the inclusive event selection using a PYTHIA 6 generated smearing matrix and prior for the unfolding process. The black bars indicate the statistical uncertainty and the green error band indicates the combined statistical and systematic uncertainty. The systematic uncertainty between the unfolding with PYTHIA 6 and HERWIG is not included.

Quantity	Inclusive jet topology		
All observables			
Pile-up and merged vertices 1–3%			
Profiles against $p_{\text{T}}^{\text{lead}}$			
Charged tracks	Unfolding	Efficiency	
$\sum p_{\text{T}}$	3%	1–7%	
$N_{\text{ch}}$	1–2%	3–4%	
$\langle p_{\text{T}} \rangle$	1%	0–4%	
Calo clusters	Unfolding	Efficiency	
$\sum E_{\text{T}},  \eta  < 4.8$	2–3%	4–6%	
$\sum E_{\text{T}},  \eta  < 2.5$	3–5%	4–6%	
Profiles against $N_{\text{ch}}$			
Charged tracks	Unfolding	Efficiency	
$\langle p_{\text{T}} \rangle$	2%	1%	
Jet related observables			
Jets	Energy resolution	JES	Efficiency
$p_{\text{T}}^{\text{lead}}$	0.3–1%	0.3–4%	0.1–2%

**Table 5.6:** Summary of the systematic uncertainties for the inclusive analysis topology. The term *unfolding* labels the systematics for unfolding process itself, estimated using different MC simulations and priors. The *efficiency* for tracks and clusters include the track reconstruction and cluster energy scale uncertainties, containing uncertainties for the material budget of the inner detector and the modeling the ATLAS calorimeter. The term *JES* combines uncertainties due to jet energy scale calibration and the jet *efficiency* labels uncertainties due to jet reconstruction efficiency.

Quantity	Exclusive dijet topology		
All observables			
Pile-up and merged vertices 1–5%			
Profiles against $p_{\text{T}}^{\text{lead}}$			
Charged tracks	Unfolding	Efficiency	
$\sum p_{\text{T}}$	3–13%	2–7%	
$N_{\text{ch}}$	3–22%	3–7%	
$\langle p_{\text{T}} \rangle$	1–9%	1%	
Calo clusters	Unfolding	Efficiency	
$\sum E_{\text{T}},  \eta  < 4.8$	5–21%	4–9%	
$\sum E_{\text{T}},  \eta  < 2.5$	1–21%	4–7%	
Profiles against $N_{\text{ch}}$			
Charged tracks	Unfolding	Efficiency	
$\langle p_{\text{T}} \rangle$	5–7%	1–4%	
Jet related observables			
Jets	Energy resolution	JES	Efficiency
$p_{\text{T}}^{\text{lead}}$	0.4–3%	1–3%	0.3–3%

**Table 5.7:** Summary of the systematic uncertainties for the exclusive analysis topology. The term *unfolding* labels the systematics for unfolding process itself, estimated using different MC simulations and priors. The *efficiency* for tracks and clusters include the track reconstruction and cluster energy scale uncertainties, containing uncertainties for the material budget of the inner detector and the modeling the ATLAS calorimeter. The term *JES* combines uncertainties due to jet energy scale calibration and the jet *efficiency* labels uncertainties due to jet reconstruction efficiency.

### 5.3 Underlying Event Results

In this section, the results of the underlying event analysis in jet events are presented. All distributions are shown after the full unfolding process including all systematic uncertainties. The majority of the presented plots have been published by the ATLAS collaboration and can be found in Ref. [183].

Unfolded distributions of the transverse momentum and energy sum densities of charged and neutral particles are presented as well as charged particle multiplicity densities and the average transverse momentum of charged particles. Most observables are shown as a function of the hard energy scale ( $p_T^{\text{lead}}$ ) for inclusive and exclusive event selection but also momentum and multiplicity distributions in slices of  $p_T^{\text{lead}}$  are presented. The observables are calculated as densities in the  $\eta - \phi$  space using the scale factor  $\delta\eta\delta\phi$ , which represents the area in  $\eta - \phi$  covered by the considered region. Two different scale factors are used for the full transverse region, depending in the considered  $\eta$  range:

$$\delta\eta\delta\phi = \delta\eta \times \delta\phi = \begin{cases} (2 \cdot 2.5) \times (2 \cdot \frac{\pi}{3}) = \frac{10\pi}{3}, & \text{transverse region } (|\eta| < 2.5) \\ (2 \cdot 4.8) \times (2 \cdot \frac{\pi}{3}) = \frac{19.2\pi}{3}, & \text{transverse region } (|\eta| < 4.8) \end{cases} \quad (5.31)$$

Subsequently two scale factors are used for both the trans-max and trans-min region, depending on the considered  $\eta$  range, which are by definition the half of the transverse region scale factors:

$$\delta\eta\delta\phi = \delta\eta \times \delta\phi = \begin{cases} (2 \cdot 2.5) \times (\frac{\pi}{3}) = \frac{5\pi}{3}, & \text{trans-max/min region } (|\eta| < 2.5) \\ (2 \cdot 4.8) \times (\frac{\pi}{3}) = \frac{9.6\pi}{3}, & \text{trans-max/min region } (|\eta| < 4.8) \end{cases} \quad (5.32)$$

#### 5.3.1 1D Observable Distributions

The one-dimensional, unfolded distributions for the transverse momentum sum density of charged particles,  $\sum p_T / \delta\eta\delta\phi$ , and the multiplicity density of charged particles,  $N_{\text{ch}} / \delta\eta\delta\phi$ , are presented in Figure 5.13, separated for three different scopes in  $p_T^{\text{lead}}$ :  $p_T^{\text{lead}} \in [20, 60]$  GeV,  $p_T^{\text{lead}} \in [60, 210]$  GeV and  $p_T^{\text{lead}} > 210$  GeV. Both observables are calculated for the transverse, trans-max and trans-min region, using only events passing the inclusive jet selection. All distributions are normalized to unity.

For both observables, a development towards larger values with increasing  $p_T^{\text{lead}}$  is observed in the transverse and trans-max region, including a shift of the mean value and an increase in the tails of the distributions. In comparison, the development within the trans-min region of relatively low, the structure around the peak is nearly unaffected, which is the dominant part of the distribution, and only the distribution tails show slight development with  $p_T^{\text{lead}}$ . The peak value is higher/lower and the spread of the distributions is wider/narrower in the trans-max/trans-min region compared to the combined transverse region. This leads to the indication that the trans-max region contains additional activity (e.g. additional QCD radiation) which is correlated to the energy scale of the hard scattering process. On the other hand, the activity in the trans-min regions shows a more independent behavior with respect the hard scattering energy scale and is therefore a reasonable candidate to measure contributions from



MPI, which are expected to be more or less independent for the hard scattering process, except for a turn on behavior at low energies<sup>12</sup>.

### 5.3.2 Profile Observable Distributions as a function of $p_T^{\text{lead}}$ and $N_{\text{ch}}$

$\sum p_T$  and  $N_{\text{ch}}$  The mean transverse momentum sum density and the mean multiplicity density of charged particles within the transverse region are shown in Figure 5.14. Both observable densities are shown as a function of the leading-jet  $p_T$  after the full inclusive and exclusive event selection. All distributions are shown after of the full unfolding process.

Both observables show a similar behavior for the inclusive and exclusive selection. Within the inclusive dataset an increase of activity with  $p_T^{\text{lead}}$  is observed. No saturation behavior against the hard scale is visible (as one would expect for the underlying event contribution), indicating that additional activity of the hard scattering contributes to the transverse region.

In contrast, a decrease of activity with  $p_T^{\text{lead}}$  has been observed within the exclusive region. The densities are more or less constant at low  $p_T^{\text{lead}}$  and start to decrease for  $p_T^{\text{lead}} > 100$  GeV. The effect is not fully understood yet. It is possible that the dijet selection rejects jets from MPI and not only from the hard scattering itself and therefore cut into the underlying event contribution. No “turn-on” curve for low energies has been found for both topologies compared to other underlying event analyses [170–174], which is a result of the relative high energy threshold of 20 GeV for the leading-jet.

The division of the transverse region into a trans-max, trans-min and trans-diff region allows a further study of the underlying event structure. The results for all three region are shown in Figure 5.15. The unfolded data points are compared to the PYTHIA 6 MC model<sup>13</sup> using the Perugia 2011 tune.

The trans-max region shows an increase of activity, for both observables, with  $p_T^{\text{lead}}$  after the inclusive event selection, similar to the behavior in the full transverse region. In contrast, the activity for the trans-min region is nearly constant against the leading-jet  $p_T$  in the inclusive selection. This supports the interpretation that the trans-min region is less effected by activity originating from the hard scattering, unlike the trans-max region. It also encourages the idea to model the underlying event activity with a constant function over a large scale in  $p_T^{\text{lead}}$  once the scale of the hard scattering is high enough.

The behavior is different for the exclusive selection.  $\sum p_T$  density is constant in the trans-max region, which indicates that the dijet selection indeed reduce the contribution of the hard scattering, but the density is falling for the trans-min region. The  $N_{\text{ch}}$  density shows a decreasing behavior for both regions. Like for the full transverse region, the behavior is not fully understood yet. Since the effect is stronger in the trans-min region, which is less affected by contributions of the hard scattering, it supports to idea that the exclusive dijet selection rejects contributions from jets originating from MPI instead of the hard scattering.

<sup>12</sup>This behavior was observed in several underlying event related measurement before, e.g. Refs. [170–174].

<sup>13</sup>The restriction to only one MC model is made for reasons of clarity and comprehensibility. The full comparisons with all MC models are shown in Figures A.5 and A.6.

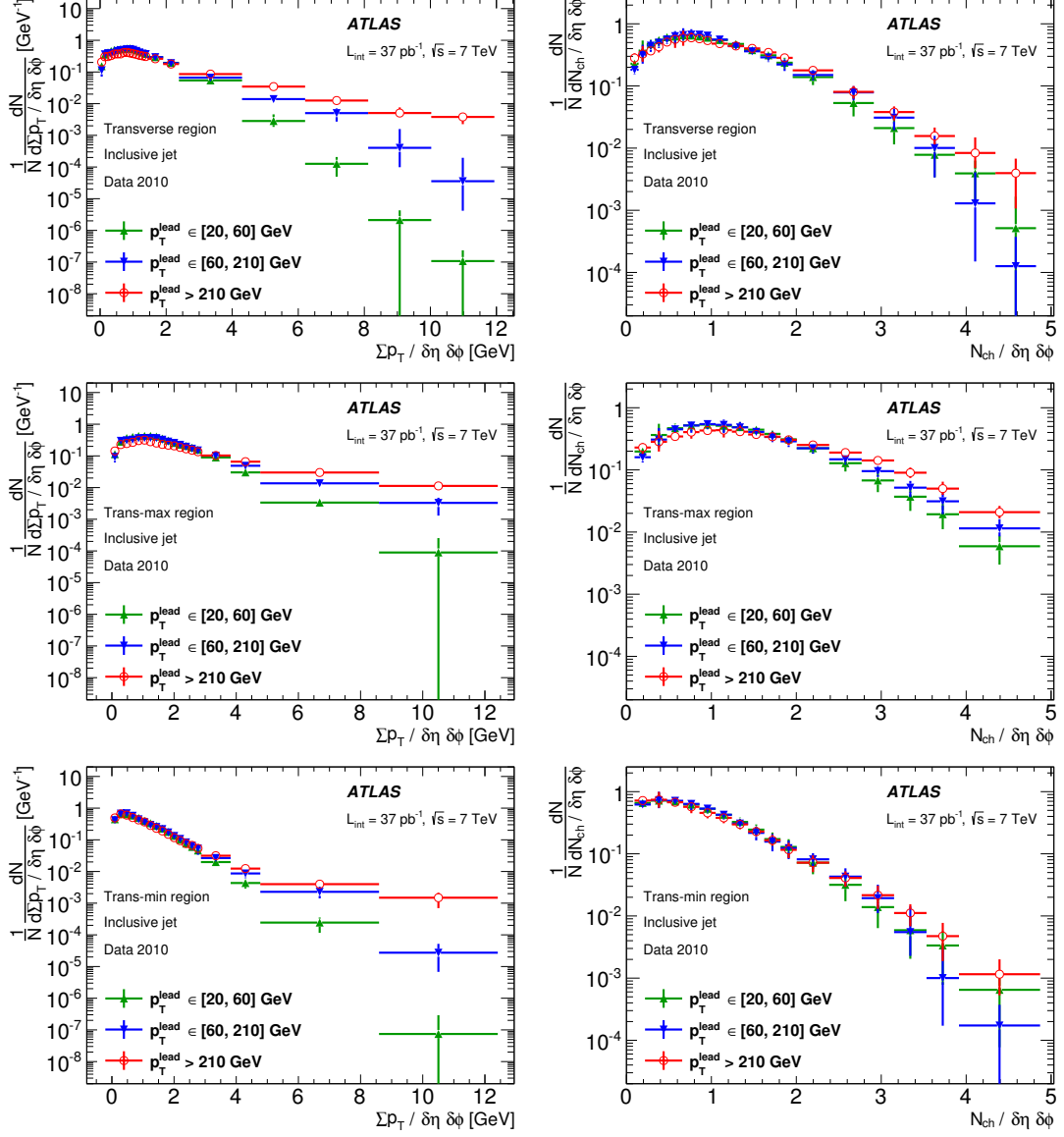


**Figure 5.13:** The densities of the transverse momentum sum,  $\Sigma p_T$ , (left column) and the multiplicity,  $N_{ch}$ , (right column) of charged particles are presented for three different scopes in  $p_T^{\text{lead}}$ . The distributions are shown for the inclusive jet event selection after the full unfolding process, for data only. The top, middle and bottom row show the full transverse, trans-max and trans-min analysis region, respectively. Each distribution has been normalized to unity. The error bars represent the combined statistical and systematic uncertainty for the corresponding  $p_T^{\text{lead}}$  scope.

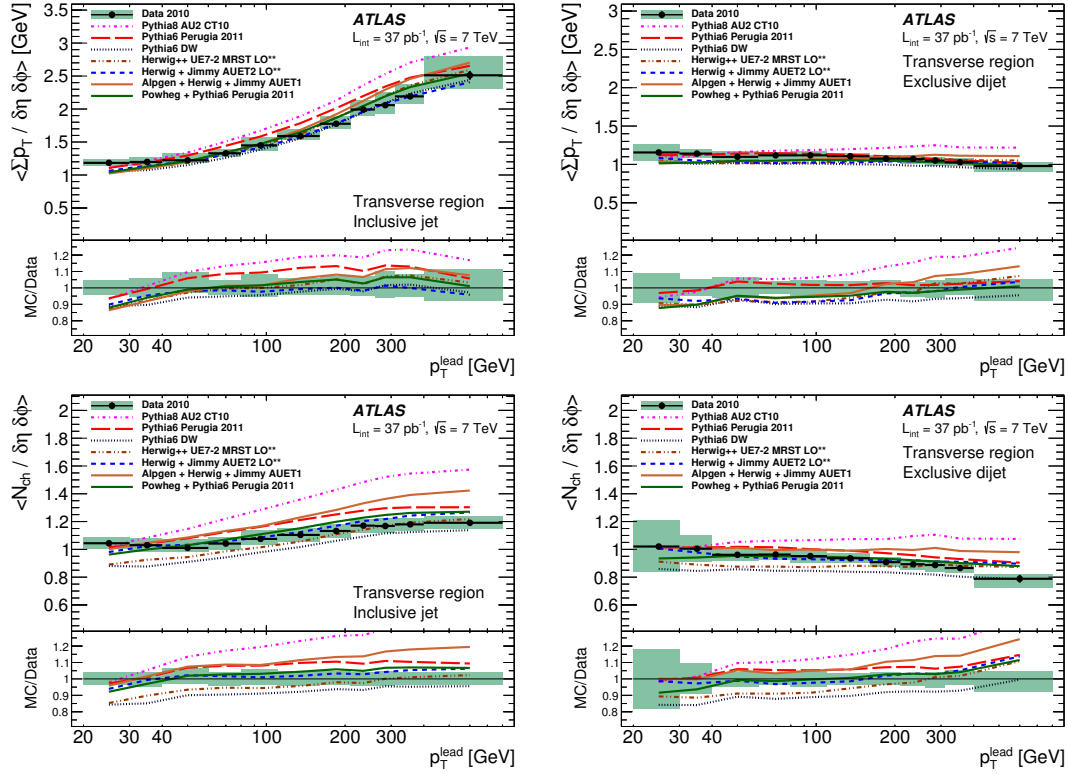


**Figure 5.14:** Mean transverse momentum sum density,  $\sum p_T / \delta\eta \delta\phi$ , (top) and the mean particle multiplicity density,  $N_{ch} / \delta\eta \delta\phi$ , (bottom) both for charged particles against  $p_T^{\text{lead}}$  are shown for the inclusive (left) and exclusive (right) event selection. The distributions are presented for the combined transverse region. The unfolded data points (black) are compared to several MC model predictions. The black error bars indicate the statistical uncertainty and the green shaded areas indicate the combined statistical and systematic uncertainty.

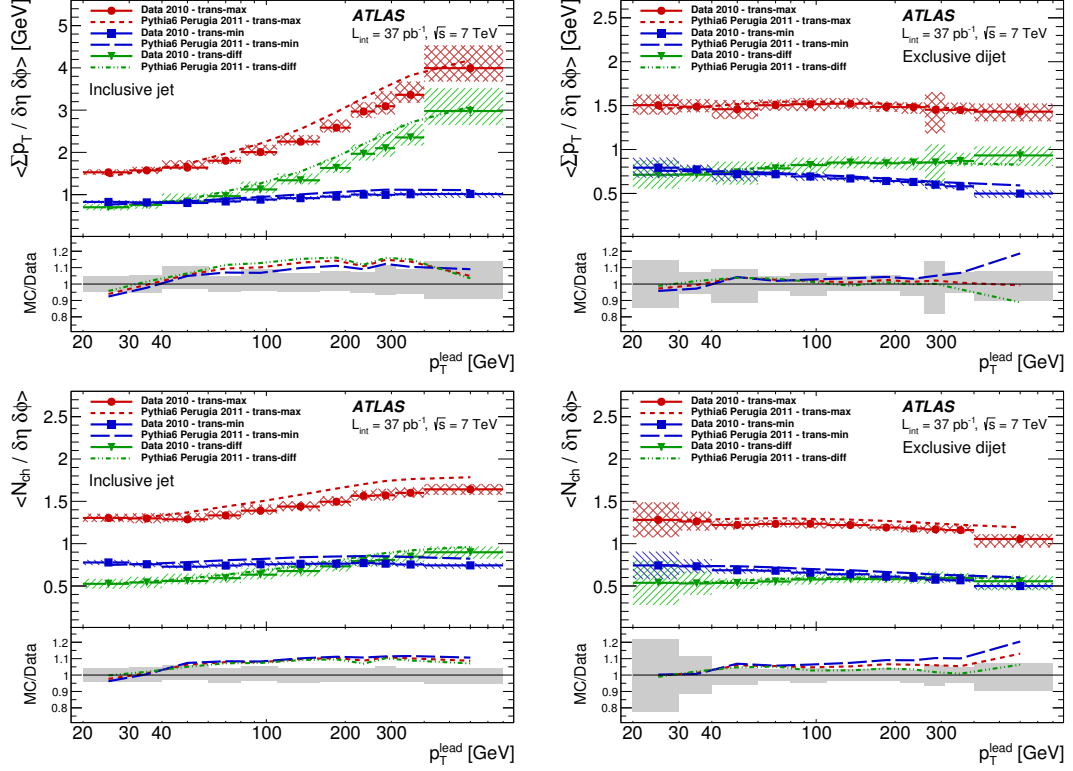


**Figure 5.15:** Mean transverse momentum sum density,  $\sum p_T / \delta\eta \delta\phi$ , (top) and the mean particle multiplicity density,  $N_{\text{ch}} / \delta\eta \delta\phi$ , (bottom) both for charged particles against  $p_T^{\text{lead}}$  are shown for the inclusive (left) and exclusive (right) event selection. The distributions are presented for the trans-max/min/diff regions. The unfolded data points are compared to the prediction of the PYTHIA6 MC model using the Perugia 2011 tune. The colored error bands in the top plot represent the combined statistical and systematic uncertainty for the corresponding region. The grey error band in the bottom part represents the envelope of the maximum combined statistical and systematic uncertainty of the trans-max and trans-min region.

The trans-diff region, defined as the event based difference between the values in the trans-max and trans-min region, is sensitive to additional radiation either from hard scattering or MPIs. Comparing the inclusive and exclusive distributions for both observables support this interpretation. The trans-diff region show to stronger increase of activity with  $p_T^{\text{lead}}$  in the inclusive region than for the exclusive region (and an almost constant behavior for  $N_{\text{ch}}$  after the exclusive selection). In both selections, the PYTHIA 6 Perugia 2011 model shows a reasonable agreement with the measurements.

General features of both observables in the inclusive selection are reproduced by the different MC models. Surprisingly, the PYTHIA models with recent tunes (e.g. PYTHIA 8 AU2 tune) are doing worse in describing the measurements compared to older tunes or other (less recently tuned) models like HERWIG++ or HERWIG+JIMMY. Also POWHEG+PYTHIA 6 can provide a reasonable description of the underlying event measurement. For the exclusive region, not all models are able to reproduce the decreasing behavior of the observables. For  $\sum p_T$  the PYTHIA 6 Perugia 2011 tune provides an excellent description but the tune underestimates the  $N_{\text{ch}}$  density. PYTHIA 8 and ALPGEN+HERWIG+JIMMY show a constant behavior for both observables but overestimate the  $\sum p_T$  and  $N_{\text{ch}}$  density for high values of  $p_T^{\text{lead}}$ . HERWIG+JIMMY is able to reproduce the  $\sum p_T$  density up to  $p_T^{\text{lead}} \sim 200$  GeV but fails to reproduce the decrease in activity and subsequently predicts a higher activity then observed in the measurements. PYTHIA 6 DW, HERWIG++ and POWHEG+PYTHIA 6 predict too little activity for both observables at low energy scales but are able to reproduce the reduced activity for high  $p_T^{\text{lead}}$ . The combination of PYTHIA 6 with POWHEG using the Perugia 2011 tunes gives a less accurate prediction than the PYTHIA 6 Perugia 2011 tune alone. One should note that Perugia 2011 was tuned for PYTHIA 6 only, so a dedicated tune for the use with POWHEG could provide better results.

**$\sum E_T$  and charged ratio** The mean transverse energy sum density,  $\sum E_T / \delta\eta\delta\phi$ , of charged and neutral particles against  $p_T^{\text{lead}}$  is shown in Figure 5.16 for the central region of the detector ( $|\eta| < 2.5$ ) and for the full coverage of the ATLAS calorimeter ( $|\eta| < 4.8$ ). Both observables are shown for the inclusive and exclusive event selection after the full unfolding procedure.

Both observables allow to study the influence of the neutral particle flow within the underlying event. For the central region, the overall behavior of the distributions is similar to the  $\sum p_T$  distribution in Figure 5.14, except that the overall density value is about 50 % to 55 % higher due the additional contribution of neutral particles. The agreement of the MC model predictions with the measurements also is comparable with the  $\sum p_T$  observables in the most cases. It is worth noting, that the predictions for ALPGEN+HERWIG+JIMMY are a lot closer to PYTHIA 8 predictions compared to  $\sum p_T$  observables.

The disagreement between data and MC models is more distinct for the full coverage. Most models underestimate the  $\sum E_T$  density for low values of  $p_T^{\text{lead}}$  and predict a more rapid increase as observed in the data for the inclusive selection (an exception is the HERWIG+JIMMY model). Similar to the case of charged particles only, most models fail to predict the decrease of activity with  $p_T^{\text{lead}}$  for the exclusive selection. This effect is more pronounced for the measurement using the full acceptance. It should be noted that the MC models are tuned using observables within

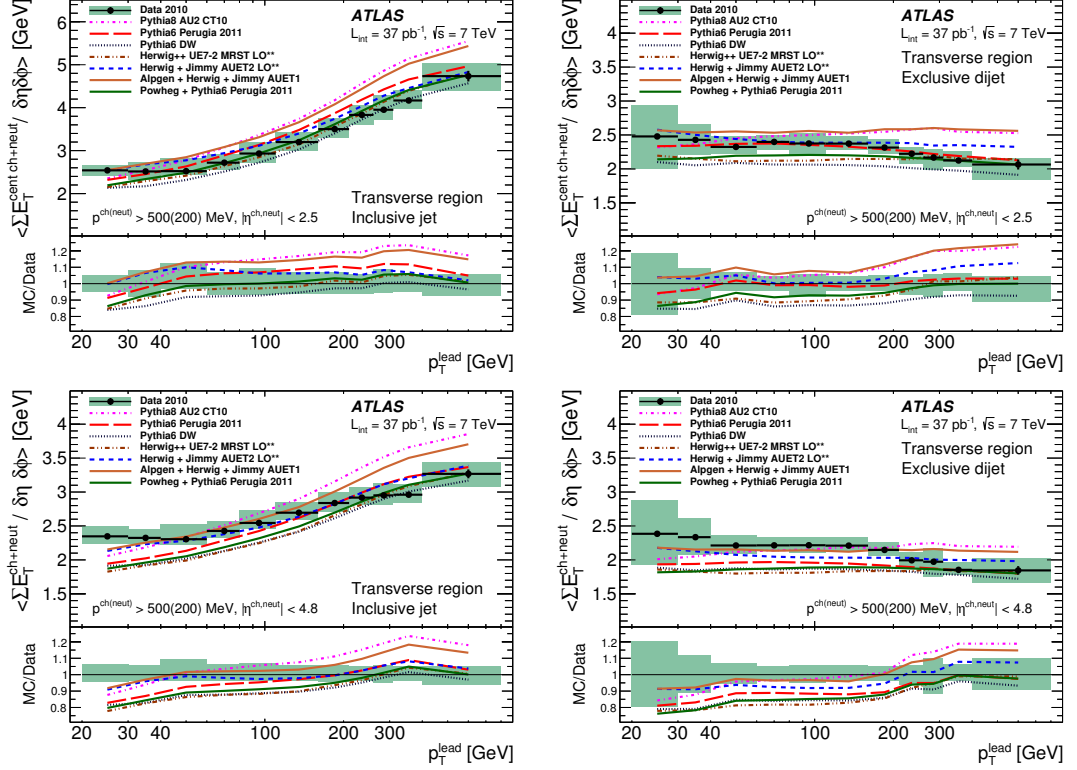


**Figure 5.16:** Mean transverse energy sum densities,  $\sum E_T / \delta\eta\delta\phi$ , of charged and neutral particles within the central region of the detector (top) and the full coverage of the calorimeter (bottom) against  $p_T^{\text{lead}}$  are shown for the inclusive (left) and exclusive (right) event selection. The central region covers a pseudorapidity of  $|\eta| < 2.5$  and the full coverage correspond to  $|\eta| < 4.8$ . The distributions are presented for the combined transverse region. The unfolded data points (black) are compared to several MC model predictions. The black error bars indicate the statistical uncertainty and the green shaded areas indicate the combined statistical and systematic uncertainty.

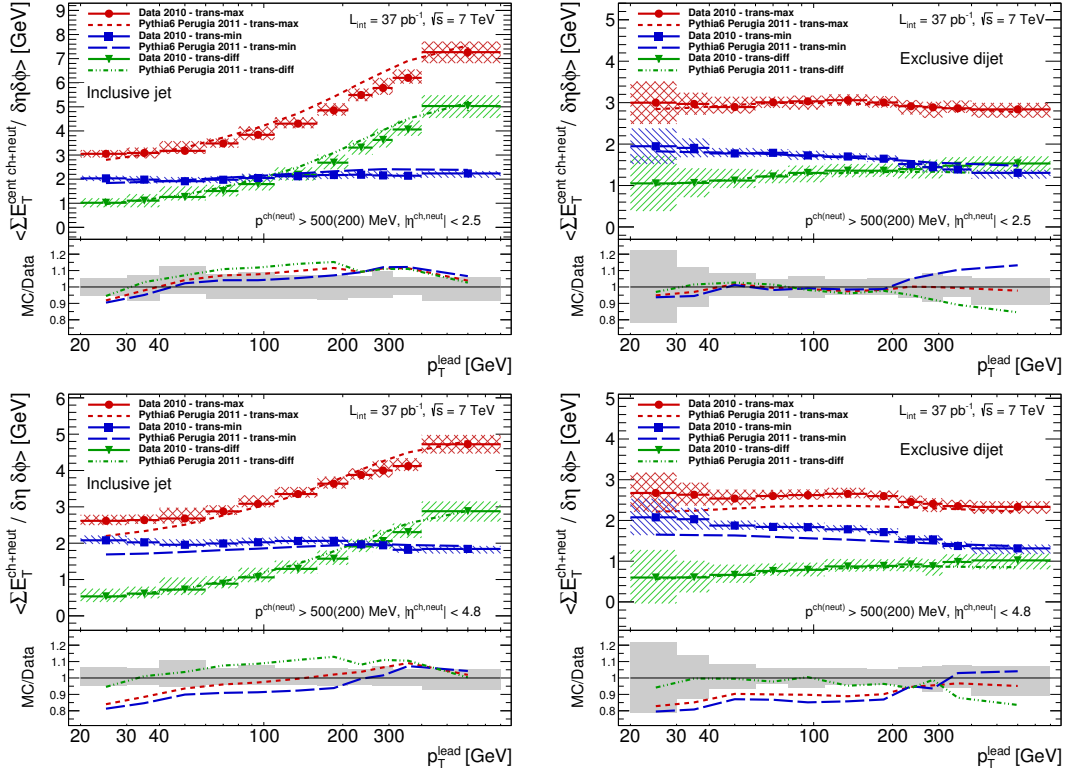


**Figure 5.17:** Mean transverse energy sum densities,  $\sum E_T / \delta\eta\delta\phi$ , of charged and neutral particles within the central region of the detector (top) and the full coverage of the calorimeter (bottom) against  $p_T^{\text{lead}}$  are shown for the inclusive (left) and exclusive (right) event selection. The distributions are presented for the trans-max/min/diff regions. The unfolded data points are compared to the prediction of the PYTHIA 6 MC model using the Perugia 2011 tune. The colored error bands in the top plot represent the combined statistical and systematic uncertainty for the corresponding region. The grey error band in the bottom part represents the envelope of the maximum combined statistical and systematic uncertainty of the trans-max and trans-min region.

the central region, which can be a possible explanation for the decrease in agreement in the high  $\eta$  regions.

The separation in the trans-max, trans-min and trans-diff region for both observables is shown in Figure 5.17. The behavior is, similar to the full transverse region, comparable with the  $\sum p_T$  observable presented in Figure 5.15 (top row). For the inclusive selection, the trans-max region shows an increasing energy density with  $p_T^{\text{lead}}$ , while the trans-min region is nearly constant (for the full acceptance a small decrease has been observed for high values of  $p_T^{\text{lead}}$  but the effect is not significant.). After the exclusive selection, the trans-max region shows a nearly constant behavior (with a slight but not significant decrease for high values of  $p_T^{\text{lead}}$ ) while the trans-min region shows a clear decrease in activity above  $\sim 200$  GeV in  $p_T^{\text{lead}}$ . The central region is reasonable modeled by the PYTHIA 6 Perugia 2011 tune but the model tends to underestimate the activity in the trans-max/min region for low values of  $p_T^{\text{lead}}$ . The trans-diff in contrast is very well modeled.

The mean fraction of the transverse momentum sum of charged particles over the transverse energy

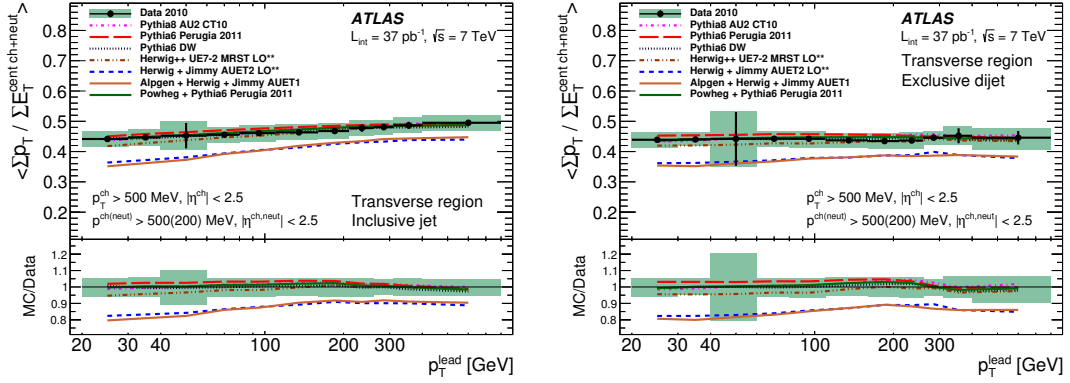


**Figure 5.18:** Profile distributions for the ratio between the transverse momentum sum of charged particles over the transverse energy sum of charged and neutral particles,  $\langle \sum p_T / \sum E_T \rangle$ , are shown for the inclusive (left) and exclusive (right) event selection. The distributions are presented for the combined transverse region. The unfolded data points (black) are compared to several MC model predictions. The black error bars indicate the statistical uncertainty and the green shaded areas indicate the combined statistical and systematic uncertainty.

sum of charged and neutral particles,  $\langle \sum p_T / \sum E_T \rangle$ , against  $p_T^{\text{lead}}$  is presented in Figure 5.18, for the inclusive and exclusive event selection. The fraction is only calculated for the central region of the ATLAS detector ( $|\eta| < 2.5$ ), since this is the maximal acceptance of the inner detector. The observable allows to measure the fraction of energy carried by charged particles within the underlying event and its development with the energy scale of the hard scattering. For the inclusive event selection, a slight increase of  $\langle \sum p_T / \sum E_T \rangle$  with  $p_T^{\text{lead}}$  has been observed with values around 0.45-0.5, while the behavior is nearly constant for the exclusive selection around  $\langle \sum p_T / \sum E_T \rangle \sim 0.45$ . The independence of the fraction of charged particles against  $p_T^{\text{lead}}$  agrees with the observation that the energy density,  $\sum E_T / \delta\eta\delta\phi$ , and the momentum density,  $\sum p_T / \delta\eta\delta\phi$ , show a very similar behavior for the central region. The fraction is reasonably modeled by the MC event generators, except for HERWIG+JIMMY and ALPGEN+HERWIG+JIMMY, which both use the same parton shower and hadronisation model. Both generators underestimate the fraction of charged particles by 10 % to 20 %. The disagreement is more distinct for the low values of  $p_T^{\text{lead}}$ . For the  $p_T^{\text{lead}}$  bin between 40 GeV to 60 GeV a large statistical uncertainty has been observed. The reason is a transition of the minimum bias trigger to the jet trigger in this region. Below 60 GeV the minimum bias trigger system is used for the online event selection and above a jet trigger is utilized. The pre-scales for the minimum bias trigger are typically larger than for the jet triggers and the number of selected events right below 60 GeV is therefore lower than right above the threshold. For most distributions, this effect is not visible and covered by the systematic uncertainties but for the ratio observables the effect becomes dominant in the considered bin.

**Mean  $p_T$  against  $p_T^{\text{lead}}$  and  $N_{\text{ch}}$**  The average of the mean transverse momentum of charged particles,  $\langle p_T \rangle$ , as a function of  $p_T^{\text{lead}}$  and the charged particle multiplicity,  $N_{\text{ch}}$ , is presented in Figure 5.19, for the inclusive and exclusive event selection. For this observable, no separation in trans-max and trans-min region is performed, because the physical definition and interpretation



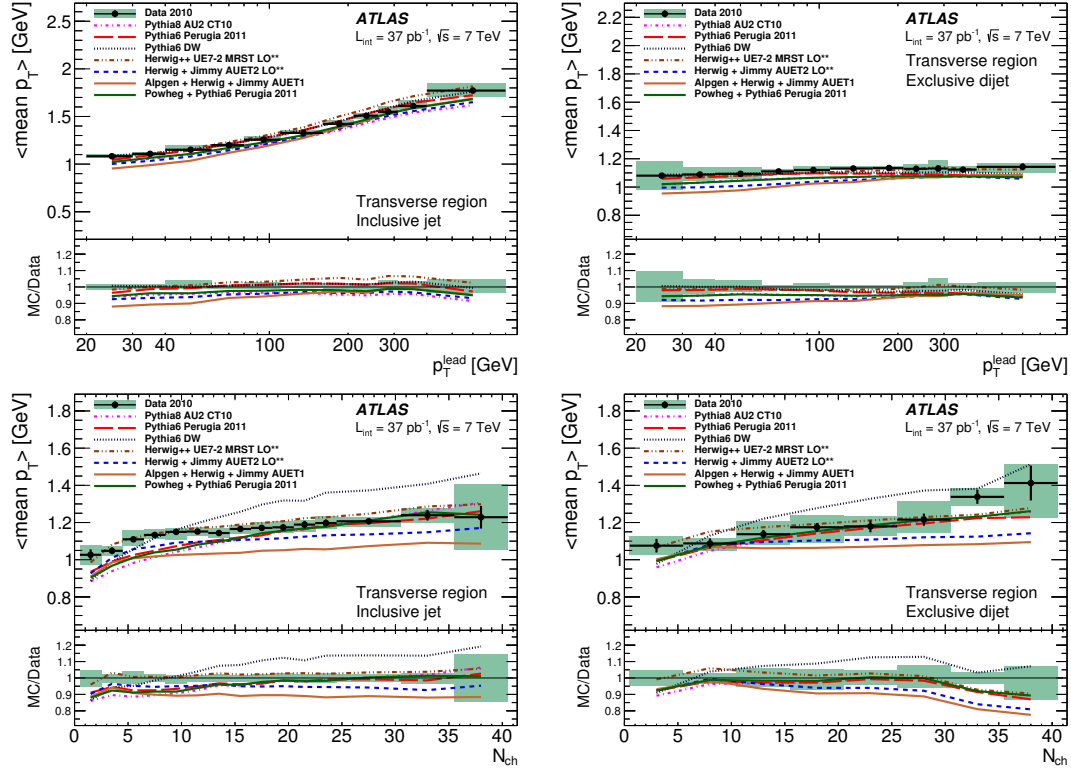


**Figure 5.19:** Profile distributions for the mean transverse momentum,  $\langle p_T \rangle$ , against  $p_T^{\text{lead}}$  (top) and  $N_{\text{ch}}$  (bottom) are shown for the inclusive (left) and exclusive (right) event selection. The distributions are presented for the combined transverse region. The unfolded data points (black) are compared to several MC model predictions. The black error bars indicate the statistical uncertainty and the green shaded areas indicate the combined statistical and systematic uncertainty.

of the transverse region with more/less activity is ambiguous.

Within the inclusive selection, the mean transverse momentum is increasing with respect to  $p_T^{\text{lead}}$ , while for the exclusive selection the mean  $p_T$  remains constant, within the combined statistical and systematic uncertainties, and therefore independent against the hard scattering scale. These properties are fairly expected from the structure of the  $\sum p_T$  and  $N_{\text{ch}}$  distributions, presented in Figure 5.14. The average value of  $\sum p_T$  (the nominator for mean  $p_T$ ) shows a stronger development with  $p_T^{\text{lead}}$  compared to  $N_{\text{ch}}$  (the denominator) in the inclusive selection, which leads to the raising structure of the mean  $p_T$ . In contrast to the inclusive region, both observables show a similar development within the exclusive region, which leads to flat behavior of the mean  $p_T$ . The MC models show a reasonable description of the mean  $p_T$  observable within 10 % around the measured data points. The description is better compared to the description of the  $\sum p_T$  and  $N_{\text{ch}}$  densities separately and the differences between the MC models are less pronounced. It should be noted that the most of the considered MC models tend to underestimate the mean  $p_T$ .

The mean transverse momentum against  $N_{\text{ch}}$  shows in increasing behavior for both the inclusive and exclusive event selection and is consistent with observations in other UE measurements, e.g. [172]. Both regions show a comparable magnitude in  $\langle p_T \rangle$  within the combined statistical

and systematic error bands.

A reasonable description of the  $\langle p_T \rangle$  distribution is provided by the HERWIG++ model for the inclusive as well as the exclusive region, in particular for low values of  $N_{\text{ch}}$ . PYTHIA 6 Perugia 2011, PYTHIA 8 AU2 and POWHEG+PYTHIA 6 provide a good description for high particle multiplicities (but underestimated the  $\langle p_T \rangle$  for low  $N_{\text{ch}}$ ) in the inclusive selection and an overall reasonable description for the exclusive selection. In contrast to the Perugia 2011 tune, the DW tune fails to reproduce the distributions and predicts a harder particle spectra then observed in the measurements. The JIMMY based MC models underestimate the  $\langle p_T \rangle$  distribution, in particular for high particle multiplicities. The effect is expected, because JIMMY does not provide a *color reconnection* procedure [215] in contrast to HERWIG++ or the PYTHIA models. HERWIG+JIMMY is slightly closer to the measurements due to a newer tune compared to ALPGEN+HERWIG+JIMMY model.

### 5.3.3 Summary

Underlying event measurements in inclusive jet and exclusive dijet events have been performed using  $37 \text{ pb}^{-1}$  of proton-proton collision data collected with the ATLAS detector at the LHC. Several observables, including track as well as cluster based observables which allow to test the charged and neutral UE contributions, sensitive to the underlying event have been measured for different energy regions of the hard scattering. The measurements have been performed to a maximum  $p_T^{\text{lead}}$  of 800 GeV, which allows to test the underlying event modeling over a large range and give a reasonable input for further tuning efforts.

A raising behavior of the activity in the transverse and trans-max region with  $p_T^{\text{lead}}$  has been observed after the inclusive event selection. In contrast, the activity in the trans-min region has shown no significant dependence with  $p_T^{\text{lead}}$ . The exclusive selection removes the increase of the activity in transverse and trans-max region and even introduces a slight decrease in activity for high values of  $p_T^{\text{lead}}$ , which seems to be more prominent in the trans-min region. The decreasing feature is not fully understood yet but it indicates that the exclusive region remove additional contributions from the hard scattering (resulting in a constant function against  $p_T^{\text{lead}}$  in the transverse region) but also removes contributions from MPI at high energy scales. Despite the decreasing structure, that flatness of the distributions in the inclusive trans-min region and exclusive transverse region supports the idea of modeling the contribution from MPI with a constant function once a certain energy scale in the hard scattering is reached and most the proton-proton collisions are central.

All observables have been compared to various MC models and tunes, providing a different modeling of MPIs, parton-showers, initial and final state radiation and the hadronisation. Overall a reasonable description of the underlying event model is provided by the majority of the models. Both HERWIG+JIMMY and HERWIG++ can reproduce the underlying event features, in particular for the inclusive event selection. An addition the more recent model HERWIG++ shows a strong improvement when compared to HERWIG+JIMMY. Also, the PYTHIA 6 model with the Perugia 2011 tune provides a good description of the underlying event structure, either standalone or in combination with POWHEG, especially after the exclusive event selection. PYTHIA 8, in

contrast, shows a tendency to overestimate the underlying event activity using the AU2 tune, which can maybe be recovered by a new tune to achieve a performance closer to PYTHIA 6 with Perugia 2011. Many MC models show problems in the description of the decreasing structure in the exclusive region, which may indicate new features in the UE contribution which are not yet covered completely by the current models. When compared to the cluster based observables, which include the neutral particle flow, the MC models exhibit problems to reproduce the distributions for the full acceptance while the description for the restricted central region ( $|\eta| < 2.5$ ) is usually slightly better. The ratio of activity between charged and neutral components is, in contrast to the neutral distributions themselves, very reasonable modeled by the event generator, except for the models using the JIMMY algorithm, which does not account for color reconnection.

In conclusion the measurements in jet events allow for the first time to test the underlying event contribution over a large energy scale up to 800 GeV, including several regions and event selection to be sensitive to different parts of the underlying event and the hard scattering. The measurements give a contribution to the further development and tuning of MC models and are incorporated into the “A14” tune series [184] provided by the ATLAS collaboration.

### 5.3.4 Comparison with other underlying event measurements

The results of the underlying event analysis in jet events have been compared by the ATLAS collaboration to the results of other underlying event analyses: including UE measurements in events with an inclusive Z boson production [216].

Two of the major results are presented in Figure 5.20, showing distributions for the  $\sum p_T$  and  $N_{\text{ch}}$  density of charged particles against the energy scale of the hard scattering in the transverse region. The definition of the hard scattering object varies between the different UE analyses. For the leading track analysis using minimum bias events [172] the transverse momentum of the leading track is used to define the direction and energy scale of the hard scattering. For the jet based analysis the transverse momentum of the leading jet is utilized and for the analysis based on Z boson events the transverse momentum of the reconstructed lepton pair is used. All three analyses are performed using proton-proton collision data at  $\sqrt{s} = 7$  TeV collected at the ATLAS detector in the years 2010 and 2011.

The distributions of the UE measurements in jet events are compared after the inclusive selection. Around 20 GeV a smooth transition between the minimum bias based and jet based analysis has been observed. This supports the idea that the slope of the underlying event contribution from zero to a (nearly) constant value cannot be observed in inclusive jet events, because the requirement that each jet needs to provide a minimal transverse momentum of 20 GeV is already too high. Below an energy scale of 50 GeV a significant difference between the underlying event contribution in minimum bias/jet events and Z boson events has been found, indicating that the development of the UE contribution is different for the considered analyses. Above 50 GeV an agreement between the jet based and Z boson based UE contribution has been observed for the  $N_{\text{ch}}$  density but the  $\sum p_T$  density is on average larger in the Z boson events. Further studies showed that the effect is dominating the trans-max region and is a result of the different

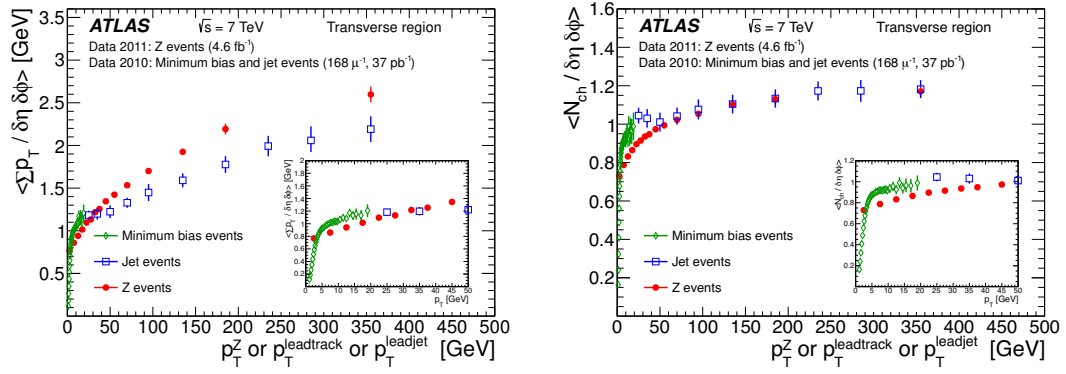


**Figure 5.20:** Mean transverse momentum sum density,  $\sum p_T / \delta\eta \delta\phi$ , (left) and the mean particle multiplicity density,  $N_{\text{ch}} / \delta\eta \delta\phi$ , (right) in the transverse region, both for charged particles, against the energy scale of the hard scattering are shown for three different underlying event analyses: UE in minimum bias event using charged particles (green), UE in jet events (blue) and UE in inclusive Z-boson events (red). The error bars represent the combined statistical and systematic uncertainty for the considered measurement. The results are taken from Ref. [216].

definitions of the hard scattering process [216, ch. 9.4].

## 6 Search for neutral MSSM Higgs bosons

Within this chapter, the search for neutral Higgs boson in the context of the *Minimal Supersymmetric Extension of the Standard Model* (MSSM) is presented with the decay of the Higgs boson in two hadronically decaying tau leptons. The search has been performed using about  $4.5 \text{ fb}^{-1}$  of proton-proton collision data taken with the ATLAS detector at LHC in the year 2011.

Searches for MSSM Higgs bosons have been already performed in the pre-LHC era. At LEP, all four collaboration (ALEPH, DELPHI, L3 and OPAL) performed measurements using  $e^+e^-$  collision data at center-of-mass energies from 91 GeV to 209 GeV [63]. The dominant production channels were the *Higgsstrahlung* ( $e^+e^- \rightarrow HZ$ ) and *Higgs pair production* ( $e^+e^- \rightarrow HH$ ), with Higgs bosons decaying either into  $b\bar{b}$  or  $\tau^+\tau^-$ . No evidence for a Higgs boson (neither SM nor BSM) has been found at LEP [63].

The search for Higgs bosons continued using proton- anti-proton collision measurements at Tevatron. In terms of BSM Higgs models, combined searches for neutral Higgs bosons in association with b-quarks [217] and for decays into  $\tau^+\tau^-$  [218] were performed by CDF and DØ using RUNII data at a center-of-mass energy of  $\sqrt{s} = 1.96 \text{ TeV}$ . In addition, searches for charged Higgs bosons have been performed by both collaborations [219, 220] using various Higgs decay channels. For the standard model Higgs boson searches, an excess of events between a mass range of 114 GeV to 140 GeV, with a local significance corresponding to 3.0 standard deviations around 125 GeV [221], has been observed, which is in agreement with the discovery of the SM Higgs boson at LHC. Apart from this, no significant indication for a BSM Higgs sector has been found.

With the start of the LHC in 2010 a broad program to investigate the origin of the electroweak symmetry breaking mechanism started at the ATLAS and CMS experiments, both for SM like Higgs bosons and for BSM models. On 4 July 2012, both experiments were able to confirm a discovery of a new particle [10, 11] with an invariant mass around 125.09 GeV [35]. Subsequently, both experiments started to measure couplings and decay rates of the newly discovered particle to the already known SM particles, in particular the decay into  $\gamma\gamma$ ,  $ZZ$  and  $WW$ ,  $\tau\tau$ ,  $b\bar{b}$ ,  $\mu^+\mu^-$  and couplings to top quarks [36]. Until today, all measurements are compatible with a SM Higgs boson, within their stated uncertainty bands.

Parallel to the search for SM Higgs boson, both experiments started programs for the search of BSM physics in general, including studies for a BSM Higgs sector. For this thesis only searches for MSSM Higgs sectors are considered. In this case, searches for charged Higgs bosons, with decays into  $WZ$ ,  $\tau\nu$  or  $q\bar{q}'$ , have been performed as well as searches for additional neutral Higgs boson, predominantly in the  $H \rightarrow \tau^+\tau^-$  decay channel but also  $\mu\mu$  and  $b\bar{b}$  decays or decays

into pairs of SM-like Higgs bosons are considered. So far, no significant deviation from the SM prediction has been found and upper limits have been estimated.

The ATLAS analyses for neutral MSSM Higgs boson searches with decays into  $\tau^+\tau^-$  will be briefly reviewed here. The first search [222] was performed using a  $36\text{ pb}^{-1}$  dataset which was recorded during the year 2010 at a center-of-mass energy of  $\sqrt{s} = 7\text{ TeV}$ . In this analysis only the full-leptonic and semi-leptonic decay channels are considered<sup>1</sup> and the first exclusion limit in  $m_A \times \tan\beta$  for a mass interval between 90 GeV to 300 GeV has been set. The next search was performed using the dataset recorded in 2011, again at  $\sqrt{s} = 7\text{ TeV}$  but with an integrated luminosity of  $4.7\text{ fb}^{-1}$  to  $4.8\text{ fb}^{-1}$  [223]. This study includes the full hadronic decay channel (in addition to the full-leptonic and semi-leptonic channel) as well as Higgs decays into two muons. Due to the increased luminosity, additional channels and improvement in the background estimation, the exclusion limits for neutral MSSM Higgs boson could be further improved and the probed  $m_A$  values are extended up to 500 GeV. The last neutral MSSM search in Run 1 has been performed using the 2012 dataset with  $\sqrt{s} = 8\text{ TeV}$  and a total integrated luminosity of  $19.5\text{ fb}^{-1}$  to  $20.3\text{ fb}^{-1}$  [224]. New methods for the background estimation in the high mass regime as well as the increased luminosity and center-of-mass energy allow a significant improvement of the exclusion limits compared to the 7 TeV analyses, setting the strongest exclusion limits for neutral MSSM searches in the di-tau decay channel with ATLAS in Run 1, up to a  $m_A$  value of 1 TeV. With the start of Run 2, the search for MSSM Higgs bosons continued and up to this point first exclusion limits have been provided during end-of-year in 2015 [225], using the first dataset at  $\sqrt{s} = 13\text{ TeV}$  with an integrated luminosity of  $3.2\text{ fb}^{-1}$ .

Within the context of the thesis, only the full hadronic decay channel will be considered. The goal of this study is the re-analysis of the 2011 dataset using the improved background estimation techniques developed for the 8 TeV dataset. A new estimation for the exclusion limit for the 2011 dataset has been performed and compared the current results for the 2011 dataset. In addition, a combination with the 8 TeV full-hadronic limits is performed and combined exclusion limits are presented.

---

<sup>1</sup>See Section 6.1.1 for details on the di-tau lepton decay channels.

## 6.1 Analysis Overview

The basic idea in the searches for new physics phenomena is to find a significant deviation between the observations and the SM predictions. Within the context of this search, the set of proton-proton interactions, recorded with the ATLAS detector in 2011, is filtered with the aim of enhancing the contribution of a possible MSSM Higgs boson signal with respect to contribution of SM processes which are able to mimic the decay structure of the signal process, referred to as *background processes*. The main objective of this analysis is therefore a precise estimation of background contribution passing the event selection and the evaluation of the corresponding systematic uncertainties.

The final interpretation of the measurement is performed with respect to an observable which provides a significant discrimination power between a possible signal process and the background prediction. For the MSSM Higgs boson search the *total transverse mass* observable is used which is closely related to the mass of the di-tau lepton systems. A possible deviation within the final discriminating observable is (usually) expressed in terms of a *p-value* to quantify the probability that the deviation can origin from a statistical fluctuation of the SM background processes. The common convention in high energy physics is to require a significance of at least five standard deviations in order to state an observation of a new phenomenon which is not reproduced by the SM. If no significant deviation is observed, it is possible to restrict the MSSM parameter space which is compatible with the observations at a certain level of confidence. Within the context of this thesis, exclusion limits within the  $m_A \times \tan \beta$  parameter space have been evaluated.

### 6.1.1 Signal Process

**Signal Topology** The main production mechanisms for neutral MSSM Higgs bosons at the LHC are the gluon-gluon fusion process and the production in association with b-quarks. Both heavy neutral bosons,  $H$  and  $A$ , are degenerated in mass (in the decoupling limit). Since the presented analysis is not sensitive to the CP properties of the given resonance, a hypothetical signal will be a superposition of both boson. In addition, no specific separation between the two production mechanisms is performed. Consequently, any possible contribution from signal processes will be a superposition of gluon-gluon fusion and b-associated production. For the purpose of visualization in the further context, only the b-associated production of the CP-odd  $A$  boson will be shown to represent a possible signal contribution<sup>2</sup>. The full set of production channels with their corresponding cross sections is considered during the limit setting.

The signal topology is characterized by a high mass resonance which decays directly into two tau leptons. Since the lifetime of the tau leptons is too short to reach a significant amount<sup>3</sup> of active detector material, they are reconstructed using their decays products. It is common practice to distinguish between the following three sub-decay channels.

<sup>2</sup>The labeling convention will be  $A_{\tan \beta}^m \times \epsilon$ , where  $m$  and  $\tan \beta$  represent the corresponding boson mass in GeV and the  $\tan \beta$  value during the event generation and  $\epsilon$  a possible scaling factor to increase the visibility of the signal.

<sup>3</sup>A small fraction of tau leptons are able to pass the first layers of the innermost pixel detector, before they decay. However, no special treatment is applied apart from the standard tau reconstruction for those cases.

**Di-leptonic decay,  $H/A \rightarrow \tau_{\text{lep}}\tau_{\text{lep}}$ :** Both tau leptons decay into lighter leptons (either electrons or muons), with a branching ratio of  $\approx 12\%$ .

**Semi-leptonic decay,  $H/A \rightarrow \tau_{\text{lep}}\tau_{\text{had}}$ :** One tau lepton decays into an electron or muon and one into hadrons, with a branching ratio of  $\approx 46\%$ .

**Hadronic decay,  $H/A \rightarrow \tau_{\text{had}}\tau_{\text{had}}$ :** Both tau leptons decay hadronically, with a branching ratio of  $\approx 42\%$ .

The leading order Feynman diagrams are shown in Figure 6.1. All three sub-decay channels

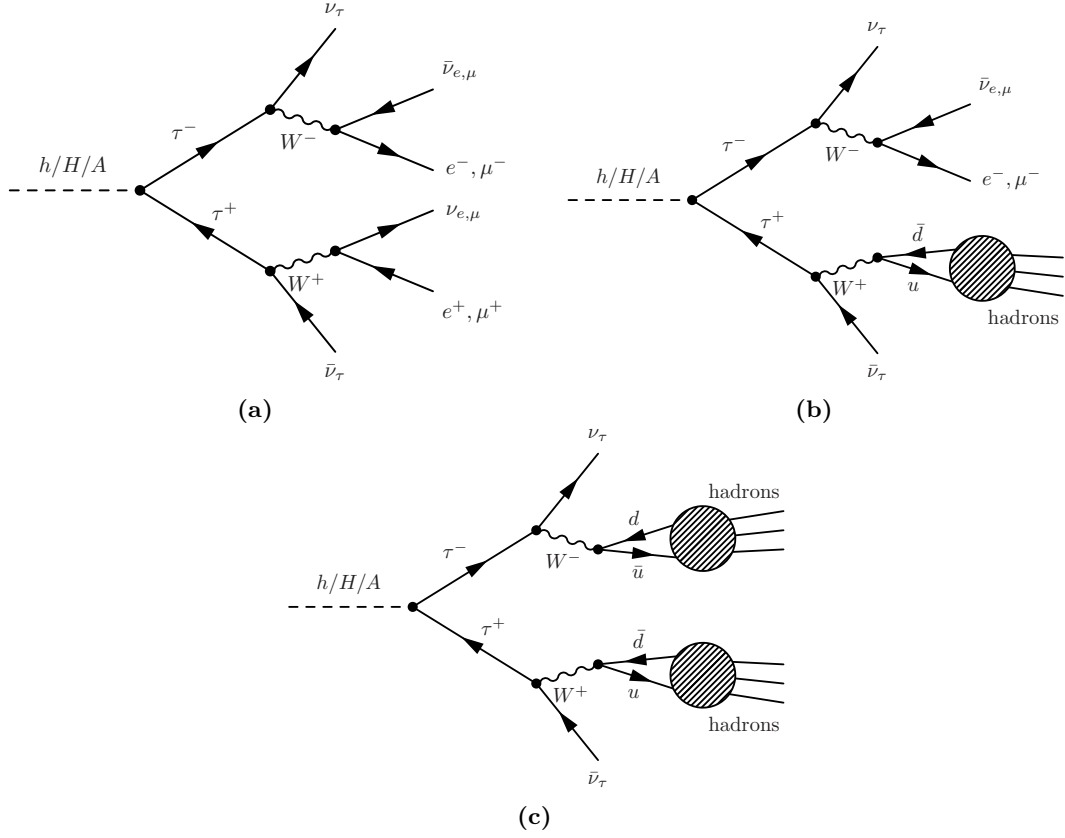


**Figure 6.1:** Leading order Feynman diagrams for the di-leptonic (a) decay channel, the semi-leptonic (b) decay channel and the hadronic (c) decay channel. The hatched areas symbolize non-perturbative hadronisation processes.

need to be treated quite differently in an experimental analysis, due to the different background composition and different particle reconstruction/identification between the single decay channels. Here, the hadronic decay channel is studied.

Both tau leptons will acquire, on average, a high transverse momentum ( $\mathcal{O}(10 - 100)$  GeV), due to the high mass of the decay resonance and will be separated by a large azimuthal angle (*back-to-back topology*). Since the decaying resonance is assumed to be electrically neutral, both tau leptons should have opposite electric charge and the generation of neutrinos during the tau



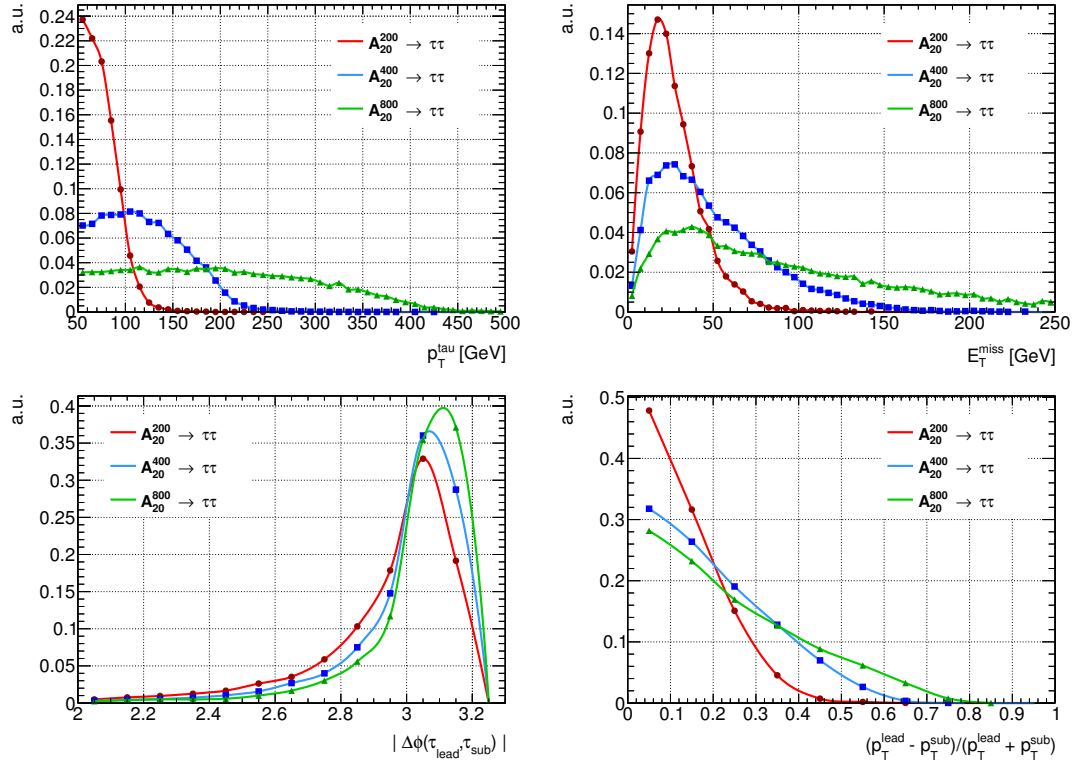


**Figure 6.2:** The visible transverse momentum of the tau leptons (top left), the missing transverse energy (top right), the azimuthal separation between the leading and sub-leading tau lepton (bottom left) and the relative  $p_T$  difference between the leading and sub-leading tau lepton (bottom right) are presented for three different values of  $m_A$  and  $\tan\beta = 20$ . A minimal requirement of  $p_T > 50$  GeV is applied to the tau candidates. The leading and sub-leading tau lepton is defined with respect to the corresponding transverse momentum. All distributions are normalized to unit area.

lepton decays will lead to a moderate amount of missing transverse energy<sup>4</sup> ( $\mathcal{O}(10 - 100)$  GeV). The corresponding distributions for three different values of  $m_A$  can be found in Figure 6.2. Potential signal events are triggered by signatures with one or two hadronically decaying tau lepton candidates.

**Simulated signal samples** Simulated samples for the neutral MSSM Higgs boson production in association with b-quarks were generated using the Sherpa MC event generator [39] version 1.4.0 and the CTEQ6L1 [206] PDF. The production of Higgs bosons via gluon-gluon fusion was simulated on next-to-leading order using POWHEG [193–195] (v1) interfaced with PYTHIA 6 [188] (v6.4) with the CTEQ6L1 PDF and the AUET2B tune [205]. All samples are generated for mass values  $m_A$  between 100 GeV to 800 GeV and a  $\tan\beta$  value of 20.

The cross sections and branching ratios for the neutral MSSM Higgs bosons within the considered benchmark scenarios are provided by the *LHC Higgs Cross Section Working Group* [67, 226, 227].

<sup>4</sup>Due the back-to-topology in the azimuthal space, the contributions of neutrinos from both tau leptons will partly cancel each other in the calculation of the missing transverse energy. Consequently,  $E_T^{\text{miss}}$  is usually significantly lower than the total amount of energy transported by the neutrinos.

The gluon-gluon fusion production cross sections,  $\sigma(gg \rightarrow H)$ , have been calculated by scaling the corresponding SM values taking the top-quark contribution,  $\sigma_{tt}$ , the bottom-quark contribution,  $\sigma_{bb}$ , and the interference terms,  $\sigma_{tb}$ , into account [67]. All three contributions have been calculated at full next-to-leading order accuracy in QCD using HIGLU [228], with NNLO order corrections for the  $\sigma_{tt}$  term which has been calculated via with GGH@NNLO [229, 230] program. Cross sections for the b-associated production have been obtained by matching the calculations in the five flavor scheme with BBH@NNLO [231] with calculations in the four flavor scheme [67, 232].

Branching ratios for the MSSM Higgs boson have been estimated by combining results [226, 227] from the HDECAY [233–235] and FEYNHIGGS [74, 236–239] program. The total decay width of  $H$  and  $A$  is expected to be of the order of 1 GeV to 10 GeV for the considered parameter space [59]. Cross sections times branching fractions, combined for  $A$  and  $H$ , for various points in the  $m_A \times \tan \beta$  space can be found in Figure 6.3 for the  $m_h^{\max}$  benchmark scenario and in Figure A.7 for the  $m_h^{\text{mod}\pm}$  benchmark scenarios.

Systematic uncertainties have been estimated to be at the order of 10 % to 20 %, depending on

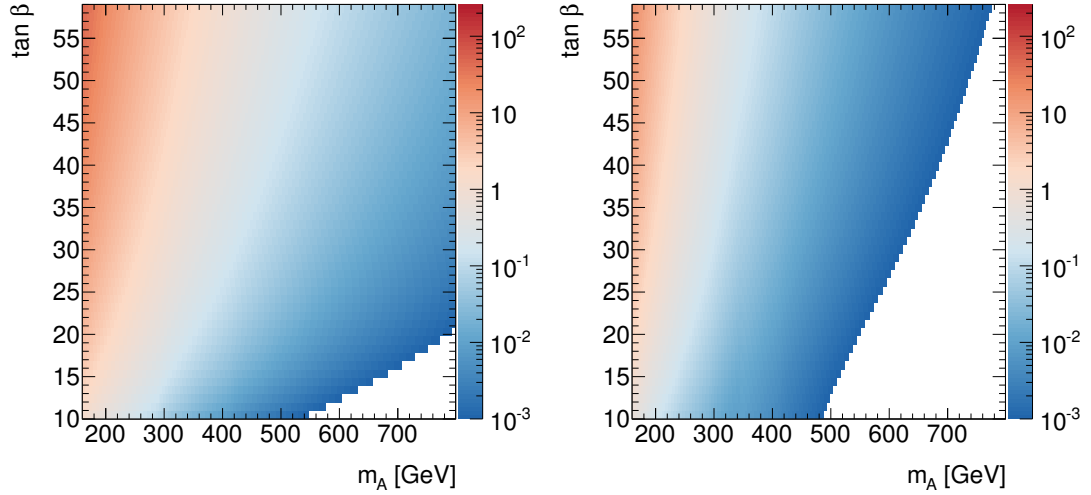


**Figure 6.3:** Cross sections times branching fractions,  $\sigma(pp \rightarrow \phi) \times \mathcal{B}(\phi \rightarrow \tau\tau)$  [pb], are presented for the b-associated production channel (left) and for the production via gluon-gluon fusion (right), combined for the pseudoscalar MSSM Higgs boson  $A$  and the scalar MSSM Higgs boson  $H$ . The distributions are calculated within the  $m_h^{\max}$  benchmark scenario at a center-of-mass energy of  $\sqrt{s} = 7$  TeV. The cross sections and branching fraction values are provided by the *LHC Higgs Cross Section Working Group*.

the considered  $m_A \times \tan \beta$  point. Uncertainties due to the renormalization and factorization scales as well as uncertainties on the utilized PDFs have been taken into account [67]. An overview about the combined cross sections times branching fractions, including the corresponding systematic uncertainties, calculated within the  $m_h^{\max}$  scenario are presented in Table 6.1.

### 6.1.2 Background Processes

All possible SM processes which are able to mimic the di-tau final state of a MSSM Higgs boson decay are considered as *background processes*. This includes processes with (at least) two real

$m_A$ [GeV]	$\tan \beta$					
	10	20	30	40	50	60
$\sigma(pp \rightarrow \phi) \times \mathcal{B}(\phi \rightarrow \tau\tau)$ in [pb]						
140	$3.20^{+0.23}_{-0.13}$	$12.68^{+0.93}_{-0.46}$	$29.27^{+2.18}_{-1.04}$	$53.02^{+3.96}_{-1.88}$	$84.11^{+6.30}_{-2.96}$	$122.86^{+9.22}_{-4.32}$
150	$2.51^{+0.18}_{-0.10}$	$9.97^{+0.74}_{-0.35}$	$22.71^{+1.69}_{-0.78}$	$40.78^{+3.05}_{-1.39}$	$64.34^{+4.81}_{-2.19}$	$93.64^{+7.01}_{-3.18}$
170	$1.50^{+0.11}_{-0.05}$	$6.04^{+0.45}_{-0.20}$	$13.68^{+1.02}_{-0.45}$	$24.48^{+1.83}_{-0.80}$	$38.53^{+2.88}_{-1.26}$	$55.97^{+4.19}_{-1.83}$
200	$0.73^{+0.05}_{-0.03}$	$3.03^{+0.23}_{-0.10}$	$6.89^{+0.52}_{-0.22}$	$12.34^{+0.93}_{-0.40}$	$19.43^{+1.47}_{-0.63}$	$28.21^{+2.13}_{-0.92}$
250	$0.25^{+0.02}_{-0.01}$	$1.12^{+0.09}_{-0.04}$	$2.59^{+0.20}_{-0.09}$	$4.66^{+0.36}_{-0.16}$	$7.34^{+0.57}_{-0.26}$	$10.67^{+0.83}_{-0.38}$
300	$0.08^{+0.01}_{-0.00}$	$0.45^{+0.04}_{-0.02}$	$1.09^{+0.09}_{-0.04}$	$2.01^{+0.16}_{-0.08}$	$3.19^{+0.26}_{-0.13}$	$4.65^{+0.38}_{-0.19}$
350	$0.03^{+0.00}_{-0.00}$	$0.19^{+0.02}_{-0.01}$	$0.49^{+0.04}_{-0.02}$	$0.92^{+0.08}_{-0.04}$	$1.49^{+0.13}_{-0.07}$	$2.19^{+0.19}_{-0.10}$
$\sigma(pp \rightarrow \phi) \times \mathcal{B}(\phi \rightarrow \tau\tau)$ in [fb]						
400	$13.99^{+1.06}_{-0.70}$	$89.47^{+7.92}_{-4.47}$	$242.19^{+21.75}_{-12.20}$	$466.70^{+42.05}_{-23.56}$	$761.46^{+68.70}_{-38.48}$	$1127.25^{+101.75}_{-56.98}$
450	$5.67^{+0.44}_{-0.30}$	$42.02^{+3.90}_{-2.27}$	$122.16^{+11.54}_{-6.67}$	$243.53^{+23.11}_{-13.35}$	$404.60^{+38.45}_{-22.20}$	$605.36^{+57.58}_{-33.23}$
500	$2.71^{+0.22}_{-0.15}$	$21.54^{+2.10}_{-1.26}$	$65.53^{+6.52}_{-3.88}$	$133.96^{+13.38}_{-7.95}$	$225.80^{+22.58}_{-13.42}$	$340.86^{+34.12}_{-20.26}$
550	$1.37^{+0.12}_{-0.08}$	$11.54^{+1.18}_{-0.73}$	$36.52^{+3.81}_{-2.34}$	$76.42^{+8.01}_{-4.92}$	$130.62^{+13.71}_{-8.42}$	$198.89^{+20.89}_{-12.82}$
600	$0.74^{+0.07}_{-0.05}$	$6.54^{+0.70}_{-0.45}$	$21.33^{+2.33}_{-1.48}$	$45.44^{+4.99}_{-3.17}$	$78.52^{+8.63}_{-5.48}$	$120.39^{+13.24}_{-8.40}$
650	$0.43^{+0.04}_{-0.03}$	$3.90^{+0.44}_{-0.29}$	$12.97^{+1.48}_{-0.97}$	$27.99^{+3.21}_{-2.09}$	$48.76^{+5.60}_{-3.65}$	$75.16^{+8.64}_{-5.63}$
700	$0.26^{+0.03}_{-0.02}$	$2.41^{+0.28}_{-0.19}$	$8.13^{+0.97}_{-0.64}$	$17.73^{+2.12}_{-1.41}$	$31.08^{+3.73}_{-2.47}$	$48.12^{+5.77}_{-3.82}$
750	$0.16^{+0.02}_{-0.01}$	$1.53^{+0.19}_{-0.13}$	$5.23^{+0.65}_{-0.44}$	$11.50^{+1.43}_{-0.96}$	$20.26^{+2.53}_{-1.70}$	$31.47^{+3.93}_{-2.63}$
800	$0.10^{+0.01}_{-0.01}$	$0.99^{+0.13}_{-0.09}$	$3.44^{+0.44}_{-0.30}$	$7.60^{+0.99}_{-0.67}$	$13.46^{+1.75}_{-1.19}$	$20.97^{+2.73}_{-1.86}$

**Table 6.1:** Cross sections times branching fractions,  $\sigma(pp \rightarrow \phi) \times \mathcal{B}(\phi \rightarrow \tau\tau)$ , are presented for various values in  $m_A \times \tan \beta$ . The cross sections are combined for the b-associated production channel and for the production via gluon-gluon fusion for the pseudoscalar MSSM Higgs boson  $A$  and the scalar MSSM Higgs boson  $H$ . The values are calculated within the  $m_h^{\text{max}}$  benchmark scenario at a center-of-mass energy of  $\sqrt{s} = 7$  TeV and have been provided by the *LHC Higgs Cross Section Working Group* [64, 65].

tau leptons in the final state as well as processes containing one or more physical objects (usually QCD induced jets, electrons, muons) which are misidentified as tau leptons (*fake taus*).

One can differentiate between two main types of background processes: irreducible and reducible background processes with respect to the given signal signature. Irreducible processes are SM processes which contain at least two real tau leptons and which cannot be separated with the considered event selection against the signal. Irreducible processes are Drell-Yan processes, in which a virtual photon or a  $Z$  gauge boson decays into a di-tau lepton pair, shown in Figure 6.4.

**Drell-Yan production with di-tau lepton decay:** Contributions from Drell-Yan processes in combination with the decay into two tau leptons,  $Z/\gamma^* \rightarrow \tau^+\tau^-$ , are estimated using simulated MC samples, generated using the ALPGEN [192] MC event generator interfaced with HERWIG+JIMMY [190, 191] (version 6.510 + 4.31) to model the parton shower, hadronisation and the underlying event. The simulations are performed using the CTEQ6L1 PDF and include up to five jets in the leading order matrix element. The corresponding cross sections are scaled to NNLO accuracy with an estimated systematic uncertainty at the order of 5 % [240, 241]. A small fraction of Drell-Yan events is selected by a fake tau lepton, when one of the real tau leptons remains outside the detector acceptance and a QCD jets is instead misidentified as a tau lepton candidate. These events are treated similar to the reducible  $W \rightarrow \tau\nu$  background. The total modeling of the Drell-Yan background is validated using an appropriated control region, described in Section 6.5.

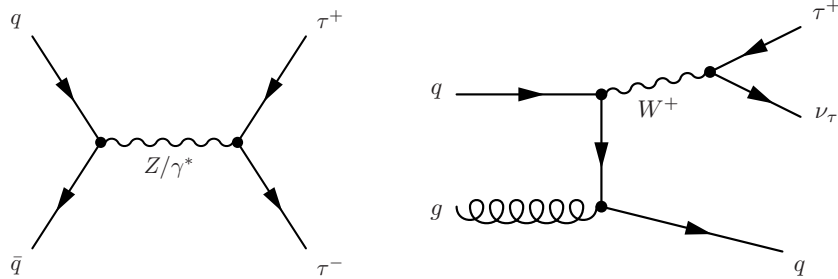


**Figure 6.4:** Exemplary leading order Feynman diagrams for the  $Z/\gamma^* \rightarrow \tau^+\tau^-$  (left) and  $W \rightarrow \tau\nu + \text{jets}$  (right) production at a hadron collider.

Reducible background processes are processes with either at least one fake tau lepton or two real tau leptons, but a topology which is significantly different from the signal topology. The two main contributions to the reducible background are either the  $W$  boson production, with a decay into a real tau lepton in addition with a jet, or QCD multi-jet events. Both processes only survive the event selection if at least one QCD jet is misidentified as a hadronically decaying tau lepton. The experimental challenge for an estimation of these processes is a bad modeling of the misidentification rate of QCD jets in the simulated samples. Data driven estimation techniques are therefore utilized to take the mis-modeling into account.

**$W$  boson production with decay into a tau lepton,  $W \rightarrow \tau\nu + \text{jets}$ :** This background process is characterized by one real tau lepton, a moderate amount of missing energy due to the neutrino of the  $W$  decay and at least one additional QCD induced jet, which is misidentified as a tau lepton. An exemplary Feynman graph can be found in Figure 6.4. The contribution is estimated

using a combined technique of simulated samples and data driven methods. Production and decay of the  $W$  boson is simulated using MC event generators. The setup is similar to the simulation of  $Z/\gamma^* \rightarrow \tau^+\tau^-$ : the leading order matrix event calculation (with up to five additional jets) has been performed using ALPGEN interfaced with HERWIG+JIMMY. The cross section is scaled to NNLO, with a considered systematic uncertainty of 5% [240, 241]. For fake tau candidates, no tau identification is applied and instead a misidentification efficiency (estimated from measured  $W \rightarrow \mu\nu$  events) is considered as additional event weight.

**QCD multi-jet production:** The term *multi-jet* involves all pure QCD scattering processes (Figure 6.5) with at least two jets in the considered detector acceptance, which are both misidentified as tau leptons. The probability for two misidentified jets in the same proton-proton collision is relatively small<sup>5</sup> which is compensated by the relative high cross section for QCD scattering processes. A completely data driven approach is utilized for the multi-jet estimation by extracting the contribution from a designated control region.

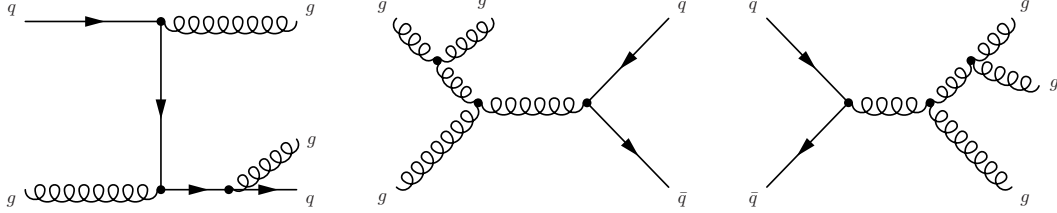


**Figure 6.5:** Exemplary Feynman diagrams for multi-jet production at a hadron collider including possible initial and final state radiations.

**Top quark production:** The production of top quarks, either in pairs of  $t\bar{t}$  or in single top production (Figure 6.6), can contribute to the final event yield due to either real tau leptons or high energy tau lepton fakes originating from the top quark decay products. The fraction of top quark events can be significantly reduced by deploying differences in the event topology compared to the signal and using the tau identification algorithm to filter out possible fake tau leptons.

The top pair production has been simulated at next-to-leading order accuracy using MC@NLO [242–244], interfaced with HERWIG+JIMMY (6.51+4.31), deploying the CTEQ6.6 [245] parton distribution function. In addition, the final cross section is normalized to an approximate next-to-next-to-leading accuracy predicted by the HATHOR software [246], with a total systematic uncertainty of  $\sim 10\%$ .

Contributions from single top quark processes, including the single top quark production in the t-channel, s-channel and in association with a  $W$  gauge boson, are estimated from simulations with ACERMC (3.8) [247] interfaced with PYTHIA 6 (6.425) using MRST LO\*\* [203] as PDF. The cross sections are normalized to approximate NNLO accuracy [248–250] and a total systematic uncertainty<sup>6</sup> of  $\sim 13\%$  is assumed. Within the further context, all processes including top quark production are collectively referred to as “top” background.

<sup>5</sup>The exact probability value depends on several parameters like the considered identification level and the transverse momentum of the tau candidates, but it is usually of the order of  $10^{-4}$  to  $10^{-6}$ .

<sup>6</sup>Following the procedure utilized in the preceding neutral MSSM Higgs analysis at  $\sqrt{s} = 7\text{ TeV}$ , the systematic uncertainty includes comparison with MCFM [251, 252] and MC@NLO as well as top mass variations.

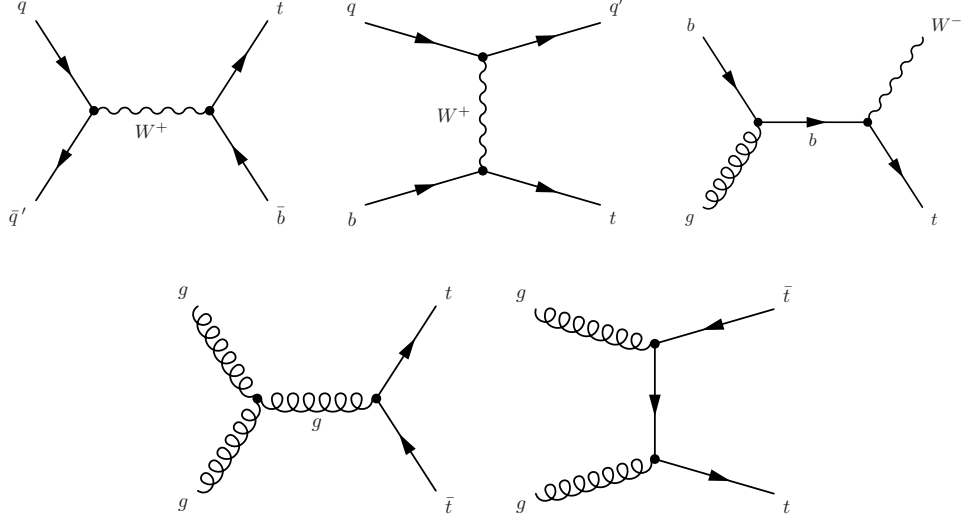


**Figure 6.6:** Exemplary Feynman diagrams for single top quark production (top) in the s-channel, t-channel and in association with a  $W$  boson (from left to right) and for the  $t\bar{t}$  production (bottom) at a hadron collider.

**Single  $W/Z$  production with decay into lighter leptons:** Vector bosons decaying into electrons or muons,  $Z \rightarrow ee/\mu\mu$  and  $W \rightarrow e\nu/\mu\nu$ , can contribute to the background, if the corresponding leptons are misidentified as 1-prong tau leptons. A possible contribution is estimated from simulations, using the same setup as for the  $Z \rightarrow \tau^+\tau^-$  and  $W \rightarrow \tau\nu$  samples. However, these processes can be greatly suppressed by rejecting events with at least one reconstructed electron or muon above a certain energy threshold and by applying dedicated lepton identification algorithms for the tau candidates.

**Single  $W/Z$  production with decay into quarks/jets:** Events with a vector boson decaying into quarks (which hadronise into jets) are heavily suppressed by the tau identification. Like the QCD scattering processes, at least two jets need to be misidentified as a tau lepton. In contrast to the QCD contribution, the smaller cross sections for the  $W/Z$  production cannot compensate for the small misidentification rate and thus leading to a vanishing contribution to the final event yield. A possible event contribution is estimated via simulated samples, using the same setup as for the  $Z \rightarrow \tau^+\tau^-$  and  $W \rightarrow \tau\nu$  samples.

**Gauge boson pair production:** Processes with two gauge bosons in the final state,  $WW$ ,  $WZ$  or  $ZZ$ , can mimic the signal signature either by including two real tau leptons or at least one fake tau lepton originating from a misidentified electron, muon or jet. The contribution to the final event yield however is small due to the relatively small cross sections and the possibility to reject this type of background events by topology-based selection criteria or via the tau identification algorithms in case of fake tau leptons. All gauge boson pair processes are estimated using simulated samples. The production via the  $q\bar{q}' \rightarrow VV$  is modeled at next-to-leading order accuracy using MC@NLO, while the production via gluon-gluon fusion,  $gg \rightarrow WW/ZZ$  is modelled at leading order using the  $gg2WW$  [253] and  $gg2ZZ$  [254] packages, respectively. For all samples, the CT10 is used as PDF and HERWIG+JIMMY to model the hadronisation process and the underlying event. Studies for systematic uncertainties regarding renormaliza-

tion and factorization scales can be found in Ref. [255]. In accord with the recommendations used in the preceding MSSM analysis, the following systematic uncertainties are assumed for the cross sections:  $\Delta\sigma = 4.9\%$  for  $q\bar{q}' \rightarrow WW$ ,  $7\%$  for  $q\bar{q}' \rightarrow WZ, ZZ$  and  $50\%$  for the gluon-gluon fusion processes. The large uncertainty for  $gg \rightarrow VV$  processes does not affect the analysis significantly, because their overall contribution to the final event yield is almost vanishing.

The contribution from single gauge boson production with decay in either electron, muon or quark and the gauge boson pair production processes are combined and referred to as *electroweak background* (EW Bkg.), since the individual contributions from each of the processes are very small.

For all simulated samples, except for the Sherpa samples used in the b-associated production, the decay of the tau leptons is performed using the TAUOLA [256] software package, while the correction for QED radiations are calculated using PHOTOS [257]. For the Sherpa samples, no external package is used and the tau decays as well as the radiative corrections are performed with the build-in functionalities. A full simulation of the ATLAS detector is performed on top of the event generation, for each utilized MC sample, using the GEANT4 [40] software package. Afterwards, the full reconstruction chain is applied to the samples in order to extract the physical objects (e.g. tau candidates, electrons, muons, ...) from the simulated detector response. The software setup is the same as the one used for the recorded data.

The complete tables of the logical dataset names can be found in Section A.4.5.

### 6.1.3 Data Sample

For this analysis, data from proton-proton collisions at the center-of-mass energy  $\sqrt{s} = 7\text{ TeV}$  is used recorded with the ATLAS detector at the LHC in the year 2011, divided into twelve Periods *A – M* (excluding period *C*). In total, an integrated luminosity of  $5.5\text{ pb}^{-1}$  was recorded of which  $4.5\text{ pb}^{-1}$  are used for this search. A peak luminosity of  $3.5 \times 10^{33}\text{ cm}^{-2}\text{ s}^{-1}$  was reached during the run, with a maximum of  $\sim 20$  pile-up interactions per bunch crossing. More details on the LHC run conditions during the year 2011 can be found in Section 3.3.

### 6.1.4 Object Selection

The object selection includes all selection criteria concerning reconstructed objects which are usually closely related to physical phenomena. For this study, the central objects are the reconstructed tau lepton candidates and their identification in order to reduce the background contribution. Electrons and muons are reconstructed to veto against background events containing one of the lighter leptons. Contributions from neutrinos, produced during the tau lepton decays, are reconstructed via the missing transverse momentum.

**Tau lepton selection:** The baseline for tau candidates are jets reconstructed from energy deposits in the calorimeter using the anti- $k_t$  [132] cluster algorithm with a distance parameter of  $R = 0.4$ . Tau candidates are required to provide a minimal transverse momentum of  $p_T^\tau > 50\text{ GeV}$  and to be located with the acceptance of the ID by requiring  $|\eta^\tau| < 2.47$ . The reconstructed

charge of a tau candidate should be  $|q^\tau| = 1e$  and one or three tracks above  $p_T^{\text{trk}} > 1 \text{ GeV}$  should be located within the inner core of tau jet cone. Tau candidates located in the crack region,  $1.37 < |\eta^\tau| < 1.52$ , of the calorimeter system are rejected. In April 30, a hardware failure caused the loss of six front-ends boards (FEBs) of the readout electronic responsible for the electromagnetic liquid argon calorimeter, which results in the lower response within the affected region in  $\eta \times \phi$  for the periods  $E - H$  (*LAr hole*). A partial recovery of four FEBs was performed during the technical stop in July 2011, which affects the remaining periods  $I - M$ . To ensure a proper tau reconstruction, candidates which are located within the affected area of

$$-0.1 < \eta^\tau < 1.55 \quad \text{and} \quad -0.9 < \phi^\tau < -0.5, \quad (6.1)$$

are rejected. All selection criteria requiring the  $\eta$  coordinate of the tau candidate are tested with respect to the pseudorapidity value of the track inside the tau core cone with the largest transverse momentum (leading track),  $\eta^{\text{lead-trk}}$ . To reject tau fakes originating from electrons, tau candidates are required to pass the *loose* working point for the cut based discrimination algorithm against electrons (see Section 4.6.3).

A BDT based tau identification against QCD is applied for the *loose* or *medium* working point, depending on the considered analysis channel.

**Jet selection:** Jets, reconstructed using the anti- $k_t$  jet clustering algorithm with a distance parameter of 0.4, are required to provide a minimal transverse momentum of  $p_T^{\text{jet}} > 50 \text{ GeV}$  and a pseudorapidity value of  $|\eta^{\text{jet}}| < 4.5$ . To suppress jets originating from pile-up vertices, only jets with a jet vertex fraction (see Section 4.5.3) above 50 % are selected. In addition a jet cleaning is performed by removing jets based on the selection criteria described in Section 4.5.4.

**Electron selection:** Electron candidates are selected by requiring a transverse momentum of at least 15 GeV. The electrons should be within  $|\eta^{\text{el}}| < 2.47$ , excluding the crack region in the calorimeter system at  $1.37 < |\eta^{\text{el}}| < 1.52$ . A possible candidate should pass the *loose* identification requirement (see Section 4.3.2) to be considered as an electron as well as certain quality requirements<sup>7</sup> provided by the ATLAS collaboration.

**Muon selection** Muon candidates are combined muons, reconstructed using the *staco* algorithm and passing the *loose* working point. They are required to have a transverse momentum of  $p_T^\mu > 10 \text{ GeV}$  and a pseudorapidity value of  $|\eta^\mu| < 2.5$ . For the associated ID track, the quality requirements presented in Section 4.4 are applied.

**Primary vertex selection** At least four tracks above a transverse momentum threshold of 500 MeV need to be associated with the primary vertex. The vertex of hard scattering is selected as the vertex with the highest  $\sum p_T^2$  of the associated tracks found in the event.

---

<sup>7</sup>For reference: a quality bit mask selection of 1446 is applied for each electron candidate.



### 6.1.5 Event Selection

For this study, the selection will predominantly follow the procedure used for the MSSM Higgs boson search in 2012 including modification necessary for the study of the 2011 data sample. Two different aspects are targeted with the event selection: one is a form of *event cleaning*, which ensures the only data recorded under well understood conditions is used, and secondly the selection is optimized to enhance the fraction of potential signal event compared to the expected background contributions.

The complete selection is separated into two steps. First a *baseline selection* is performed, which includes predominantly the cleaning requirements for the data events and the basic object selection steps. On top the baseline selection, the final event selection is performed which consists of two orthogonal categories defined by the utilized trigger requirement: a category for events triggered by a di-tau signature, *di-tau trigger* (DTT), and a category for events triggered by a single tau signature, *single tau trigger* (STT).

**Baseline selection:** Every proton-proton collision event recorded with the ATLAS detector is required to pass several quality criteria, to ensure the measurement was performed under stable beam constitution with all detector systems fully operational<sup>8</sup>, collectively termed *event cleaning*. On top, an extra selection is performed to reject event with possible errors or noise bursts in the calorimeter system.

At least one primary vertex should be reconstructed within each proton-proton collision event, following the vertex selection criteria discussed in Section 6.1.4.

Tau, electron and muon candidates as well as jets are selected following the object selection criteria described in Section 6.1.4. At least two<sup>9</sup> tau candidates need pass the selection, with no tau identification applied at this point. The tau candidate with the highest and second highest transverse momentum will be referred to as *leading* and *sub-leading* tau, respectively, indicated by the superscripts *lead* and *sub*. Events with at least one electron or muon candidate, passing the object selection, are rejected (*electron* and *muon veto*). Finally an *overlap removal* between reconstructed jets and tau candidates is performed, removing jets overlapping within a distance<sup>10</sup> of  $\Delta R < 0.2$  in  $\eta \times \phi$  with one of the tau candidates in order to avoid a possible double counting of objects.

The event yield summary for the baseline selection is presented in Table 6.2. For the baseline selection, no QCD multi-jet estimation is performed and only simulation based background yields are stated.

<sup>8</sup>The selection of data events has been provided by *Data Quality Group* of the ATLAS collaboration in form a *good run list*. For reference, the following good run list is used during the study:

`data11_7TeV.periodAllYear_DetStatus-v36-pro10-02_CoolRunQuery-00-04-08_All_Good.xml`.

<sup>9</sup>Within the majority of events only two tau candidates are found passing the relative high  $p_T$  threshold of 50 GeV. The fraction of events with more than two candidates is found to be around 3.8% for the STT category and below 1% for the DTT category.

<sup>10</sup>The distance is measured between the reconstructed jet and tau axis.

	$Z/\gamma^* \rightarrow \tau\tau$	$W \rightarrow \tau\nu$	EW Bkg.	Top
Event cleaning	$31\,240 \pm 110$	$71\,650 \pm 340$	$87\,610 \pm 270$	$231\,410 \pm 210$
Jet cleaning	$30\,850 \pm 110$	$71\,240 \pm 340$	$87\,420 \pm 270$	$231\,000 \pm 210$
LAr hole	$30\,330 \pm 110$	$70\,020 \pm 330$	$85\,360 \pm 270$	$223\,260 \pm 200$
$N_{\text{vtx}} > 0$	$30\,330 \pm 110$	$70\,020 \pm 330$	$85\,360 \pm 270$	$223\,260 \pm 200$
Muon veto	$29\,700 \pm 100$	$69\,380 \pm 330$	$83\,630 \pm 270$	$166\,890 \pm 190$
Electron veto	$29\,220 \pm 100$	$68\,900 \pm 330$	$80\,420 \pm 260$	$120\,360 \pm 180$
$N_\tau > 1$	$8450 \pm 50$	$23\,550 \pm 180$	$12\,620 \pm 100$	$13\,350 \pm 60$

**Table 6.2:** Expected number of event for non multi-jet background processes in the baseline selection are presented after each selection requirement. A comparison with the observed number of events is not performed, since no dedicated trigger requirement is applied during the baseline selection. The stated uncertainty values for each individual background process correspond to the respective statistical uncertainty.

**Di-tau trigger category:** The DTT category is defined using events which are triggered based on a di-tau signature, searching of tau candidates with  $E_T > 29$  GeV and 20 GeV. During the run, the corresponding L1 threshold for the trigger were raised to account for the increasing luminosity (see Section 4.8.4). A summary about the utilized trigger tags for a given run interval can be found in Table 6.3. To ensure that the DTT category is orthogonal to the STT category, the transverse momentum of the leading tau candidate is required to below 150 GeV. The leading and sub-leading tau candidates are required to match the tau objects used on trigger level within a distance of  $\Delta R < 0.2$  in  $\eta \times \phi$  to ensure that the trigger was fired by the same objects which are supposed to be two main tau leptons. A tau identification requirement is applied for both tau candidates using the BDT based identification algorithm at the *medium* working point. Since the expected signal is electrical neutral, both tau candidates are required to have opposite sign in the electric charge, which is implemented by forcing the charge product,  $q_{\text{lead}} \times q_{\text{sub}}$ , to be equal -1. The azimuthal separation between the leading and sub-leading tau candidate is required to be  $|\Delta\phi_{\text{lead,sub}}| > 2.7$ , to enhanced events containing a *back-to-back* topology. Finally the missing transverse energy,  $E_T^{\text{miss}}$ , should be above 10 GeV and the total sum of transverse energy in the event,  $\sum E_T$ , should be above 160 GeV.

run interval	trigger name
177986 - 187815	EF_tau29_medium1_tau20_medium1
188902 - 191933	EF_tau29T_medium1_tau20T_medium1
177986 - 184169	EF_tau125_medium
185353 - 191933	EF_tau125_medium1

**Table 6.3:** Trigger tags for the di-tau and single tau trigger used for a given run interval during the analysis of the 2011 data set. All trigger were un-prescaled during the 2011 data taking.

**Single tau trigger category:** The single tau trigger category is defined using events which are triggered by a single tau lepton signature above  $p_T^\tau > 125$  GeV (see Table 6.3 for the considered

trigger tags per run interval). The tau candidate on trigger level is matched with the leading tau candidate within a distance of 0.2 in  $\eta \times \phi$ . In order to ensure a constant trigger efficiency against the transverse momentum of the tau candidate and to ensure the orthogonality with respect to the DTT category, the transverse momentum of the leading tau need to be above 150 GeV. A BDT tau identification using the *loose* working point is applied for the leading and sub-leading tau candidate. Similar to the DTT category, an opposite sign requirement and a  $|\Delta\phi_{\text{lead,sub}}| > 2.7$  requirement is applied but for this category no selection criteria for  $E_{\text{T}}^{\text{miss}}$  or  $\sum E_{\text{T}}$  are applied.

A summary of the full event selection can be found in Table 6.4.

Baseline Selection	
event cleaning	
object selection	
$N_{\tau} \geq 2$	
$N_{\text{el}} + N_{\text{mu}} = 0$	
overlap removal with with $\Delta R < 0.2$	
DTT	STT
di-tau trigger	single tau trigger
trigger match with $\tau_{\text{lead}}$ and $\tau_{\text{sub}}$ ( $\Delta R < 0.2$ )	trigger match with $\tau_{\text{lead}}$ ( $\Delta R < 0.2$ )
$p_{\text{T}}^{\text{lead}} \leq 150 \text{ GeV}$	$p_{\text{T}}^{\text{sub}} > 150 \text{ GeV}$
$\tau_{\text{lead}}$ medium BDT identification	$\tau_{\text{lead}}$ loose BDT identification
$\tau_{\text{sub}}$ medium BDT identification	$\tau_{\text{sub}}$ loose BDT identification
$E_{\text{T}}^{\text{miss}} > 10 \text{ GeV}$	
$\sum E_{\text{T}} > 160 \text{ GeV}$	
$q_{\text{lead}} \times q_{\text{sub}} = -1$	
$ \Delta\phi_{\text{lead,sub}}  > 2.7$	

**Table 6.4:** Event selection summary for the neutral MSSM Higgs boson search.

### 6.1.6 Total Transverse Mass

The reconstructed mass of the di-tau systems provides a significant separation power to distinguish between a possible MSSM Higgs boson process and the SM background and is therefore used as the final discriminating observable. Due to (at least) two neutrinos in the decay channel, it is not possible to reconstruct the mass of the di-tau system completely but rather using an approximation based on the reconstructed visible parts of the hadronic tau decays and the missing transverse momentum vector.

For this study, the total transverse mass,

$$m_T^{\text{tot}} = \sqrt{m_T^2(\tau_{\text{lead}}, \tau_{\text{sub}}) + m_T^2(\tau_{\text{lead}}, E_T^{\text{miss}}) + m_T^2(\tau_{\text{sub}}, E_T^{\text{miss}})}, \quad (6.2)$$

of the di-tau system and the missing transverse momentum vector is utilized. The three components represent the transverse mass values between the leading and sub-leading tau candidate as well as the combinations with the missing transverse momentum vector:

$$m_T^2(\tau_{\text{lead}}, \tau_{\text{sub}}) = 2p_T^{\text{lead}} p_T^{\text{sub}} [1 - \cos \Delta\phi(\vec{p}_T^{\text{lead}}, \vec{p}_T^{\text{sub}})] \quad (6.3)$$

$$m_T^2(\tau_{\text{lead}}, E_T^{\text{miss}}) = 2p_T^{\text{lead}} E_T^{\text{miss}} [1 - \cos \Delta\phi(\vec{p}_T^{\text{lead}}, \vec{E}_T^{\text{miss}})] \quad (6.4)$$

$$m_T^2(\tau_{\text{sub}}, E_T^{\text{miss}}) = 2p_T^{\text{sub}} E_T^{\text{miss}} [1 - \cos \Delta\phi(\vec{p}_T^{\text{sub}}, \vec{E}_T^{\text{miss}})], \quad (6.5)$$

neglecting the mass values of the tau leptons. For a MSSM signal process, the total transverse mass observable is characterized by a reconstructed mean mass value below the true Higgs boson mass and a relatively large resolution. The effect is typically stronger for larger values of  $m_A$ . Distributions for three example mass points are presented in Figure 6.7.

The advantage of the total transverse mass distribution compared to other mass reconstruction

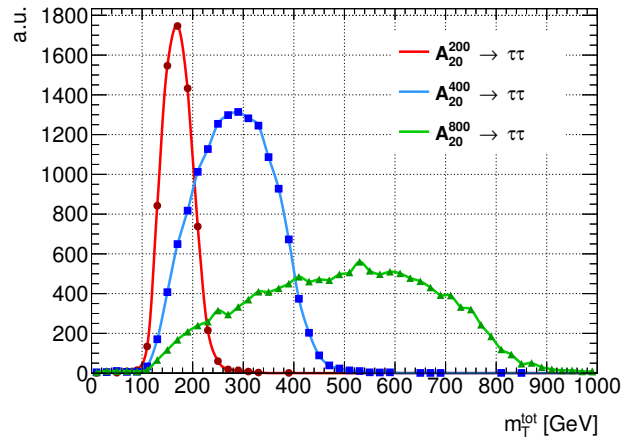


**Figure 6.7:** Exemplary total transverse mass distributions for three different MSSM Higgs boson mass values.

methods like the *missing mass calculator* [258] is the behavior of the observable on the SM background processes. In particular, the dominant QCD multi-jet processes are typically shifted towards lower  $m_T^{\text{tot}}$  values, resulting in an increased significance especially towards higher Higgs mass values.

## 6.2 Background Estimation

An overview about the considered background processes can be found in Section 6.1.2. Except for the QCD multi-jet background, all processes are estimated using simulated samples generated with the appropriated Monte Carlo event generators and passed through a full detector simulation.

Although the predictions of the simulation are in general very accurate, it is still necessary to correct for certain types of mis-modeling and deviation between the MC predictions and the measured data samples. All corrections are applied in form of an *event weight* to the MC samples, thus the expected number of simulated events passing the event selection,  $N^{\text{MC}}$ , is not just the number of pure MC events but instead the product of weights,  $w_{C_j}$ , for each correction,  $C_j$ :

$$N^{\text{MC}} = \sum_i \left( \prod_{j=1}^M w_{C_j}(i) \right) \quad \text{with } C_j \in \{C_1 \dots C_M\}, \quad (6.6)$$

where  $i \in [1, \dots, N]$  represents the index over the uncorrected MC events. Possible correction factors from the MC generators as well as scale factor for higher order corrections are applied in the same way.

Four main classes of corrections are considered: corrections of the pile-up spectrum, corrections on the trigger requirements, corrections for true tau lepton decays and corrections on the estimation of the fake tau lepton background.

Tau candidates originating from true tau lepton decays in the simulations are treated the same way as tau lepton candidates in data: identification via the BDT based algorithm and a corresponding electron veto. Differences between data and simulation are corrected using the corresponding weights. Unfortunately, this procedure cannot be used for tau leptons candidates which originate from QCD jets. The misidentification rate between data and simulation is significantly different and MC generator depended, due to the different modeling of the jet substructure during the simulation. The substructure is dominantly defined by the hadronisation process, which cannot be described using perturbation theory and is instead modeled using phenomenological approaches, implemented in different ways in the event generators.

Instead of applying the identification algorithm on fake tau candidates, data driven approaches are utilized for this analysis. For fake candidates in non QCD multi-jet events, a fake rate measured in a  $W \rightarrow \mu\nu$  control region is applied instead of the tau identification.

Pure QCD multi-jet background is estimated from data using side-band measurements. Different estimation techniques are utilized for the DTT and STT region, exploiting the individual trigger structure of each region. For the DTT region, the QCD multi-jet contribution is estimated using a side-band method with three control regions while contribution in the STT region is estimated based on a scaling of a single side-band control region using QCD scale factor derived from an auxiliary measurement.

### 6.2.1 Pile-up Reweighting

Differences between the pile-up distribution measured in data and simulated samples are to some extent expected. The conditions of the proton beams change during the data taking period, which results in a change of the pile-up spectrum, while the simulated samples<sup>11</sup> are produced under some assumption for the average interactions per bunch-crossing,  $\mu$ . A weight,  $w_{\text{pile-up}}$ , is applied to normalize the  $\mu$  distribution in the simulation to the measured spectrum. The final  $\mu$  spectra for the DTT and STT categories are presented in Figure 6.8, showing a reasonable agreement between the measurements and the predictions within the combined statistical and systematic uncertainties.

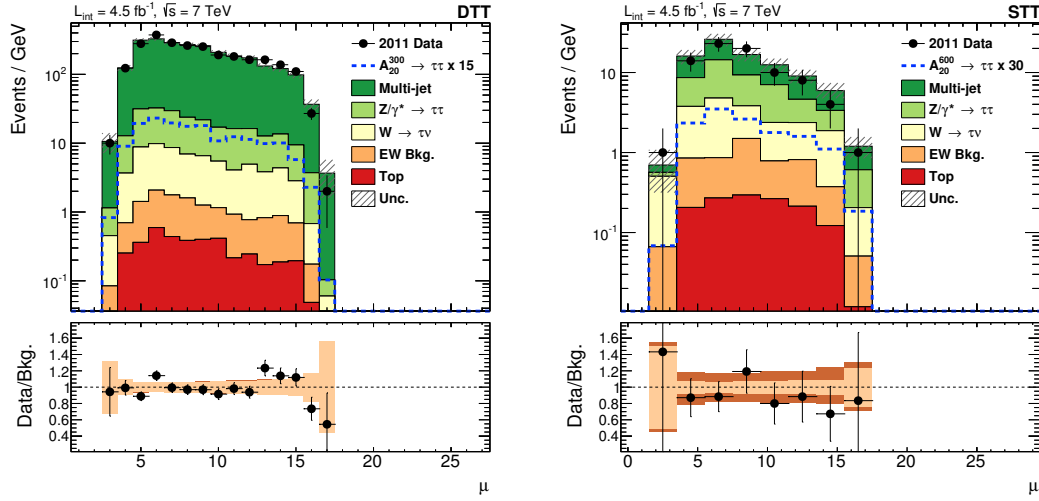


**Figure 6.8:** Average interactions per bunch-crossing for the DTT (left) and STT (right) category. The observed data points (black dots) are compared to the SM expectation. The contributions from the individual processes (colored areas) are added up (stacked) and the combined statistical and systematic uncertainty is illustrated by the hatched area. A possible signal contribution is shown in the blue line (unstacked). The bottom area displays the ratio between the measurements and the SM prediction in which the light band represents the statistical uncertainty and the dark band the combined statistical and systematic uncertainty on the background prediction.

### 6.2.2 Trigger Corrections

The trigger decisions for the data samples have been emulated in the simulated samples and correction factors,  $w_{\text{trig}}$ , are applied to account for differences between the trigger efficiency in data and the emulation. Details on the trigger scale factors are presented in Section 4.8.4. The corresponding systematic uncertainties on the scale factors are taken into account for the total uncertainty on the predicted yields. Trigger scale factors for the single tau trigger were not available for the analysis and no scale factor is applied. Crosschecks between the predicted yields in the STT category and the measured data have shown that the effect of the missing trigger scale factors vanish after the  $p_{\text{T}}^{\text{lead}}$  criteria of 150 GeV for the leading tau candidate. The trigger scale factors are only applied if the tau candidate signature which fired the trigger originate from

<sup>11</sup>More details about the pile-up simulation in ATLAS can be for example found in Ref. [46].

a real tau lepton. Events triggered by a fake tau lepton are scaled using the misidentification rate, described in Section 6.2.4.

### 6.2.3 Tau Lepton Corrections

Scale factors are applied for the tau identification,  $w_{\text{tau-ID}}$ , against QCD jets and for the electron veto,  $w_{\text{el.-veto}}$ . In both cases, the weights parametrize the differences of the identification algorithms between the simulations and the measurements extracted from tag and probe measurements. The scale factor for the tau identification are set to unity, following the recommendation of the ATLAS collaboration at the time<sup>12</sup>. For the electron veto on tau candidates, the scale factors are parametrized in  $\eta$  and range from 0.70(5) to 1.24(5).

An additional correction for the *tau energy scale* is applied, discussed in Section 4.6.2.

### 6.2.4 Tau Fakes in Non QCD Multi-jet Background

For tau candidates originating from quarks or gluons in simulated events, no tau identification is applied, because the performance of the tau identification algorithm differs significantly between the simulation and real data. The primary cause of this effect is the imperfect modeling of hadronisation process leading to differences in the substructure of the underlying jet. Since the tau identification is based on the substructure observables, the performance of the identification algorithm is sensitive to the modeling details.

This problem affects the background estimation for all processes include at least one fake tau candidate: dominantly  $W \rightarrow \tau\nu$  but also single top,  $t\bar{t}$  and double vector boson processes are effected. To a lesser extent, events containing two real tau leptons are affected too, like  $Z \rightarrow \tau\tau$ , if at least one of the two real tau leptons is located outside the considered cinematic region and instead a accompanying QCD-induced jet is reconstructed as a possible tau candidate.

To account for these effects, a mixture of data driven and simulation based methods is used to estimate the background contribution. The overall event topology is extracted from the simulations but instead of applying the tau identification algorithm on a fake tau candidate, the event is weighted by the expected rate of which the corresponding fake tau candidate will pass the identification algorithm,

$$w_{\text{jet} \rightarrow \tau} = f_{\text{jet} \rightarrow \tau}, \quad (6.7)$$

where  $f_{\text{jet} \rightarrow \tau}$  is referred to as *misidentification rate* or *misidentification efficiency*. The misidentification rate is estimated from a  $W \rightarrow \mu\nu + \text{jets}$  control region measured in data, where the muon is used to identify the process and the accompanying jet to probe the fake rate. Details on the control region, the estimation of the misidentification rate as well as the results are presented in Section 6.3. Fake tau candidates are defined as reconstructed tau candidates with no true tau lepton on particle level within a radius of  $\Delta R = 0.2$  around the reconstructed tau axis. If both

<sup>12</sup>Details can be found in Section 4.6.5.

tau candidates in the event are fakes, the product of both fake rates is applied as event weight,

$$w_{\text{jet} \rightarrow \tau} = f_{\text{jet} \rightarrow \tau}(\tau_{\text{lead}}) \times f_{\text{jet} \rightarrow \tau}(\tau_{\text{sub}}). \quad (6.8)$$

Applying the misidentification rate directly instead of correcting the MC simulations after the tau identification also helps to diminish statistical fluctuations of the background predictions. The fake rates are usually at the order of a few percent and an application of the tau identification would lead to a drastic reduction of the MC events passing the event selection, thus reducing the amount of statistic. Although it is possible to avoid statistical fluctuation by generating more MC events, the number of simulated events is limited in practice by the available CPU time and storage space. By reweighting, instead of rejecting the simulated events, a larger part of the considered phase-space can be represented and thus reducing possible dependency of the background estimation on fluctuation induced by low statistics.

### 6.2.5 QCD Multi-jet Estimation in the Di-Tau Trigger Region

The QCD multi-jet estimation within the DTT region is performed using a side-band method, splitting the phase space into four orthogonal regions. Starting with the selection of the DTT region, which is described in Section 6.1.5 and within the further context referred to as region *A*, the side-bands are defined by inverting certain selection criteria<sup>13</sup>:

**Region B** inversion of the charge-product  $q_{\text{lead}} \times q_{\text{sub}}$  between the leading and sub-leading tau candidate, changing the selection from a opposite sign (OS) region into a same sign (SS) region,

**Region C** inversion of the  $E_{\text{T}}^{\text{miss}}$  requirement by forcing  $E_{\text{T}}^{\text{miss}} < 10 \text{ GeV}$  but still requiring the OS criteria between both tau candidates,

**Region D** inversion of the charge-product and the  $E_{\text{T}}^{\text{miss}}$  requirement.

An illustration of the different side-bands can be found in Figure 6.9. The expected number of QCD multi-jet events within a given bin  $i$ ,  $\langle N_{\text{QCD},i}^A \rangle$ , in the signal region *A* can be estimated with

$$\langle N_{\text{QCD},i}^A \rangle = (N_{\text{data},i}^B - \langle N_{\text{bkg},i}^B \rangle) \times R_{\text{OS/SS}}, \quad (6.9)$$

where  $N_{\text{data},i}^B$  represents the observed number of event in the region *B* and  $\langle N_{\text{bkg},i}^B \rangle$  representing the expected non multi-jet background contribution. The scale factor  $R_{\text{OS/SS}}$  numbers the normalization difference between the OS and SS region and is estimated from the low  $E_{\text{T}}^{\text{miss}}$  regions *C* and *D*:

$$R_{\text{OS/SS}} = \frac{\sum_i (N_{\text{data},i}^C - \langle N_{\text{bkg},i}^C \rangle)}{\sum_i (N_{\text{data},i}^D - \langle N_{\text{bkg},i}^D \rangle)}. \quad (6.10)$$

The expected number of background events within a given region  $X \in \{B, C, D\}$  is defined as the sum of all non multi-jet processes  $j$  estimated from simulations,

$$\langle N_{\text{bkg},i}^X \rangle = \sum_j^{\text{process}} \langle N_{j,i}^X \rangle. \quad (6.11)$$

---

<sup>13</sup>Within the literature the method is sometimes referred to as *ABCD* method.



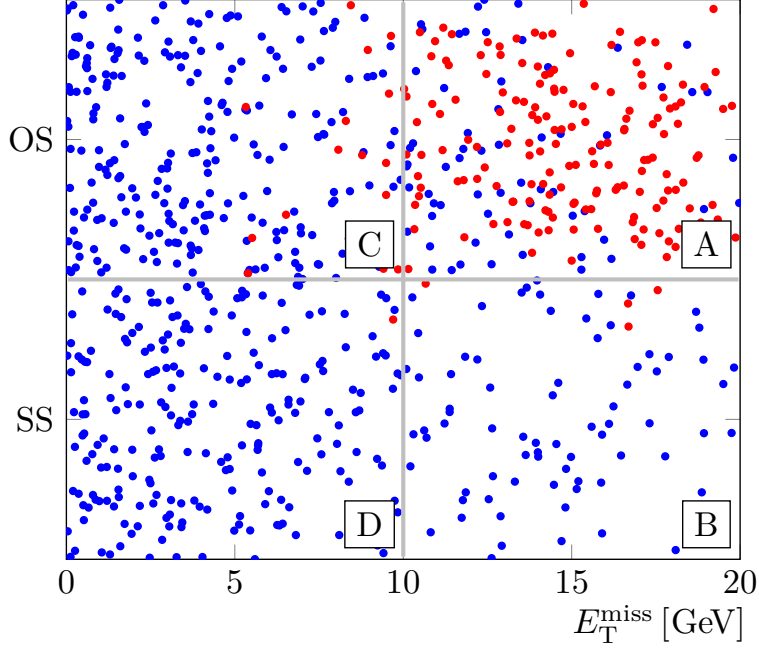


**Figure 6.9:** Illustration of the side-band selection used for the QCD multi-jet estimation in the DTT region. The red and blue points represent a possible MSSM Higgs signal and the multi-jet background contribution, respectively.

For each simulated process, the corresponding correction weights are applied, including the appropriate misidentification rates for the OS or SS region.

Since the shape of the QCD contribution is extracted from the SS region (region *B*) and scaled to the OS region, the method is only valid if the corresponding distributions show no significant difference in shape between OS and SS. In order to validate this requirement, the shapes of the considered distributions within region *C* and *D* are compared against each other, both normalized to one. The results for a selected set of distributions are shown in Figure 6.10 and within the statistical uncertainty no significant deviation between the OS and SS region is found.

The performance of the estimation method is tested using a *validation region* (VR), which is defined similar to the DTT signal region with the exception that both tau candidates are required to fail to *loose* tau identification level instead of passing the *medium* one. Both fail tau identification requirements ensure the absence of a possible MSSM signal contribution within the validation region and enrich the fraction of QCD multi-jet background in the data. The side-bands *B*, *C* and *D* are again defined by a splitting in OS/SS and  $E_T^{\text{miss}} = 10$  GeV including the fail identification requirements.

The final event yields for all four region in the validation selection are presented in Table A.3, showing a reasonable agreement between the observed number of events and background estimation which is dominated by the multi-jet background. A full summary of the event yield for each selection requirement within the validation region *A* is presented in Table A.4.

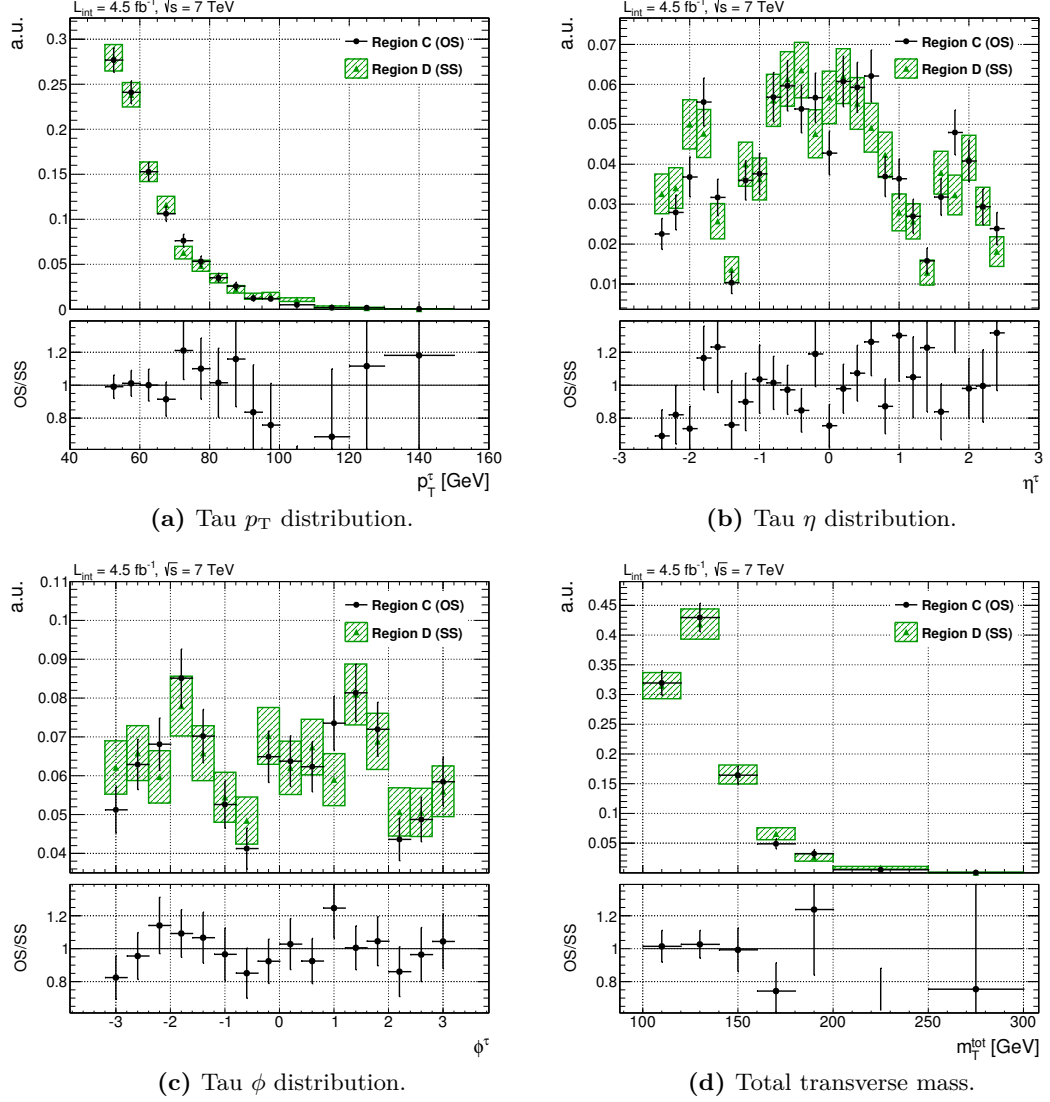


**Figure 6.10:** Observed number of events for various kinematic distributions of the tau candidates as well as the total transverse mass distribution are shown for region  $C$  (back dots) and region  $D$  (filled area) used in the QCD estimation method. The expected number of background events is subtracted and both distributions are normalized to one. The total transverse mass distribution is limited up to 300 GeV due to a lack of statistics in the low  $E_T^{\text{miss}}$  regions. The stated uncertainty bands correspond to the statistical uncertainties.

The results of the validation for a selected set of observables are presented in Figure 6.11 and Figure 6.12, showing an excellent agreement between the estimated multi-jet background and the observed number of events within the combined statistical and systematic uncertainties.

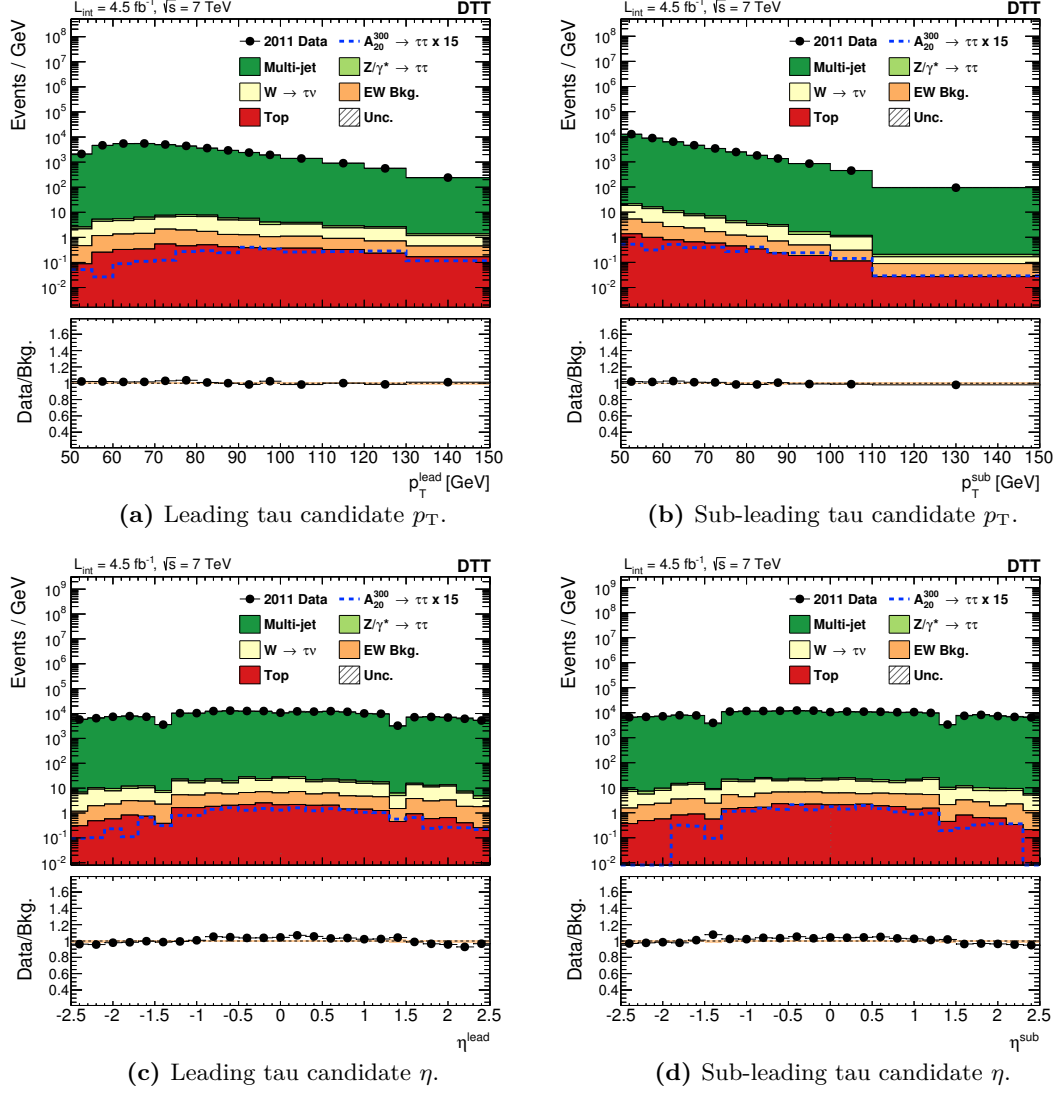


**Figure 6.11:** Kinematic distributions of the leading and sub-leading tau candidate within the DTT validation region. The observed data points (black dots) are compared to the SM expectation. The contributions from the individual processes (colored areas) are added up (stacked) and the combined statistical and systematic uncertainty is illustrated by the hatched area. A possible signal contribution is shown in the blue line (unstacked). The bottom area displays the ratio between the measurements and the SM prediction in which the light band represents the statistical uncertainty and the dark band the combined statistical and systematic uncertainty on the background prediction.

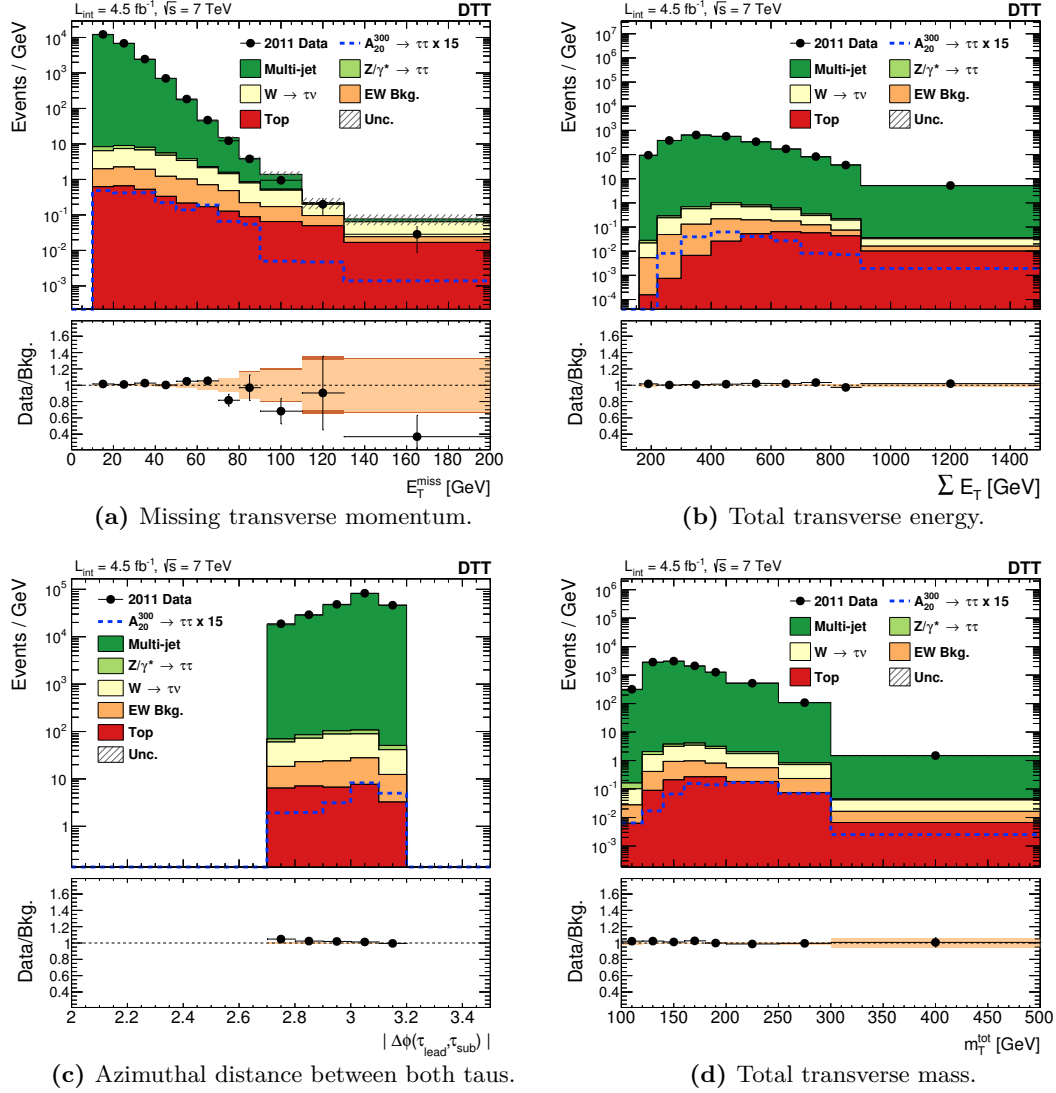


**Figure 6.12:** Distributions related to the di-tau system and the missing transverse momentum within the DTT validation region. The observed data points (black dots) are compared to the SM expectation. The contributions from the individual processes (colored areas) are added up (stacked) and the combined statistical and systematic uncertainty is illustrated by the hatched area. A possible signal contribution is shown in the blue line (unstacked). The bottom area displays the ratio between the measurements and the SM prediction in which the light band represents the statistical uncertainty and the dark band the combined statistical and systematic uncertainty on the background prediction.

### 6.2.6 QCD Multi-jet Estimation in the Single-Tau Trigger Region

The QCD multi-jet contribution within the STT region is, like the DTT region, estimated using a side-band control region but with the difference, that the sub-leading tau candidate is unbiased in terms of a tau identification on trigger level. This effect can be observed in BDT score distribution of the leading and sub-leading tau candidate, presented in Figure 6.13, showing a shift in the BDT score distribution of the leading tau toward larger values compared to the sub-leading tau, which is a consequence of tau identification criteria applied by the single tau trigger. The large difference between the observed number of events and the combined background prediction is due to the missing QCD multi-jet contribution which is not estimated at this stage.

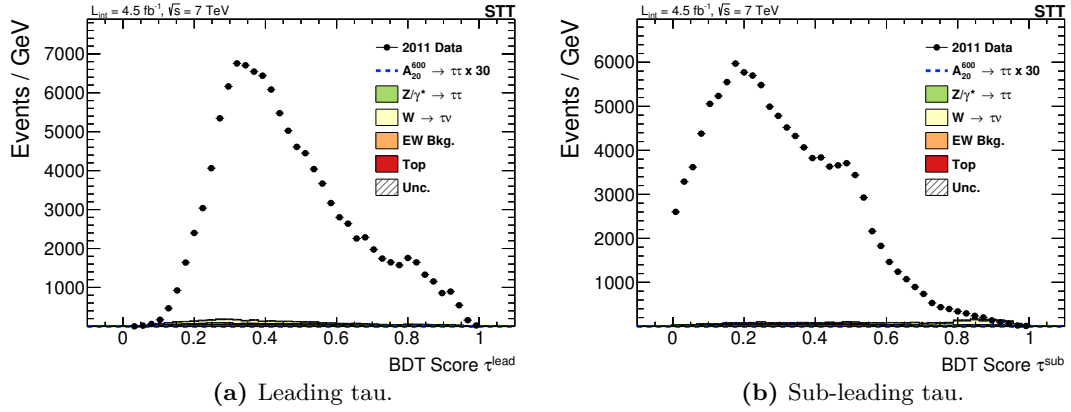


**Figure 6.13:** BDT scores distributions for the leading and sub-leading tau candidate are presented after the single tau trigger requirement and  $p_T^{\text{lead}} > 150$  GeV. The observed data points (black dots) are compared to the SM expectation. The contributions from the individual processes (colored areas) are added up (stacked) and the combined statistical and systematic uncertainty is illustrated by the hatched area. No QCD multi-jet estimation is performed at this point.

The side-band for the signal region *A* is now defined by inverting the identification requirement for the sub-leading tau only:

**Region B** sub-leading tau candidate is required to fail the loose tau identification level instead of passing it.

The shape and normalization of the QCD multi-jet contribution within region *A* is now extracted from the side-band via a *transfer factor*,

$$f_{\text{pass} \rightarrow \text{fail}}(p_T, N_{\text{trk}}, q_{\text{lead}} \times q_{\text{sub}}) = \frac{N^{\text{pass}}(p_T, N_{\text{trk}})}{N^{\text{fail}}(p_T, N_{\text{trk}})} \bigg|_{q_{\text{lead}} \times q_{\text{sub}}}, \quad (6.12)$$

where  $N^{\text{pass/fail}}$  represent the number of tau candidates which pass or fail a certain tau identification level, parametrized in the  $p_T$  of the tau candidates, the number of associated tracks (1-prong or 3-prong) and the charge product between the leading and sub-leading candidate. The transfer factors are determined within a di-jet control region and are discussed in detail in Section 6.4. Three different charge product combinations have been study during the transfer factor measurement: no charge product requirement (NoS), opposite charge sign (OS) and same charge sign (SS), between both candidates. Since a relative insensitivity of the transfer factor

on the charge product has been observed, the version without a charge product is used for the QCD estimation including the remaining differences between OS and SS as systematic uncertainty.

Subsequently, the expected number of multi-jet events in region  $A$  and bin  $i$  can be estimated with

$$\langle N_{\text{QCD},i}^A \rangle = \sum_j N_i^B(p_{\text{T},j}, N_{\text{trk},j}) \times f_{\text{pass} \rightarrow \text{fail}}(p_{\text{T},j}, N_{\text{trk},j}), \quad (6.13)$$

where  $N_i^B(p_{\text{T},j}, N_{\text{trk},j})$  represents the observed number of events in region  $B$  for a certain bin  $j$  in  $p_{\text{T}}$  and  $N_{\text{trk}}$ .

A validation of the estimation method is performed within the SS regions of  $A$  and  $B$  by inverting the charge product requirement to  $q_{\text{lead}} \times q_{\text{sub}} = 1$ . The final event yields within the validation region as well as a summary of the observed number of events and background predictions are provided in Table 6.5 and Table A.5, respectively.

	Region A	Region B
Multi-jet	39.0 $\pm$ 1.5	—
$Z/\gamma^* \rightarrow \tau\tau$	2.55 $\pm$ 0.25	10.9 $\pm$ 1.2
$W \rightarrow \tau\nu$	6.6 $\pm$ 1.3	31 $\pm$ 5
EW Bkg.	1.34 $\pm$ 0.30	14.0 $\pm$ 1.9
Top	0.39 $\pm$ 0.04	6.8 $\pm$ 0.5
Comb. background prediction	49.9 $\pm$ 2.0	63 $\pm$ 5
Observed number of events	47	3670

**Table 6.5:** The expected number of events of various SM processes and the estimated QCD multi-jet contribution within the STT signal validation region  $A$  are presented and compared to the observed number of events. The stated uncertainty for each process correspond to the respective statistical uncertainty. The disparity in the observed number of events in region  $B$  and the combined background prediction is due to the missing QCD contribution.

Within the validation region, a reasonable agreement between the observed number of events and the background predictions could be confirmed, proving the reliability of the multi-jet estimation method. A sufficient level of agreement within the statistical and systematic uncertainties has been also confirmed for various distributions, of which a selected set is presented in Figure 6.14 and Figure 6.15. The validity of the distributions is restricted due to the relative low number of event passing STT selection requirements.

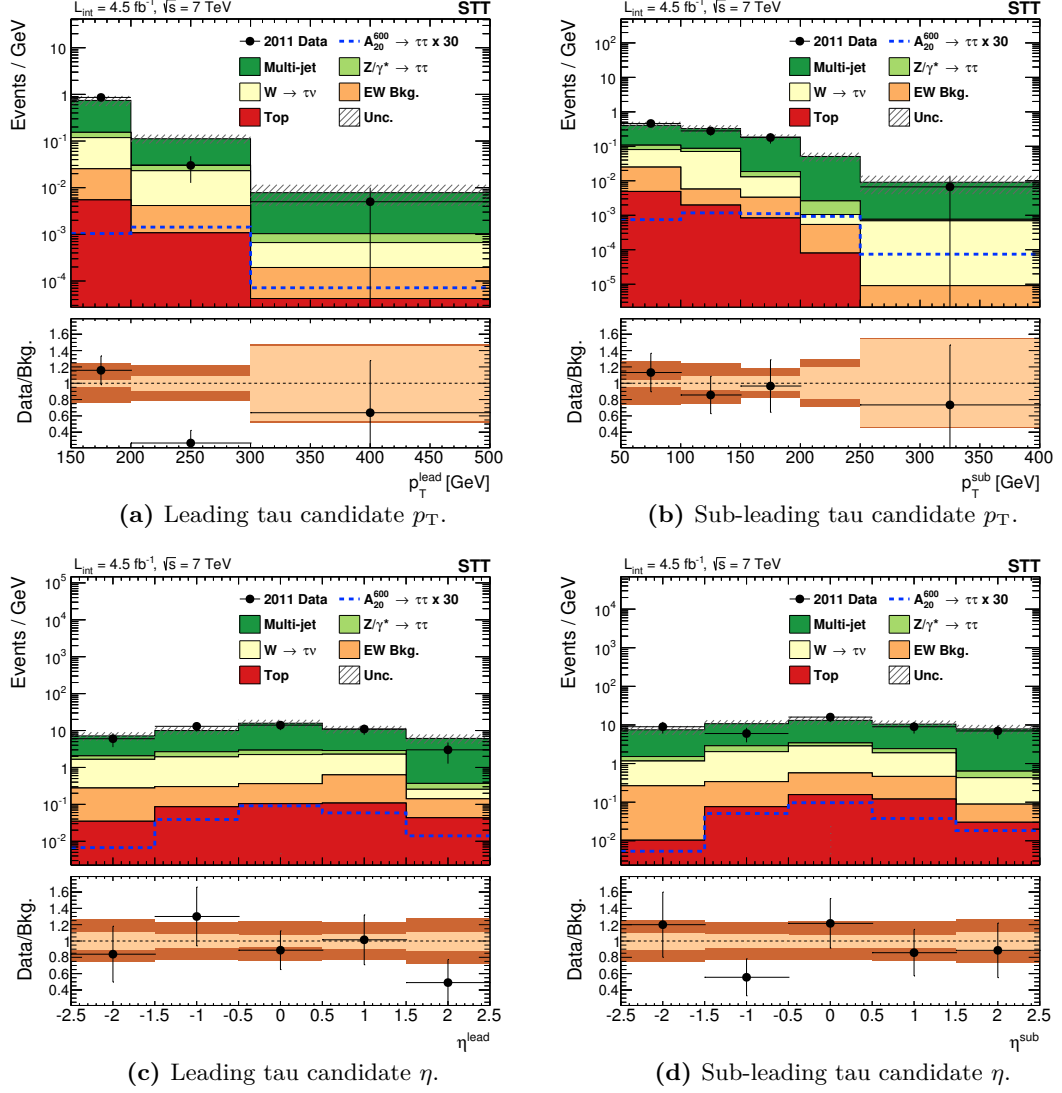


**Figure 6.14:** Kinematic distributions of the leading and sub-leading tau candidate within the STT validation region. The observed data points (black dots) are compared to the SM expectation. The contributions from the individual processes (colored areas) are added up (stacked) and the combined statistical and systematic uncertainty is illustrated by the hatched area. A possible signal contribution is shown in the blue line (unstacked). The bottom area displays the ratio between the measurements and the SM prediction in which the light band represents the statistical uncertainty and the dark band the combined statistical and systematic uncertainty on the background prediction.



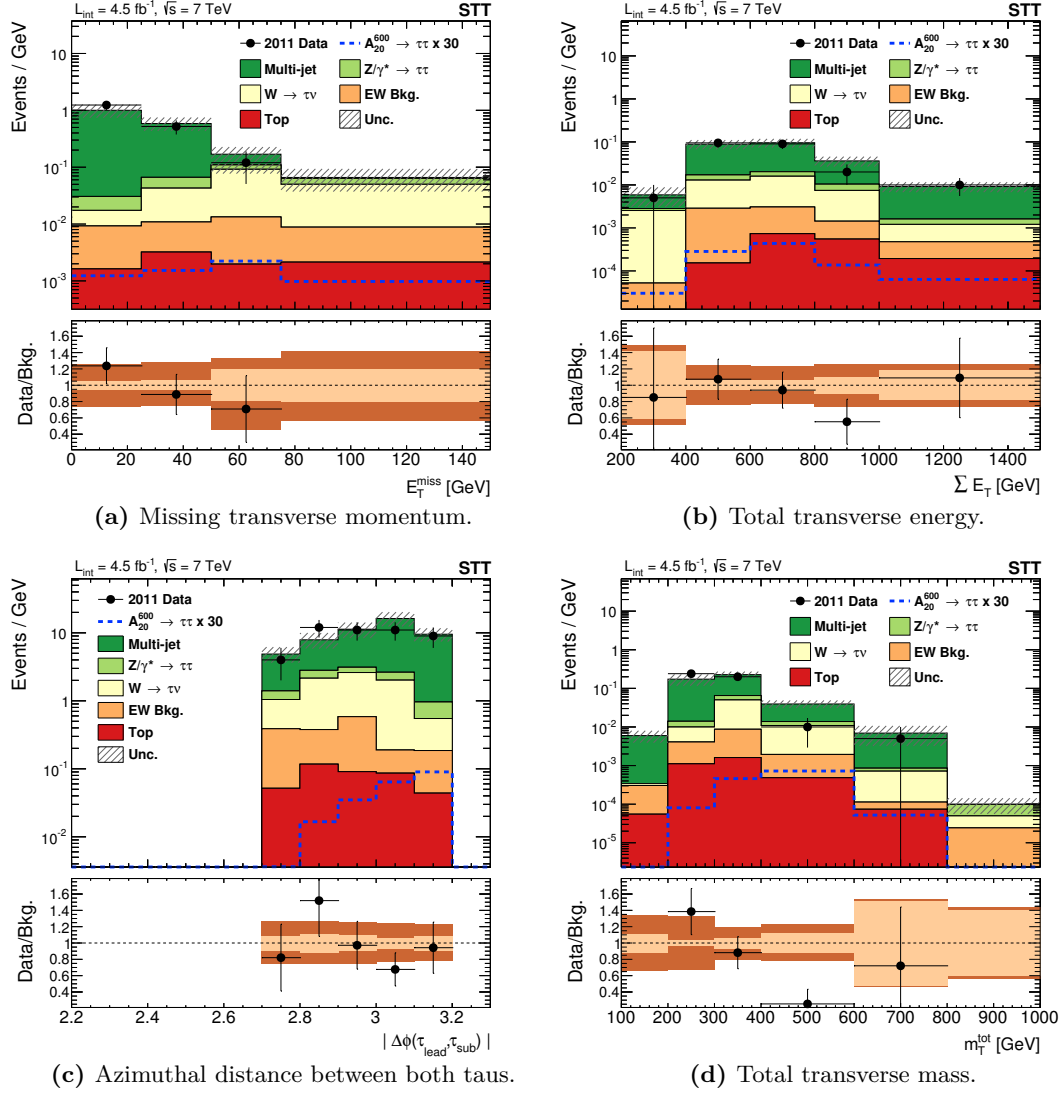


**Figure 6.15:** Distributions related to the di-tau system and the missing transverse momentum within the STT validation region. The observed data points (black dots) are compared to the SM expectation. The contributions from the individual processes (colored areas) are added up (stacked) and the combined statistical and systematic uncertainty is illustrated by the hatched area. A possible signal contribution is shown in the blue line (unstacked). The bottom area displays the ratio between the measurements and the SM prediction in which the light band represents the statistical uncertainty and the dark band the combined statistical and systematic uncertainty on the background prediction.

## 6.3 Measurement of the Tau Misidentification Efficiency

The probability to misclassify QCD-induced jets as a hadronically decaying tau lepton, referred to as *misidentification* or *fake rate*, has been measured in a  $W \rightarrow \mu\nu + \text{jets}$  control region, using proton-proton interactions at center-of-mass energy of  $\sqrt{s} = 7 \text{ TeV}$  recorded with the ATLAS detector in 2011 at the LHC. Using measurements of the fake rate from data allows to account for the differences between the sub-structure modeling of QCD-induced jets predicted by the simulation and the measurements, thus allowing an accurate estimation of background events including at least one fake tau from simulated proton-proton interactions.

The utilized data set for the control region corresponds to a total integrated luminosity of about  $4.5 \text{ fb}^{-1}$  and is selected orthogonal to the signal region of the MSSM Higgs boson search by requiring at least one reconstructed muon in the recorded proton-proton event. To quantify the differences in the misidentification efficiency, the results from the measurements are compared to predictions from simulations deploying the same MC event generator samples used for the MSSM Higgs search. The dominant  $W \rightarrow \mu\nu$  process has been generated using the ALPGEN event generator interfaced with HERWIG+JIMMY, with up to five additional jets on matrix element level. Details on the generation of the remaining processes can be found in Section 6.1.2.

### 6.3.1 Overview of the Misidentification Efficiency Measurement

The measurement of the fake rate is performed using a *tag-and-probe* method. Within this method one defines a *tag* object to identify the considered process and a *probe* object to test the tau identification. The probe objects in this case are the reconstructed muon and the neutrino (which is recognized in form of missing transverse energy in the proton-proton collision event) from the  $W$  decay. The muon in the control region represents the real hadronically decaying tau lepton in the  $W \rightarrow \tau\nu$  process, which is the dominant background containing tau fakes apart from pure QCD multi-jet processes, using the lepton universality of the  $W$  boson decay process. Consequently, the probe object is an accompanying QCD jet which pass the tau reconstruction and thus is a possible candidate to measure the misidentification efficiency of the tau identification algorithm.

The probe jet can be either a quark or gluon induced jet (see Figure 6.16). Due to the differences in the substructure of quark and gluon jets, the fake rate itself is sensitive to the relative fraction of quark and gluon jets in the control region.

#### Object Selection

For reconstructed tau candidates, electrons and jets the selection criteria of the MSSM Higgs boson search used, described in Section 6.1.4. For reconstructed muons, the selection criteria are stricter compared to the MSSM search to ensure a high purity selection of  $W \rightarrow \mu\nu$  events.

Combined muons, based on the *staco* reconstruction algorithm, are utilized passing the *tight* working point. The kinematic phase-space is defined by a minimal transverse momentum of  $p_{\text{T}}^{\mu} > 26 \text{ GeV}$  and a pseudorapidity rapidity of  $|\eta^{\mu}| < 2.4$ . All muon candidates are required to

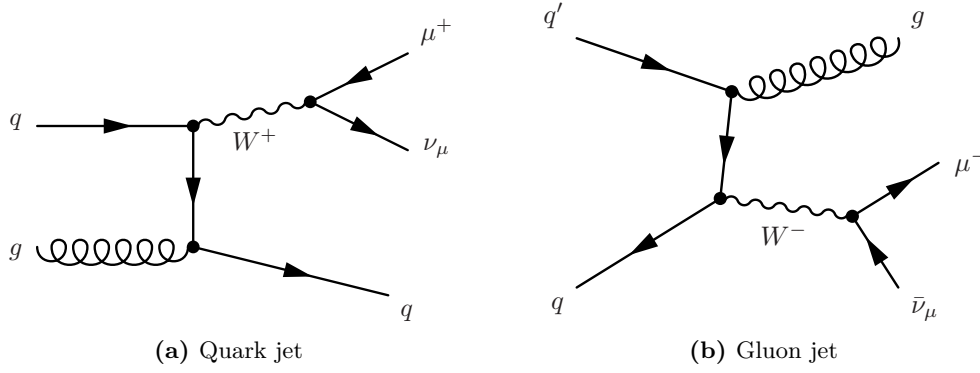


**Figure 6.16:** Exemplary leading order Feynman diagrams for the  $W \rightarrow \mu\nu + \text{jet}$  production with either an accompanying quark or gluon jet.

pass the additional quality criteria for the associated ID track, described in Section 4.4. To suppress muons originating from hadron decays, an isolation requirement is applied by comparing the activity within a certain cone around the muon trajectory with transverse momentum of the muon candidate. For this analysis, a calorimeter based isolation criteria has been deployed: the isolation of the muon is expressed as the sum of the energy deposits within a radius of  $\Delta R < 0.4$  around the muon axis relative to the transverse momentum of the muon,

$$\frac{\sum E_{\text{T}}^{\text{cone0.4}}}{p_{\text{T}}^{\mu}} = \frac{\sum_i^{N_{\text{cells}}(\Delta R < 0.4)} E_{\text{T},i}}{p_{\text{T}}^{\mu}}. \quad (6.14)$$

A correction based on the reconstructed number of primary interaction vertices is applied to the isolation observable in order to subtract the expected contribution from pile-up, provided by the ATLAS collaboration. Muons are defined as isolated if  $\frac{\sum E_{\text{T}}^{\text{cone0.4}}}{p_{\text{T}}^{\mu}} < 0.06$ , which removes the majority of the QCD multi-jet background.

### Event Selection

The event selection starts with the same general event quality criteria used for the MSSM baseline selection, described in Section 6.1.5. Hadronically decaying tau leptons, jets, muons and electrons are required to pass the selection criteria mention above, without the muon isolation criteria at this point. Events with at least on electron candidate are rejected (*electron veto*). The event should contain exactly one muon candidate passing the object selection, events with several muons are rejected (*di-muon veto*). After this point, an overlap removal is applied to avoid double counting of reconstructed object: jets and reconstructed taus are removed if they overlap with a reconstructed muon and jets are also removed if they overlap with a reconstructed tau candidate.

The events are triggered using un-prescaled, single muon trigger with a threshold of  $p_{\text{T}}^{\mu} > 18 \text{ GeV}$ . During the 2011 data taking period, the L1 threshold was increased to account for the increased instantaneous luminosity, resulting a trigger switch during the 2011 run. The trigger names and the corresponding run number and periods are summarized in Table 6.6. For both trigger, the reconstructed muon candidate is required to overlap with the corresponding muon trigger object within  $\Delta R < 0.2$  to ensure that the event has been triggered by the considered *tag* muon.

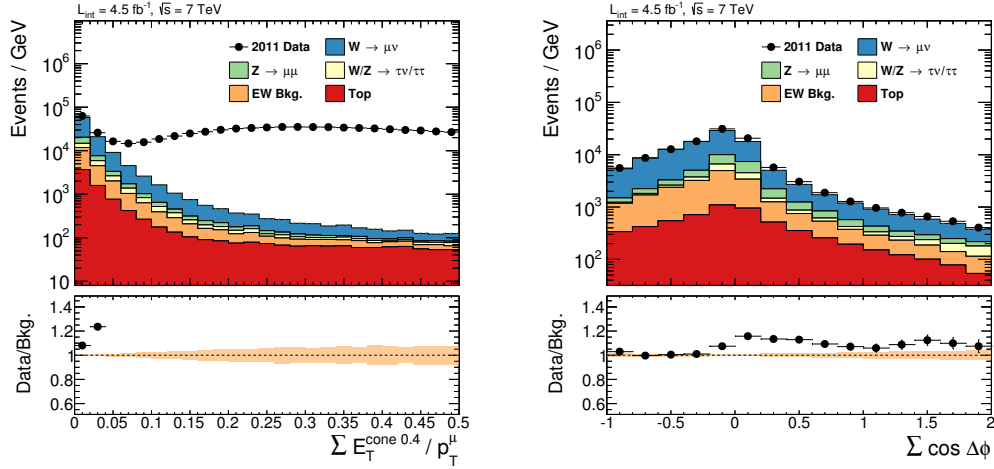
Trigger	Run number interval	Period interval
EF_mu18_MG	177986 – 186493	B - I
EF_mu18_MG_medium	186516 – 191933	J - M

**Table 6.6:** Muon trigger used for the  $W \rightarrow \mu\nu$  control region.

Once an event passes the baseline criteria above, the  $p_T$  threshold for the muon candidate is increased to  $p_T^\mu > 40$  GeV and the isolation criteria is applied in order to suppress background processes, in particular QCD multi-jet. At least one reconstructed tau object is required to pass the selection and if more than one candidate is found the tau object with the highest transverse momentum is utilized as probe candidate. To further suppress background processes and to increase the purity of  $W \rightarrow \mu\nu$  events the following relationship in the azimuthal plane between the missing transverse energy,  $E_T^{\text{miss}}$ , the muon and tau candidate is required:

$$\sum \cos \Delta\phi = \cos(\Delta\phi(\tau, E_T^{\text{miss}})) + \cos(\Delta\phi(\mu, E_T^{\text{miss}})) < -0.15. \quad (6.15)$$

Distributions for the muon isolation observable and the  $\sum \cos \Delta\phi$  observable are presented in Figure 6.17, before the selection requirement on the considered observables has been applied, highlighting the rejection efficiency against the QCD multi-jet background, which is the missing contribution between the data and the SM prediction.



(a) Muon isolation after the baseline selection and before the isolation requirement. (b)  $\sum \cos \Delta\phi$  after the muon isolation requirement and  $p_T^\mu > 40$  GeV.

**Figure 6.17:** Distributions for the selection of the  $W \rightarrow \mu\nu$  control region. The observed data points (black dots) are compared to the SM expectation, which are estimated from simulations excluding QCD multi-jet. The contributions from the individual processes (colored areas) are added up (stacked) and the combined statistical uncertainty is illustrated by the hatched area. The bottom area displays the ratio between the measurements and the SM prediction in which the light band represents the statistical uncertainty on the background prediction.

The observed number of events and the background prediction after the full selection chain are summarized in Table 6.7 and after each individual selection criteria in Table 6.8. In total, an estimated purity of  $\sim 70\%$  of  $W \rightarrow \mu\nu$  events is achieved, with a total estimated contribution

	yield	$f_{\text{pred.}}[\%]$
$W \rightarrow \mu\nu$	$42\,210 \pm 180$	69.89
$Z \rightarrow \mu\mu$	$3683 \pm 30$	6.1
$W/Z \rightarrow \tau\nu/\tau\tau$	$1240 \pm 40$	2.06
EW Bkg.	$8690 \pm 60$	14.4
Top	$3167 \pm 8$	5.25
Comb. background prediction	$59\,000 \pm 190$	97.7
Observed number of events	60 387	

**Table 6.7:** Final event yields for the predictions of various SM processes in the  $W \rightarrow \mu\nu$  control region are presented and compared to the observed number of events. In addition, the estimated relative contribution of each background to the data,  $f_{\text{pred.}}$ , is shown. The stated uncertainty for each background process correspond to the respective statistical uncertainty.

from QCD multi-jet processes of about 2.3 %. For the background estimation scale factors for the muon trigger, muon identification and muon isolation are applied to account for deviations between simulations and the measurements.

The distributions for the transverse momentum and pseudorapidity of the tau candidate after the full selection are presented in Figure 6.18. For both, a reasonable agreement between the measurements and the predictions from the simulations has been found within the statistical and systematic uncertainties. The systematic uncertainties are dominated by the uncertainties on the muon scale factor and are estimated to be at the order of 2 % to 5 %.

In contrast, observables related to the sub-structure of tau jets show a significant shift between the measurements and predictions from the Monte Carlo simulations. Three exemplary observables used for the tau identification algorithm as well as the corresponding BDT score are presented in Figure 6.19. The mis-modeling has been found to be more dominant in observables related to charged particles only, for examples the number of tracks in the isolation annulus, compared to the cluster based observables. In general, the sub-structure of simulated QCD jets tend to be closer to the structure of real hadronically decaying tau leptons, resulting on average in a higher BDT score compared with the measurements and thus resulting in an increased fake rate.

### 6.3.2 Results of the Misidentification Efficiency Measurement

The misidentification rate or misidentification efficiency is defined as the observed number of reconstructed tau candidates passing certain identification level,  $N_{\tau}^{\text{pass}}$ , over the total number of reconstructed tau candidates,  $N_{\tau}$ ,

$$f_{\text{jet} \rightarrow \tau}(p_{\text{T}}, N_{\text{trk}}, q_{\text{lead}} \times q_{\text{sub}}) = \frac{N_{\tau}^{\text{pass}}(p_{\text{T}}, N_{\text{trk}}, q_{\mu} \times q_{\tau})}{N_{\tau}(p_{\text{T}}, N_{\text{trk}}, q_{\mu} \times q_{\tau})} \quad (6.16)$$

The fake rate is parametrized in the transverse momentum,  $p_{\text{T}}$ , of the tau candidate, the number of associate tracks in the core region,  $N_{\text{trk}}$  (one or three prong), and the charge product between

	Observed	$W \rightarrow \mu\nu$	$Z \rightarrow \mu\mu$	$W/Z \rightarrow \tau\nu/\tau\tau$	EW Bkg.	Top
Muon trigger	8 188 212	$214\,400 \pm 400$	$44\,610 \pm 120$	$28\,320 \pm 160$	$49\,500 \pm 150$	$34\,720 \pm 40$
Electron veto	7 993 634	$209\,400 \pm 400$	$43\,170 \pm 110$	$27\,020 \pm 160$	$44\,520 \pm 140$	$26\,830 \pm 40$
$N_\mu > 0$	2 432 226	$161\,840 \pm 350$	$38\,060 \pm 100$	$14\,950 \pm 120$	$34\,920 \pm 120$	$19\,115 \pm 28$
Di-muon veto	2 404 583	$159\,640 \pm 350$	$22\,640 \pm 80$	$14\,720 \pm 110$	$34\,110 \pm 120$	$17\,807 \pm 27$
Min. one tau candidate	1 314 009	$111\,900 \pm 290$	$15\,340 \pm 70$	$10\,400 \pm 100$	$23\,990 \pm 100$	$13\,191 \pm 23$
Muon isolation	181 090	$102\,950 \pm 280$	$14\,130 \pm 60$	$9190 \pm 90$	$21\,690 \pm 90$	$9550 \pm 15$
$p_T^\mu > 40\text{ GeV}$	121 920	$75\,240 \pm 230$	$11\,300 \pm 60$	$4480 \pm 60$	$16\,310 \pm 80$	$6823 \pm 12$
$\sum \cos \Delta\phi < -0.15$	60 387	$42\,210 \pm 180$	$3683 \pm 30$	$1240 \pm 40$	$8690 \pm 60$	$3167 \pm 8$

**Table 6.8:** Observed number of events and background predictions in the  $W \rightarrow \mu\nu$  control region are presented after each selection requirement. The stated uncertainty values for each individual background process correspond to the respective statistical uncertainty.

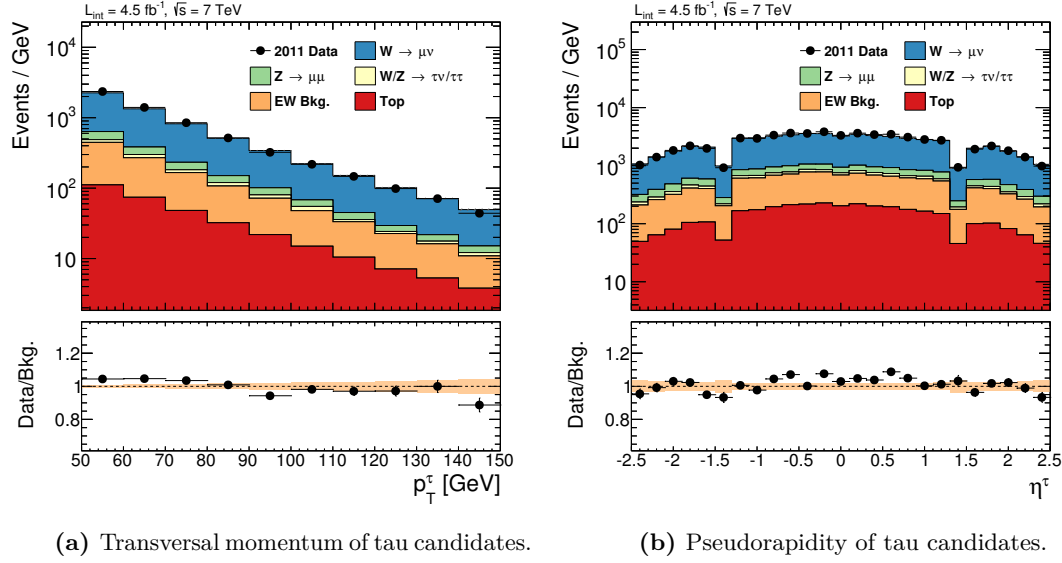


**Figure 6.18:** Kinematic distributions of reconstructed tau candidates in the  $W \rightarrow \mu\nu$  control region. The observed data points (black dots) are compared to the SM expectation, which are estimated from simulations excluding QCD multi-jet. The contributions from the individual processes (colored areas) are added up (stacked) and the combined statistical uncertainty is illustrated by the hatched area. The bottom area displays the ratio between the measurements and the SM prediction in which the light band represents the statistical uncertainty on the background prediction.

the muon and the considered tau candidate,  $q_\mu \times q_\tau$ .

A parametrization in the transverse momentum of the fake tau allows to account for the  $p_T$  dependence of the sub-structure observables and thus the  $p_T$  dependence of the tau identification efficiency while the differentiation in  $N_{\text{trk}}$  is necessary because the underlying BDT algorithms are different for 1-prong and 3-prong tau candidates. The classification of the charge product,  $q_\mu \times q_\tau$ , follows the same convention used of the MSSM Higgs boson search: a charge product of  $-1$  is referred to as *opposite sign* (OS) and a charge product of  $1$  as *same sign* (SS). Distinguishing between OS and SS allow to account for a different fraction of quark and gluon initiated jets faking the tau decay. A quark induced jet is in general more likely to fake a hadronic tau decay compared to a gluon induced jet, due to property of gluon jets to create a wider spread in the energy and particle flow during the hadronisation process. The leading tau candidate, with respect to  $p_T$ , is more likely to be a quark induced jet in the OS region compared to SS region. In opposite sign the recoiling quark jet with respect to the  $W$  boson can be reconstructed as a tau candidate, while a quark jet with the same charge as the muon need to be produced in an additional QCD radiation process.

The misidentification rates are measured for six different variations of the identification level requirements: the *loose* and medium working point are tested with and without an additional tau trigger selection. For the trigger based selection, the considered tau candidates are required pass either the EF\_tau20\_medium1 or EF\_tau29\_medium1 tau trigger in addition to the offline tau identification in order to estimate a possible bias of the trigger identification on misidentification

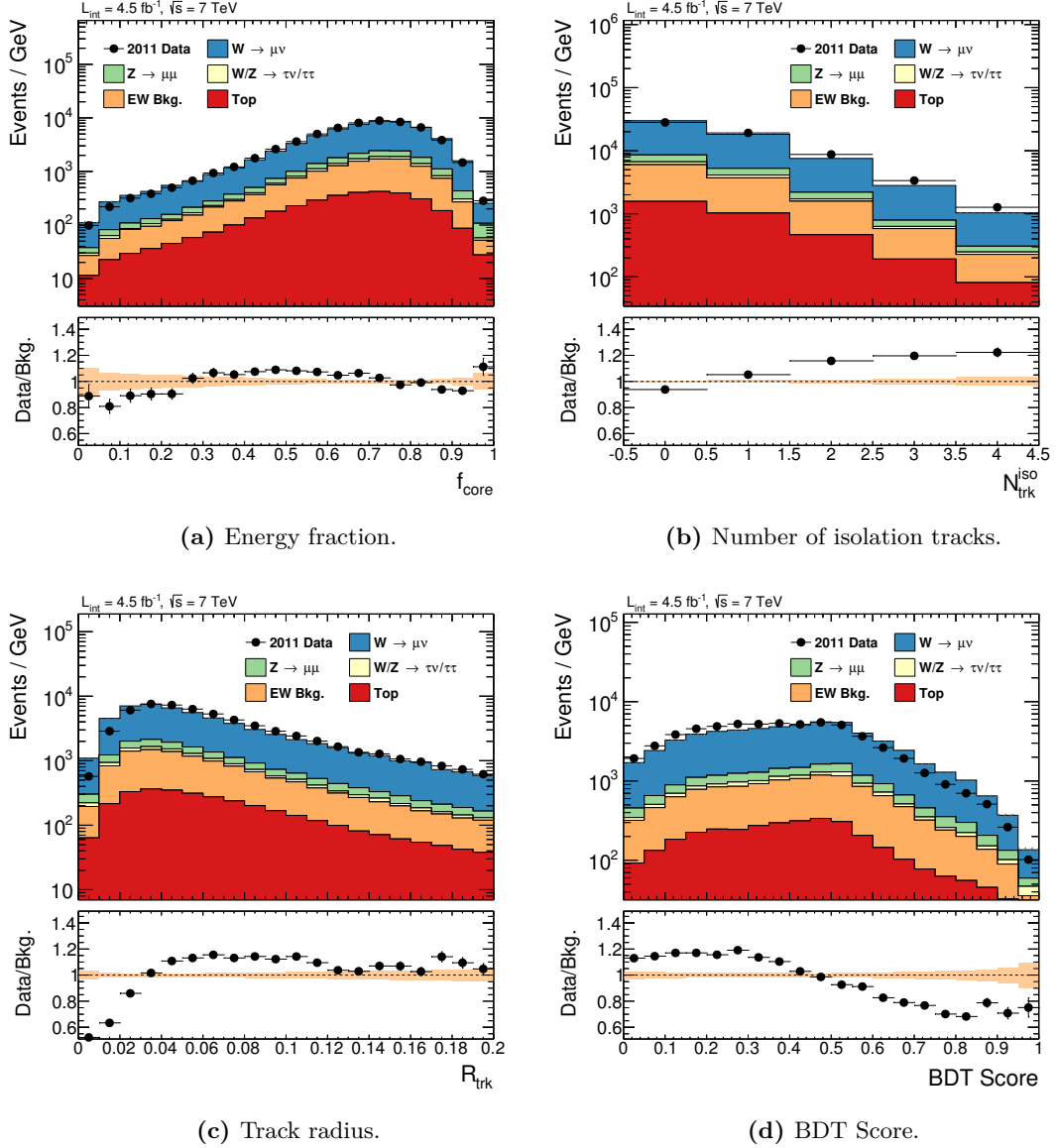


**Figure 6.19:** Substructure distributions of reconstructed tau candidates in the  $W \rightarrow \mu\nu$  control region. The observed data points (black dots) are compared to the SM expectation, which are estimated from simulations excluding QCD multi-jet. The contributions from the individual processes (colored areas) are added up (stacked) and the combined statistical uncertainty is illustrated by the hatched area. The bottom area displays the ratio between the measurements and the SM prediction in which the light band represents the statistical uncertainty on the background prediction.



rate.

Both single tau trigger correspond to the trigger algorithms used in the di-tau trigger region of the MSSM Higgs boson search and the estimated misidentification rates with the trigger requirements are used for the leading and sub-leading tau candidate depending on which single trigger item has been fired by the considered reconstructed tau. For the single tau trigger region a `EF_tau125_medium(1)` trigger is applied for the leading tau candidate. Unfortunately, a reasonable measurement of the misidentification rates in addition with a trigger threshold above 125 GeV was not possible due to very low number of fake tau candidates passing the selection in the  $W \rightarrow \mu\nu$  control region. The misidentification rate is therefore approximated using the `EF_tau29_medium1` trigger based fake rate.

The results for the misidentification rate measurements are presented in Figure 6.20, Figure 6.21 and Figure 6.22 for the *loose* identification point with no trigger requirement and for the *medium* identification point with a trigger requirement at 20 GeV and 29 GeV, respectively. Despite a difference in the overall normalization, the general trend between the different identification requirements is very similar. Tau candidates with one charged particle are in general more likely to be misidentified as a hadronically decaying tau lepton than their 3-prong counterparts. The simulations for the 1-prong candidates show in general in a better agreement with the data, while the simulations for 3-prong jets is up to factor of four larger compared to the measurements. It is also noticeable, that the misidentification rate is larger in the OS region compared to the corresponding SS region. This behavior is expected, due to the fact that the probability for a fake tau jet to originate from the hadronisation process of a quark instead of a gluon is enlarged in the OS region.

The stated uncertainty intervals are *Clopper-Pearson* [259] intervals estimated for a confidence level of 68.3% and include the statistical uncertainty only. A possible impact of the systematic uncertainties, arising from the muon object and muon trigger related scale factors, on the misidentification rate has been estimated and found to be negligible ( $< 1\%$ ) compared to the statistical uncertainty.

The detailed values for the misidentification rates are summarized in Table 6.9, Table 6.10 and Table 6.11.

In addition to the misidentification rate, the *fail-identification* rate,  $f_{\text{fail}}$ , has been measured as the fraction of tau candidates which not able to pass a certain identification requirement. Definition and parametrization of the fail-identification rate is similar to the misidentification rate, except that the number of observed tau candidates passing a certain level,  $N_{\tau}^{\text{pass}}$ , is replaced by the number of observed tau candidates which fail to pass the corresponding level,  $N_{\tau}^{\text{fail}}$ . In the case of the trigger requirement, the tau candidates are still required to pass the tau trigger but fail the offline tau identification. Although the fail-identification rate is not required directly for event selection used in the MSSM Higgs boson search, it is a necessary auxiliary measurement to estimate the fake tau contribution in various control and validation regions used for evaluation of QCD multi-jet estimation techniques. The values for the fail-identification rates are summarized in Section A.4.3.

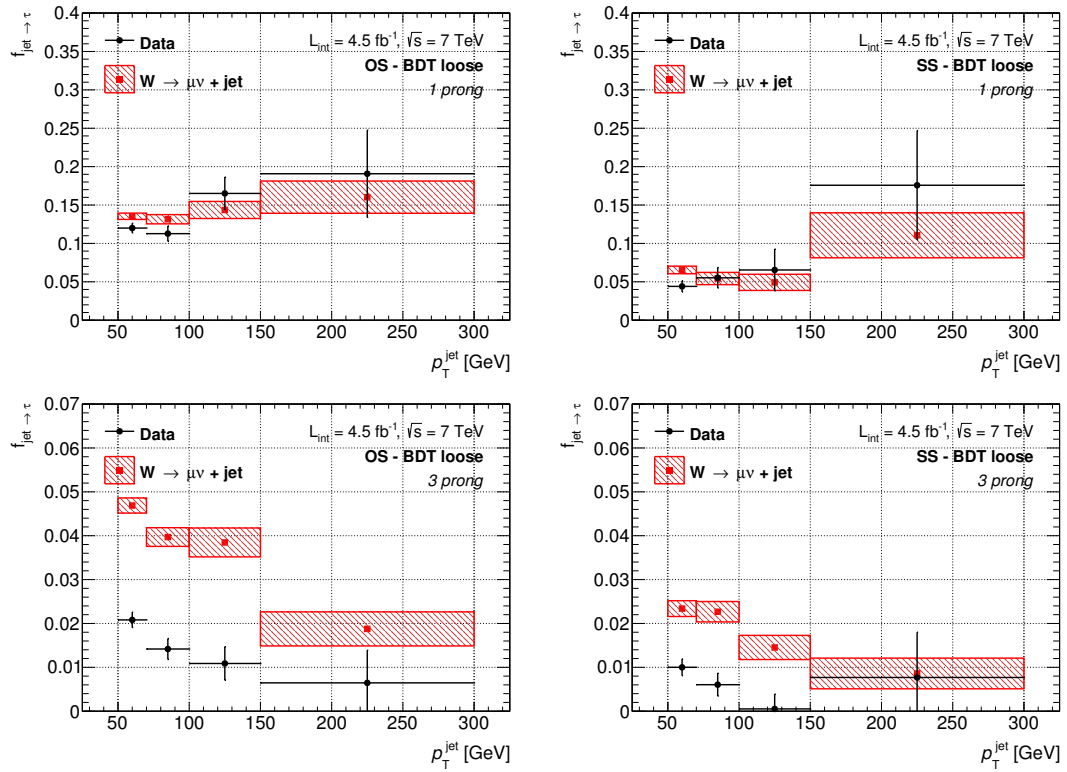


**Figure 6.20:** Observed probabilities for the misidentification of jets as hadronically decaying tau leptons in the  $W \rightarrow \mu\nu$  control region are compared with the predictions estimated using Monte Carlo simulations. The *loose* working point without any additional trigger requirement is presented for 1-prong (top) and 3-prong (bottom) tau candidates in the OS (left) and SS (right) region.

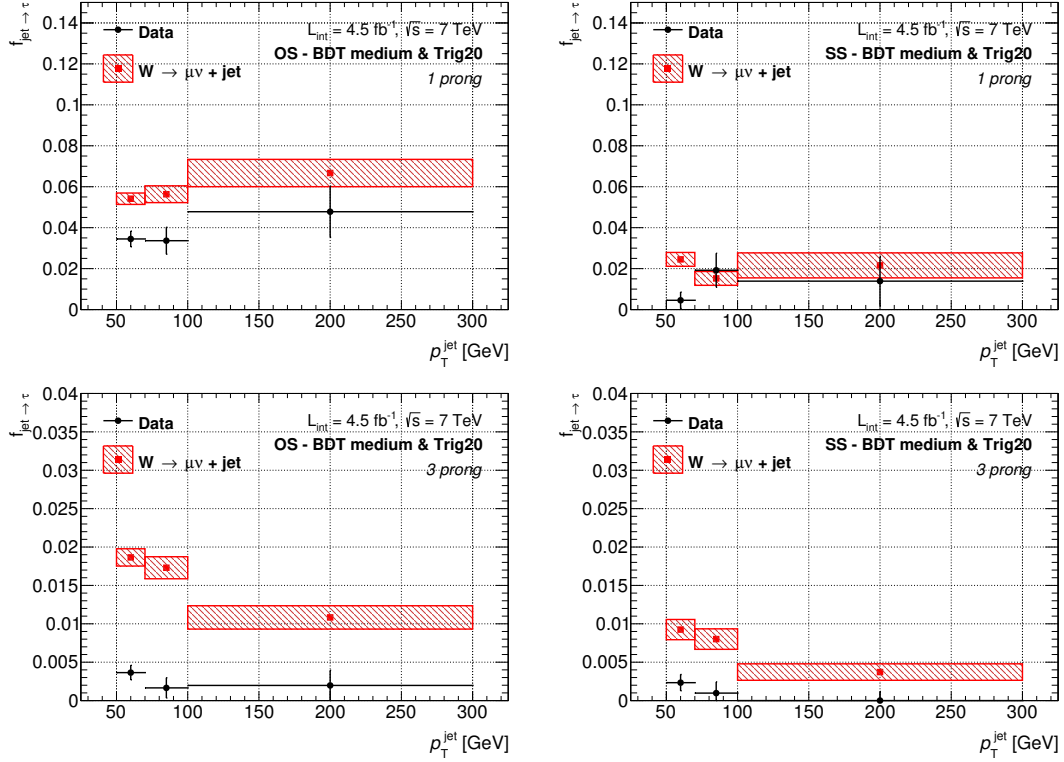


**Figure 6.21:** Observed probabilities for the misidentification of jets as hadronically decaying tau leptons in the  $W \rightarrow \mu\nu$  control region are compared with the predictions estimated using Monte Carlo simulations. The *medium* working point in addition with a `EF_tau20_medium1` trigger requirement is presented for 1-prong (top) and 3-prong (bottom) tau candidates in the OS (left) and SS (right) region.

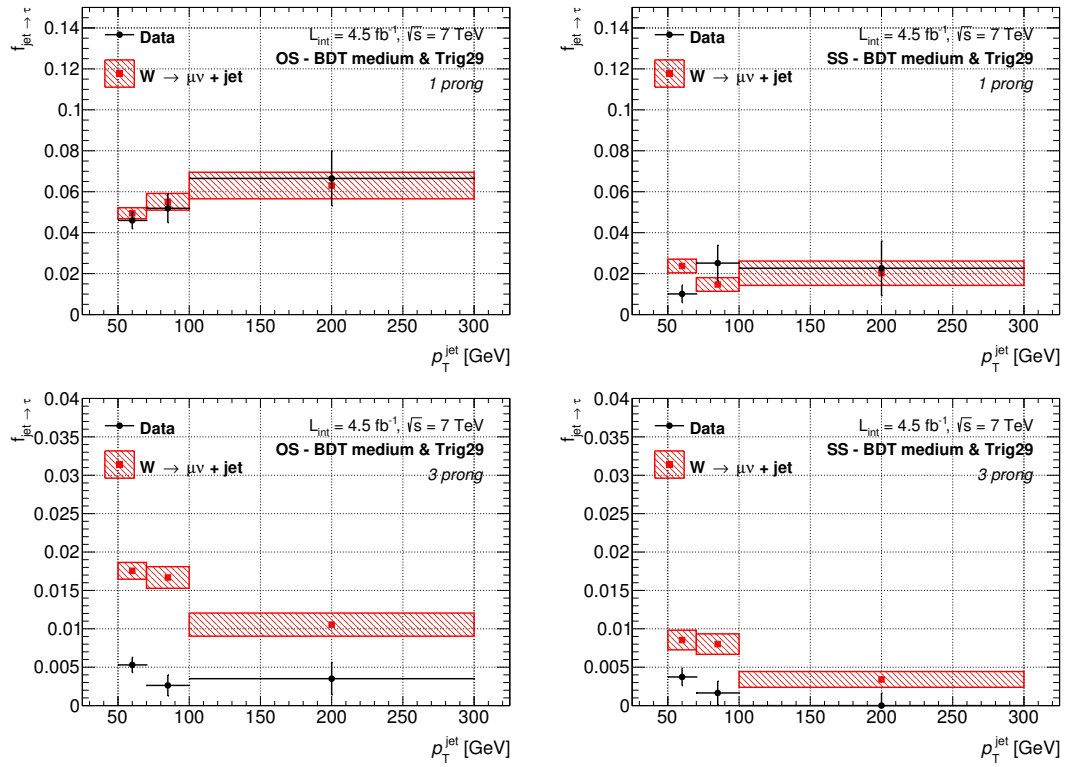


**Figure 6.22:** Observed probabilities for the misidentification of jets as hadronically decaying tau leptons in the  $W \rightarrow \mu\nu$  control region are compared with the predictions estimated using Monte Carlo simulations. The *medium* working point in addition with a `EF_tau29_medium1` trigger requirement is presented for 1-prong (top) and 3-prong (bottom) tau candidates in the OS (left) and SS (right) region.

		$p_{\text{T}}^{\tau}$ interval in [GeV]			
$q_{\mu} \times q_{\tau}$	BDT level	50 – 70	70 – 100	100 – 150	> 150
<i>1 prong</i>					
OS	loose	$12.0^{+0.6}_{-0.6}$	$11.3^{+1.0}_{-1.0}$	$16.5^{+2.1}_{-2.1}$	$19^{+6}_{-6}$
	medium	$8.2^{+0.5}_{-0.5}$	$7.9^{+0.9}_{-0.9}$	$9.4^{+1.7}_{-1.7}$	$5^{+4}_{-4}$
SS	loose	$4.4^{+0.7}_{-0.7}$	$5.5^{+1.3}_{-1.3}$	$6.5^{+2.7}_{-2.7}$	$18^{+7}_{-7}$
	medium	$2.8^{+0.6}_{-0.6}$	$4.0^{+1.1}_{-1.1}$	$4.1^{+1.8}_{-1.8}$	$6^{+5}_{-5}$
<i>3 prong</i>					
OS	loose	$2.08^{+0.17}_{-0.17}$	$1.42^{+0.24}_{-0.24}$	$1.1^{+0.4}_{-0.4}$	$0.6^{+0.7}_{-0.6}$
	medium	$1.05^{+0.13}_{-0.13}$	$0.67^{+0.18}_{-0.18}$	$0.71^{+0.29}_{-0.29}$	$0.4^{+0.4}_{-0.4}$
SS	loose	$1.00^{+0.19}_{-0.19}$	$0.60^{+0.26}_{-0.26}$	$0.05^{+0.34}_{-0.05}$	$0.8^{+1.0}_{-0.8}$
	medium	$0.70^{+0.15}_{-0.15}$	$0.24^{+0.19}_{-0.19}$	$0.00^{+0.25}_{-0.0}$	$1.5^{+1.0}_{-1.0}$

**Table 6.9:** Misidentification efficiencies [%] for fake tau candidates measured in the  $W \rightarrow \mu\nu + \text{jet}$  control region using proton-proton collision events at  $\sqrt{s} = 7 \text{ TeV}$  recorded with the ATLAS detector in 2011. No additional trigger requirements for the tau candidates have been applied. The stated uncertainties correspond to Clopper-Pearson intervals, estimated for a confidence level of 68.3 %.

		$p_T^\tau$ interval in [GeV]		
$q_\mu \times q_\tau$	BDT level	50 – 70	70 – 100	> 100
<i>1 prong</i>				
OS	loose	$4.5^{+0.4}_{-0.4}$	$4.0^{+0.7}_{-0.7}$	$7.4^{+1.5}_{-1.5}$
	medium	$3.4^{+0.4}_{-0.4}$	$3.4^{+0.7}_{-0.7}$	$4.8^{+1.3}_{-1.3}$
SS	loose	$0.9^{+0.5}_{-0.5}$	$2.7^{+1.0}_{-1.0}$	$1.4^{+1.4}_{-1.4}$
	medium	$0.5^{+0.4}_{-0.4}$	$1.9^{+0.8}_{-0.8}$	$1.4^{+1.2}_{-1.2}$
<i>3 prong</i>				
OS	loose	$0.76^{+0.12}_{-0.12}$	$0.45^{+0.18}_{-0.18}$	$0.37^{+0.27}_{-0.27}$
	medium	$0.36^{+0.10}_{-0.10}$	$0.17^{+0.13}_{-0.13}$	$0.20^{+0.20}_{-0.20}$
SS	loose	$0.22^{+0.13}_{-0.13}$	$0.00^{+0.17}_{-0.0}$	$0.00^{+0.13}_{-0.0}$
	medium	$0.23^{+0.11}_{-0.11}$	$0.10^{+0.15}_{-0.10}$	$0.00^{+0.12}_{-0.0}$

**Table 6.10:** Misidentification efficiencies [%] for fake tau candidates measured in the  $W \rightarrow \mu\nu + \text{jet}$  control region using proton-proton collision events at  $\sqrt{s} = 7 \text{ TeV}$  recorded with the ATLAS detector in 2011. In addition to the tau identification a trigger requirement using the `EF_tau20_medium1` trigger has been applied for the tau candidate.

$q_\mu \times q_\tau$	BDT level	$p_T^\tau$ interval in [GeV]		
		50 – 70	70 – 100	> 100
<i>1 prong</i>				
OS	loose	$6.3^{+0.5}_{-0.5}$	$6.4^{+0.8}_{-0.8}$	$10.2^{+1.6}_{-1.6}$
	medium	$4.6^{+0.4}_{-0.4}$	$5.2^{+0.7}_{-0.7}$	$6.6^{+1.3}_{-1.3}$
SS	loose	$1.5^{+0.5}_{-0.5}$	$3.6^{+1.0}_{-1.0}$	$3.6^{+1.7}_{-1.7}$
	medium	$1.0^{+0.4}_{-0.4}$	$2.5^{+0.9}_{-0.9}$	$2.3^{+1.3}_{-1.3}$
<i>3 prong</i>				
OS	loose	$1.07^{+0.13}_{-0.13}$	$0.79^{+0.19}_{-0.19}$	$0.70^{+0.29}_{-0.29}$
	medium	$0.53^{+0.10}_{-0.10}$	$0.26^{+0.14}_{-0.14}$	$0.35^{+0.21}_{-0.21}$
SS	loose	$0.51^{+0.14}_{-0.14}$	$0.11^{+0.18}_{-0.11}$	$0.00^{+0.17}_{-0.0}$
	medium	$0.37^{+0.11}_{-0.11}$	$0.16^{+0.15}_{-0.15}$	$0.00^{+0.16}_{-0.0}$

**Table 6.11:** Misidentification efficiencies [%] for fake tau candidates measured in the  $W \rightarrow \mu\nu + \text{jet}$  control region using proton-proton collision events at  $\sqrt{s} = 7 \text{ TeV}$  recorded with the ATLAS detector in 2011. In addition to the tau identification a trigger requirement using the `EF_tau29_medium1` trigger has been applied for the tau candidate.

## 6.4 Measurement of the Tau Identification Transfer Factor

The tau identification transfer factor,  $f_{\text{pass} \rightarrow \text{fail}}$ , describes the amount of jets, originating from the hadronisation processes of quarks or gluons, which would pass a certain tau identification criteria over the amount of jets failing the considered tau identification, defined in Eq. (6.12). The transfer factor has been measured in a di-jet control region, using proton-proton interactions at center-of-mass energy of  $\sqrt{s} = 7 \text{ TeV}$  recorded with the ATLAS detector in 2011 at the LHC and is used to estimate the contribution of multi-jet events (in the STT region only), in which two jets are misidentified as hadronically decaying tau leptons. Similar to the measurement of the misidentification efficiency for fake tau candidates, the extraction of the transfer factor from measurements allows to avoid a possible mis-modeling of the jet substructure in the simulations and thus avoiding a mis-modeling of the tau identification behavior.

The utilized data set for the control region corresponds to a total integrated luminosity of about  $4.5 \text{ fb}^{-1}$ . Considering the overwhelming cross sections for pure QCD interactions at a hadron collider, it is expected that the dominated contribution for this control region originates from QCD multi-jet processes. Other SM background interactions are estimated based on simulations using the background estimation methodology stated in Section 6.2.

### 6.4.1 Overview of the Transfer Factor Measurement

Similar to the measurement of the misidentification efficiencies, the transfer factor is measured using a *tag and probe* method within a di-jet topology. The optimization of the di-jet control region is performed with respect to the following aspects:

- the phase space of the control region should be relatively close to the signal region in the MSSM analysis in order to retrieve a representative measurement of the transfer factor,
- at the same time a possible contamination of the real hadronic tau decays, and thus possible MSSM signal, should be negligible,
- and the number of tau candidates passing the identification requirement should be large enough to perform a reasonable parametrization of the transfer factor.

For the selection of reconstructed objects, in particular the reconstructed tau candidates and vertices, no modification with respect to the MSSM search is made. The event selection is a simplified version of the main STT region: after the same event cleaning requirements, at least one reconstructed vertex and two reconstructed tau candidates with  $p_T > 50 \text{ GeV}$  are required. Instead of a single tau trigger, the events are selected using jet based triggers, requiring a jet above a threshold of 75 GeV, 100 GeV, 135 GeV, 180 GeV and 240 GeV, respectively<sup>14</sup>. The transverse momentum of the leading tau candidate is required to be  $p_T^{\text{lead}} > 150 \text{ GeV}$  and the azimuthal distance between both tau candidates should be  $|\Delta\phi_{\text{lead,sub}}| > 2.7$ . The leading tau candidate is defined as the *tag* object and sub-leading tau candidate is the *probe* object, which is used for the

<sup>14</sup>Technical detail: the considered trigger tags are EF\_jX\_a4tc\_EFFS with  $X \in \{75, 100, 135, 180, 240\}$ . All utilized jet triggers are pre-scaled and the average pre-scale per trigger usually decreases with an increase of the trigger threshold (the 240 trigger is almost un-prescaled). Since the measurement of the transfer factor is an object and not event based quantity, the pre-scales do not effect the measurement.

transfer factor estimation. To further enrich multi-jet processes, no tau identification requirement is applied for both tau candidates. The final event yield summary for the di-jet control region is presented in Table 6.12, highlighting the dominant contribution of QCD multi-jet processes, which are not estimated from MC predictions and thus represent the missing difference between the observed number of events and the remaining SM background processes.

	Data	$Z/\gamma^* \rightarrow \tau\tau$	$W \rightarrow \tau\nu$	EW Bkg.	Top
Jet trigger	257 251	1352 $\pm$ 12	6000 $\pm$ 60	24 550 $\pm$ 100	7034 $\pm$ 25
$N_\tau > 1$	220 336	306 $\pm$ 6	639 $\pm$ 17	3715 $\pm$ 32	1344 $\pm$ 11
$N_{\text{vtx}} > 0$	220 336	306 $\pm$ 6	639 $\pm$ 17	3715 $\pm$ 32	1344 $\pm$ 11
$p_T^{\text{lead}} > 150 \text{ GeV}$ and $ \Delta\phi  > 2.7$	90 301	110.7 $\pm$ 3.5	290 $\pm$ 12	306 $\pm$ 10	292 $\pm$ 6

**Table 6.12:** Observed number of events and background predictions in the di-jet control region are presented after each selection requirement. The background predictions are normalized to an effective luminosity value taking the trigger pre-scales into account. The stated uncertainty values for each individual background process correspond to the respective statistical uncertainty.

Due the pre-scales of the jet triggers, the observed number of events are compared to predictions which are normalized to an effective luminosity value taking the pre-scales into account.

#### 6.4.2 Results of the Transfer Factor Measurement

The transfer factor is now evaluated by the number of probe tau candidates passing the *loose* tau identification working point over the number of probe candidates failing the identification. As already stated in Eq. (6.12),  $f_{\text{pass} \rightarrow \text{fail}}$  is parametrized in the transverse momentum of the probe tau candidate, the number of associated tracks (1-prong or 3-prong) and the charge product between the tag and probe candidate. Besides the usually split of the charge product in an opposite sign and same sign region, the transfer factor is also evaluated with no charge product requirement, referred to as *no-sign* (NoS) region.

Transfer factors for 1-prong and 3-prong tau candidates are presented in Figure 6.23 for different charge product selection requirements. Systematic uncertainties are estimated by varying the charge product requirement and by forcing a minimal tau BDT score of 0.2 for the tag candidate, symmetrizing both uncertainties. Both variations affect the fraction of quark to gluon initiated jets in the test sample and thus affecting the average probability of a tau candidate to pass the tau identification and therefore covering for discrepancies in the quark/gluon fraction between the di-jet control region and signal region. The systematic uncertainties predominantly affect the low  $p_T$  1-prong candidates, while the uncertainties for the high  $p_T$  1-prong candidates or 3-prong candidates are dominated by the statistical uncertainty. A full summary of the transfer factor values is provided in Table 6.13 and Table 6.14.



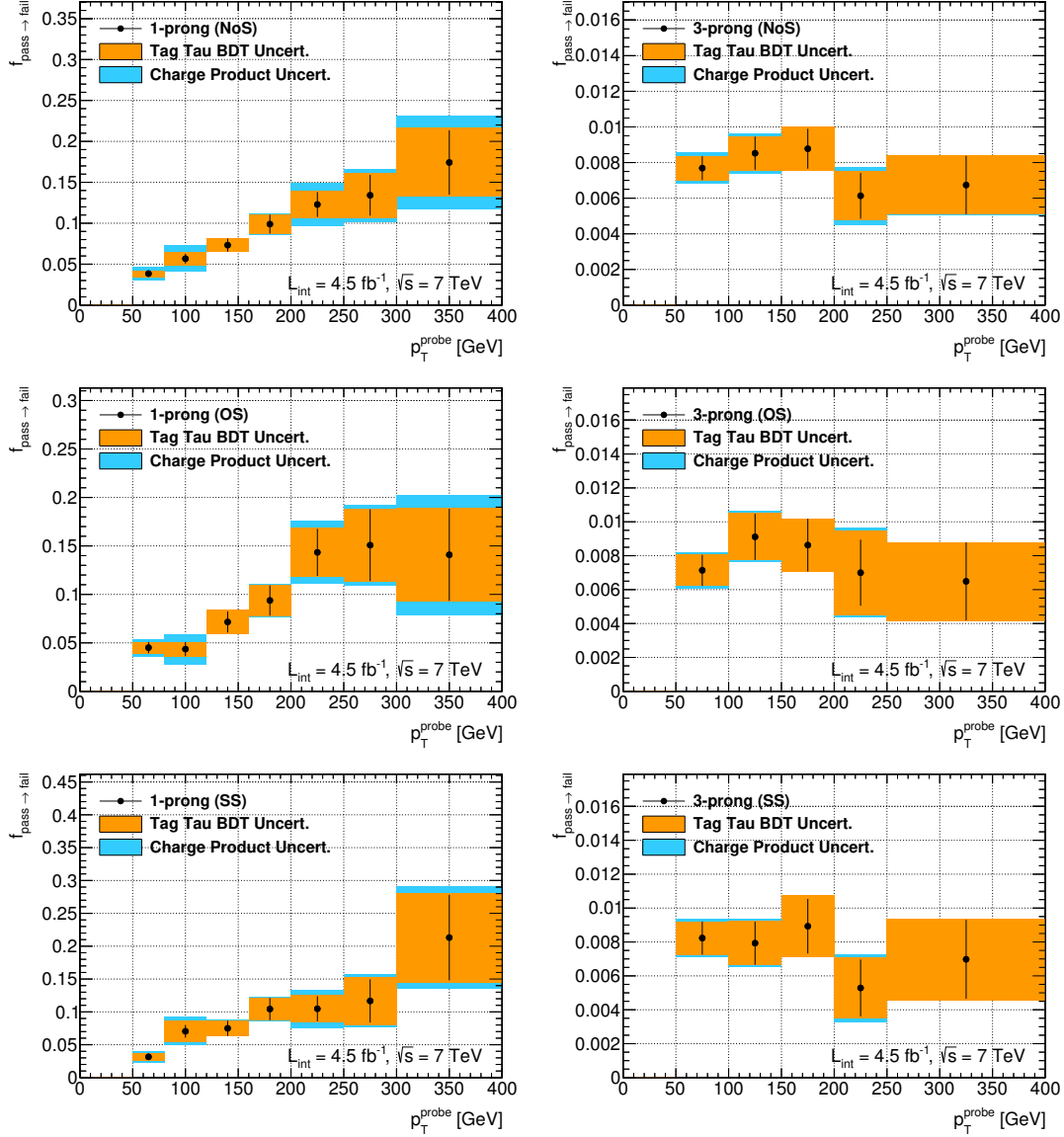


**Figure 6.23:** Tau identification transfer factor as a function of the transverse momentum of the tau candidate, measured for 1-prong (left) and 3-prong (right) tau candidates in *no-sign* (top), *opposite sign* (middle) and *same sign* (bottom) di-jet events. The black dots represent the mean transfer factor for a given  $p_T$  interval with the black line representing the statistical uncertainty. The blue and orange shaded areas represent additional systematic uncertainties arising from variation of the charge product requirement and a selection criteria on the tau identification BDT score of the tag candidate.

		$p_T^\tau$ interval in [GeV]						
$q_{\text{lead}} \times q_{\text{sub}}$	50 – 80	80 – 120	120 – 160	160 – 200	200 – 250	250 – 300	> 300	
NoS	$0.038 \pm 0.008$	$0.057 \pm 0.016$	$0.073 \pm 0.008$	$0.099 \pm 0.013$	$0.123 \pm 0.026$	$0.134 \pm 0.032$	$0.17 \pm 0.06$	
OS	$0.045 \pm 0.009$	$0.044 \pm 0.016$	$0.072 \pm 0.012$	$0.094 \pm 0.017$	$0.143 \pm 0.032$	$0.15 \pm 0.04$	$0.14 \pm 0.06$	
SS	$0.032 \pm 0.009$	$0.070 \pm 0.021$	$0.075 \pm 0.012$	$0.104 \pm 0.018$	$0.105 \pm 0.029$	$0.12 \pm 0.04$	$0.21 \pm 0.08$	

**Table 6.13:** Tau identification transfer factors for 1-prong tau candidates estimated from the di-jet control region. The stated uncertainties combine the statistical and systematic uncertainties.

		$p_T^\tau$ interval in [GeV]				
$q_{\text{lead}} \times q_{\text{sub}}$	50 – 100	100 – 150	150 – 200	200 – 250	> 250	
NoS	$0.0077 \pm 0.0009$	$0.0085 \pm 0.0011$	$0.0088 \pm 0.0012$	$0.0061 \pm 0.0016$	$0.0067 \pm 0.0017$	
OS	$0.0071 \pm 0.0011$	$0.0091 \pm 0.0015$	$0.0086 \pm 0.0016$	$0.0070 \pm 0.0026$	$0.0065 \pm 0.0023$	
SS	$0.0082 \pm 0.0011$	$0.0079 \pm 0.0014$	$0.0089 \pm 0.0018$	$0.0053 \pm 0.0020$	$0.0070 \pm 0.0024$	

**Table 6.14:** Tau identification transfer factors for 3-prong tau candidates estimated from the di-jet control region. The stated uncertainties combine the statistical and systematic uncertainties.

## 6.5 Validation of the $Z/\gamma^* \rightarrow \tau\tau$ Modeling

Drell-Yan processes with two hadronically decaying tau leptons in the final state rank among the irreducible backgrounds with respect to a possible MSSM Higgs signature and are estimated from MC based simulations. The modeling of the simulation has been verified in a data driven side band which is defined orthogonal to the final signal selection.

In order to enrich the fraction of Drell-Yan processes within the side band and simultaneous avoid a possible contribution of signal, a selection towards  $Z/\gamma^*$  particles with a significant boost along the transversal plane has been applied. The side band is defined as a variant of the DTT selection:

1. Baseline and object selection, which are identical to the MSSM Higgs search.
2. Di-tau trigger requirement, identical to the DTT region.
3. Both tau candidates are required to pass the *medium* tau identification working point and to have opposite electric charges.

In addition to these basic DTT selection criteria the following list of requirements are applied to enrich boosted Drell-Yan processes and to simultaneously suppress QCD multi-jet background:

$$E_T^{\text{miss}} > 25 \text{ GeV}, \quad (6.17)$$

$$\cos \Delta\phi(\vec{p}_T^{\text{sub}}, \vec{E}_T^{\text{miss}}) > 0.0, \quad (6.18)$$

$$\cos \Delta\phi(\vec{p}_T^{\text{lead}}, \vec{p}_T^{\text{sub}}) > 0.2, \quad (6.19)$$

where  $\Delta\phi(\vec{p}_T^{\text{lead}}, \vec{p}_T^{\text{sub}})$  and  $\Delta\phi(\vec{p}_T^{\text{sub}}, \vec{E}_T^{\text{miss}})$  represent the azimuthal distance between the leading and sub-leading tau candidate and the sub-leading tau candidate and the missing transverse momentum vector, respectively. Equation (6.19) ensures the orthogonality to the signal region by limiting the azimuthal distance between both tau candidates to a maximal value of 1.37. In contrast to the DTT region, no  $p_T^{\text{lead}} < 150 \text{ GeV}$  requirement has been applied to cover the modeling of the high momentum tail, although the statistics are relatively small.

Similar to the DTT region, the multi-jet background is estimated using a splitting into three additional side bands, based on the charge product between both tau candidates and (in contrast to the  $E_T^{\text{miss}}$  based splitting in the DTT region) the inversion of the tau identification requirement:

**Region B** both tau candidates are required to have the same electric charge (SS),  $q_{\text{lead}} \times q_{\text{sub}} = 1$ ,

**Region C** both tau candidates are required to fail the *medium* tau identification working point and have opposite electric charge (OS),

**Region D** both tau candidates are required to fail the *medium* tau identification working point and have the same electric charge (SS).

The final event yields for each region are summarized in Table 6.15 showing an expected purity of the Drell-Yan contribution of about 72 %. Within the Drell-Yan validation region (A), an excess in the total number of events in data is observed with respect to the SM background

predictions, with a significance of  $1.2 \sigma$ .

	Region A	Region B	Region C	Region D
Multi-jet	14 $\pm 5$	—	—	—
$Z/\gamma^* \rightarrow \tau\tau$	44.7 $\pm 2.7$	0.57 $\pm 0.30$	15.5 $\pm 1.5$	1.94 $\pm 0.21$
$W \rightarrow \tau\nu$	2.34 $\pm 0.23$	0.30 $\pm 0.04$	13.2 $\pm 1.0$	5.5 $\pm 0.5$
EW Bkg.	0.90 $\pm 0.10$	0.118 $\pm 0.027$	4.6 $\pm 0.5$	2.37 $\pm 0.33$
Top	0.54 $\pm 0.08$	0.072 $\pm 0.005$	8.39 $\pm 0.26$	3.74 $\pm 0.15$
Comb. background prediction	62 $\pm 5$	1.06 $\pm 0.3$	41.7 $\pm 1.9$	13.5 $\pm 0.7$
Observed number of events	78	11	1181	845

**Table 6.15:** Final event yields for various SM processes and the estimated QCD multi-jet contribution in the Drell-Yan validation regions are presented and compared to the observed number of events. The stated uncertainty for each process correspond to the respective statistical uncertainty.

The slight mis-modeling occurs to an increased degree toward larger values of  $E_T^{\text{miss}}$  (Figure 6.24) but the effect on the total transverse mass is rather small and covered by the combined statistical and systematic uncertainties. Overall, the significance of Drell-Yan control region is limited due to the relative low number of events passing the validation selection.

In conclusion, with regard to the small number of events, no significant mis-modeling of the Drell-Yan background in the  $m_T^{\text{tot}}$  distribution has been observed. A full summary of the event yields for each selection requirement within the validation is presented in Table A.9.

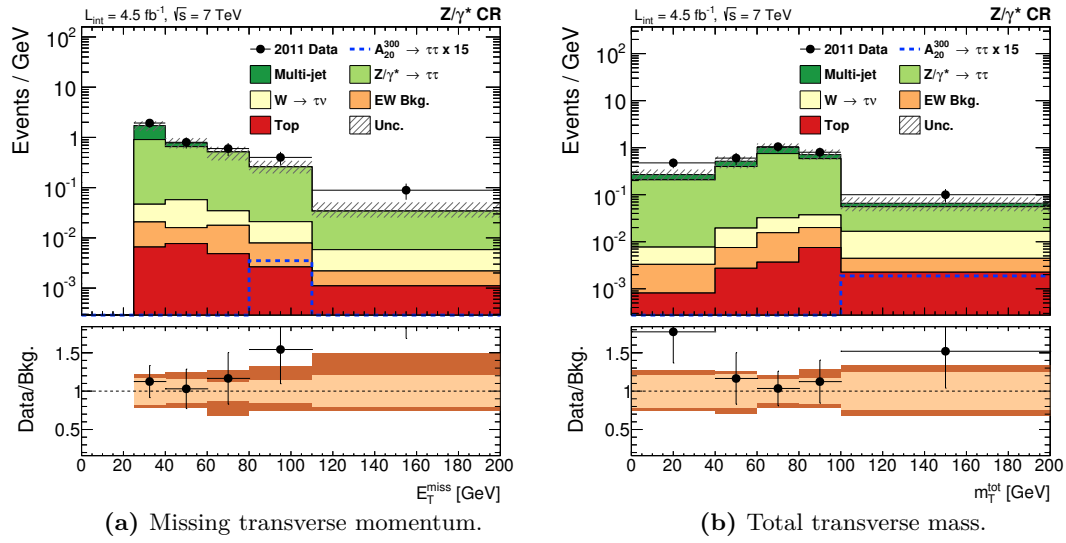


**Figure 6.24:** Distributions of the  $m_T^{\text{tot}}$  and  $E_T^{\text{miss}}$  observable within the Drell-Yan validation region. The observed data points (black dots) are compared to the SM expectation. The contributions from the individual processes (colored areas) are added up (stacked) and the combined statistical and systematic uncertainty is illustrated by the hatched area. A possible signal contribution is shown in the blue line (unstacked). The bottom area displays the ratio between the measurements and the SM prediction in which the light band represents the statistical uncertainty and the dark band the combined statistical and systematic uncertainty on the background prediction.

## 6.6 Systematic Uncertainties

In order to allow a reasonable physical interpretation of the measurements, it is necessary to quantify the possible lack of knowledge on the background prediction in form of *systematic uncertainties*, which are (in general) derived individually for each possible background process. Five main categories of possible source for uncertainties are considered: *theory uncertainties*, *modeling uncertainties*, *detector related uncertainties*, *uncertainties from data driven estimation techniques* and *uncertainties related to the luminosity*.

**Theory Uncertainties** Theoretical calculations are (mostly) performed up to certain finite order in perturbation theory, resulting in a systematic uncertainty on the predicted cross sections due to the non-consideration of the remaining orders. The cross section uncertainties for the various SM background processes and the MSSM Higgs signal processes have been discussed in Section 6.1.1 and Section 6.1.2, respectively.

**Modeling Uncertainties** The term *modeling uncertainties* comprises all sources of uncertainties which are associated with the simulation of the proton-proton interaction using Monte Carlo event generators, excluding the simulation of the detector response. The systematics are evaluated for the MSSM Higgs boson production. The estimation procedure for the modeling uncertainties is relatively complex and discussed separately in Section 6.6.1.

**Detector related Uncertainties** The detector related uncertainties comprise all sources of uncertainties related the reconstruction or identification of physical objects based on the detector response, excluding the misidentification rate and the transfer factor which are treated separately, and uncertainties based in the triggers.

This includes uncertainties related to reconstructed hadronic tau decays, jets and missing transverse momentum vector. Possible sources of uncertainties related to reconstructed electrons or muons have been evaluated, but the impact is found to be negligible due the electron and muon veto, which are applied in the baseline selection.

Uncertainties related to hadronic tau decays are expressed in terms of uncertainties on the scale factors of the tau identification, the tau energy scale und the tau electron veto. The effect of the scale factor uncertainties on the final  $m_T^{\text{tot}}$  distributions is evaluated by adding  $\pm 1\sigma$  to the scale factors (correlated between both tau candidates) and reiterating the analysis. In contrast to the remaining uncertainties, which are treated as uncertainties on the overall normalization, a significant change in the shape the  $m_T^{\text{tot}}$  distribution after applying the tau energy scale shift has been observed. To account for the influence of the  $m_T^{\text{tot}}$  shape, the uncertainty of the tau energy scale is not a simple normalization difference, but instead the difference in each individual bin of the  $m_T^{\text{tot}}$  distribution is considered as systematic uncertainty. With an impact of about 5 % to 30 %, the uncertainties related to the reconstructed hadronic tau decays are one of the dominant uncertainties sources for the MSSM Higgs boson search.

Several systematic uncertainties related to the reconstruction and calibration of jets are considered,

including: uncertainties arising from differences of the jet resolution in data and simulations and uncertainties related to the jet energy scale. The jet energy scale uncertainties comprise:

- a reduced set of six nuisance parameters (five eigenvectors and one residual element of the covariance matrix),
- statistical and modeling uncertainties related the  $\eta$ -intercalibration method,
- uncertainties on the in-time and out-of-time pile-up corrections,
- effects of nearby jets on the energy scale,
- uncertainties for high- $p_T$  jet, which are calibrated using a balancing technique in multi-jet events,
- and uncertainties related to energy scale correction terms based on the flavor of the originating parton, including a separate treatment for jets which are likely to include  $B$ -hadrons.

Details on each individual component can be found in Ref. [135]. Since no directly selection requirement on jets is performed, the jet related uncertainties affect the final observables indirectly via the recalculation of the missing transverse momentum. The uncertainties are propagated by shifting the corresponding components by  $\pm 1\sigma$  and subsequently re-performing the analysis with the shifted  $E_T^{\text{miss}}$ . Thus, the effect of each component is relatively small and the jet uncertainties are combined to a single jet related nuisance parameter.

Systematic uncertainties on the scale and resolution of the missing transverse momentum vector have been considered, again by shifting the corresponding parameter by  $\pm 1\sigma$  and re-performing the selection with the corrected  $E_T^{\text{miss}}$  term. Similar to the jet related uncertainties, the effects of the individual uncertainties on the final  $m_T^{\text{tot}}$  distribution are small and thus combined to a single  $E_T^{\text{miss}}$  related nuisance parameter.

Uncertainties related to the di-tau and single tau trigger scale factors are taken into account by shifting the scale factors by  $\pm 1\sigma$  and analyze the impact on the normalization of the predicted number of events. For the di-tau trigger, the uncertainty is found to be at the order of 3.3 % to 4.3 %, while for the single tau trigger a constant 5 % shift in the normalization is applied.

**Uncertainties from Data Driven Estimation Techniques** This class of uncertainties comprise the uncertainties originating from the misidentification efficiency and the transfer factor, discussed in the Sections 6.3 and 6.4. Similar to the scale factors, the effect on the final  $m_T^{\text{tot}}$  distributions is estimated by scaling the corresponding efficiency and transfer factor by  $\pm 1\sigma$  and subsequently reiterating the analysis. If both tau candidates are originating from QCD jets, the shift in the misidentification efficiency is applied simultaneous for both candidates. Since the misidentification efficiency is only applied to QCD jets passing the tau reconstruction, the uncertainty affects dominantly background processes with at least one fake tau candidate, including  $W \rightarrow \tau\nu$ , processes with top quarks and the remaining electroweak background. The effect of the misidentification uncertainty is, beside of the tau energy scale, one the major uncertainties on the final number of events and is found to be at the order of 11 % to 20 % for

the DTT selection and 25 % to 35 % for the STT selection. The uncertainty of the transfer factor propagates to an uncertainty of  $\pm 32\%$  on the final number of QCD multi-jet events in the STT region. Both uncertainties are treated as single overall normalization uncertainties, with no significant effect on the  $m_T^{\text{tot}}$  shape.

**Luminosity Uncertainty** A total systematic uncertainty of  $\delta\mathcal{L}/\mathcal{L} = 1.8\%$  has been estimated on the luminosity value in 2011 by the ATLAS collaboration [112]. The uncertainty is based on results of van der Meer scans, taking various sources like the beam posing or the emittance growth of the beam into account.

An overview about of the systematic uncertainties for each considered background component and an exemplary signal sample is provided in Table 6.16 and Table 6.17 for the DTT and STT region, respectively.

	Multi-jet	$Z/\gamma^* \rightarrow \tau\tau$	$W \rightarrow \tau\nu$	EW Bkg.	Top	$A_{20}^{300}$
Tau ID	+0.6 -0.7	+12.5 -11.8	+6.5 -6.5	+6.7 -6.6	+9.1 -8.8	+12.9 -12.1
Tau Energy Scale	+0.5 -0.7	5 – 25	5 – 22	5 – 25	8 – 25	5 – 30
Tau Electron Veto	+0.6 -0.6	+11.9 -11.3	+6.0 -6.0	+6.3 -6.2	+9.0 -8.7	+12.6 -11.8
Tau Mis-ID Eff.	+0.4 -0.4	+1.3 -1.3	+17.6 -18.4	+17.9 -19.1	+11.0 -12.2	+0.0 +0.0
$E_T^{\text{miss}}$	+0.4 -0.2	+1.4 -1.0	+0.7 -0.1	+0.4 -0.8	+0.1 -0.1	+0.2 -0.5
Jet	+0.1 -0.1	+0.6 -0.6	+0.0 -0.5	+0.2 -0.2	+0.2 -0.2	+0.1 -0.2
Trigger	-0.2 +0.2	+4.3 -2.9	+3.5 -3.5	+3.3 -3.3	+3.5 -3.3	+3.8 -3.7
Cross Section	—	+5.0 -5.0	+5.0 -5.0	+7.0 -7.0	+10.0 -10.0	+29.3 -29.2

**Table 6.16:** Systematic uncertainties for background and signal processes evaluated for the DTT selection. Paired uncertainty values represent the uncertainty on the normalization obtained by a  $\pm 1\sigma$  variation of the associated systematic component, while the interval uncertainties represent bin-by-bin related uncertainty values. The stated intervals outline the expected uncertainty values on the  $m_T^{\text{tot}}$  distribution. For the signal, the uncertainties of the b-associated production for a mass hypotheses of  $m_A = 300$  GeV and  $\tan\beta = 20$  are exemplarily presented.

### 6.6.1 Determination of the Modeling Uncertainties

The usage of Monte Carlo event generators implies the necessity to set additional parameters which are a-priori unknown. This includes parameters related to the *renormalization* and *factorization* scales [12], scale parameter to match contributions from the parton shower to the given matrix element, parameter which control the amount of initial and final state radiation as well as the choice of the considered *parton-density-function* (PDF).

The impact of each parameter is estimated in terms of the acceptance,  $A^{\text{MC}}$ , which is defined as the number of events passing the event selection requirements,  $N^{\text{MC}}$ , divided by the total



	Multi-jet	$Z/\gamma^* \rightarrow \tau\tau$	$W \rightarrow \tau\nu$	EW Bkg.	Top	$A_{40}^{600}$
Tau ID	—	+10.8 −10.2	+5.7 −5.7	+4.5 −4.5	+6.0 −5.9	+11.0 −10.4
Tau Energy Scale	—	10 – 25	10 – 28	8 – 24	12 – 30	5 – 19
Tau Electron Veto	—	+11.9 −11.2	+6.0 −6.0	+5.4 −5.4	+6.9 −6.7	+12.6 −11.9
Tau Mis-ID Eff.	—	+3.9 −3.8	+32.6 −34.9	+33.0 −33.5	+27.6 −24.9	+0.0 +0.0
Tau Transfer Factor	+32.1 −32.3	—	—	—	—	—
$E_T^{\text{miss}}$	—	+0.6 −0.6	+0.2 −0.2	+0.1 −0.1	+0.2 −0.2	+0.1 −0.1
Jet	—	+0.6 −0.6	+0.1 −0.1	+0.1 −0.1	+0.4 −0.4	+0.1 −0.1
Trigger	—	+5.0 −5.0	+5.0 −5.0	+5.0 −5.0	+5.0 −5.0	+5.0 −5.0
Cross Section	—	+5.0 −5.0	+5.0 −5.0	+7.0 −7.0	+10.0 −10.0	+11.6 −7.3

**Table 6.17:** Systematic uncertainties for background and signal processes evaluated for the STT selection. Paired uncertainty values represent the uncertainty on the normalization obtained by a  $\pm 1\sigma$  variation of the associated systematic component, while the interval uncertainties represent bin-by-bin related uncertainty values. The stated intervals outline the expected uncertainty values on the  $m_T^{\text{tot}}$  distribution. For the signal, the uncertainties of the b-associated production for a mass hypotheses of  $m_A = 600 \text{ GeV}$  and  $\tan \beta = 40$  are exemplarily presented.

number of generated events,  $N_{\text{tot}}^{\text{MC}}$ ,

$$A^{\text{MC}} = \frac{N^{\text{MC}}}{N_{\text{tot}}^{\text{MC}}} . \quad (6.20)$$

Any dependency of the acceptance on variations of the parameters is considered as a systematic modeling uncertainty:

$$\delta A^{\text{MC}} = |A_{\text{variation}}^{\text{MC}} - A_{\text{nominal}}^{\text{MC}}| . \quad (6.21)$$

The generation of Monte Carlo samples for each parameter variation is a resource-intensive process in terms of CPU usage and storage capacity. Due to limited resources, the acceptance studies have been performed without a dedicated detector simulation using particle level spectra after the hadronisation process. However, the impact of the detector simulation (and the sub-sequent reconstruction chain) on the acceptance dependency between the parameter variations is tested for a single parameter variation and is found to be insignificant. The particle level studies are performed using the Rivet analysis framework [260], by emulating the selection requirements for the detector level objects on particle level.

The presented studies have been performed in the context of the MSSM Higgs boson search using proton-proton collisions recorded at a center-of-mass energy of 8 TeV with the ATLAS detector in 2012 [224]. The 8 TeV results are applied for the 7 TeV data set, relying on the assumption that the uncertainty values are comparable between a center-of-mass energy of 7 TeV to 8 TeV within the estimated precision. This assumption is motivated by the fact, that the Monte Carlo generator setup is similar between both analyses and that the acceptance is unaffected by the overall change in the normalization<sup>15</sup> due to the increased cross section. The

<sup>15</sup>Any modification in the overall normalization equally affects the nominator and denominator in the acceptance formula.

modeling uncertainties are only considered for the two different signal processes: the MSSM Higgs boson production in association with b-quarks using the Sherpa [39] and the production via gluon-gluon fusion, generated with POWHEG+PYTHIA 6 [188, 193–195].

### Selection Requirements on Particle Level

Electron and muon particles are required to have a transverse momentum,  $p_T$ , of at least 15 GeV and 10 GeV, respectively and to be located within  $|\eta| < 2.4$ . Electron particles which are located within  $|\eta| \in [1.37, 1.52]$  are rejected in order to emulate the exclusion of electrons within the crack region of the ATLAS calorimeter. Hadronically decaying tau leptons are reconstructed by combining the four momentum vectors of all visible and stable<sup>16</sup> particles associated to the tau decay. The resulting transverse momentum of the visible tau decay system,  $p_{T,\text{vis}}^{\text{had}}$ , is required to be above 50 GeV and the pseudorapidity to be  $|\eta_{\text{vis}}^\tau| < 2.4$ , for both the leading and sub-leading tau lepton. Similar to the electrons, the crack region of  $1.37 < \eta_{\text{vis}}^\tau < 1.52$  is excluded.

An event is selected if the leading and sub-leading tau lepton have opposite electric charge and if no electron or muons particle, passing the selection requirements above, is found (emulating the lepton veto on detector level). In addition, both tau leptons are required to be separated in the azimuthal direction by  $|\Delta\phi(\tau_{\text{lead}}, \tau_{\text{sub}})| > 2.7$ . Based in the transverse momentum of the leading tau lepton,  $p_T^{\text{lead}}$ , an additional separation into two regions is performed, which corresponds to the single and di-tau trigger analysis regions on detector level: every event with  $p_T^{\text{lead}} < 150$  GeV is treated as a di-tau triggered event and otherwise as a single tau triggered event. For the di-tau triggered category, additional selection requirements on the missing transverse momentum,  $E_T^{\text{miss}} > 10$  GeV, and the total sum of transverse energy,  $\sum E_T > 160$  GeV, are performed. Both are calculated by combining the four momentum vectors of all stable and visible particles (excluding neutrinos) within  $|\eta| < 4.9$ .

### Modeling Uncertainties of the neutral MSSM Higgs Boson Production

For the b-associated MSSM Higgs boson production, the following set of parameter variations is considered:

**CKKW** The CKKW parameter [39] defines the matching scale between the matrix element calculation and the parton shower evolution. The nominal value of  $\sqrt{\frac{20}{E_{\text{CMS}}}}$  is changed to  $\sqrt{\frac{15}{E_{\text{CMS}}}}$  and  $\sqrt{\frac{30}{E_{\text{CMS}}}}$  for the down and up variation, respectively. The parameter  $E_{\text{CMS}}$  represents the center-of-mass energy.

**Factorization Scale** The factorization scale is weighted with a scaling factor of  $w = 0.5/2.0$  for the down/up variation, respectively.

**Renormalization Scale** The renormalization scale is weighted with a scaling factor of  $w = 0.9/1.1$  for the down/up variation, respectively.

**PDF Variation** The impact the parton-distribution function is evaluated by taking the difference in acceptance between the CT10 [169] and the CTEQ6L1 [206] PDF into account. The uncertainty is symmetrized for the up and down variation.

---

<sup>16</sup>This includes all particles with a proper lifetime  $\tau > 0.3 \times 10^{-10}$  s, with the exception of neutrinos.

$m_A$ [GeV]	250		300		500		700	
	DTT	STT	DTT	STT	DTT	STT	DTT	STT
CKKW15	0.5	-3.3	-0.1	-5.9	1.2	-0.3	2.3	0.6
CKKW30	0.2	9.8	-0.9	8.4	-0.9	-1.0	-1.4	-1.1
Fac. Scale $\downarrow$	-4.3	12.1	-2.8	0.5	-1.0	-1.6	-2.1	0.0
Fac. Scale $\uparrow$	4.5	-21.2	3.4	-8.1	2.8	1.4	1.3	1.6
Ren. Scale $\downarrow$	-0.3	3.1	0.6	-0.3	0.6	-1.0	-1.4	0.2
Ren. Scale $\uparrow$	-0.4	0.4	-0.4	-0.2	1.6	-0.7	-0.7	0.4
CTEQ6L1	1.1	-9.1	1.1	-1.7	3.6	1.5	2.3	1.9
Total	4.7	25.3	3.7	11.8	5.0	2.6	4.1	2.8

**Table 6.18:** Modeling uncertainties (in %) for the b-associated production of neutral MSSM Higgs bosons using the Sherpa Monte Carlo event generator.

For the production via the gluon-gluon fusion process, the factorization scale, the renormalization scale and the impact of the PDF are evaluated using the same procedure as for the b-associated production. In addition, the amount of initial and final state radiation is varied by scaling the corresponding value of the strong coupling parameter,  $\alpha_S$ , by  $\pm 20\%$ . The specified variations are following the internal recommendations at the time.

The uncertainty estimation is performed for mass value of the CP-odd Higgs boson,  $m_A$ , of 250 GeV, 400 GeV, 500 GeV and 700 GeV and  $\tan\beta = 20$  with about  $2 \times 10^5$  generated events per variation. The uncertainties for the remaining mass points are approximated with the uncertainties the closest mass point above.

In total, a systematic modeling uncertainties of 3.7% to 5.0% and 2.6% to 25.3% are found for the b-associated production in the di-tau and single tau triggered region, respectively, while for the production via gluon-gluon fusion uncertainty values of 1.2% to 2.4% and 1.1% to 8.2% are estimated. A full summary of the uncertainty values is provided in Table 6.18 and Table 6.19 for the b-associated production and the production via gluon-gluon fusion, respectively.

$m_A$ [GeV]	250		300		500		700	
	DTT	STT	DTT	STT	DTT	STT	DTT	STT
FSR $\downarrow$	0.3	-0.4	-0.8	0.1	0.1	-0.1	-0.8	-0.2
FSR $\uparrow$	-0.1	-3.7	-0.1	-0.4	0.8	0.2	-1.3	-0.1
ISR $\downarrow$	0.2	0.7	0.9	-0.2	1.0	0.8	0.1	0.6
ISR $\uparrow$	-0.6	5.9	-1.1	-1.2	-0.2	-0.5	-1.7	-0.8
Fac./Ren. Scale $\downarrow$	-0.9	-0.6	-0.7	0.3	0.4	0.1	1.1	-0.3
Fac./Ren. Scale $\uparrow$	-0.6	3.1	0.3	0.0	1.1	-0.1	-0.8	0.0
CTEQ6L1	-0.2	2.9	0.0	-0.7	0.2	0.7	0.4	-0.6
Total	1.2	8.2	1.6	1.5	1.7	1.1	2.4	1.1

**Table 6.19:** Modeling uncertainties (in %) for the production of neutral MSSM Higgs bosons in gluon-gluon fusion processes using the POWHEG Monte Carlo event generator.

## 6.7 Measurement Results

Within this chapter, the results of the MSSM Higgs boson search are presented for the DTT and STT regions. The observed number of events are compared to the SM background predictions, which are normalized to a luminosity of  $\sim 4.5 \text{ fb}^{-1}$ , including the full set of background correction weights and systematic uncertainties.

The final event yields for the individual background components and the observed number of events are presented in Table 6.20. For the DTT selection a total number of 2565 events are observed, which is in perfect agreement with the combined background prediction of  $2560 \pm 130 \text{ (stat.)} \pm 50 \text{ (syst.)}$  events. For the STT selection a total number of  $88.3 \pm 2.8 \text{ (stat.)} \pm 15 \text{ (syst.)}$  events is expected from the SM background and in total 81 events are observed. Similar to the DTT region, the observed number of events in the STT region is in good agreement with the SM prediction, within the given statistical and systematic uncertainties.

	DTT Region				STT Region			
	stat.		syst.		stat.		syst.	
Multi-jet	2320	$\pm 130$	$\pm 30$		39.7	$\pm 1.3$	$\pm 11$	
$Z/\gamma^* \rightarrow \tau\tau$	171	$\pm 5$	$\pm 40$		28.8	$\pm 1.9$	$\pm 8$	
$W \rightarrow \tau\nu$	56.8	$\pm 2.0$	$\pm 14$		14.4	$\pm 1.6$	$\pm 7$	
EW Bkg.	10.4	$\pm 0.4$	$\pm 2.5$		3.9	$\pm 0.5$	$\pm 1.6$	
Top	3.92	$\pm 0.26$	$\pm 0.8$		1.39	$\pm 0.13$	$\pm 0.6$	
Combined background	2560	$\pm 130$	$\pm 50$		88.3	$\pm 2.8$	$\pm 15$	
Observed number of events	2565				81			

**Table 6.20:** Final event yields for the predictions of various SM processes and the estimated QCD multi-jet contribution for the DTT and STT region are presented and compared to the observed number of events.

The event yields for each individual selection requirement are presented in Table 6.21 and Table 6.22 for the DTT and STT region, respectively.

The total transverse mass distributions for DTT and the STT region are presented in Figure 6.25, showing a good concordance between the predicted background distributions and the observed number of events. Within the possible resolution, which is dominantly restricted by the available number of events especially in the STT region, no local excess above the SM expectation is observed. For the  $m_T^{\text{tot}}$  distribution in the STT region, a slight systematic deficit in the number of observed events compared to the background prediction is observed above  $m_T^{\text{tot}} > 300 \text{ GeV}$ , which is reasonably covered by the combined statistical and systematic uncertainty.

To ensure a reasonable modeling of event kinematics, several auxiliary distributions for the DTT and STT selection are provided. Distributions of the transverse momenta and pseudorapidity

	Data	Comb. Bkg.	Multi-jet	$Z/\gamma^* \rightarrow \tau\tau$	$W \rightarrow \tau\nu$	EW Bkg.	Top
Di-tau trigger	943 651	—	—	$6980 \pm 40$	$21\,840 \pm 180$	$11\,700 \pm 100$	$12\,380 \pm 60$
BDT medium $\tau_{\text{lead}}$	77 104	—	—	$1808 \pm 19$	$4170 \pm 80$	$1038 \pm 22$	$392.2 \pm 3.3$
BDT medium $\tau_{\text{sub}}$	7542	—	—	$334 \pm 7$	$110.9 \pm 2.5$	$23.6 \pm 0.6$	$11.8 \pm 0.4$
$p_{\text{T}}^{\text{lead}} < 150 \text{ GeV}$	7520	—	—	$332 \pm 7$	$110.7 \pm 2.5$	$23.6 \pm 0.6$	$11.7 \pm 0.4$
$q_{\text{lead}} \times q_{\text{sub}} = -1 \text{ (OS)}$	4326	—	—	$322 \pm 7$	$97.6 \pm 2.4$	$20.6 \pm 0.6$	$10.7 \pm 0.4$
$ \Delta\phi(\tau_{\text{lead}}, \tau_{\text{sub}})  > 2.7$	3427	—	—	$209 \pm 6$	$60.7 \pm 2.1$	$11.1 \pm 0.4$	$4.04 \pm 0.27$
$E_{\text{T}}^{\text{miss}} > 10 \text{ GeV}$	2582	$2570 \pm 130$	$2320 \pm 130$	$172 \pm 5$	$57.0 \pm 2.0$	$10.4 \pm 0.4$	$3.92 \pm 0.26$
$\sum E_{\text{T}} > 160 \text{ GeV}$	2565	$2560 \pm 130$	$2320 \pm 130$	$171 \pm 5$	$56.8 \pm 2.0$	$10.4 \pm 0.4$	$3.92 \pm 0.26$

**Table 6.21:** Observed number of events and background predictions in the DTT region are presented after each selection requirement. The stated uncertainty values for each individual background process correspond to the respective statistical uncertainty.

	Data	Comb. Bkg.	Multi-jet	$Z/\gamma^* \rightarrow \tau\tau$	$W \rightarrow \tau\nu$	EW Bkg.	Top
Single tau trigger	198 234	—	—	$4270 \pm 40$	$16\,360 \pm 150$	$10\,950 \pm 100$	$12\,710 \pm 60$
$p_{\text{T}}^{\text{lead}} > 150 \text{ GeV}$	112 533	—	—	$455 \pm 9$	$1600 \pm 40$	$877 \pm 22$	$919 \pm 16$
BDT loose $\tau_{\text{lead}}$	11 132	—	—	$109 \pm 4$	$169 \pm 10$	$71 \pm 5$	$47.1 \pm 1.4$
BDT loose $\tau_{\text{sub}}$	226	$199 \pm 4$	$105.5 \pm 2.1$	$49.9 \pm 2.4$	$31.3 \pm 2.2$	$8.5 \pm 0.7$	$3.45 \pm 0.19$
$q_{\text{lead}} \times q_{\text{sub}} = -1 \text{ (OS)}$	140	$131.3 \pm 3.4$	$54.3 \pm 1.4$	$46.1 \pm 2.4$	$22.1 \pm 1.8$	$6.2 \pm 0.6$	$2.59 \pm 0.18$
$ \Delta\phi(\tau_{\text{lead}}, \tau_{\text{sub}})  > 2.7$	81	$88.3 \pm 2.8$	$39.7 \pm 1.3$	$28.8 \pm 1.9$	$14.4 \pm 1.6$	$3.9 \pm 0.5$	$1.39 \pm 0.13$

**Table 6.22:** Observed number of events and background predictions in the STT region are presented after each selection requirement. The stated uncertainty values for each individual background process correspond to the respective statistical uncertainty.

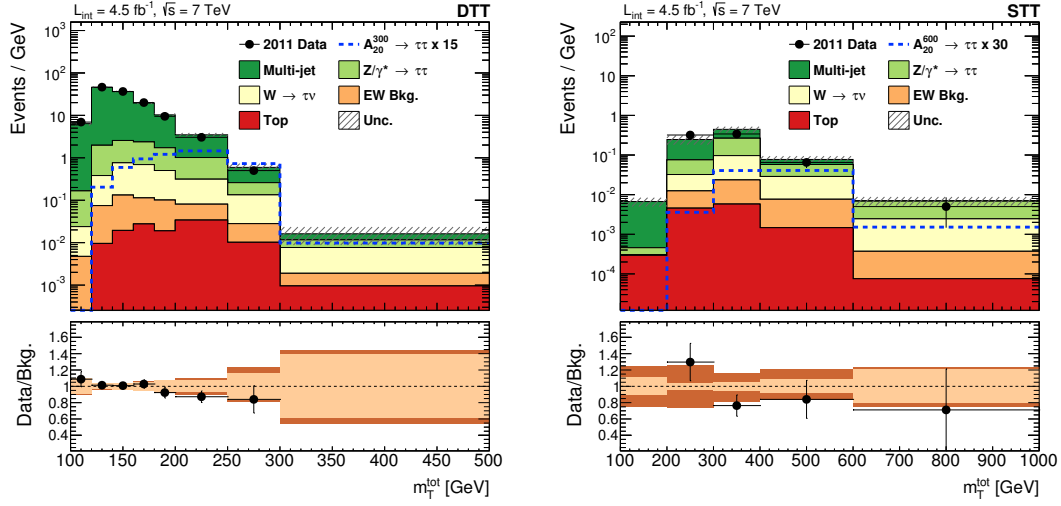


**Figure 6.25:** Total transverse mass distribution for the DTT (left) and STT (right) region. The observed data points (black dots) are compared to the SM expectation. The contributions from the individual processes (colored areas) are added up (stacked) and the combined statistical and systematic uncertainty is illustrated by the hatched area. A possible signal contribution is shown in the blue line (unstacked). The bottom area displays the ratio between the measurements and the SM prediction in which the light band represents the statistical uncertainty and the dark band the combined statistical and systematic uncertainty on the background prediction.

values of the leading and sub-leading tau candidates are presented in Figure 6.26 and Figure 6.27, respectively. The overall modeling of the tau kinematics is reasonably covered by the background predictions, except for a slight systematic shift in the transverse momentum of the sub-leading tau in the STT region (which is still covered by the combined uncertainty band) and a single bin fluctuation observed in the  $\eta^{\text{sub}}$  distribution.

The azimuthal angle between both tau candidates,  $|\Delta\phi(\tau_{\text{lead}}, \tau_{\text{sub}})|$ , is present in Figure 6.28, showing a good agreement for both the DTT and STT selection.

In Figure 6.29, the missing transverse momentum and the sum of the transverse energy are presented, testing the modeling of these observables, which are in particular sensitive to the contributions of neutrino particles. While the modeling of both observables is in good agreement with the observation for the DTT selection, a systematic shift between data and prediction is observed in the STT region. The shift is especially visible for  $E_T^{\text{miss}} > 40$  GeV or  $\sum E_T > 600$  GeV. For both observables, the combined background contribution surpasses the observed number of events, nevertheless the shift is covered by the combined statistical and systematic uncertainty.

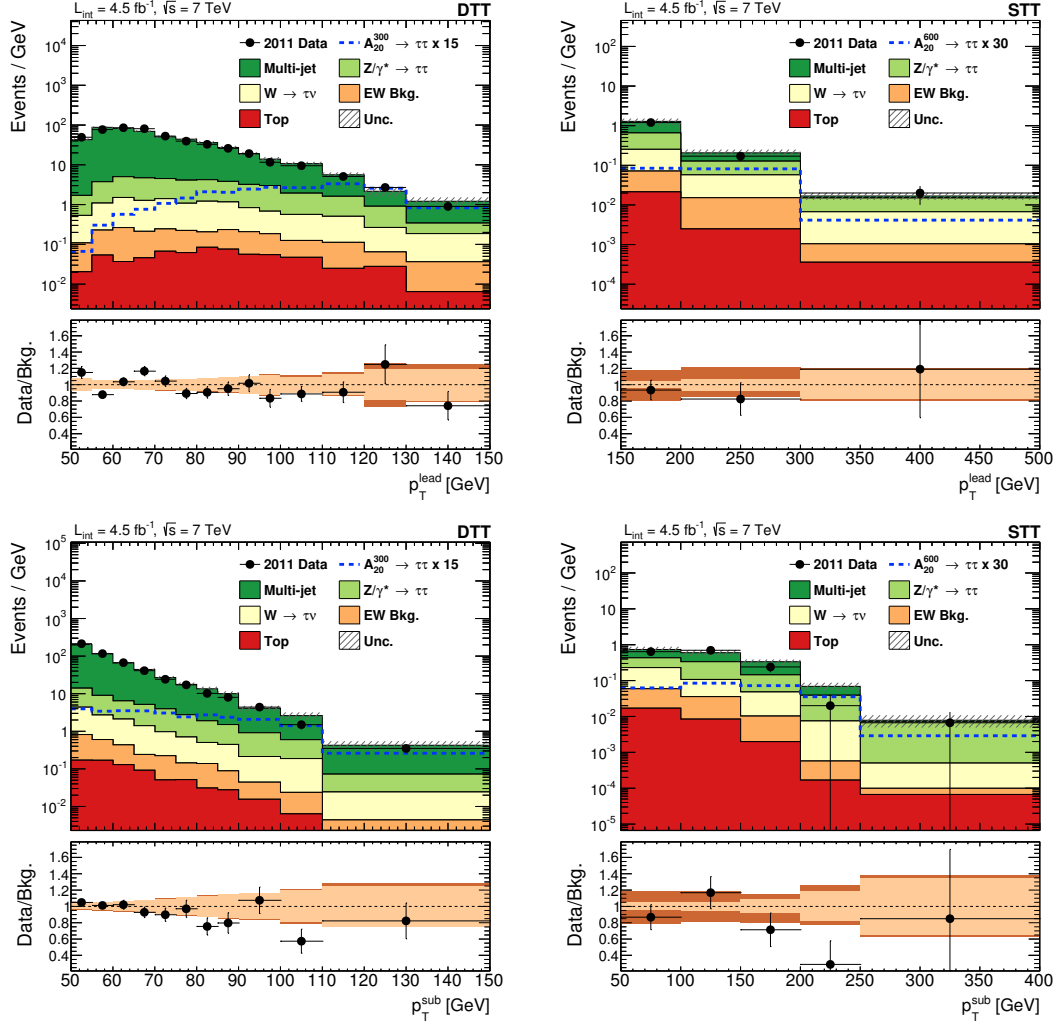


**Figure 6.26:** Transverse momentum for the leading (top) and sub-leading (bottom) tau candidate measured in the DTT (left) and STT (right) region. The observed data points (black dots) are compared to the SM expectation. The contributions from the individual processes (colored areas) are added up (stacked) and the combined statistical and systematic uncertainty is illustrated by the hatched area. A possible signal contribution is shown in the blue line (unstacked). The bottom area displays the ratio between the measurements and the SM prediction in which the light band represents the statistical uncertainty and the dark band the combined statistical and systematic uncertainty on the background prediction.



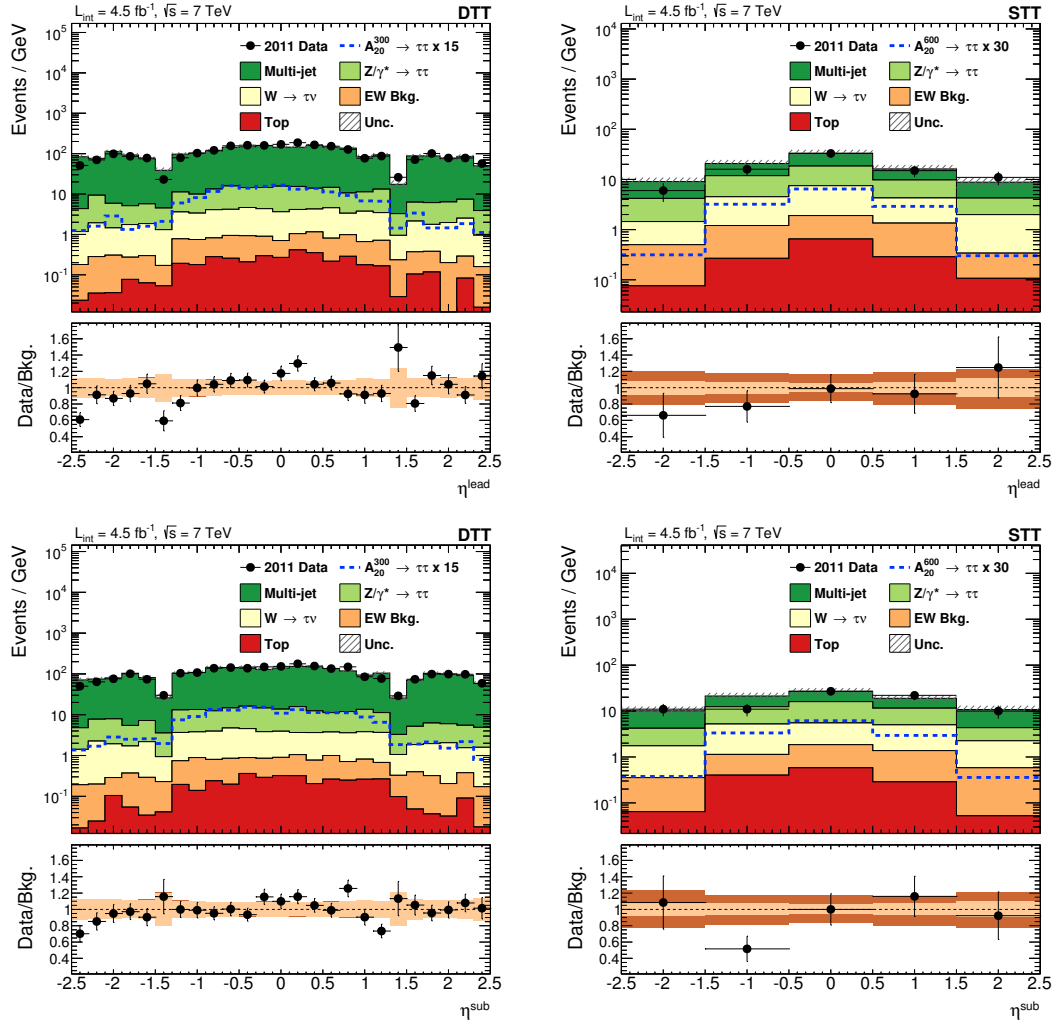


**Figure 6.27:** Pseudorapidity for the leading (top) and sub-leading (bottom) tau candidate measured in the DTT (left) and STT (right) region. The observed data points (black dots) are compared to the SM expectation. The contributions from the individual processes (colored areas) are added up (stacked) and the combined statistical and systematic uncertainty is illustrated by the hatched area. A possible signal contribution is shown in the blue line (unstacked). The bottom area displays the ratio between the measurements and the SM prediction in which the light band represents the statistical uncertainty and the dark band the combined statistical and systematic uncertainty on the background prediction.

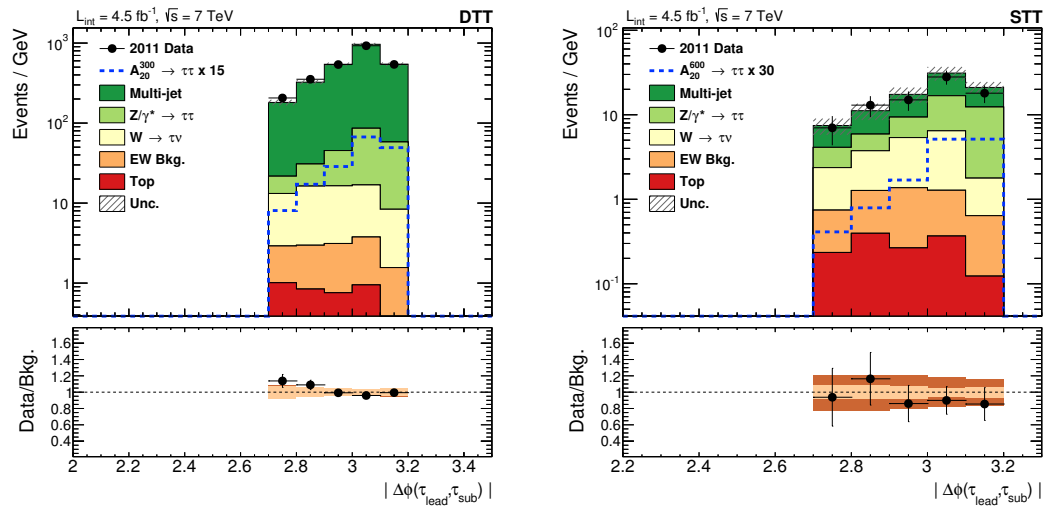


**Figure 6.28:** Azimuthal distance between the leading and sub-leading tau candidate in the DTT (left) and STT (right) region. The observed data points (black dots) are compared to the SM expectation. The contributions from the individual processes (colored areas) are added up (stacked) and the combined statistical and systematic uncertainty is illustrated by the hatched area. A possible signal contribution is shown in the blue line (unstacked). The bottom area displays the ratio between the measurements and the SM prediction in which the light band represents the statistical uncertainty and the dark band the combined statistical and systematic uncertainty on the background prediction.

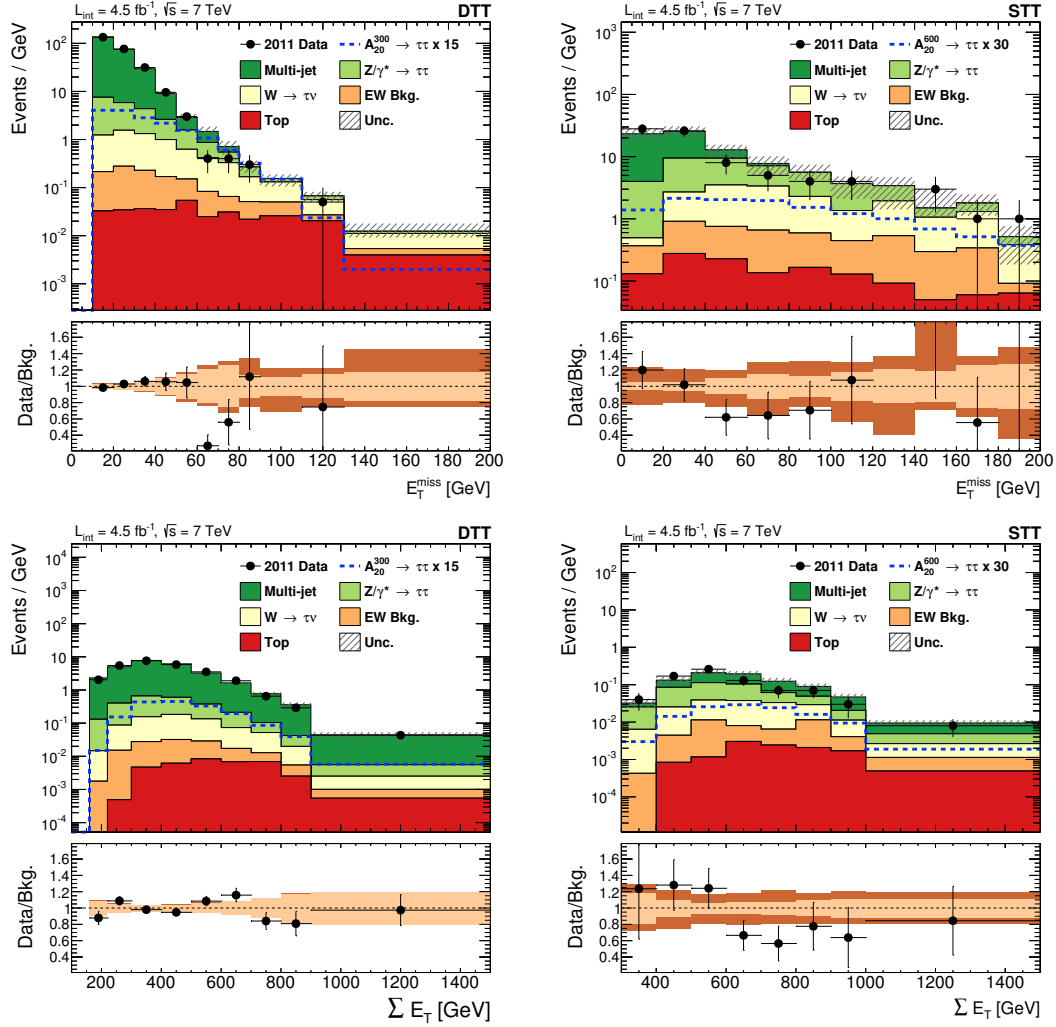


**Figure 6.29:** Missing transverse momentum (left) and total sum of transverse energy (right) in the DTT (left) and STT (right) region. The observed data points (black dots) are compared to the SM expectation. The contributions from the individual processes (colored areas) are added up (stacked) and the combined statistical and systematic uncertainty is illustrated by the hatched area. A possible signal contribution is shown in the blue line (unstacked). The bottom area displays the ratio between the measurements and the SM prediction in which the light band represents the statistical uncertainty and the dark band the combined statistical and systematic uncertainty on the background prediction.

## 6.8 Limit Setting

In searches for new physical phenomena, it is common to quantify the agreement between a considered theory and an acquired set of measurements in form a statistical significance, usually in form a *p-value* or a *significance level*. It is of particular interest, whether the measurements are in agreement with a hypothesis including only SM processes or an alternative hypothesis including new physical phenomena in addition to the SM.

Within the MSSM, only a positive contribution to the SM background processes with two hadronic decaying tau leptons is expected. Since no significant excess above the SM expectation is observed, an *exclusion limit* is evaluated, providing an estimation for the part of the  $m_A \times \tan \beta$  parameter space which can be disproved with a certain level of confidence. Exclusion limits for the analysis of the 2011 dataset are provided in the  $m_h^{\max}$  and  $m_h^{\text{mod}\pm}$  MSSM benchmark scenarios. In addition, the exclusion limits for the combination of the 2011 and 2012 dataset are stated.

### 6.8.1 Theoretical Foundation

The limits are derived using the method of profile likelihood, which is briefly summarized here for the case of a single alternative hypothesis.

The baseline is the definition of two hypotheses, the *null hypothesis* (or *background only hypothesis*),  $H_0$ , in which only SM processes contribute to the given measurement, and the *alternative hypothesis* (or *signal + background hypothesis*),  $H_1$ , which includes a signal model in addition to the SM contribution. Both hypotheses are expressed mathematically in form of probability density functions,

$$f(\mathbf{x}|H), \quad (6.22)$$

which represent the probability to obtain a set of measurements  $\mathbf{x} = (x_1, x_2, \dots, x_N)$  under the assumption that the hypothesis  $H$  is realized.

For the MSSM search, the measured data set is provided in form of a histogram:

$$\mathbf{x} = (n_1^{\text{obs}}, n_2^{\text{obs}}, \dots, n_N^{\text{obs}}), \quad (6.23)$$

where  $n_i^{\text{obs}}$  represent the observed number of events in the bin  $i$  of the total transverse mass distribution. The expected number of events,  $n_i^{\text{exp}}$ , can be expressed in the form:

$$n_i^{\text{exp}} = \mu s_i + b_i, \quad (6.24)$$

where  $s_i$  represent the nominal expected number of signal events and  $b_i$  the number of expected background events for the considered bin  $i$  of the mass distribution. The strength of the signal process is parametrized by an additional parameter  $\mu$ , where  $\mu = 0$  represents the background only hypothesis. The signal strength parameter is the final parameter of interest and extracted via a fit to the measured data sample.

The number of events in each bin is assumed to be described by a Poisson probability density function,

$$\mathcal{P}_i(n_i^{\text{obs}}; \mu, \boldsymbol{\theta}) = \frac{(\mu s_i + b_i)^{n_i^{\text{obs}}}}{n_i^{\text{obs}}!} e^{-(\mu s_i + b_i)}, \quad (6.25)$$

which allows the following definition of a likelihood function as a product of the Poisson distributions over all bins,

$$L(\mathbf{x}^{\text{obs}}; \mu, \boldsymbol{\theta}) = \prod_i^N \mathcal{P}_i(n_i^{\text{obs}}; \mu, \boldsymbol{\theta}) \quad (6.26)$$

$$= \prod_i^N \frac{(\mu s_i(\boldsymbol{\theta}) + b_i(\boldsymbol{\theta}))^{n_i^{\text{obs}}}}{n_i^{\text{obs}}!} e^{-(\mu s_i(\boldsymbol{\theta}) + b_i(\boldsymbol{\theta}))}. \quad (6.27)$$

In general, the expected number of signal and background events,

$$s_i(\boldsymbol{\theta}) \text{ and } b_i(\boldsymbol{\theta}), \quad (6.28)$$

depend on a set of additional *nuisance parameters*

$$\boldsymbol{\theta} = (\theta_1, \theta_2, \dots, \theta_m) \quad (6.29)$$

which are (in the most cases) a priori unknown and need to be extracted during the fit to the data sample, in addition to the signal strength parameter. The nuisance parameters represent the statistical,  $\gamma_q$ , and systematic uncertainties,  $\alpha_p$ ,

$$\boldsymbol{\theta} = (\boldsymbol{\alpha}; \boldsymbol{\gamma}) = (\alpha_1, \dots, \alpha_{m_p}; \gamma_1, \dots, \gamma_{m_q}) \text{ with } m_p + m_q = m, \quad (6.30)$$

where the systematic uncertainties<sup>17</sup> are in general constrained by auxiliary measurements.

### Likelihood Template Model

The complete likelihood model for the MSSM Higgs boson search is constructed using the *HistFactory* [261] framework. For the systematic uncertainties, the values  $\alpha_p$  are assumed to be described by a Gaussian distribution,

$$\mathcal{G}(\alpha_p) = \frac{1}{\sqrt{2\pi}\sigma_p} \exp \left[ -\frac{(a_p - \alpha_p)^2}{2\sigma_p^2} \right], \quad (6.31)$$

where  $a_p$  represents the corresponding auxiliary measurement and  $\sigma_p$  the corresponding uncertainty [261]. The parameter  $\alpha_p$  is scaled to ensure that the nominal value of the Gaussian distribution is zero with a variance of unity [261]. Subsequently, a variation of  $\alpha_p$  by a factor of  $\pm 1$  corresponds to a variation of the considered systematic uncertainty of  $\pm 1\sigma$ . The conversion between the scaled parameter  $\alpha_p$  and the actual effect on the average signal and background value is provided using interpolation methods [261].

Statistical uncertainties, arising from either a limited amount of generated events in the MC

<sup>17</sup>Here, the  $\alpha_p$  represent systematic uncertainties for the overall normalization uncertainties as well as uncertainties related to the shape of the distribution.

samples or due to a limited amount of events in the sideband regions for the data driven background estimations, are taken into account as nuisance parameters for the mean number of expected background events<sup>18</sup>,

$$b_i(\boldsymbol{\alpha}_i, \gamma_i), \quad (6.32)$$

To restrict the number of nuisance parameters during the fit, the statistical uncertainty per bin is only considered for the combined background

$$b_i(\boldsymbol{\alpha}_i, \gamma_i) := \gamma_i b_i(\boldsymbol{\alpha}_i), \quad (6.33)$$

instead of each contribution individually. The parameter  $\gamma_i$  allows to account for a possible difference between the true number of expected background events and the number obtained from the Monte Carlo simulations. The statistical uncertainties are modeled using a Poisson constraint term,

$$\mathcal{P}(m_i; \gamma_i \tau_i) = \frac{(\gamma_i \tau_i)^{m_i}}{m_i!} e^{-\gamma_i \tau_i}, \quad (6.34)$$

where

$$\tau_i = \left( \frac{b_i}{\delta_i} \right)^2 \quad (6.35)$$

with  $\delta_i$  representing the total statistical uncertainty of the combined background. The method itself is based on results of R. Barlow and C. Beeston [262] using the implementation within the *HistFactory* framework [261]. Since the Poisson distribution is undefined for non-integer values, the distribution is evaluated based on the *Gamma* function, using the functionality of the *RooPoisson* package [263].

Given the definitions above, the full likelihood model can be written in the form

$$L(\mathbf{x}^{\text{obs}}; \mu, \boldsymbol{\theta}(\boldsymbol{\alpha}, \boldsymbol{\gamma})) = \prod_c \prod_i^N \mathcal{P}_i(n_i^{\text{obs}}; \mu, \boldsymbol{\alpha}, \boldsymbol{\gamma}) \cdot \mathcal{P}(\tau_i; \gamma_i \tau_i) \prod_p^{m_p} \mathcal{G}(\alpha_p), \quad (6.36)$$

where the parameter  $c$  characterize the product over the considered analysis categories:  $c \in \{\text{DTT}, \text{STT}\}$ .

### Test Statistic and p-Values for Exclusion Limits

The agreement between a hypothesis, with a specified signal strength  $\mu$ , and a given observation is now determined using the following likelihood ratio as *test statistic*<sup>19</sup>,

$$t(\mu) = -2 \ln \lambda(\mu) = -2 \ln \frac{L(\mu, \hat{\boldsymbol{\theta}})}{L(\hat{\mu}, \hat{\boldsymbol{\theta}})}, \quad (6.37)$$

which is constructed from the measured data set  $\mathbf{x}^{\text{obs}}$  and is a function of the strength parameter  $\mu$ . The nominator represents the *conditional maximized likelihood function*, where  $\hat{\boldsymbol{\theta}}$  is the conditional maximum likelihood estimator for the nuisance parameter set  $\boldsymbol{\theta}$  for a specific value of  $\mu$ . In contrast, the denominator represents the *unconditional maximized likelihood function*,

<sup>18</sup>Statistical uncertainties on the expected signal contributions are not considered.

<sup>19</sup>The parameter  $\mathbf{x}^{\text{obs}}$  is suppressed within the further context.

where  $\hat{\mu}$  and  $\hat{\theta}$  are the maximum likelihood estimators for the signal strength and the nuisance parameter set which maximize the likelihood function simultaneously.

Due to the natural logarithm, the test statistic can take values between zero to  $\infty$ , where values close to zero correspond to a good agreement between the observation and the assumed signal strength  $\mu$  and, subsequently, an increase of  $t(\mu)$  implies a greater incompatibility between the measurement and the considered hypothesis.

Two additional requirements are demanded for the test statistic:

1. since the goal is the determination of an *upper* limit on the signal strength parameter  $\mu$ , hypotheses in which  $\mu$  is below the unconditional maximum likelihood estimator  $\hat{\mu}$  are not considered and the test statistic is set to zero;
2. the expected contribution from the MSSM signal model is always positive, which is represented in the test statistic by replacing the unconditional maximum likelihood function in the denominator for negative values of  $\hat{\mu}$  with the conditional maximum likelihood function for the background only hypotheses ( $\mu = 0$ ).

Both requirements lead to the following modified version of the test statistic,

$$t(\mu) := \tilde{q}_\mu = \begin{cases} -2 \ln \frac{L(\mu, \hat{\theta})}{L(0, \hat{\theta}(\mu=0))} & \hat{\mu} < 0, \\ -2 \ln \frac{L(\mu, \hat{\theta})}{L(\hat{\mu}, \hat{\theta})} & 0 \leq \hat{\mu} < \mu, \\ 0 & \hat{\mu} > \mu, \end{cases} \quad (6.38)$$

where  $\hat{\theta}(\mu = 0)$  represents the conditional maximum likelihood estimators for the nuisance parameter set in the case of the background only hypothesis.

The incompatibility between a measurement and a given hypothesis is quantified by the *p-value*

$$p_\mu^{\text{obs}} = \int_{\tilde{q}_\mu^{\text{obs}}}^{\infty} f(\tilde{q}_\mu | \mu') d\tilde{q}_\mu, \quad (6.39)$$

which is the integral over the probability density function of the test statistic (*sampling distribution*),  $f(\tilde{q}_\mu | \mu')$ , starting from the measured value of the test statistic for a specific value of  $\mu$  up to  $+\infty$  (Figure 6.30). The parameter  $\mu'$  represents the signal strength in the measured data set. The p-value correspond to the probability to obtain a data set from the given hypothesis which is at least at the same level of disagreement (or worse) with the hypothesis itself compared to the observed data set, under the assumption that the considered hypothesis is realized in nature.

In case of a discovery, the p-value is estimated for the background only hypothesis to quantify the disagreement between the measurement and SM only hypothesis and a discovery of a new phenomenon is usually claimed if the p-value is below  $2.87 \times 10^{-7}$  which corresponds to a

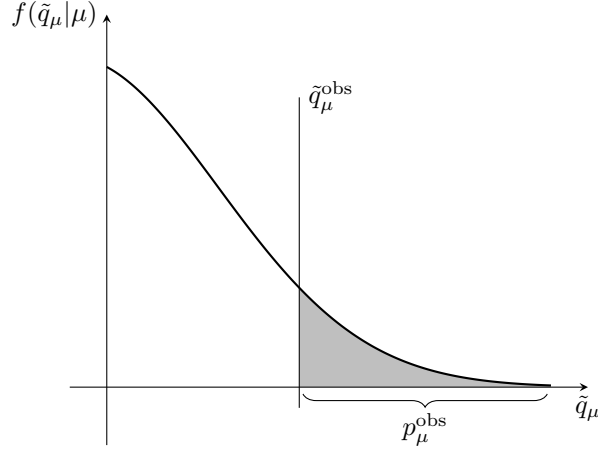


**Figure 6.30:** Illustration of the observed p-value estimation from the probability density function,  $f(\tilde{q}_\mu|\mu)$ , of the test statistic.

significance<sup>20</sup> of  $Z = 5\sigma$ . For an exclusion limit instead, the p-value is calculated against a hypothesis with  $\mu > 0$  in order to estimate the corresponding value of  $\mu$  at which the disagreement with the data is at least  $p_\mu^{\text{obs}} = 0.05$ , which corresponds to a confidence level of 95 %.

### Asymptotic Approximation of the Sampling Distribution

In order to evaluate the p-value given in Eq. (6.39) it is necessary to obtain the sampling distribution  $f(\tilde{q}_\mu|\mu')$ . Within this study<sup>21</sup>, an asymptotic approximation of the sampling distribution [264] is used. Alternatively, it is possible to derive the sampling distribution via Monte Carlo methods but these techniques require (in general) a sufficient amount of pseudo-experiments to populate the tails of the sampling distribution, which involves a substantial amount of computing resources and computing time.

The mathematical basis is the following approximation of the likelihood ratio, based on results of Wald [264, 265],

$$-2 \ln \lambda(\mu) = \frac{(\mu - \hat{\mu})^2}{\sigma^2} + \mathcal{O}(1/\sqrt{N}) , \quad (6.40)$$

for a single parameter of interest. The maximum likelihood estimator  $\hat{\mu}$  is described by a Gaussian distribution with a mean value  $\mu'$  and a standard deviation  $\sigma$ . Neglecting the additional terms of the order  $\mathcal{O}(1/\sqrt{N})$ , where  $N$  represents the size of the data sample, allows the following approximation of the test statistic [264]:

$$\tilde{q}_\mu = \begin{cases} \frac{\mu^2}{\sigma^2} - \frac{2\mu\hat{\mu}}{\sigma^2} & \hat{\mu} < 0, \\ \frac{(\mu - \hat{\mu})^2}{\sigma^2} & 0 \leq \hat{\mu} < \mu, \\ 0 & \hat{\mu} > \mu, \end{cases} \quad (6.41)$$

<sup>20</sup>The significance  $Z = \Phi^{-1}(1 - p)$  is defined as the number of standard deviations of a Gaussian distribution it would take to find a value above  $Z$  with the probability  $p$ . The function  $\Phi^{-1}$  is inverse of the cumulative Gaussian distribution.

<sup>21</sup>The same method has been utilized for the equivalent MSSM studies based on the 2011 and 2012 data sets.



and the sampling distribution [264],

$$f(\tilde{q}_\mu|\mu') = \Phi\left(\frac{\mu' - \mu}{\sigma}\right) \delta(\tilde{q}_\mu) + \begin{cases} \frac{1}{2} \frac{1}{\sqrt{2\pi}} \frac{1}{\sqrt{\tilde{q}_\mu}} \exp\left[-\frac{1}{2} \left(\sqrt{\tilde{q}_\mu} - \frac{\mu - \mu'}{\sigma}\right)^2\right] & 0 < \tilde{q}_\mu \leq \frac{\mu^2}{\sigma^2}, \\ \frac{1}{\sqrt{2\pi}(2\mu/\sigma)} \exp\left[-\frac{1}{2} \frac{(\tilde{q}_\mu - \mu^2 - 2\mu\mu'/\sigma^2)^2}{(2\mu/\sigma)^2}\right] & \tilde{q}_\mu > \frac{\mu^2}{\sigma^2}, \end{cases} \quad (6.42)$$

which follows a *non-central chi-square distribution*. The symbol  $\Phi$  represents the cumulative distribution of a normal Gaussian, with a mean of zero and the variance equals one.

Within this approximation, the p-value can be expressed with

$$p_\mu = 1 - F(\tilde{q}_\mu|\mu' = \mu) \quad (6.43)$$

where  $F(\tilde{q}_\mu|\mu')$  represents the cumulative sampling distribution,

$$F(\tilde{q}_\mu|\mu') = \begin{cases} \Phi\left(\sqrt{\tilde{q}_\mu} - \frac{\mu - \mu'}{\sigma}\right) & 0 < \tilde{q}_\mu \leq \frac{\mu^2}{\sigma^2}, \\ \Phi\left(\frac{\tilde{q}_\mu - \mu^2 - 2\mu\mu'/\sigma^2}{2\mu/\sigma}\right) & \tilde{q}_\mu > \frac{\mu^2}{\sigma^2}. \end{cases} \quad (6.44)$$

### Asimov Data Set

The *Asimov data set* [264] is an artificially constructed data set, which is defined via the maximum likelihood estimator of the theory parameters. By definition, the estimators for all parameters return the true parameter values if the likelihood function is evaluated with the Asimov data set instead of the observed data set,

$$\lambda_A(\mu) = \frac{L_A(\mu, \hat{\boldsymbol{\theta}})}{L_A(\hat{\mu}, \hat{\boldsymbol{\theta}})} = \frac{L_A(\mu, \hat{\boldsymbol{\theta}})}{L_A(\mu', \boldsymbol{\theta})}, \quad (6.45)$$

where  $\mu'$  and  $\boldsymbol{\theta}$  represent the true values for the signal strength and the nuisance parameters, respectively. The function  $L_A$  represents the likelihood function evaluated using the Asimov data set.

The Asimov data set can be used to determine the variance  $\sigma$  on the estimator of the signal strength,  $\hat{\mu}$  [264]. Using the Asimov data set for Eq. (6.40) (neglecting the  $\mathcal{O}(1/\sqrt{N})$  terms) leads to

$$-2 \ln \lambda_A(\mu) = \frac{(\mu - \mu')^2}{\sigma^2}, \quad (6.46)$$

where the signal strength estimator,

$$\hat{\mu} = \mu', \quad (6.47)$$

is set to its true value due the properties of the Asimov data set. Subsequently, the variance  $\sigma$  can be expressed in the form

$$\sigma^2 = \frac{(\mu - \mu')^2}{\tilde{q}_{\mu,A}}, \quad (6.48)$$

where  $\tilde{q}_{\mu,A}$  represents the test statistic (Eq. (6.41)) evaluated for the Asimov data set.

### Expected and Observed Upper Limit

The observed upper limit on the signal strength,  $\mu_{\text{up}}^{\text{obs}}$ , is derived from the p-value given in Eq. (6.39) and Eq. (6.43) using the  $CL_S$  method [266]. Within this method, the p-value is replaced by

$$p'_\mu = \frac{p_\mu}{1 - p_b}, \quad (6.49)$$

where  $p_b$  represents the reversed p-value for a background only data set,

$$p_b = 1 - \int_{\tilde{q}_\mu^{\text{obs}}}^{\infty} f(\tilde{q}_\mu|0) d\tilde{q}_\mu. \quad (6.50)$$

If a p-value is found to be below a specified threshold  $\alpha$ , the corresponding signal strength is defined to be excluded at a confidence level (CL) of  $1 - \alpha$  and the upper limit on the signal strength is defined as the  $\mu$  value which satisfies

$$p'_{\mu_{\text{up}}} = \alpha. \quad (6.51)$$

It is common practice for upper limits to set  $\alpha = 0.05$  and subsequently quote the upper limits at a confidence level of 95 %. Using the approximation from Eq. (6.40), the upper limit can be expressed with

$$\mu_{\text{up}}^{\text{obs}} = \hat{\mu} + \sigma \Phi^{-1}(1 - \alpha). \quad (6.52)$$

where  $\Phi^{-1}$  represents the inverse of the cumulative distribution of a normal Gaussian [264].

The *median*, or *expected*, upper limit including the corresponding uncertainties can be evaluated using the Asimov data set. Since for an upper limit, the alternative hypothesis is the background only hypothesis, the assumed signal strength  $\mu'$  is set to zero [264]. For the  $CL_S$  method, the median limit can be expressed by

$$\mu_{\text{up} \pm k\sigma} = \sigma [\Phi^{-1}(1 - \alpha \Phi(k)) \pm k], \quad (6.53)$$

with

$$\sigma = \frac{\mu}{\sqrt{\tilde{q}_{\mu, \Lambda}}}. \quad (6.54)$$

The uncertainties on the upper limit are reflected by variation of  $\hat{\mu}$  by a factor of

$$k = \dots, -2, -1, 0, 1, 2, \dots \quad (6.55)$$

multiplied with  $\sigma$ .

Subsequently, the expected upper limit for  $k = 0$  is

$$\mu_{\text{up}}^{\text{exp}} = \mu_{\text{up}}^{\text{med}} = \sigma \Phi^{-1}(1 - 0.5\alpha). \quad (6.56)$$

### Interpretation of the Upper Limits Within the $m_A \times \tan \beta$ Plane

The resulting upper limits on the signal strength parameters are interpreted within the  $m_A \times \tan \beta$  plane by determining the contour with the requirement

$$\mu_{\text{up}} = 1, \quad (6.57)$$

bordering the region in the parameter space in which the nominal MSSM hypothesis is excluded with CL of 95%. The upper limits are determined for a fixed grid of points  $(m_A^i, \tan \beta^j)$ :

$$m_A^i = \{140, 150, 170, 200, 250, 300, 350, 400, 450, 500, 550, 600, 650, 700, 750, 800\},$$

and

$$\tan \beta^j = \{10, 13, 15, 16, 20, 23, 25, 26, 30, 35, 40, 45, 50, 55, 60\}.$$

The  $\mu_{\text{up}}$  contour is evaluated using a linear interpolation between neighboring points in  $m_A$  and  $\tan \beta$ . For contour values above 60 in  $\tan \beta$ , the interpolation is performed using upper limits values within the  $\tan \beta = [55, 60]$  interval.

### 6.8.2 Exclusion Limits for the 2011 Data Set

Upper limits for the search of MSSM Higgs bosons using the 2011 data set recorded with the ATLAS detector are presented at a confidence level of 95 %, interpreted within the  $m_A \times \tan \beta$  plane for the  $m_h^{\max}$  and  $m_h^{\text{mod}\pm}$  benchmark scenarios.

The results for the  $m_h^{\max}$  scenario are shown in Figure 6.31a for the combination between the DTT and STT analysis category and in Figure 6.31b for the individual channels, both for a mass range of 140 GeV to 800 GeV in  $m_A$ . The observed upper limit is found to be in a reasonable agreement with of the expected limit of a background only Asimov data sample. While the upper limit in the relative low mass spectrum ( $m_A < 350$  GeV) is dominated by the DTT category, the STT category provides a significant sensitivity boost for the high mass spectrum ( $m_A > 350$  GeV), which contributes to the large improvement compared to the previous analysis of the 2011 data set [223]. For the mass region below 160 GeV, the expected sensitivity is found to be below the sensitivity of the previous analysis, presumably due to missing categorization in b-tagged jets in the re-analysis. However, the sensitivity in the relative low mass region is usually dominated by the di-leptonic and semi-leptonic decay channels, while the hadronic decay channel improves the sensitivity towards higher mass values.

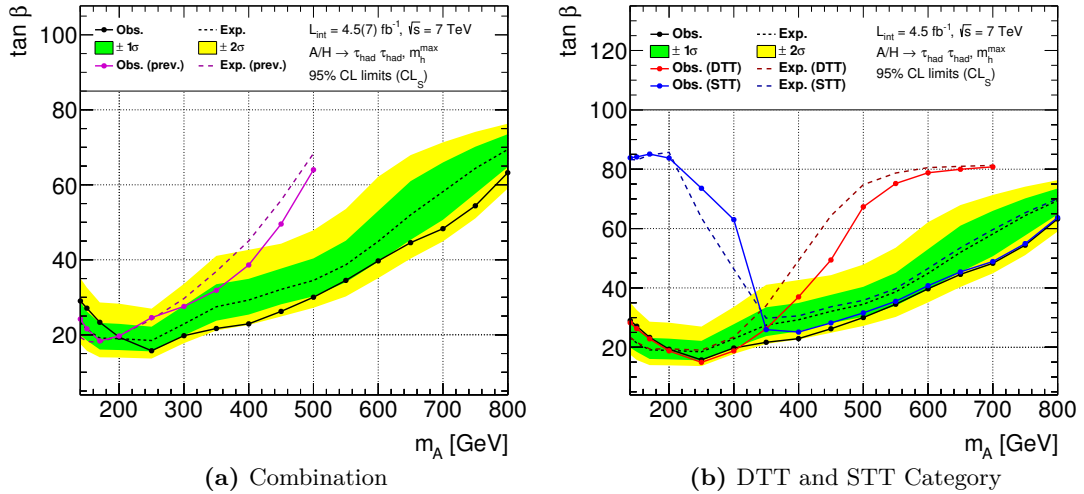


**Figure 6.31:** Upper limits on  $m_A \times \tan \beta$  for the nominal MSSM Higgs boson hypothesis in the  $m_h^{\max}$  benchmark scenario are presented. The solid black line represents the observed limit, while the dashed black line represents the expected median limit with the corresponding  $\pm 1\sigma$  and  $\pm 2\sigma$  uncertainty bands, indicated by the shaded areas. The parameter region above the observed limit is excluded at a confidence level of 95 %.

A summary for the upper limit  $\tan \beta$  values in the  $m_h^{\max}$  benchmark scenario is provided in Table 6.23.

The corresponding observed upper limits on  $\mu$  as a function of  $m_A$  and  $\tan \beta$  are presented in Figure 6.32, using a linear interpolation method to estimate the upper limits between the considered grid points (Section 6.8.1).

$m_A$ [GeV]	observed	expected	$+2\sigma$	$+1\sigma$	$-1\sigma$	$-2\sigma$
140	28.9	23.0	34.9	28.5	19.7	17.3
150	26.9	21.2	32.3	25.9	18.3	15.6
170	23.3	19.0	28.4	22.9	15.9	13.9
200	19.4	18.9	28.1	22.8	15.8	13.8
250	15.8	18.4	26.7	22.0	15.5	13.6
300	19.7	22.8	33.3	27.5	19.7	17.6
350	21.5	27.1	40.3	33.0	23.4	20.9
400	22.7	28.9	41.9	34.5	25.0	22.4
450	25.9	31.6	43.6	37.1	27.8	24.6
500	29.7	34.2	47.1	39.8	29.9	26.9
550	34.2	38.3	52.7	44.6	33.7	29.9
600	39.3	44.5	61.4	52.4	39.1	34.8
650	44.2	51.4	67.4	60.3	44.8	39.9
700	47.8	57.5	71.0	65.5	50.0	44.5
750	53.9	63.9	73.9	69.8	57.1	50.4
800	62.8	69.1	76.1	73.3	64.3	58.4

**Table 6.23:** Upper limit  $\tan\beta$  values for the nominal MSSM  $m_h^{\max}$  benchmark scenario at a confidence level of 95%.

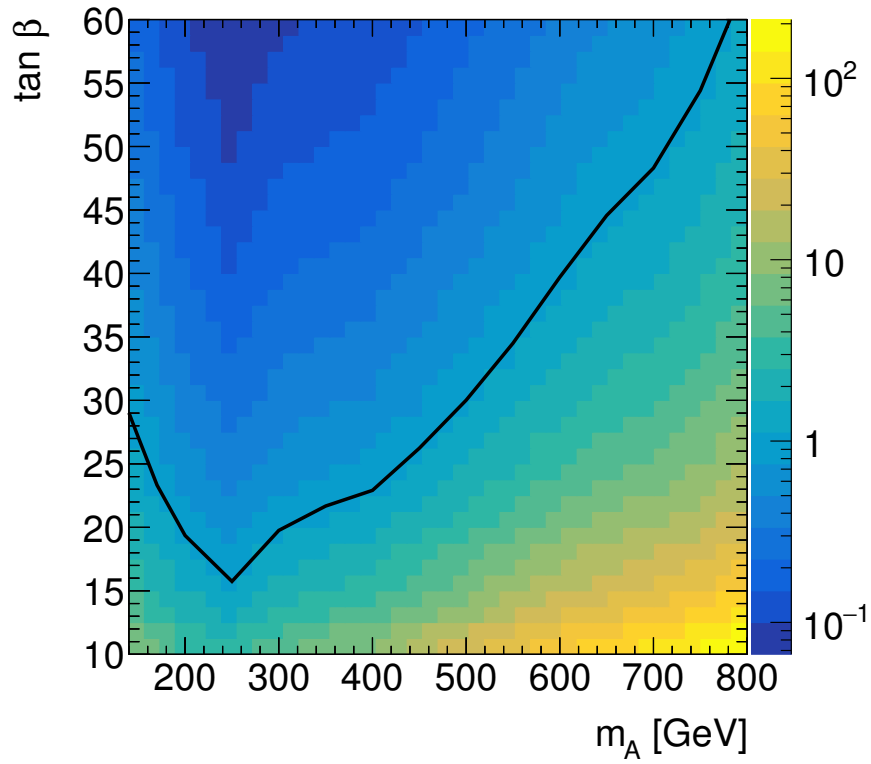


**Figure 6.32:** Observed upper limit of  $\mu$  at a confidence level of 95 % parametrized in  $m_A$  and  $\tan \beta$  for the  $m_h^{\text{max}}$  benchmark scenario. The solid black line represents the contour for  $\mu_{\text{up}} = 1$ .

Exclusion limits for the  $m_h^{\text{mod-}}$  and  $m_h^{\text{mod+}}$  benchmark scenarios are presented in Figure 6.33a and Figure 6.33b, respectively, both with a combination of the DTT and STT category. The general behavior of the  $m_h^{\text{mod}}$  scenarios is similar to the  $m_h^{\text{max}}$  scenario: the sensitivity of the  $m_h^{\text{mod-}}$  scenario is about one unit in  $\tan\beta$  weaker for the low mass range ( $m_A < 400$  GeV), while the sensitivity of the  $m_h^{\text{mod+}}$  scenario is reduced by a factor of 1 to 2 values in  $\tan\beta$  for the full mass range.

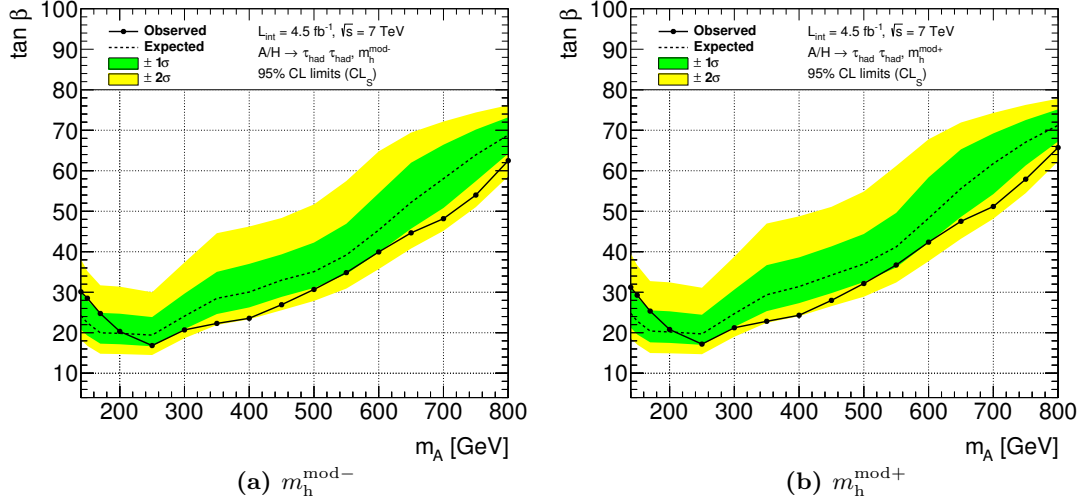


**Figure 6.33:** Upper limits on  $m_A \times \tan\beta$  for the nominal MSSM Higgs boson hypothesis in the  $m_h^{\text{mod-}}$  (left) and  $m_h^{\text{mod+}}$  (right) benchmark scenario are presented. The solid black line represents the observed limit, while the dashed black line represents the expected median limit with the corresponding  $\pm 1\sigma$  and  $\pm 2\sigma$  uncertainty bands, indicated by the shaded areas. The parameter region above the observed limit is excluded at a confidence level of 95 %.

### Post-Fit $m_T^{\text{tot}}$ Distributions

The total transverse mass distributions for the DTT and STT category after a conditional maximum likelihood fit for the background only hypothesis ( $\mu = 0$ ) are presented in Figure 6.34a and Figure 6.34b, respectively. The estimated combined post-fit background is reduced by a factor of 10 % to 20 % compared to the pre-fit measurements for  $m_T^{\text{tot}}$  values above 180 GeV in the DTT category and  $m_T^{\text{tot}}$  values above 300 GeV in the STT category, to account for the observed overestimation of the background composition compared to the measurements. For mass values above 300 GeV in the DTT category a rather strong reduction of about 60 % is observed, due to the fact, that no data events are found for this region. However, the effect on the final limit is small, because the exclusion limits for mass hypotheses sensitive to this region are dominated by the STT category.

A summary of the expected event yields for each individual background process after of the conditional maximum likelihood fit is provided in Table 6.24. The stated uncertainty values correspond to the combined statistical and systematic uncertainty value after the fit. For the DTT category, the combined mean number of background events is slightly reduced from  $2560 \pm 130$  (stat.)  $\pm 50$  (syst.) to  $2540 \pm 40$  (comb.), and for the STT category from  $88.3 \pm$

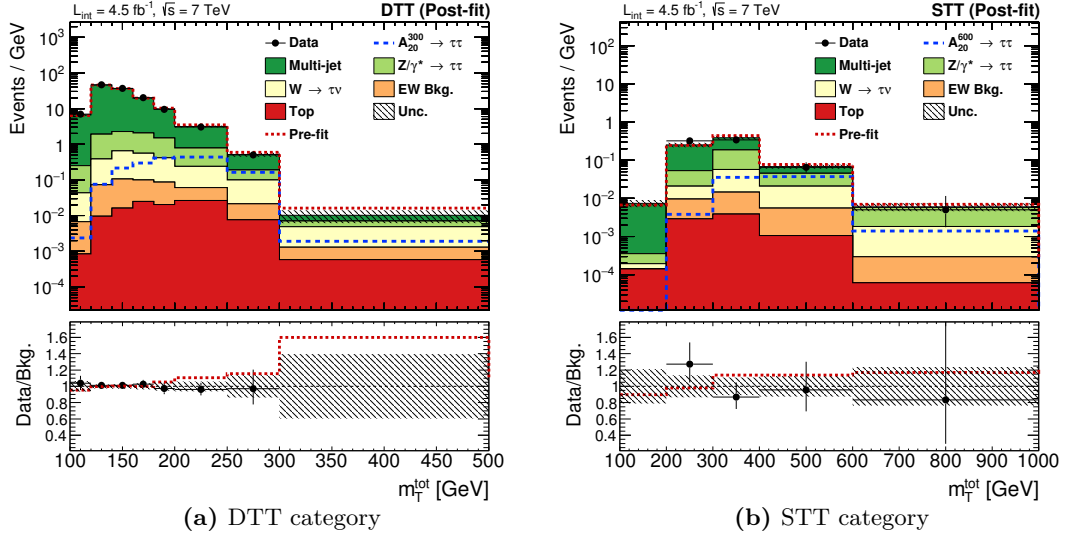


**Figure 6.34:** Post-fit distributions of the total transverse mass observable for the DTT (left) and STT (right) region. The observed data points (black dots) are compared to the SM expectations, estimated through a conditional maximum likelihood fit for the background only hypothesis ( $\mu = 0$ ). The contributions from the individual processes (colored areas) are added up (stacked) and the combined statistical and systematic uncertainty after the fit is illustrated by the hatched area. A possible signal contribution is shown in the blue line (unstacked). The bottom area displays the ratio between the measurements and the SM prediction. The pre-fit estimation for the combined SM background is represented by the red line.

$2.8(\text{stat.}) \pm 15(\text{syst.})$  to  $82 \pm 8(\text{comb.})$ . In both categories, the estimated multi-jet background is in general increased, while the estimated event numbers for the remaining processes are reduced by the likelihood fit, in particular the estimations for the  $Z \rightarrow \tau\tau$  and  $W \rightarrow \tau\nu$  processes.

### Validation of the Maximum Likelihood Estimators

In order to verify the validity of the obtained upper limits, the *pull distributions* of the maximum likelihood estimators for the nuisance parameter  $\hat{\theta}$  are tested using pseudo-experiments. The pull of a given nuisance parameter  $\theta_i$  is defined by,

$$\frac{\hat{\theta}_i - \theta_i^{\text{gen}}}{\sigma(\theta_i)} \quad (6.58)$$

where  $\hat{\theta}_i$  represents the estimator for the given nuisance parameter,  $\theta_i^{\text{gen}}$  represents the value used for the generation of the pseudo-experiments and  $\sigma(\theta_i)$  represents the estimated uncertainty. If the pull is unbiased and the estimated uncertainty is reliable, it is expected that the pull distribution can be described by a normalized Gaussian distribution with a mean around zero and a standard deviation of unity [267].

Pull distributions are generated for a Higgs boson mass of  $m_A = 300 \text{ GeV}$  and  $\tan \beta = 20$  and presented for the six major nuisance parameter in Figure 6.35, focusing on the  $\alpha$  parameter. The nuisance parameter are determined for a signal strength parameter of  $\mu = \mu' = 1$ . The black line



	DTT Region		STT Region	
Multi-jet	2331	$\pm 34$	44	$\pm 8$
$Z/\gamma^* \rightarrow \tau\tau$	153	$\pm 20$	25.3	$\pm 3.3$
$W \rightarrow \tau\nu$	45	$\pm 7$	9.4	$\pm 3.2$
EW Bkg.	8.2	$\pm 1.3$	2.7	$\pm 0.8$
Top	3.2	$\pm 0.4$	1.02	$\pm 0.24$
Combined post-fit background	2540	$\pm 40$	82	$\pm 8$
Observed number of events	2565		81	

**Table 6.24:** Expected number of events for various SM processes in the DTT and STT category are presented and compared to the observed number of events. The background predictions are estimated from a conditional likelihood fit to the background only hypothesis ( $\mu = 0$ ). The stated uncertainty for each process correspond to the combined statistical and systematic uncertainty derived by the fit.

represents the pull distribution obtained from the pseudo-experiments and the red line represents a  $\chi^2$  fit to a Gaussian function.

The pull distributions for tau related nuisance parameter show a slight deviation from the expected mean value of zero, indicating a slight bias, which is covered well within the  $1\sigma$  uncertainty interval. For the transfer factor and the tau energy scale, the standard deviation of the pull distributions is narrower, indicating that the uncertainty represented by the considered nuisance parameter is slightly overestimated. However, to constrain is relatively light and is not expected to affect the limit significantly. The pull distributions for the remaining nuisance parameter can be found in Section A.4.6, mostly following the expected normal Gaussian distribution.

An overview of the unconditional maximum likelihood estimators,  $\hat{\theta}$ , is provided in Figure 6.36 for two different  $m_A$  and  $\tan\beta$  values, showing the result of the estimators with their corresponding uncertainties,  $\Delta\theta$ , as well as the impact of each estimator on  $\hat{\mu}$ . The impact is estimated differently for *pre-fit* and *post-fit* by shifting the corresponding unconditional maximum likelihood estimator either with a factor of 1.0,

$$\hat{\theta}_{i,\text{pre-fit}} = \hat{\theta}_i \pm 1.0 \quad (6.59)$$

for the pre-fit impact or with a factor of  $\Delta\theta$ ,

$$\hat{\theta}_{i,\text{post-fit}} = \hat{\theta}_i \pm \Delta\theta_i \quad (6.60)$$

for the post-fit impact. The impact,  $\Delta\hat{\mu}$ , is now defined as difference between the unconditional maximum likelihood estimator  $\hat{\mu}$  and the maximum likelihood estimator derived with the shifted nuisance parameter:

$$\Delta\hat{\mu}_{i,\text{pre-fit}} = \hat{\mu} - \hat{\mu}(\theta_i = \hat{\theta}_{i,\text{pre-fit}}) \quad (6.61)$$

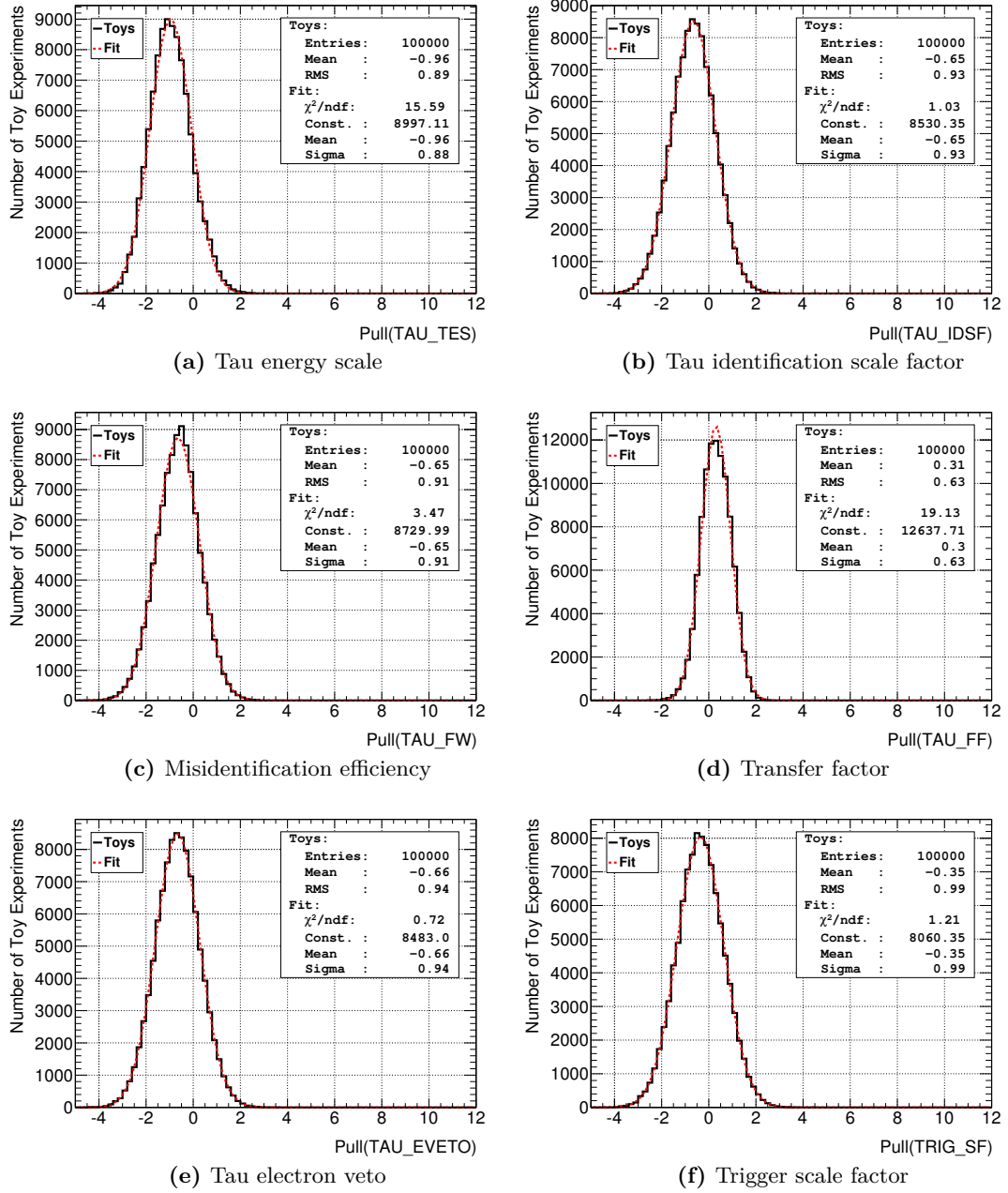


**Figure 6.35:** Pull distributions for the nuisance parameters related to the tau energy scale (a), the tau identification scale factor (b), the misidentification efficiency (c), the transfer factor (d), the tau electron veto scale factor (e) and the trigger scale factors (f).

and

$$\Delta\hat{\mu}_{i,\text{post-fit}} = \hat{\mu} - \hat{\mu}(\theta_i = \hat{\theta}_{i,\text{post-fit}}) \quad (6.62)$$

for the pre-fit and post-fit impact, respectively.

The nuisance parameter related to the tau energy scale, the tau misidentification efficiency and the tau transfer factor are usually the parameters with the largest impact on  $\hat{\mu}$ , due the relative large uncertainties on these parameters. The pulls for these parameters also show the largest deviations around zero, however the deviations are always located well within the  $1\sigma$  uncertainty band for all considered  $m_A$  and  $\tan\beta$  points.

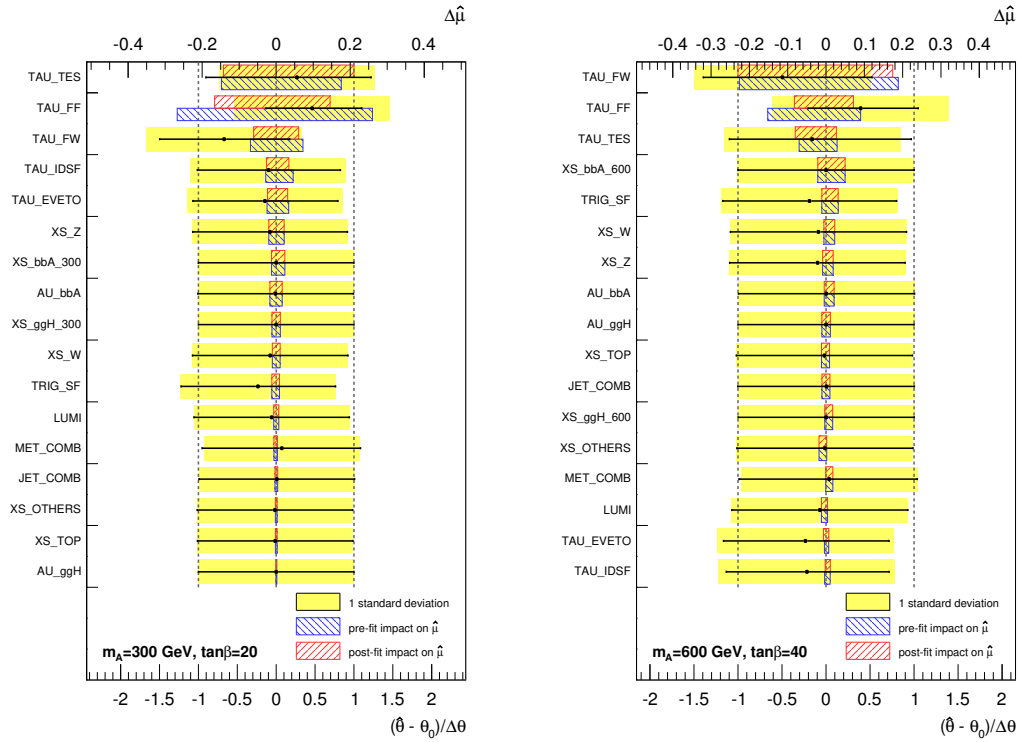


**Figure 6.36:** Summary for the maximum likelihood estimator pulls (black points) for the nuisance parameters presented for two different  $m_A$  and  $\tan\beta$  values. The black bars indicate the estimated uncertainty. The impact on the estimated signal strength  $\hat{\mu}$  is indicated by the red and blue bars for the pre-fit and post-fit impact, respectively.

A legend for the nuisance parameter name convention is provided in Section A.4.6.

The correlation between the single nuisance parameters is presented in Figure 6.37. Overall the parameters are uncorrelated with a slight negative correlation of about  $\sim -0.1$  between the tau energy scale, the tau identification scale factor and the tau misidentification efficiency.

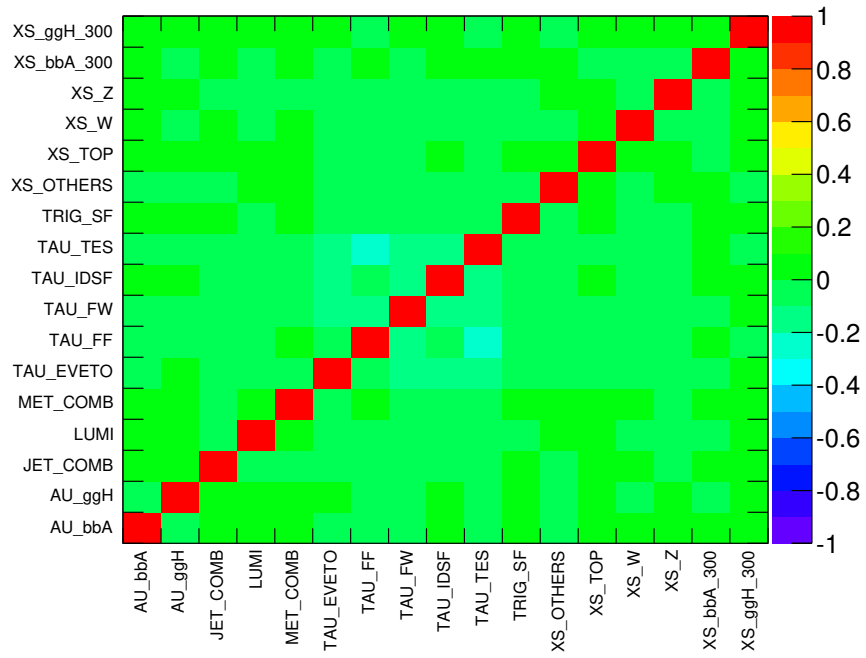


**Figure 6.37:** Correlation matrix between the considered nuisance parameter, evaluated for a signal hypothesis at  $m_A = 300$  GeV and  $\tan \beta = 20$ .

### 6.8.3 Exclusion Limits for the combined 2011 and 2012 Dataset

Combined upper limits for the search of MSSM Higgs bosons using the 2011 and 2012 data set recorded with the ATLAS detector are presented in Figure 6.38, based on proton-proton collisions with a luminosity of  $4.5 \text{ fb}^{-1}$  and  $19.5 \text{ fb}^{-1}$ , respectively.

The nuisance parameter between both data set are assumed to be in-dependent between each other, except for the modeling uncertainties and uncertainties related the cross sections of the signal and background processes. The luminosity uncertainty of the 2012 data set has been evaluated to 2.8 % (see Section 3.3.1).

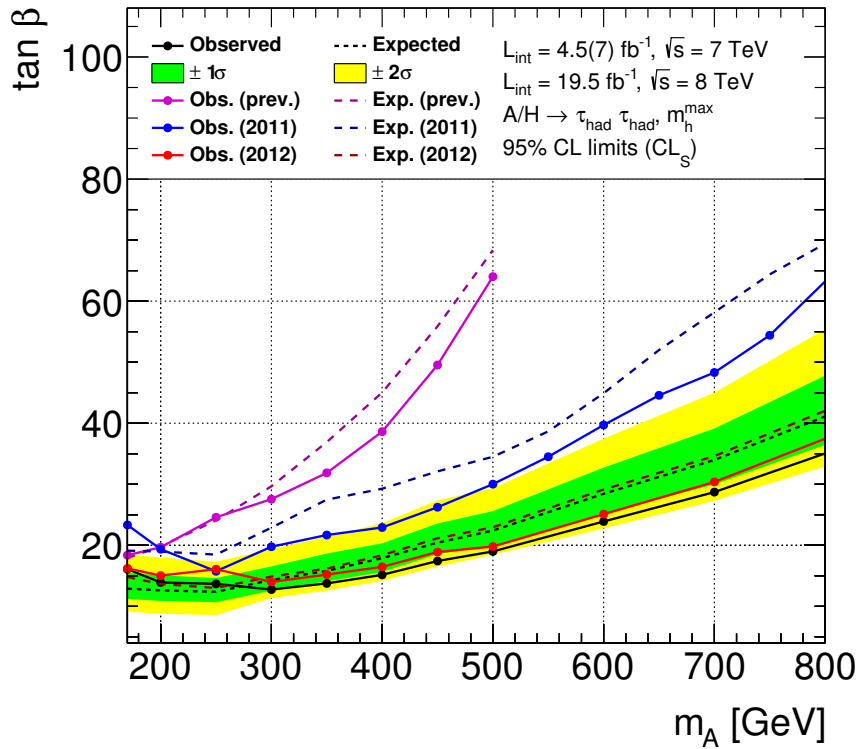


**Figure 6.38:** Combined upper limits using the 2011 and 2012 data set on  $m_A \times \tan \beta$  for the nominal MSSM Higgs boson hypothesis within the  $m_h^{\max}$  benchmark scenario are presented. The solid black line represents the observed limit, while the dashed black line represents the expected median limit with the corresponding  $\pm 1\sigma$  and  $\pm 2\sigma$  uncertainty bands, indicated by the shaded areas. The parameter region above the observed limit is excluded at a confidence level of 95 %. The combined upper limit is compared to the limits obtain for the individual data set.

In general, the behavior of the 2011 upper limit and the equivalent 2012 data set analysis is very similar, with the exception that the 2012 data set analysis is more sensitive to the MSSM Higgs signal due to the increased luminosity and the higher center-of-mass energy of  $\sqrt{s} = 8 \text{ TeV}$ . Subsequently, the combined limit is dominated by the results of the 2012 data set, however the addition of the 2011 data allows a slight improvement of about  $\sim 1 - 3$  units in  $\tan \beta$ .

The corresponding combined upper limits on  $m_A \times \tan \beta$  for the  $m_h^{\text{mod}-}$  and  $m_h^{\text{mod}+}$  benchmark scenarios are presented in Figure 6.39. Similar to the  $m_h^{\text{max}}$  scenario, the combined limits are dominated by the measurements based on the 2012 data set with a light improvement from the 2011 measurement.

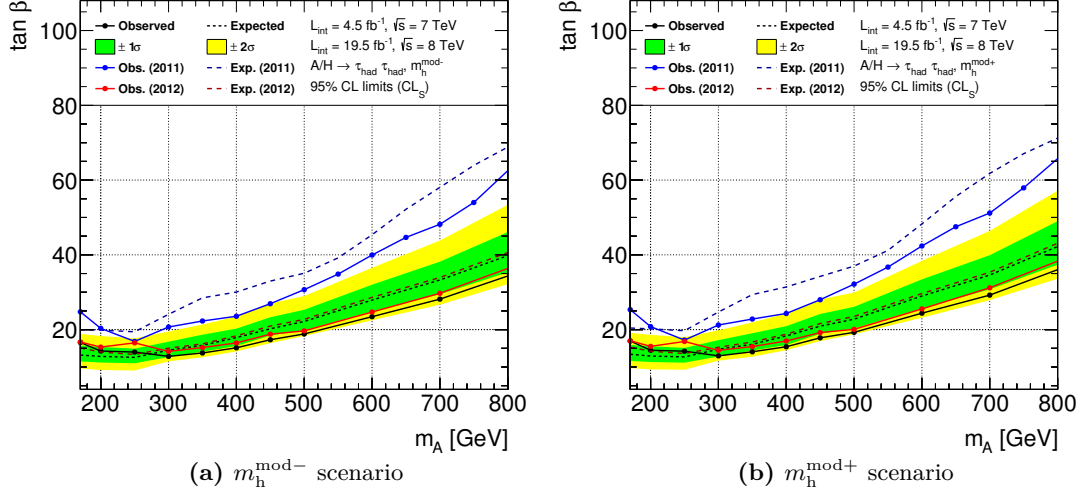


**Figure 6.39:** Combined upper limits using the 2011 and 2012 data set on  $m_A \times \tan \beta$  for the nominal MSSM Higgs boson hypothesis within the  $m_h^{\text{mod}-}$  and  $m_h^{\text{mod}+}$  benchmark scenario are presented. The solid black line represents the observed limit, while the dashed black line represents the expected median limit with the corresponding  $\pm 1\sigma$  and  $\pm 2\sigma$  uncertainty bands, indicated by the shaded areas. The parameter region above the observed limit is excluded at a confidence level of 95 %.

## 6.9 Summary and Outlook

The search for neutral MSSM Higgs boson decaying into two hadronically decaying tau leptons using proton-proton collisions with a luminosity of  $4.5 \text{ fb}^{-1}$ , recorded with the ATLAS detector at LHC, is presented. Several modifications, based on methods developed during the analysis of the 2012 data set, compared to the predecessor analysis [223] are implemented, leading to a significant improvement of the sensitivity.

The modifications include the categorization between the di-tau trigger and single tau trigger category, the implementation of the latest recommendations for the object reconstruction and identification and the estimation of the  $m_T^{\text{tot}}$  spectrum. Two main auxiliary measurements are performed: the measurement of  $W \rightarrow \mu\nu + \text{jets}$  final states to estimate the misidentification efficiency and the measurement of the tau identification transfer factors within a dedicated di-jet control region, which are utilized for QCD multi-jet estimation in the single tau trigger category.

After the full event selection, in total 2565 events are observed in the di-tau trigger category and 81 events in the single tau trigger category. Both are compared to the respective SM background predictions (post-fit) of  $2540 \pm 40 \text{ (comb.)}$  events and  $82 \pm 8 \text{ (comb.)}$  events.

No significant excess above the SM expectation is observed and upper limits on  $m_A \times \tan\beta$  at a confidence level of 95 % for the  $m_h^{\text{max}}$  (Figure 6.40),  $m_h^{\text{mod-}}$  and  $m_h^{\text{mod+}}$  benchmark scenarios are evaluated. A considerably improvement in the upper limits is achieved, extending the mass range up to  $m_A \sim 800 \text{ GeV}$  with an improvement of about  $\sim 30$  units in  $\tan\beta$  (around 450 GeV to 500 GeV), which is largely boosted by the introduction of the single tau trigger category.

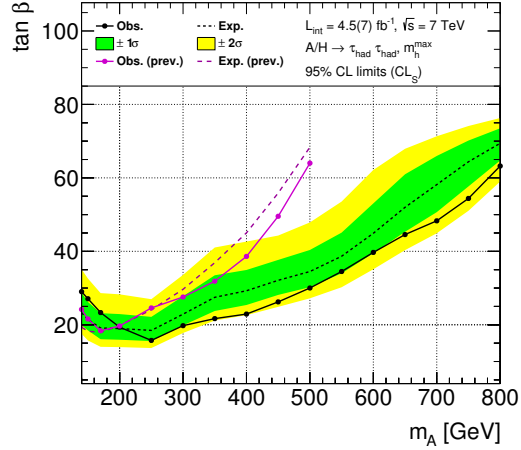


**Figure 6.40:** Upper limit for the  $m_h^{\text{max}}$  benchmark scenario at 95 % CL.

An addition, a combination with the results from the 2012 data set is performed, leading to the small improvement of about 1 – 3 units in  $\tan\beta$  within the upper limits, compared to the 2012 limits only.

The di-tau decay channel is a promising channel for the search of neutral MSSM Higgs bosons, which allows to test a significant part of MSSM parameter phase space, especially the high  $\tan\beta$  regions. The presented analysis is accord with current searches for BSM physics and the archived results and improved upper limits allow a stronger constrain of possible BSM hypotheses.

The MSSM Higgs boson search has been continued with the first data sets taken during the early

Run 2 phase of the LHC experiment at an increased center-of-mass energy of  $\sqrt{s} = 13$  TeV, using the methods developed during Run 1. So far, also in the first results of Run 2 no significant excess above the SM expectation is found and the upper limits are pushed beyond the Run 1 limits [268,269], taking advantage of the increased center-of-mass energy.

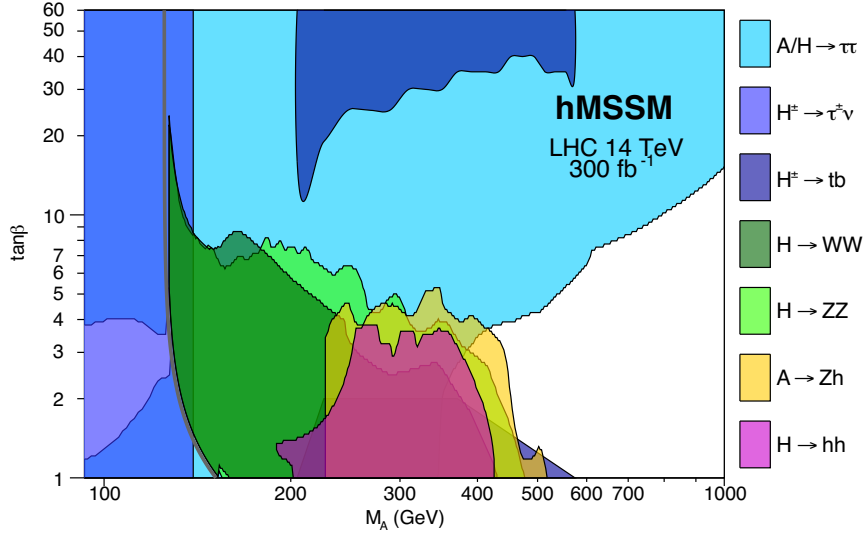


**Figure 6.41:** Expected 95 % CL sensitivities to the MSSM Higgs sector for various final states at the LHC. The sensitivities are derived within the  $m_A \times \tan \beta$  plane of the hMSSM model with a center-of-mass energy of  $\sqrt{s} = 14$  TeV and an integrated luminosity of  $300 \text{ fb}^{-1}$  [270].

More data and the combination of different search channels are needed to cover the  $m_A \times \tan \beta$  plane in the MSSM model. The upcoming data from the LHC will allow further studies for physics beyond the SM, including new scenarios which are not covered by this thesis, like the *hMSSM* model [271], in which the Higgs boson mass of  $m_h \simeq 125$  GeV and a SUSY breaking scale above 1 TeV are taken into account. The expected sensitivities at the LHC for  $\sqrt{s} = 14$  TeV at an integrated luminosity of  $300 \text{ fb}^{-1}$  can be found in Figure 6.41.

This will show if an extended Higgs sector at the TeV scale, as in the MSSM, is realized in nature or if alternative models need to be considered. It is also possible that the SM is capable of describing nature up to Planck energy scales, requiring different explanations for dark matter, CP violation and other challenges to the SM.



# A Appendix

## A.1 Standard Model of Particle Physics and MSSM

### A.1.1 MSSM Higgs Boson Sector

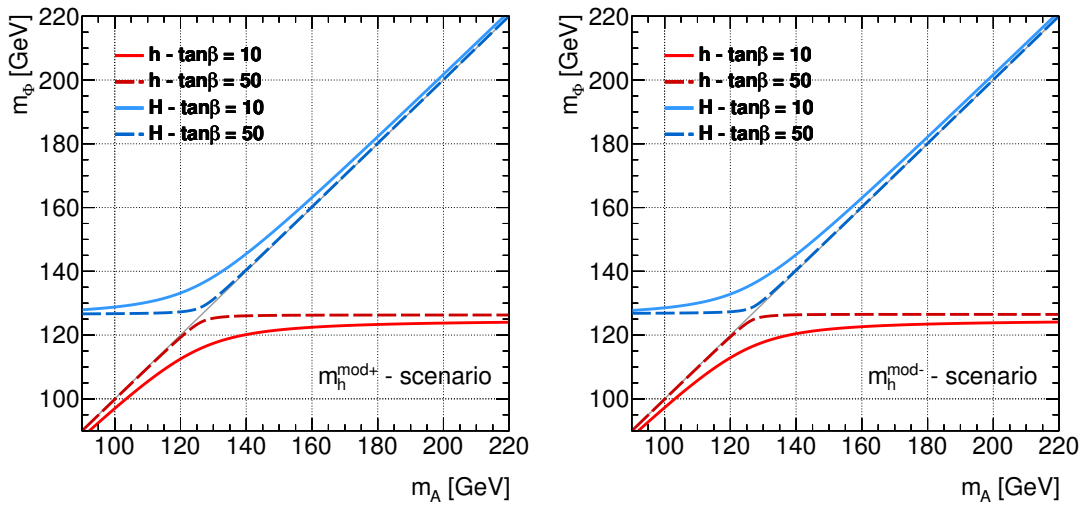


**Figure A.1:** Development of the neutral, CP-even Higgs boson masses,  $m_h$  and  $m_H$ , as a function of mass of the CP-odd Higgs boson  $A$  for two different values in  $\tan\beta$ . The left plot shows the results for the  $m_h^{\text{mod}+}$  and the right plot for the  $m_h^{\text{mod}-}$  benchmark scenario, respectively. The benchmark points are provided by the *LHC Higgs Cross Section Working Group* [64, 65].

## A.2 Reconstruction and Identification

### A.2.1 Tau Identification Against QCD-induced Jets - Observables

The following section contains the definitions of observables used for the identification of hadronic tau lepton decays against QCD-induced jets. The definitions for 1-prong and multi-prong candidates can be found in Table A.1 and Table A.2, respectively. The corresponding distributions are presented in Figure A.2 and Figure A.3.

#### 1-prong Observables

Observable	Symbol	Description
Impact parameter significance of the leading track	$S_{\text{lead trk}}$	Significance of the impact parameter in the transversal plane, $d_0$ , for the leading track (with respect to $p_T$ ) within the core region of the tau candidate:
$S_{\text{lead trk}} = \frac{d_0}{\delta d_0},$		
where $\delta d_0$ represents the estimated uncertainty on the impact parameter.		
Number of isolation tracks	$N_{\text{trk}}^{\text{iso}}$	Number of tracks with a distance of $0.2 < \Delta R < 0.4$ with respect to the tau candidate axis (isolation region).

**Table A.1:** Definition of observables used for the tau identification against QCD-induced jets [147]. The given observables are used for 1-prong tau candidates only.

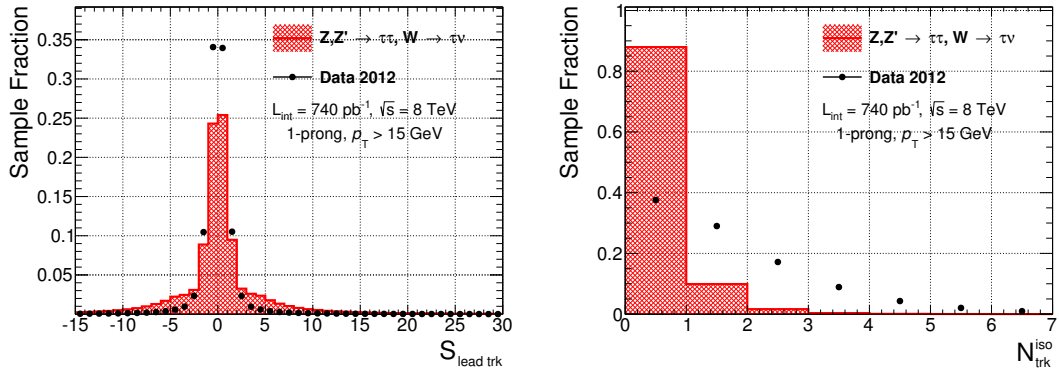


**Figure A.2:** Distributions for the impact parameter significance of the leading track (left) and the number of isolation tracks (right) for 1-prong tau leptons are shown. Predictions for real tau leptons, which are taken from simulations of  $Z \rightarrow \tau^+\tau^-$ ,  $Z' \rightarrow \tau\tau$  and  $W \rightarrow \tau\nu$  processes, are compared with distributions from QCD-induced jets, which are measured using early 2012 data recorded with the ATLAS detector.

## Multi-prong Observables

Observable	Symbol	Description
Maximum track distance	$\Delta R_{\max}$	Maximum distance of a track within the core cone ( $\Delta R < 0.2$ ) to the tau candidate axis.
Transverse flight path significance	$S_T^{\text{flight}}$	Significance of the distance, $L_T^{\text{flight}}$ , between the secondary vertex, which is associated with the tau lepton candidate and a possible tau decay vertex, to the primary vertex:
$S_T^{\text{flight}} = \frac{L_T^{\text{flight}}}{\delta L_T^{\text{flight}}},$		
<p>where <math>\delta L_T^{\text{flight}}</math> represents estimated uncertainty on the distance observable.</p>		
Track system mass	$m_{\text{trk}}$	Invariant mass of the track system. All tracks (from core and isolation region) associated with the tau candidate are considered.

**Table A.2:** Definition of observables used for the tau identification against QCD-induced jets [147]. The given observables are used for multi-prong tau candidates only.

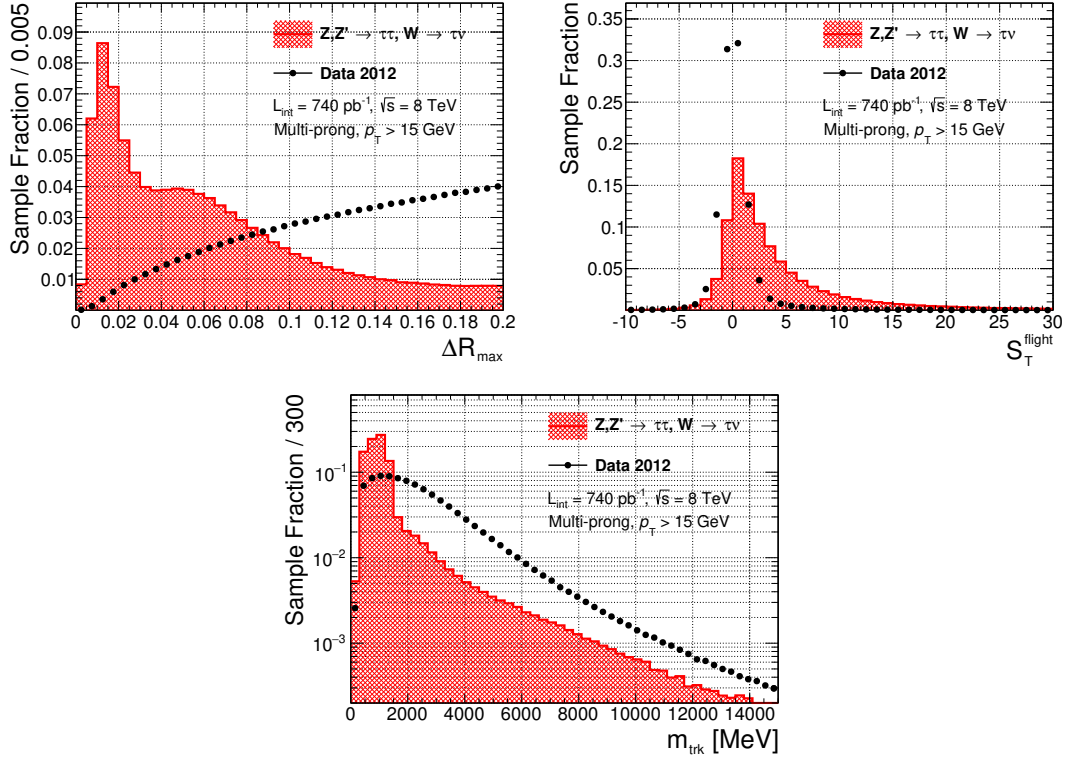


**Figure A.3:** Distributions for the maximum track distance (top left), the transverse flight path significance (top right) and the track system mass (bottom) for multi-prong tau leptons are shown. Predictions for real tau leptons, which are taken from simulations of  $Z \rightarrow \tau^+\tau^-$ ,  $Z' \rightarrow \tau\tau$  and  $W \rightarrow \tau\nu$  processes, are compared with distributions from QCD-induced jets, which are measured using early 2012 data recorded with the ATLAS detector.

## A.3 Underlying Event

### A.3.1 Merged Vertex Effect

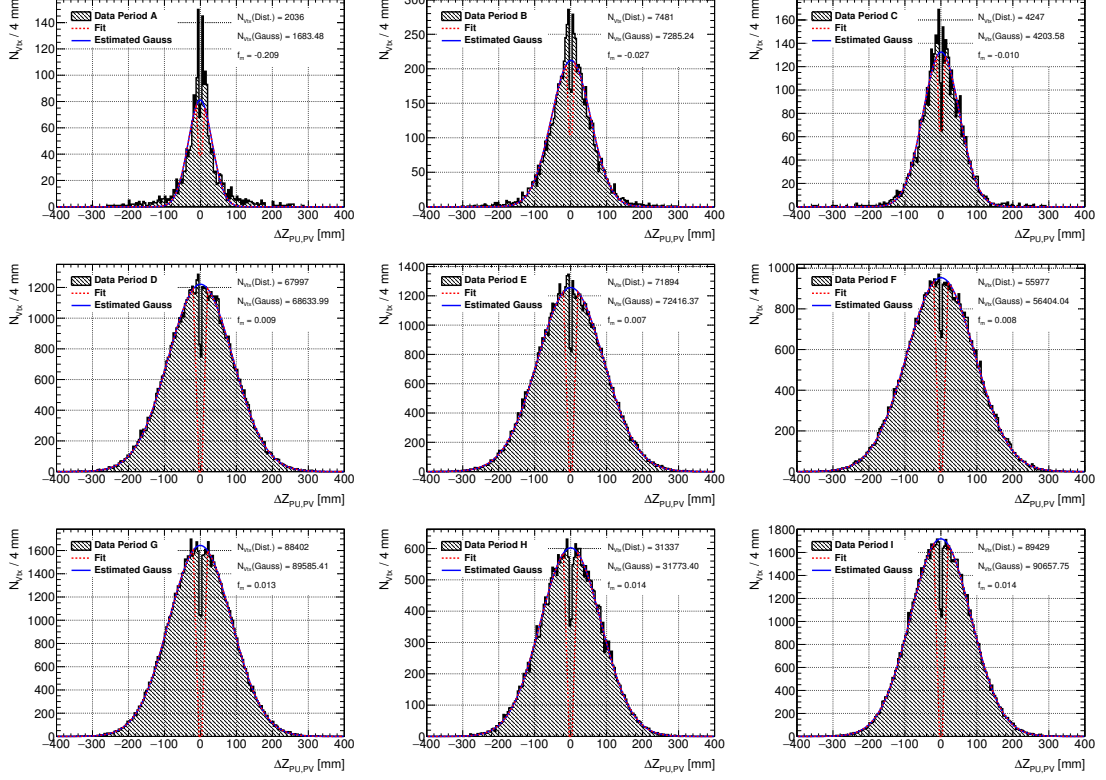


**Figure A.4:**  $\Delta Z_{PV,PU}$  distribution shown independently for each 2010 data taking period.

The red lines represents the fit results for a Gaussian distribution with a gap around  $\Delta Z = 0$  and the blue line represents the estimation for a full Gaussian without merged vertices. The non-Gaussian shape in the earlier periods is a result of frequent changes in the run conditions within these periods.

### A.3.2 Results for $\sum p_T/\delta\eta\delta\phi$ and $N_{ch}/\delta\eta\delta\phi$ in trans-max and trans-min region

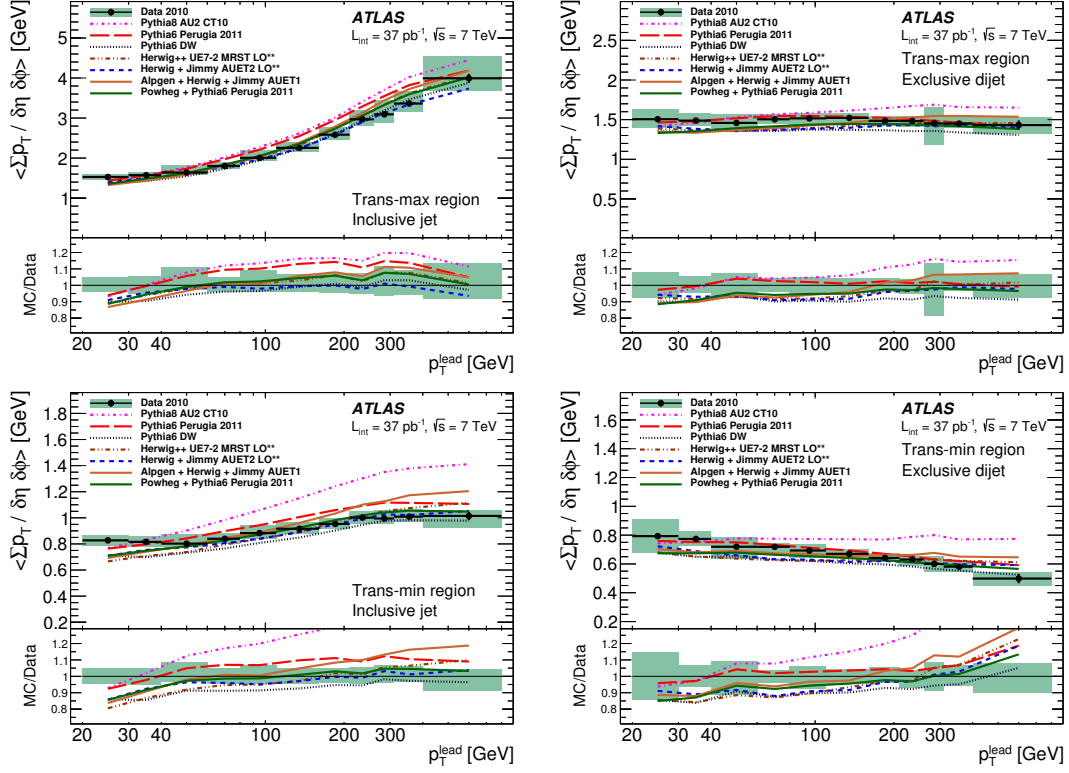


**Figure A.5:** Mean transverse momentum sum densities,  $\sum p_T/\delta\eta\delta\phi$ , for charged particles against  $p_T^{\text{lead}}$  are shown for the inclusive (left) and exclusive (right) event selection and for the trans-max (top) and trans-min (bottom) region. The distributions are presented for the combined transverse region. The unfolded data points (black) are compared to several MC model predictions. The black error bars indicate the statistical uncertainty and the green shaded areas indicate the combined statistical and systematic uncertainty.

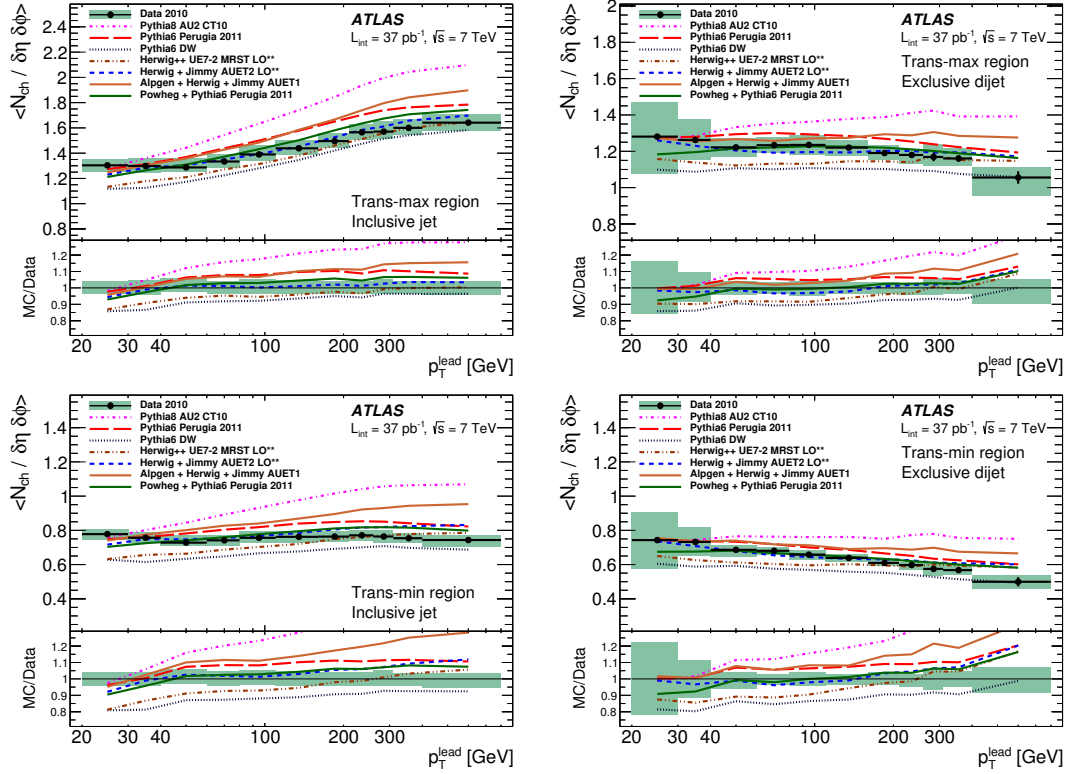


**Figure A.6:** mean particle multiplicity densities,  $N_{\text{ch}}/\delta\eta\delta\phi$ , for charged particles against  $p_T^{\text{lead}}$  are shown for the inclusive (left) and exclusive (right) event selection and for the trans-max (top) and trans-min (bottom) region. The distributions are presented for the combined transverse region. The unfolded data points (black) are compared to several MC model predictions. The black error bars indicate the statistical uncertainty and the green shaded areas indicate the combined statistical and systematic uncertainty.

## A.4 Search for neutral MSSM Higgs boson

### A.4.1 Cross Sections for neutral MSSM Higgs bosons

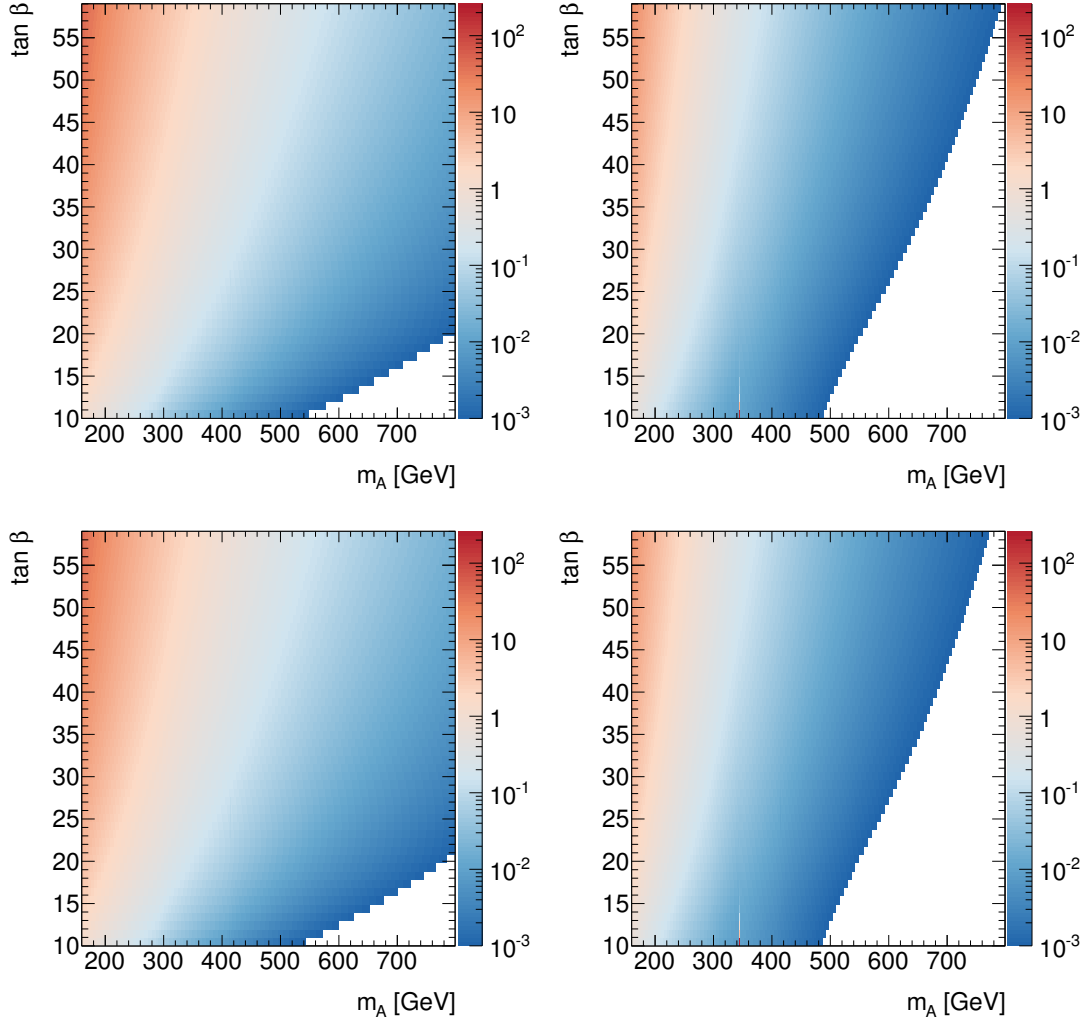


**Figure A.7:** Cross sections times branching fractions,  $\sigma(pp \rightarrow \phi) \times \mathcal{B}(\phi \rightarrow \tau\tau)$  [pb], are presented for the b-associated production channel (left) and for the production via gluon-gluon fusion (right), combined for the pseudoscalar MSSM Higgs boson  $A$  and the scalar MSSM Higgs boson  $H$ . The distributions are calculated within the  $m_h^{\text{mod-}}$  (top) and  $m_h^{\text{mod+}}$  (bottom) benchmark scenarios at a center-of-mass energy of  $\sqrt{s} = 7\text{ TeV}$ . The cross sections and branching fraction values are provided by the *LHC Higgs Cross Section Working Group*.

## A.4.2 Background Estimation

	Region A		Region B		Region C	Region D
Multi-jet	221 200	$\pm 1300$	—	—	—	—
$Z/\gamma^* \rightarrow \tau\tau$	$66.0 \pm 2.1$		$38.1 \pm 1.1$		$7.6 \pm 0.7$	$4.2 \pm 0.4$
$W \rightarrow \tau\nu$	$245 \pm 8$		$73.4 \pm 3.4$		$16.3 \pm 1.9$	$5.4 \pm 1.0$
EW Bkg.	$74.4 \pm 2.0$		$27.9 \pm 1.1$		$5.3 \pm 0.5$	$1.44 \pm 0.21$
Top	$31.0 \pm 0.5$		$13.17 \pm 0.27$		$2.96 \pm 0.13$	$1.13 \pm 0.07$
Comb. background prediction	221 700	$\pm 1300$	153	$\pm 4$	$32.2 \pm 2.1$	$12.2 \pm 1.1$
Observed number of events	224 928		201 262		75 816	68 901

**Table A.3:** The expected number of events of various SM processes and the estimated QCD multi-jet contribution for the signal region *A* within the DTT validation regions are presented and compared to the observed number of events. The stated uncertainty for each process correspond to the respective statistical uncertainty.



	Data	Comb. Bkg.	Multi-jet	$Z/\gamma^* \rightarrow \tau\tau$	$W \rightarrow \tau\nu$	EW Bkg.	Top
Di-tau trigger	943 651	—	—	6980 $\pm$ 40	21 840 $\pm$ 180	11 700 $\pm$ 100	12 380 $\pm$ 60
Fail BDT loose $\eta_{\text{lead}}$	819 279	—	—	1301 $\pm$ 15	3780 $\pm$ 60	1706 $\pm$ 20	1714 $\pm$ 9
Fail BDT loose $\tau_{\text{sub}}$	708 336	—	—	192.3 $\pm$ 3.1	565 $\pm$ 10	197.1 $\pm$ 3.0	171.8 $\pm$ 1.0
$p_{\text{T}}^{\text{lead}} < 150 \text{ GeV}$	699 885	—	—	190.6 $\pm$ 3.1	563 $\pm$ 10	195.9 $\pm$ 3.0	170.8 $\pm$ 1.0
$q_{\text{lead}} \times q_{\text{sub}} = -1 \text{ (OS)}$	370 212	—	—	121.8 $\pm$ 2.7	425 $\pm$ 9	141.8 $\pm$ 2.7	118.8 $\pm$ 0.9
$ \Delta\phi(\eta_{\text{lead}}, \tau_{\text{sub}})  > 2.7$	301 704	—	—	73.6 $\pm$ 2.2	261 $\pm$ 8	79.7 $\pm$ 2.1	34.0 $\pm$ 0.5
$E_{\text{T}}^{\text{miss}} > 10 \text{ GeV}$	225 462	222 100 $\pm$ 1300	221 600 $\pm$ 1300	66.0 $\pm$ 2.1	245 $\pm$ 8	74.4 $\pm$ 2.0	31.0 $\pm$ 0.5
$\sum E_{\text{T}} > 160 \text{ GeV}$	224 928	221 700 $\pm$ 1300	221 200 $\pm$ 1300	66.0 $\pm$ 2.1	245 $\pm$ 8	74.4 $\pm$ 2.0	31.0 $\pm$ 0.5

**Table A.4:** Observed number of events and background predictions in the DTT validation region  $\mathcal{A}$  are presented after each selection requirement. The stated uncertainty values for each individual background process correspond to the respective statistical uncertainty.

	Data	Comb. Bkg.	Multi-jet	$Z/\gamma^* \rightarrow \tau\tau$	$W \rightarrow \tau\nu$	EW Bkg.	Top
Single tau trigger	198 234	—	—	4270 $\pm$ 40	16360 $\pm$ 150	10950 $\pm$ 100	12710 $\pm$ 60
$p_T^{\text{lead}} > 150$ GeV	112 533	—	—	455 $\pm$ 9	1600 $\pm$ 40	877 $\pm$ 22	919 $\pm$ 16
BDT loose $\tau_{\text{lead}}$	11132	—	—	109 $\pm$ 4	169 $\pm$ 10	71 $\pm$ 5	47.1 $\pm$ 1.4
BDT loose $\tau_{\text{sub}}$	226	199 $\pm$ 4	105.5 $\pm$ 2.1	49.9 $\pm$ 2.4	31.3 $\pm$ 2.2	8.5 $\pm$ 0.7	3.45 $\pm$ 0.19
$q_{\text{lead}} \times q_{\text{sub}} = 1$ (SS)	86	67.3 $\pm$ 2.1	51.2 $\pm$ 1.5	3.81 $\pm$ 0.34	9.2 $\pm$ 1.3	2.2 $\pm$ 0.4	0.86 $\pm$ 0.06
$ \Delta\phi(\tau_{\text{lead}}, \tau_{\text{sub}})  > 2.7$	47	49.9 $\pm$ 2.0	39.0 $\pm$ 1.5	2.55 $\pm$ 0.25	6.6 $\pm$ 1.3	1.34 $\pm$ 0.30	0.39 $\pm$ 0.04

**Table A.5:** Observed number of events and background predictions in the STT validation region  $A$  are presented after each selection requirement. The stated uncertainty values for each individual background process correspond to the respective statistical uncertainty.

### A.4.3 Fail-identification rate for QCD Jets to Hadronic Tau Decays

Fail-identification efficiencies [%] for tau candidates measured in the  $W \rightarrow \mu\nu + \text{jet}$  control region are summarized in Table A.6 without any trigger requirement and in Table A.7 and Table A.8 in addition with a EF\_tau20\_medium1 and EF\_tau29\_medium1 trigger requirement.

$q_\mu \times q_\tau$	BDT level	$p_T^\tau$ interval in [GeV]			
		50 – 70	70 – 100	100 – 150	> 150
<i>1 prong</i>					
OS	loose	$88.0^{+0.6}_{-0.6}$	$88.7^{+1.0}_{-1.0}$	$83.5^{+2.1}_{-2.1}$	$81^{+6}_{-6}$
	medium	$91.8^{+0.5}_{-0.5}$	$92.1^{+0.9}_{-0.9}$	$90.6^{+1.7}_{-1.7}$	$95^{+4}_{-4}$
SS	loose	$95.6^{+0.7}_{-0.7}$	$94.5^{+1.3}_{-1.3}$	$93.5^{+2.7}_{-2.7}$	$82^{+7}_{-7}$
	medium	$97.2^{+0.6}_{-0.6}$	$96.0^{+1.1}_{-1.1}$	$95.9^{+1.8}_{-1.8}$	$94^{+5}_{-5}$
<i>3 prong</i>					
OS	loose	$97.92^{+0.17}_{-0.17}$	$98.58^{+0.24}_{-0.24}$	$98.9^{+0.4}_{-0.4}$	$99.4^{+0.6}_{-0.7}$
	medium	$98.95^{+0.13}_{-0.13}$	$99.33^{+0.18}_{-0.18}$	$99.29^{+0.29}_{-0.29}$	$99.6^{+0.4}_{-0.4}$
SS	loose	$99.00^{+0.19}_{-0.19}$	$99.40^{+0.26}_{-0.26}$	$99.95^{+0.05}_{-0.34}$	$99.2^{+0.8}_{-1.0}$
	medium	$99.30^{+0.15}_{-0.15}$	$99.76^{+0.19}_{-0.19}$	$100.0^{+0.0}_{-0.25}$	$98.5^{+1.0}_{-1.0}$

**Table A.6:** Fail-identification efficiencies [%] for fake tau candidates measured in the  $W \rightarrow \mu\nu + \text{jet}$  control region using proton-proton collision events at  $\sqrt{s} = 7 \text{ TeV}$  recorded with the ATLAS detector in 2011. No additional trigger requirements for the tau candidates have been applied. The stated uncertainties correspond to Clopper-Pearson intervals, estimated for a confidence level of 68.3%.

		$p_{\text{T}}^{\tau}$ interval in [GeV]		
$q_{\mu} \times q_{\tau}$	BDT level	50 – 70	70 – 100	> 100
<i>1 prong</i>				
OS	loose	$9.1^{+0.6}_{-0.6}$	$11.6^{+1.0}_{-1.0}$	$10.2^{+2.0}_{-2.0}$
	medium	$10.2^{+0.6}_{-0.6}$	$12.2^{+1.1}_{-1.1}$	$12.9^{+2.1}_{-2.1}$
SS	loose	$5.4^{+0.8}_{-0.8}$	$5.2^{+1.6}_{-1.6}$	$2.5^{+2.7}_{-2.5}$
	medium	$5.9^{+0.9}_{-0.9}$	$5.9^{+1.7}_{-1.7}$	$2.5^{+2.8}_{-2.5}$
<i>3 prong</i>				
OS	loose	$8.49^{+0.31}_{-0.31}$	$11.2^{+0.5}_{-0.5}$	$14.3^{+0.9}_{-0.9}$
	medium	$8.89^{+0.32}_{-0.32}$	$11.4^{+0.5}_{-0.5}$	$14.5^{+0.9}_{-0.9}$
SS	loose	$6.0^{+0.4}_{-0.4}$	$7.4^{+0.7}_{-0.7}$	$10.4^{+1.3}_{-1.3}$
	medium	$6.0^{+0.4}_{-0.4}$	$7.3^{+0.7}_{-0.7}$	$10.2^{+1.3}_{-1.3}$

**Table A.7:** Fail-identification efficiencies [%] for fake tau candidates measured in the  $W \rightarrow \mu\nu + \text{jet}$  control region using proton-proton collision events at  $\sqrt{s} = 7 \text{ TeV}$  recorded with the ATLAS detector in 2011. In addition to the tau identification a trigger requirement using the `EF_tau20_medium1` trigger has been applied for the tau candidate.

$q_\mu \times q_\tau$	BDT level	$p_\text{T}^\tau$ interval in [GeV]		
		50 – 70	70 – 100	> 100
<i>1 prong</i>				
OS	loose	$9.7^{+0.6}_{-0.6}$	$15.0^{+1.1}_{-1.1}$	$13.3^{+2.0}_{-2.0}$
	medium	$11.4^{+0.6}_{-0.6}$	$16.3^{+1.1}_{-1.1}$	$16.8^{+2.2}_{-2.2}$
SS	loose	$6.8^{+0.8}_{-0.8}$	$8.2^{+1.6}_{-1.6}$	$7.3^{+2.8}_{-2.8}$
	medium	$7.4^{+0.9}_{-0.9}$	$9.3^{+1.7}_{-1.7}$	$8.6^{+2.9}_{-2.9}$
<i>3 prong</i>				
OS	loose	$10.79^{+0.32}_{-0.32}$	$15.2^{+0.6}_{-0.6}$	$19.9^{+1.0}_{-1.0}$
	medium	$11.33^{+0.33}_{-0.33}$	$15.7^{+0.6}_{-0.6}$	$20.2^{+1.0}_{-1.0}$
SS	loose	$7.5^{+0.4}_{-0.4}$	$10.2^{+0.7}_{-0.7}$	$16.0^{+1.4}_{-1.4}$
	medium	$7.6^{+0.4}_{-0.4}$	$10.1^{+0.7}_{-0.7}$	$15.8^{+1.4}_{-1.4}$

**Table A.8:** Fail-identification efficiencies [%] for fake tau candidates measured in the  $W \rightarrow \mu\nu + \text{jet}$  control region using proton-proton collision events at  $\sqrt{s} = 7 \text{ TeV}$  recorded with the ATLAS detector in 2011. In addition to the tau identification a trigger requirement using the `EF_tau29_medium1` trigger has been applied for the tau candidate.



A.4.4 Validation of the  $Z/\gamma^* \rightarrow \tau\tau$  Modeling

	Data	Comb. Bkg.	Multi-jet	$Z/\gamma^* \rightarrow \tau\tau$	$W \rightarrow \tau\nu$	EW Bkg.	Top
Di-tau trigger	943 651	—	—	6980 $\pm$ 40	21 840 $\pm$ 180	11 700 $\pm$ 100	12 380 $\pm$ 60
BDT medium $\tau_{\text{lead}}$	77 104	—	—	1808 $\pm$ 19	4170 $\pm$ 80	1038 $\pm$ 22	392.2 $\pm$ 3.3
BDT medium $\tau_{\text{sub}}$	7542	—	—	334 $\pm$ 7	110.9 $\pm$ 2.5	23.6 $\pm$ 0.6	11.8 $\pm$ 0.4
$q_{\text{lead}} \times q_{\text{sub}} = -1$ (OS)	4339	4040 $\pm$ 60	3580 $\pm$ 60	324 $\pm$ 7	97.8 $\pm$ 2.4	20.6 $\pm$ 0.6	10.8 $\pm$ 0.4
$E_{\tau}^{\text{miss}} > 25$ GeV	304	281 $\pm$ 15	170 $\pm$ 15	69.2 $\pm$ 3.2	29.1 $\pm$ 1.1	7.10 $\pm$ 0.34	5.51 $\pm$ 0.31
$\cos \Delta\phi(\vec{p}_{\tau}^{\text{sub}}, \vec{E}_{\tau}^{\text{miss}})$	179	177 $\pm$ 11	94 $\pm$ 11	57.9 $\pm$ 2.9	17.4 $\pm$ 0.9	4.19 $\pm$ 0.27	3.39 $\pm$ 0.25
$\cos \Delta\phi(\vec{p}_{\tau}^{\text{lead}}, \vec{p}_{\tau}^{\text{sub}})$	78	62 $\pm$ 5	14 $\pm$ 5	44.7 $\pm$ 2.7	2.34 $\pm$ 0.23	0.90 $\pm$ 0.10	0.54 $\pm$ 0.08

**Table A.9:** Observed number of events and background predictions in the Drell-Yan validation region are presented after each selection requirement. The stated uncertainty values for each individual background process correspond to the respective statistical uncertainty.

## A.4.5 Signal and Background Samples

dataset name	production tag	$m_A \text{ GeV} \times \tan \beta$	k-factor	filter efficiency
<i>gluon-gluon fusion</i>				
nc11_7TeV.125596.PowHegPythia_ggHtautauhh_MA100TB20	e873_s1310_s1300_r3043_r2993_p851	$100 \times 20$	1.0	1.0
nc11_7TeV.125597.PowHegPythia_ggHtautauhh_MA110TB20	e873_s1310_s1300_r3043_r2993_p851	$110 \times 20$	1.0	1.0
nc11_7TeV.125598.PowHegPythia_ggHtautauhh_MA120TB20	e873_s1310_s1300_r3043_r2993_p851	$120 \times 20$	1.0	1.0
nc11_7TeV.125599.PowHegPythia_ggHtautauhh_MA130TB20	e873_s1310_s1300_r3043_r2993_p851	$130 \times 20$	1.0	1.0
nc11_7TeV.125600.PowHegPythia_ggHtautauhh_MA140TB20	e873_s1310_s1300_r3043_r2993_p851	$140 \times 20$	1.0	1.0
nc11_7TeV.125601.PowHegPythia_ggHtautauhh_MA150TB20	e873_s1310_s1300_r3043_r2993_p851	$150 \times 20$	1.0	1.0
nc11_7TeV.125602.PowHegPythia_ggHtautauhh_MA170TB20	e873_s1310_s1300_r3043_r2993_p851	$170 \times 20$	1.0	1.0
nc11_7TeV.125603.PowHegPythia_ggHtautauhh_MA200TB20	e873_s1310_s1300_r3043_r2993_p851	$200 \times 20$	1.0	1.0
nc11_7TeV.125604.PowHegPythia_ggHtautauhh_MA250TB20	e873_s1310_s1300_r3043_r2993_p851	$250 \times 20$	1.0	1.0
nc11_7TeV.125605.PowHegPythia_ggHtautauhh_MA300TB20	e873_s1310_s1300_r3043_r2993_p851	$300 \times 20$	1.0	1.0
nc11_7TeV.125606.PowHegPythia_ggHtautauhh_MA350TB20	e873_s1372_s1370_r3043_r2993_p851	$350 \times 20$	1.0	1.0
nc11_7TeV.125607.PowHegPythia_ggHtautauhh_MA400TB20	e873_s1372_s1370_r3043_r2993_p851	$400 \times 20$	1.0	1.0
nc11_7TeV.125608.PowHegPythia_ggHtautauhh_MA450TB20	e873_s1372_s1370_r3043_r2993_p851	$450 \times 20$	1.0	1.0
nc11_7TeV.125609.PowHegPythia_ggHtautauhh_MA500TB20	e908_s1372_s1370_r3043_r2993_p851	$500 \times 20$	1.0	1.0
nc11_7TeV.125638.PowHegPythia_ggHtautauhh_MA550TB20	e931_s1372_s1370_r3043_r2993_p851	$550 \times 20$	1.0	1.0
nc11_7TeV.125610.PowHegPythia_ggHtautauhh_MA600TB20	e873_s1310_s1300_r3043_r2993_p851	$600 \times 20$	1.0	1.0
nc11_7TeV.125639.PowHegPythia_ggHtautauhh_MA650TB20	e931_s1372_s1370_r3043_r2993_p851	$650 \times 20$	1.0	1.0
nc11_7TeV.125640.PowHegPythia_ggHtautauhh_MA700TB20	e901_s1310_s1300_r3043_r2993_p851	$700 \times 20$	1.0	1.0
nc11_7TeV.125641.PowHegPythia_ggHtautauhh_MA750TB20	e901_s1372_s1370_r3043_r2993_p851	$750 \times 20$	1.0	1.0
nc11_7TeV.125642.PowHegPythia_ggHtautauhh_MA800TB20	e901_s1310_s1300_r3043_r2993_p851	$800 \times 20$	1.0	1.0
<i>b-associated production</i>				
nc11_7TeV.109921.SherpabbAtautauhh_MA100TB20	e931_s1310_s1300_r3043_r2993_p851	$100 \times 20$	1.0	1.0
nc11_7TeV.125561.SherpabbAtautauhh_MA110TB20	e931_s1310_s1300_r3043_r2993_p851	$110 \times 20$	1.0	1.0
nc11_7TeV.109925.SherpabbAtautauhh_MA120TB20	e931_s1310_s1300_r3043_r2993_p851	$120 \times 20$	1.0	1.0
nc11_7TeV.125562.SherpabbAtautauhh_MA130TB20	e931_s1310_s1300_r3043_r2993_p851	$130 \times 20$	1.0	1.0
nc11_7TeV.125563.SherpabbAtautauhh_MA140TB20	e931_s1310_s1300_r3043_r2993_p851	$140 \times 20$	1.0	1.0
nc11_7TeV.125564.SherpabbAtautauhh_MA150TB20	e931_s1310_s1300_r3043_r2993_p851	$150 \times 20$	1.0	1.0
nc11_7TeV.125565.SherpabbAtautauhh_MA170TB20	e931_s1310_s1300_r3043_r2993_p851	$170 \times 20$	1.0	1.0
nc11_7TeV.109922.SherpabbAtautauhh_MA200TB20	e931_s1310_s1300_r3043_r2993_p851	$200 \times 20$	1.0	1.0
nc11_7TeV.125566.SherpabbAtautauhh_MA250TB20	e931_s1310_s1300_r3043_r2993_p851	$250 \times 20$	1.0	1.0
nc11_7TeV.109920.SherpabbAtautauhh_MA300TB20	e931_s1310_s1300_r3043_r2993_p851	$300 \times 20$	1.0	1.0
nc11_7TeV.125567.SherpabbAtautauhh_MA350TB20	e997_s1372_s1370_r3043_r2993_p851	$350 \times 20$	1.0	1.0
nc11_7TeV.109923.SherpabbAtautauhh_MA400TB20	e997_s1372_s1370_r3043_r2993_p851	$400 \times 20$	1.0	1.0
nc11_7TeV.125568.SherpabbAtautauhh_MA450TB20	e997_s1372_s1370_r3043_r2993_p851	$450 \times 20$	1.0	1.0
nc11_7TeV.109924.SherpabbAtautauhh_MA500TB20	e997_s1372_s1370_r3043_r2993_p851	$500 \times 20$	1.0	1.0
nc11_7TeV.125633.SherpabbAtautauhh_MA550TB20	e931_s1372_s1370_r3043_r2993_p851	$550 \times 20$	1.0	1.0
nc11_7TeV.109125.SherpabbAtautauhh_MA600TB20	e931_s1310_s1300_r3043_r2993_p851	$600 \times 20$	1.0	1.0
nc11_7TeV.125634.SherpabbAtautauhh_MA650TB20	e931_s1372_s1370_r3043_r2993_p851	$650 \times 20$	1.0	1.0
nc11_7TeV.125635.SherpabbAtautauhh_MA700TB20	e931_s1310_s1300_r3043_r2993_p851	$700 \times 20$	1.0	1.0
nc11_7TeV.125636.SherpabbAtautauhh_MA750TB20	e931_s1372_s1370_r3043_r2993_p851	$750 \times 20$	1.0	1.0
nc11_7TeV.125637.SherpabbAtautauhh_MA800TB20	e931_s1310_s1300_r3043_r2993_p851	$800 \times 20$	1.0	1.0

Table A.10: Logical dataset names, k-factors and filter efficiencies for the simulated MSSM Higgs boson samples.

dataset name	production tag $Z \rightarrow \tau\tau$	cross section [pb]	k-factor	filter efficiency
mc11_7TeV.116270.AlpgenJimmyZtautauhp0_M1110to40_pt20	e959_s1310_s1300_r3043_r2993_p851	$3.06 \times 10^3$	1.22	1.0
mc11_7TeV.128510.AlpgenJimmyZtautauhp0_M11150to250_pt20	e997_s1372_s1370_r3043_r2993_p851	$1.69 \times 10^0$	1.25	1.0
mc11_7TeV.128520.AlpgenJimmyZtautauhp0_M11250to400_pt20	e997_s1372_s1370_r3043_r2993_p851	$2.03 \times 10^{-1}$	1.25	1.0
mc11_7TeV.128530.AlpgenJimmyZtautauhp0_M11400_pt20	e997_s1372_s1370_r3043_r2993_p851	$3.36 \times 10^{-2}$	1.25	1.0
mc11_7TeV.107671.AlpgenJimmyZtautauhp0_pt20	e835_s1299_s1300_r3043_r2993_p851	$6.68 \times 10^2$	1.25	1.0
mc11_7TeV.116271.AlpgenJimmyZtautauhp1_M1110to40_pt20	e959_s1310_s1300_r3043_r2993_p851	$8.49 \times 10^1$	1.22	1.0
mc11_7TeV.128511.AlpgenJimmyZtautauhp1_M11150to250_pt20	e997_s1372_s1370_r3043_r2993_p851	$5.64 \times 10^{-1}$	1.25	1.0
mc11_7TeV.128521.AlpgenJimmyZtautauhp1_M11250to400_pt20	e997_s1372_s1370_r3043_r2993_p851	$9.32 \times 10^{-2}$	1.25	1.0
mc11_7TeV.128531.AlpgenJimmyZtautauhp1_M11400_pt20	e997_s1372_s1370_r3043_r2993_p851	$2.11 \times 10^{-2}$	1.25	1.0
mc11_7TeV.107671.AlpgenJimmyZtautauhp1_pt20	e835_s1299_s1300_r3043_r2993_p851	$1.35 \times 10^2$	1.25	1.0
mc11_7TeV.116272.AlpgenJimmyZtautauhp2_M1110to40_pt20	e959_s1310_s1300_r3043_r2993_p851	$4.15 \times 10^1$	1.22	1.0
mc11_7TeV.128512.AlpgenJimmyZtautauhp2_M11150to250_pt20	e997_s1372_s1370_r3043_r2993_p851	$1.88 \times 10^{-1}$	1.25	1.0
mc11_7TeV.128522.AlpgenJimmyZtautauhp2_M11250to400_pt20	e997_s1372_s1370_r3043_r2993_p851	$3.40 \times 10^{-2}$	1.25	1.0
mc11_7TeV.128532.AlpgenJimmyZtautauhp2_M11400_pt20	e997_s1372_s1370_r3043_r2993_p851	$8.43 \times 10^{-3}$	1.25	1.0
mc11_7TeV.107672.AlpgenJimmyZtautauhp2_pt20	e835_s1299_s1300_r3043_r2993_p851	$4.04 \times 10^1$	1.25	1.0
mc11_7TeV.116273.AlpgenJimmyZtautauhp3_M1110to40_pt20	e959_s1310_s1300_r3043_r2993_p851	$8.36 \times 10^0$	1.22	1.0
mc11_7TeV.128513.AlpgenJimmyZtautauhp3_M11150to250_pt20	e997_s1372_s1370_r3043_r2993_p851	$5.75 \times 10^{-2}$	1.25	1.0
mc11_7TeV.128523.AlpgenJimmyZtautauhp3_M11250to400_pt20	e997_s1372_s1370_r3043_r2993_p851	$1.08 \times 10^{-2}$	1.25	1.0
mc11_7TeV.128533.AlpgenJimmyZtautauhp3_M11400_pt20	e997_s1372_s1370_r3043_r2993_p851	$2.75 \times 10^{-3}$	1.25	1.0
mc11_7TeV.107673.AlpgenJimmyZtautauhp3_pt20	e835_s1299_s1300_r3043_r2993_p851	$1.12 \times 10^1$	1.25	1.0
mc11_7TeV.116274.AlpgenJimmyZtautauhp4_M1110to40_pt20	e959_s1310_s1300_r3043_r2993_p851	$1.85 \times 10^0$	1.22	1.0
mc11_7TeV.128514.AlpgenJimmyZtautauhp4_M11150to250_pt20	e997_s1372_s1370_r3043_r2993_p851	$1.59 \times 10^{-2}$	1.25	1.0
mc11_7TeV.128524.AlpgenJimmyZtautauhp4_M11250to400_pt20	e997_s1372_s1370_r3043_r2993_p851	$3.04 \times 10^{-3}$	1.25	1.0
mc11_7TeV.128534.AlpgenJimmyZtautauhp4_M11400_pt20	e997_s1372_s1370_r3043_r2993_p851	$7.80 \times 10^{-4}$	1.25	1.0
mc11_7TeV.107674.AlpgenJimmyZtautauhp4_pt20	e835_s1299_s1300_r3043_r2993_p851	$2.79 \times 10^0$	1.25	1.0
mc11_7TeV.116275.AlpgenJimmyZtautauhp5_M1110to40_pt20	e959_s1310_s1300_r3043_r2993_p851	$4.60 \times 10^{-1}$	1.22	1.0
mc11_7TeV.128515.AlpgenJimmyZtautauhp5_M11150to250_pt20	e997_s1372_s1370_r3043_r2993_p851	$4.70 \times 10^{-3}$	1.25	1.0
mc11_7TeV.128525.AlpgenJimmyZtautauhp5_M11250to400_pt20	e997_s1372_s1370_r3043_r2993_p851	$9.20 \times 10^{-4}$	1.25	1.0
mc11_7TeV.128535.AlpgenJimmyZtautauhp5_M11400_pt20	e997_s1372_s1370_r3043_r2993_p851	$2.30 \times 10^{-4}$	1.25	1.0
mc11_7TeV.107675.AlpgenJimmyZtautauhp5_pt20	e835_s1299_s1300_r3043_r2993_p851	$7.69 \times 10^{-1}$	1.25	1.0
$W \rightarrow \tau\nu + \text{jets}$				
mc11_7TeV.107700.AlpgenJimmyWtautauhp0_pt20	e835_s1299_s1300_r3043_r2993_p851	$6.92 \times 10^3$	1.2	1.0
mc11_7TeV.107701.AlpgenJimmyWtautauhp1_pt20	e835_s1299_s1300_r3043_r2993_p851	$1.30 \times 10^3$	1.2	1.0
mc11_7TeV.107702.AlpgenJimmyWtautauhp2_pt20	e835_s1299_s1300_r3043_r2993_p851	$3.78 \times 10^2$	1.2	1.0
mc11_7TeV.107703.AlpgenJimmyWtautauhp3_pt20	e835_s1299_s1300_r3043_r2993_p851	$1.02 \times 10^2$	1.2	1.0
mc11_7TeV.107704.AlpgenJimmyWtautauhp4_pt20	e835_s1299_s1300_r3043_r2993_p851	$2.56 \times 10^1$	1.2	1.0
mc11_7TeV.107705.AlpgenJimmyWtautauhp5_pt20	e835_s1299_s1300_r3043_p851	$6.99 \times 10^0$	1.2	1.0

Table A.11: Logical dataset names, cross sections, k-factors and filter efficiencies for the simulated  $Z \rightarrow \tau\tau$  and  $W \rightarrow \tau\nu$  production.



dataset name	production tag	cross section [pb]	k-factor	filter efficiency
$Z \rightarrow e^+e^-/\mu^+\mu^-$				
mc11_7TeV.116250.AlpgenJimmyZeeNp0_M1110to40_pt20	e959_s1310_s1300_r3043_r2993_p851	$3.06 \times 10^3$	1.22	1.0
mc11_7TeV.107650.AlpgenJimmyZeeNp0_pt20	e835_s1299_s1300_r3043_p851	$6.68 \times 10^2$	1.25	1.0
mc11_7TeV.116251.AlpgenJimmyZeeNp1_M1110to40_pt20	e959_s1310_s1300_r3043_r2993_p851	$8.49 \times 10^1$	1.22	1.0
mc11_7TeV.107651.AlpgenJimmyZeeNp1_pt20	e835_s1299_s1300_r3043_r2993_p851	$1.34 \times 10^2$	1.25	1.0
mc11_7TeV.116252.AlpgenJimmyZeeNp2_M1110to40_pt20	e944_s1310_s1300_r3043_r2993_p851	$4.14 \times 10^1$	1.22	1.0
mc11_7TeV.107652.AlpgenJimmyZeeNp2_pt20	e835_s1299_s1300_r3043_r2993_p851	$4.05 \times 10^1$	1.25	1.0
mc11_7TeV.116253.AlpgenJimmyZeeNp3_M1110to40_pt20	e944_s1310_s1300_r3043_r2993_p851	$8.38 \times 10^0$	1.22	1.0
mc11_7TeV.107653.AlpgenJimmyZeeNp3_pt20	e835_s1299_s1300_r3043_r2993_p851	$1.12 \times 10^1$	1.25	1.0
mc11_7TeV.116254.AlpgenJimmyZeeNp4_M1110to40_pt20	e944_s1310_s1300_r3043_r2993_p851	$1.85 \times 10^0$	1.22	1.0
mc11_7TeV.107654.AlpgenJimmyZeeNp4_pt20	e835_s1299_s1300_r3043_r2993_p851	$2.88 \times 10^0$	1.25	1.0
mc11_7TeV.116255.AlpgenJimmyZeeNp5_M1110to40_pt20	e944_s1310_s1300_r3043_p851	$4.60 \times 10^{-1}$	1.22	1.0
mc11_7TeV.107655.AlpgenJimmyZeeNp5_pt20	e835_s1299_s1300_r3043_r2993_p851	$8.30 \times 10^{-1}$	1.25	1.0
mc11_7TeV.116260.AlpgenJimmyZmumuNp0_M1110to40_pt20	e959_s1310_s1300_r3043_p851	$3.05 \times 10^3$	1.22	1.0
mc11_7TeV.107660.AlpgenJimmyZmumuNp0_pt20	e835_s1299_s1300_r3043_r2993_p851	$6.69 \times 10^2$	1.25	1.0
mc11_7TeV.116261.AlpgenJimmyZmumuNp1_M1110to40_pt20	e959_s1310_s1300_r3043_r2993_p851	$8.49 \times 10^1$	1.22	1.0
mc11_7TeV.107661.AlpgenJimmyZmumuNp1_pt20	e835_s1299_s1300_r3043_r2993_p851	$1.34 \times 10^2$	1.25	1.0
mc11_7TeV.116262.AlpgenJimmyZmumuNp2_M1110to40_pt20	e944_s1310_s1300_r3043_r2993_p851	$4.15 \times 10^1$	1.22	1.0
mc11_7TeV.107662.AlpgenJimmyZmumuNp2_pt20	e835_s1299_s1300_r3043_r2993_p851	$4.03 \times 10^1$	1.25	1.0
mc11_7TeV.116263.AlpgenJimmyZmumuNp3_M1110to40_pt20	e944_s1310_s1300_r3043_p851	$8.38 \times 10^0$	1.22	1.0
mc11_7TeV.107663.AlpgenJimmyZmumuNp3_pt20	e835_s1299_s1300_r3043_r2993_p851	$1.12 \times 10^1$	1.25	1.0
mc11_7TeV.116264.AlpgenJimmyZmumuNp4_M1110to40_pt20	e944_s1310_s1300_r3043_p851	$1.85 \times 10^0$	1.22	1.0
mc11_7TeV.107664.AlpgenJimmyZmumuNp4_pt20	e835_s1299_s1300_r3043_r2993_p851	$2.75 \times 10^0$	1.25	1.0
mc11_7TeV.116265.AlpgenJimmyZmumuNp5_M1110to40_pt20	e944_s1310_s1300_r3043_r2993_p851	$4.60 \times 10^{-1}$	1.22	1.0
mc11_7TeV.107665.AlpgenJimmyZmumuNp5_pt20	e835_s1299_s1300_r3043_r2993_p851	$7.69 \times 10^{-1}$	1.25	1.0
$W \rightarrow e\nu/\mu\nu + \text{jets}$				
mc11_7TeV.107680.AlpgenJimmyWenuNp0_pt20	e825_s1299_s1300_r3043_r2993_p851	$6.92 \times 10^3$	1.2	1.0
mc11_7TeV.107681.AlpgenJimmyWenuNp1_pt20	e825_s1299_s1300_r3043_r2993_p851	$1.30 \times 10^3$	1.2	1.0
mc11_7TeV.107682.AlpgenJimmyWenuNp2_pt20	e825_s1299_s1300_r3043_r2993_p851	$3.78 \times 10^2$	1.2	1.0
mc11_7TeV.107683.AlpgenJimmyWenuNp3_pt20	e825_s1299_s1300_r3043_r2993_p851	$1.01 \times 10^2$	1.2	1.0
mc11_7TeV.107684.AlpgenJimmyWenuNp4_pt20	e825_s1299_s1300_r2920_r2900_p851	$2.59 \times 10^1$	1.2	1.0
mc11_7TeV.107685.AlpgenJimmyWenuNp5_pt20	e825_s1299_s1300_r3043_p851	$6.92 \times 10^0$	1.2	1.0
mc11_7TeV.107690.AlpgenJimmyWenuNp0_pt20	e825_s1299_s1300_r3043_r2993_p851	$6.92 \times 10^3$	1.2	1.0
mc11_7TeV.107691.AlpgenJimmyWenuNp1_pt20	e825_s1299_s1300_r3043_r2993_p851	$1.30 \times 10^3$	1.2	1.0
mc11_7TeV.107692.AlpgenJimmyWenuNp2_pt20	e825_s1299_s1300_r3043_r2993_p851	$3.78 \times 10^2$	1.2	1.0
mc11_7TeV.107693.AlpgenJimmyWenuNp3_pt20	e825_s1299_s1300_r3043_r2993_p851	$1.02 \times 10^2$	1.2	1.0
mc11_7TeV.107694.AlpgenJimmyWenuNp4_pt20	e825_s1299_s1300_r3043_r2993_p851	$2.56 \times 10^1$	1.2	1.0
mc11_7TeV.107695.AlpgenJimmyWenuNp5_pt20	e825_s1299_s1300_r3043_r2993_p851	$7.04 \times 10^0$	1.2	1.0

Table A.12: Logical dataset names, cross sections, k-factors and filter efficiencies for the simulated  $Z \rightarrow e^+e^-/\mu^+\mu^-$  and  $W \rightarrow e\nu/\mu\nu + \text{jets}$  production.

Table A.13: Logical dataset names, cross sections, k-factors and filter efficiencies for the simulated  $W \rightarrow q\bar{q}' + \text{jets}$ , single top and  $t\bar{t}$  production.

dataset name	production tag $W \rightarrow q\bar{q}' + \text{jets}$	cross section [pb]	k-factor	filter efficiency
mc11_7TeV.107280.AlpgenJimmyWbbFullNp0_pt20	e887_s1310_s1300_r3043_r2993_p851	$4.74 \times 10^1$	1.2	1.0
mc11_7TeV.107281.AlpgenJimmyWbbFullNp1_pt20	e887_s1310_s1300_r3043_r2993_p851	$3.57 \times 10^1$	1.2	1.0
mc11_7TeV.107282.AlpgenJimmyWbbFullNp2_pt20	e887_s1310_s1300_r3043_r2993_p851	$1.73 \times 10^1$	1.2	1.0
mc11_7TeV.107283.AlpgenJimmyWbbFullNp3_pt20	e887_s1310_s1300_r3043_r2993_p851	$7.61 \times 10^0$	1.2	1.0
mc11_7TeV.117293.AlpgenMcNp0_pt20	e887_s1310_s1300_r3043_r2993_p851	$6.44 \times 10^2$	1.2	1.0
mc11_7TeV.117294.AlpgenMcNp1_pt20	e887_s1310_s1300_r3043_r2993_p851	$2.05 \times 10^2$	1.2	1.0
mc11_7TeV.117295.AlpgenMcNp2_pt20	e887_s1310_s1300_r3043_r2993_p851	$5.09 \times 10^1$	1.2	1.0
mc11_7TeV.117296.AlpgenMcNp3_pt20	e887_s1310_s1300_r3043_r2993_p851	$1.14 \times 10^1$	1.2	1.0
mc11_7TeV.117297.AlpgenMcNp4_pt20	e887_s1310_s1300_r3043_r2993_p851	$2.77 \times 10^0$	1.2	1.0
mc11_7TeV.117284.AlpgenMcFullNp0_pt20	e887_s1310_s1300_r3043_r2993_p851	$1.28 \times 10^2$	1.2	1.0
mc11_7TeV.117285.AlpgenMcFullNp1_pt20	e887_s1310_s1300_r3043_r2993_p851	$1.05 \times 10^2$	1.2	1.0
mc11_7TeV.117286.AlpgenMcFullNp2_pt20	e887_s1310_s1300_r3043_r2993_p851	$5.21 \times 10^1$	1.2	1.0
mc11_7TeV.117287.AlpgenMcFullNp3_pt20	e887_s1310_s1300_r3043_r2993_p851	$1.70 \times 10^1$	1.2	1.0
<i>top production</i>				
mc11_7TeV.105500.AcerMC_Wt	e825_s1310_s1300_r3043_r2993_p851	$1.56 \times 10^1$	1.0	1.0
mc11_7TeV.105200.TTbar_McAtNLO_Jimmy	e835_s1272_s1274_r3043_r2993_p851	$1.65 \times 10^2$	1.0	0.54259
mc11_7TeV.105204.TTbar_FullHad_McAtNLO_Jimmy	e825_s1310_s1300_r3043_r2993_p851	$1.65 \times 10^2$	1.0	0.45741
mc11_7TeV.117363.st_schan_enu_AcerMC	e825_s1310_s1300_r3043_r2993_p851	$5.00 \times 10^{-1}$	1.0	1.0
mc11_7TeV.117364.st_schan_munu_AcerMC	e825_s1310_s1300_r3043_r2993_p851	$5.00 \times 10^{-1}$	1.0	1.0
mc11_7TeV.117365.st_schan_tauuu_AcerMC	e825_s1310_s1300_r3043_r2993_p851	$5.00 \times 10^{-1}$	1.0	1.0
mc11_7TeV.117360.st_tchan_enu_AcerMC	e835_s1310_s1300_r3043_r2993_p851	$6.93 \times 10^0$	1.0	1.0
mc11_7TeV.117361.st_tchan_munu_AcerMC	e835_s1310_s1300_r3043_r2993_p851	$6.93 \times 10^0$	1.0	1.0
mc11_7TeV.117362.st_tchan_tauuu_AcerMC	e825_s1310_s1300_r3043_r2993_p851	$6.93 \times 10^0$	1.0	1.0

dataset name	production tag <i>di-boson production</i>	cross section [pb]	k-factor	filter efficiency
mc11_7TeV.105971.McAtNlo.JIMMY_WmZ_lnull	e872_s1310_s1300_r3043_r2993_p851	$8.80 \times 10^{-2}$	1.0	1.0
mc11_7TeV.105970.McAtNlo.JIMMY_WmZ_lnuqq	e872_s1310_s1300_r3043_r2993_p851	$9.20 \times 10^{-1}$	1.0	1.0
mc11_7TeV.106028.McAtNlo.JIMMY_WmZ_lnutautau	e872_s1310_s1300_r3043_r2993_p851	$4.40 \times 10^{-2}$	1.0	1.0
mc11_7TeV.105972.McAtNlo.JIMMY_WmZ_qql1	e872_s1310_s1300_r3043_r2993_p851	$2.74 \times 10^{-1}$	1.0	1.0
mc11_7TeV.113191.McAtNlo.JIMMY_WmZ_qqtautau	e872_s1310_s1300_r3043_r2993_p851	$1.37 \times 10^{-1}$	1.0	1.0
mc11_7TeV.106027.McAtNlo.JIMMY_WmZ_tautnull	e872_s1310_s1300_r3043_r2993_p851	$4.40 \times 10^{-2}$	1.0	1.0
mc11_7TeV.106029.McAtNlo.JIMMY_WmZ_tautautau	e872_s1310_s1300_r3043_r2993_p851	$2.20 \times 10^{-2}$	1.0	1.0
mc11_7TeV.105921.McAtNlo.JIMMY_WpWm_enunu	e872_s1310_s1300_r3043_r2993_p851	$5.24 \times 10^{-1}$	1.0	1.0
mc11_7TeV.105922.McAtNlo.JIMMY_WpWm_enununu	e872_s1310_s1300_r3043_r2993_p851	$5.24 \times 10^{-1}$	1.0	1.0
mc11_7TeV.105923.McAtNlo.JIMMY_WpWm_enutaunu	e872_s1310_s1300_r3043_r2993_p851	$5.24 \times 10^{-1}$	1.0	1.0
mc11_7TeV.105925.McAtNlo.JIMMY_WpWm_munuenu	e872_s1310_s1300_r3043_r2993_p851	$5.24 \times 10^{-1}$	1.0	1.0
mc11_7TeV.105924.McAtNlo.JIMMY_WpWm_mununu	e872_s1310_s1300_r3043_p851	$5.24 \times 10^{-1}$	1.0	1.0
mc11_7TeV.105926.McAtNlo.JIMMY_WpWm_munutaunu	e872_s1310_s1300_r3043_p851	$5.24 \times 10^{-1}$	1.0	1.0
mc11_7TeV.105928.McAtNlo.JIMMY_WpWm_tanuenu	e872_s1310_s1300_r3043_r2993_p851	$5.24 \times 10^{-1}$	1.0	1.0
mc11_7TeV.105929.McAtNlo.JIMMY_WpWm_tanununu	e872_s1310_s1300_r3043_r2993_p851	$5.24 \times 10^{-1}$	1.0	1.0
mc11_7TeV.105927.McAtNlo.JIMMY_WpWm_tautautau	e872_s1310_s1300_r3043_r2993_p851	$5.24 \times 10^{-1}$	1.0	1.0
mc11_7TeV.105941.McAtNlo.JIMMY_WpZ_lnull	e893_s1310_s1300_r3043_r2993_p851	$1.61 \times 10^{-1}$	1.0	1.0
mc11_7TeV.105940.McAtNlo.JIMMY_WpZ_lnuqq	e872_s1310_s1300_r3043_p851	$1.70 \times 10^0$	1.0	1.0
mc11_7TeV.106025.McAtNlo.JIMMY_WpZ_lnutautau	e872_s1310_s1300_r3043_r2993_p851	$8.20 \times 10^{-2}$	1.0	1.0
mc11_7TeV.105942.McAtNlo.JIMMY_WpZ_qql1	e872_s1310_s1300_r3043_r2993_p851	$5.06 \times 10^{-1}$	1.0	1.0
mc11_7TeV.113190.McAtNlo.JIMMY_WpZ_qqtautau	e872_s1310_s1300_r3043_r2993_p851	$2.55 \times 10^{-1}$	1.0	1.0
mc11_7TeV.106024.McAtNlo.JIMMY_WpZ_tautnull	e872_s1310_s1300_r3043_r2993_p851	$8.10 \times 10^{-2}$	1.0	1.0
mc11_7TeV.106026.McAtNlo.JIMMY_WpZ_tautautau	e872_s1310_s1300_r3043_r2993_p851	$4.10 \times 10^{-2}$	1.0	1.0
mc11_7TeV.106036.McAtNlo.JIMMY_ZZ_2l2tau	e872_s1310_s1300_r3043_p851	$2.60 \times 10^{-2}$	1.0	1.0
mc11_7TeV.106037.McAtNlo.JIMMY_ZZ_4tau	e872_s1310_s1300_r3043_r2993_p851	$6.00 \times 10^{-3}$	1.0	1.0
mc11_7TeV.105931.McAtNlo.JIMMY_ZZ_l1l1	e872_s1310_s1300_r3043_p851	$2.55 \times 10^{-2}$	1.0	1.0
mc11_7TeV.105932.McAtNlo.JIMMY_ZZ_l1l1qq	e872_s1310_s1300_r3043_p851	$1.52 \times 10^{-1}$	1.0	1.0
mc11_7TeV.105930.McAtNlo.JIMMY_ZZ_l1qq	e872_s1310_s1300_r3043_r2993_p851	$5.30 \times 10^{-1}$	1.0	1.0
mc11_7TeV.113192.McAtNlo.JIMMY_ZZ_tautauqq	e893_s1310_s1300_r3043_r2993_p851	$7.70 \times 10^{-2}$	1.0	1.0
mc11_7TeV.106011.gg2WW0240_JIMMY_WW_enunu	e872_s1310_s1300_r3043_r2993	$2.66 \times 10^{-1}$	1.0	1.0
mc11_7TeV.106012.gg2WW0240_JIMMY_WW_enununu	e968_s1310_s1300_r3043_r2993	$1.55 \times 10^1$	1.0	0.0009895
mc11_7TeV.106013.gg2WW0240_JIMMY_WW_enutaunu	e968_s1310_s1300_r3043_r2993	$1.55 \times 10^1$	1.0	0.0009899
mc11_7TeV.106015.gg2WW0240_JIMMY_WW_munuenu	e968_s1310_s1300_r3043_r2993	$1.55 \times 10^1$	1.0	0.0009232
mc11_7TeV.106014.gg2WW0240_JIMMY_WW_mununu	e968_s1310_s1300_r3043_r2993	$1.55 \times 10^1$	1.0	0.0009869
mc11_7TeV.106016.gg2WW0240_JIMMY_WW_munutaunu	e968_s1310_s1300_r3043_r2993	$1.55 \times 10^1$	1.0	0.000989
mc11_7TeV.106018.gg2WW0240_JIMMY_WW_tanuenu	e968_s1310_s1300_r3043_r2993	$1.55 \times 10^1$	1.0	0.0009288
mc11_7TeV.106019.gg2WW0240_JIMMY_WW_tanununu	e968_s1310_s1300_r3043_r2993	$1.55 \times 10^1$	1.0	0.0009219
mc11_7TeV.106017.gg2WW0240_JIMMY_WW_tautautau	e968_s1310_s1300_r3043_r2993	$1.55 \times 10^1$	1.0	0.0009289

Table A.14: Logical dataset names, cross sections, k-factors and filter efficiencies for the simulated production of two gauge bosons.

### A.4.6 Exclusion Limits

#### Exclusion Limits for the 2011 Data Set

Summary tables for the upper limit  $\tan\beta$  values in the  $m_h^{\text{mod-}}$  and  $m_h^{\text{mod+}}$  benchmark scenarios are provided in Table A.15 and Table A.16, respectively.

$m_A$ [GeV]	observed	expected	$+2\sigma$	$+1\sigma$	$-1\sigma$	$-2\sigma$
140	29.9	24.0	37.9	29.8	20.6	18.2
150	28.4	22.3	34.9	27.8	19.2	16.5
170	24.7	19.9	31.4	24.7	17.1	14.7
200	20.4	19.8	31.1	24.5	17.0	14.7
250	16.9	19.3	29.8	23.7	16.6	14.4
300	20.7	23.9	37.0	29.4	20.7	18.5
350	22.1	28.1	44.0	34.6	24.3	21.7
400	23.3	29.7	45.3	36.4	25.9	23.0
450	26.5	32.6	47.6	38.9	28.5	25.2
500	30.2	34.8	50.8	41.7	30.6	27.5
550	34.6	38.8	56.6	46.3	34.2	30.5
600	39.6	44.9	64.2	53.8	39.5	35.3
650	44.3	51.6	69.0	61.4	45.1	40.3
700	47.7	57.4	71.9	66.0	50.2	44.7
750	53.5	63.5	74.2	69.9	56.8	50.5
800	62.0	68.5	76.0	73.0	63.8	58.1

**Table A.15:** Upper limit  $\tan\beta$  values for the nominal MSSM  $m_h^{\text{mod-}}$  benchmark scenario at a confidence level of 95%. The upper limits are estimated using the 2011 data set recorded with the ATLAS detector.

$m_A$ [GeV]	observed	expected	$+2\sigma$	$+1\sigma$	$-1\sigma$	$-2\sigma$
140	31.0	24.5	39.3	30.9	21.0	18.5
150	29.1	22.7	36.3	28.6	19.4	16.9
170	25.3	20.2	32.5	25.3	17.4	14.9
200	20.9	20.1	32.2	25.1	17.4	14.9
250	17.2	19.6	30.8	24.3	16.9	14.6
300	21.2	24.5	38.5	30.3	21.3	18.9
350	22.6	29.0	46.2	36.1	25.0	22.2
400	24.0	30.9	47.9	38.0	26.9	23.8
450	27.6	33.8	50.1	40.6	29.5	26.1
500	31.7	36.5	54.1	43.8	32.1	28.6
550	36.3	40.7	60.4	49.0	35.7	32.0
600	41.9	47.7	67.3	57.6	41.7	37.2
650	47.0	54.9	71.5	64.8	48.1	42.8
700	50.6	61.3	74.0	68.8	53.7	47.7
750	57.3	66.7	76.1	72.3	60.8	54.0
800	65.3	71.1	77.7	75.0	66.9	61.9

**Table A.16:** Upper limit  $\tan\beta$  values for the nominal MSSM  $m_h^{\text{mod}+}$  benchmark scenario at a confidence level of 95%. The upper limits are estimated using the 2011 data set recorded with the ATLAS detector.

### Validation of the Maximum Likelihood Estimators

The pull distributions of the remaining nuisance parameters are provided in Figure A.8 and Figure A.9. All distribution are estimated using the pseudo-experiments with signal hypothesis at  $m_A = 300$  GeV and  $\tan \beta = 20$ .

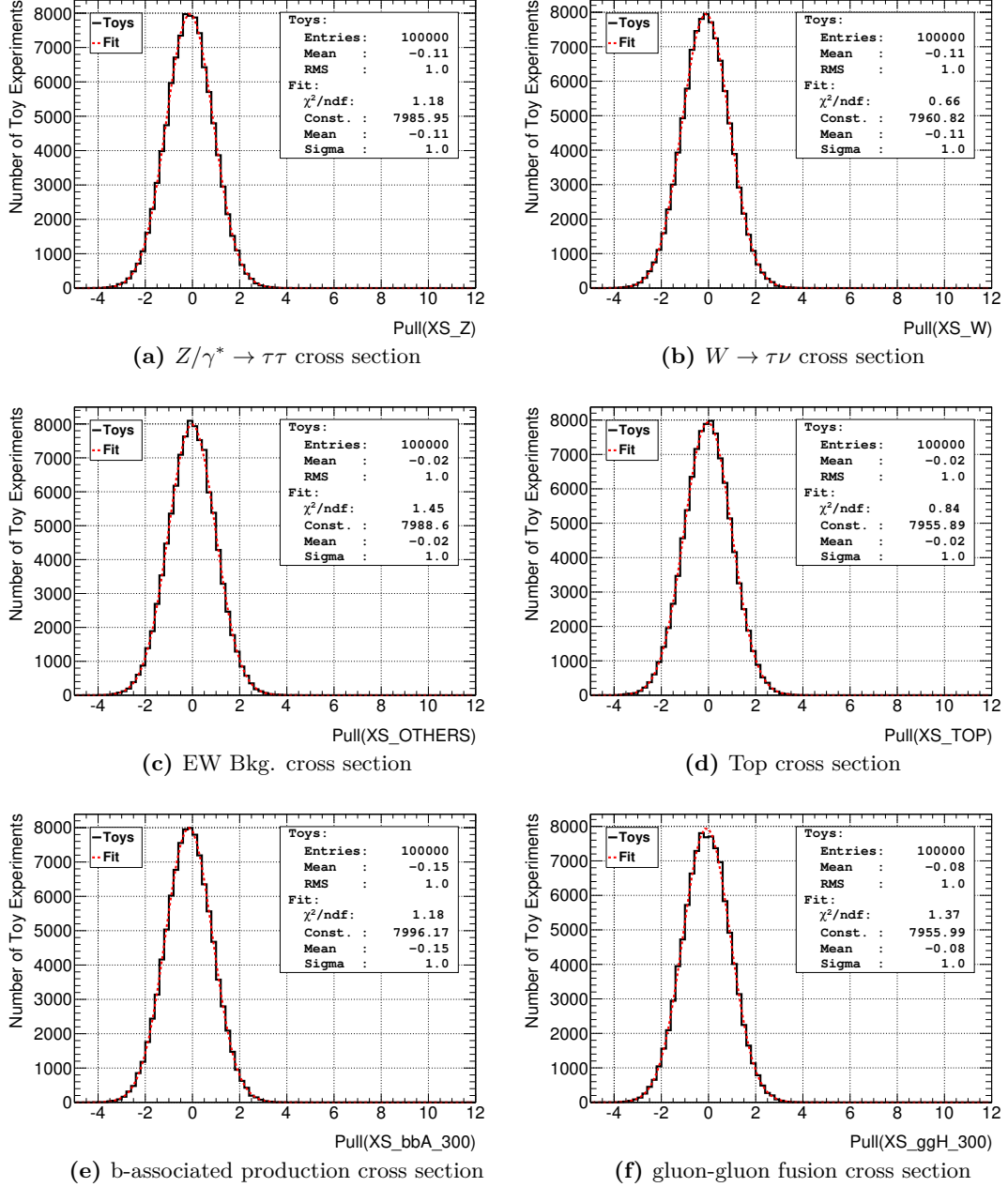


**Figure A.8:** Pull distributions for the nuisance parameters related to the cross sections of the signal and background processes.

A legend for the nuisance parameter name convention is provided in Table A.17.

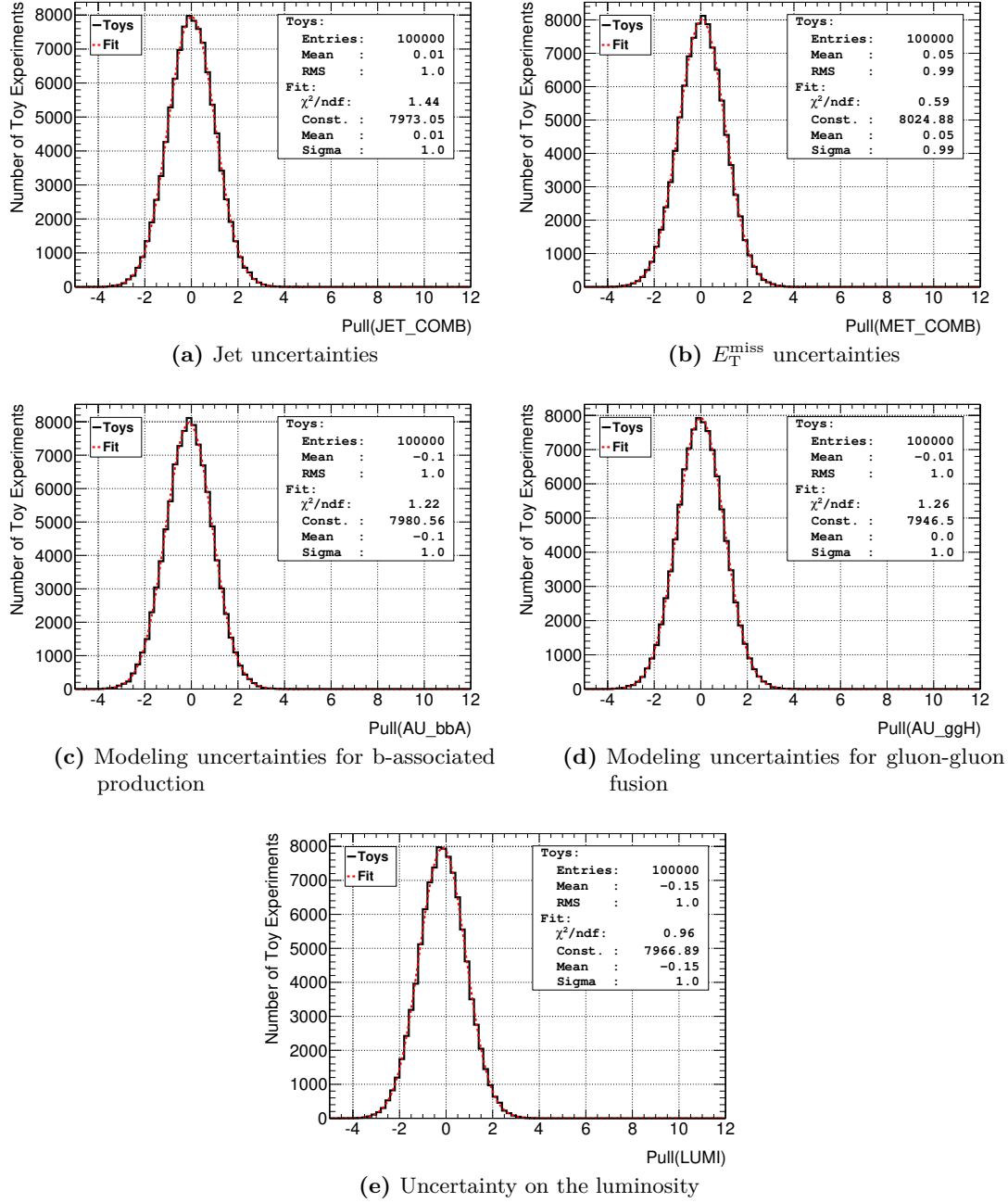


**Figure A.9:** Pull distributions for the nuisance parameters related to jets (a),  $E_T^{\text{miss}}$  (b), modeling (c-d) and luminosity (e).

Symbol	Description
TAU_IDS	Uncertainty on the scale factor for the tau identification, for the <i>loose</i> and <i>medium</i> working point, respectively.
TAU_TES	Uncertainty related to the reconstructed tau lepton energy scale.
TAU_FF	Uncertainty on the tau lepton transfer factor, used for the QCD multi-jet estimation in the STT category.
TAU_FW	Uncertainty on the tau misidentification efficiency.
TAU_EVETO	Uncertainty on the scale factor for the tau electron veto algorithm.
TRIG_SF	Uncertainty on the trigger scale factor, for both the di-tau and single-tau trigger.
JET_COMB	Combined value for the all jet related uncertainty sources, discussed in Section 6.6.
MET_COMB	Combined value for the all $E_T^{\text{miss}}$ related uncertainty sources, discussed in Section 6.6.
LUMI	Uncertainty on the estimated luminosity.
AU_bbA	Uncertainty on the modeling of b-associated MSSM Higgs production.
AU_ggH	Uncertainty on the modeling of MSSM Higgs production via gluon-gluon fusion.
XS_Z	Cross section uncertainty for the $Z \rightarrow \tau\tau$ production.
XS_W	Cross section uncertainty for the $W \rightarrow \tau\nu$ production.
XS_OTHERS	Combined cross section uncertainty for the remaining electroweak background.
XS_TOP	Combined cross section uncertainty for $t\bar{t}$ and single top production.
XS_bbA_400	Cross section uncertainty for the b-associated production of the $A$ and $H$ Higgs boson.
XS_ggH_400	Cross section uncertainty for the production of the $A$ and $H$ Higgs boson via the gluon-gluon fusion process.

**Table A.17:** Legend for the nuisance parameter.



# List of Figures

2.1	Illustration of the Higgs potential in the one-dimensional case. . . . .	8
2.2	Illustration of the scalar Higgs potential . . . . .	10
2.3	Summary of measurements for $\alpha_S(Q^2)$ . . . . .	11
2.4	Development of the neutral, CP-even Higgs bosons masses . . . . .	22
2.5	Neutral MSSM Higgs production in association with heavy quarks. . . . .	24
2.6	Neutral MSSM Higgs production in association with b-quarks. . . . .	24
2.7	Production cross sections for neutral MSSM Higgs bosons . . . . .	25
2.8	Neutral MSSM Higgs production via gluon-gluon fusion . . . . .	26
2.9	Neutral MSSM Higgs production via vector boson interactions . . . . .	27
2.10	MSSM Higgs boson branching ratios . . . . .	29
3.1	LHC Layout . . . . .	37
3.2	Accelerator Complex at CERN . . . . .	38
3.3	ATLAS Detector . . . . .	39
3.4	ATLAS coordinate system . . . . .	40
3.5	ATLAS Calorimeter System . . . . .	43
3.6	ATLAS Calorimeter System . . . . .	45
3.7	Peak luminosity and pile-up as a function of time during Run 1 . . . . .	49
4.1	Electron efficiency and scale factors . . . . .	55
4.2	Muon reconstruction efficiency . . . . .	57
4.3	Relative jet resolution as a function of the average transverse jet momenta . . . . .	61
4.4	Tau decay diagram . . . . .	64
4.5	Resolution in $p_T^\tau$ . . . . .	67
4.6	Performance of the discrimination between electrons and tau leptons . . . . .	68
4.7	Observables for tau lepton identification for 1 and multi-prong tau leptons . . . . .	71
4.8	LLH score for tau id . . . . .	73
4.9	Tau LLH thresholds . . . . .	74
4.10	Tau identification efficiency against $p_T$ using LLH . . . . .	75
4.11	Tau identification efficiency against $N_{Vtx}$ using LLH . . . . .	76
4.12	BDT score for tau id . . . . .	77
4.13	Tau identification efficiency against $p_T$ and $N_{Vtx}$ using BDT . . . . .	77
4.14	Signal efficiencies vs. background rejection in early 2012 . . . . .	78
4.15	Signal efficiencies vs. background rejection in 2011 . . . . .	78
4.16	Systematic uncertainty on the missing transverse momentum . . . . .	80
4.17	ATLAS cross sections measurements for SM processes . . . . .	82
4.18	Minimum Bias Trigger Efficiency . . . . .	84

4.19	Jet Trigger Efficiency . . . . .	85
4.20	Muon Trigger Efficiency . . . . .	85
4.21	Tau Trigger Efficiency . . . . .	87
5.1	Illustration of multiple parton scattering . . . . .	89
5.2	Parton distribution functions . . . . .	90
5.3	Two-jet production Feynman diagrams . . . . .	92
5.4	Illustration Underlying Event Regions . . . . .	94
5.5	Jet Topology . . . . .	95
5.6	Track Reconstruction Efficiency . . . . .	105
5.7	Convergence Behavior for Bayesian Iterative Unfolding . . . . .	109
5.8	Smearing Matrices for Single Observables . . . . .	111
5.9	Smearing Matrices for Correlated Observables against $p_T^{\text{lead}}$ . . . . .	112
5.10	Smearing Matrix for $\langle p_T \rangle$ against $N_{\text{ch}}$ . . . . .	113
5.11	Merged Vertex Estimation . . . . .	114
5.12	Systematic uncertainties for the $\sum p_T$ density against $p_T^{\text{lead}}$ . . . . .	119
5.13	1D Distributions for different $p_T^{\text{lead}}$ ranges . . . . .	124
5.14	Profile distributions for $\sum p_T$ and $N_{\text{ch}}$ against $p_T^{\text{lead}}$ in the transverse region . . .	125
5.15	Profile distributions for $\sum p_T$ and $N_{\text{ch}}$ against $p_T^{\text{lead}}$ in the trans-max/min/diff region . . . . .	126
5.16	Profile distributions for $\sum E_T$ against $p_T^{\text{lead}}$ in the transverse region . . . . .	128
5.17	Profile distributions for $\sum E_T$ against $p_T^{\text{lead}}$ in the trans-max/min/diff region . .	129
5.18	Profile distributions for $\langle \sum p_T / \sum E_T \rangle$ in the transverse region . . . . .	130
5.19	Profile distributions for $\langle p_T \rangle$ in the transverse region . . . . .	131
5.20	Comparison between different underlying event analyses . . . . .	134
6.1	$H/A \rightarrow \tau^+ \tau^-$ decay channels . . . . .	138
6.2	Signal properties . . . . .	139
6.3	Cross sections for $H/A$ production within the $m_h^{\text{max}}$ benchmark scenario . . . . .	140
6.4	Feynman diagrams for Z/W production at the LHC . . . . .	142
6.5	Feynman diagrams for QCD multi-jet production at the LHC . . . . .	143
6.6	Feynman diagrams for the single top and $t\bar{t}$ production at the LHC . . . . .	144
6.7	Total transverse mass distributions for MSSM Higgs signal . . . . .	150
6.8	Average interactions per bunch-crossing in DTT and STT . . . . .	152
6.9	Illustration of the side-band method in the DTT region . . . . .	155
6.10	Shape comparison between the OS/SS region . . . . .	156
6.11	Kinematic distributions of the leading and sub-leading tau candidate within the DTT validation region . . . . .	158
6.12	Di-tau distributions within the DTT validation region . . . . .	159
6.13	BDT score distributions for the STT region . . . . .	160
6.14	Kinematic distributions of the leading and sub-leading tau candidate within the STT validation region . . . . .	162
6.15	Di-tau distributions within the STT validation region . . . . .	163
6.16	$W \rightarrow \mu\nu + \text{jets}$ production . . . . .	165
6.17	Muon isolation and $\sum \cos \Delta\phi$ in the $W \rightarrow \mu\nu$ control region . . . . .	166

6.20	Jet misidentification rates for the loose working point . . . . .	172
6.21	Jet misidentification rates for the medium/tau20 trigger working point . . . . .	173
6.22	Jet misidentification rates for the medium/tau29 trigger working point . . . . .	174
6.23	Tau identification transfer factor . . . . .	179
6.24	$m_T^{\text{tot}}$ and $E_T^{\text{miss}}$ distributions within the Drell-Yan validation region . . . . .	183
6.25	Total transverse mass distribution for DTT and STT . . . . .	193
6.26	Transverse momentum of both tau candidates for DTT and STT . . . . .	194
6.27	Pseudorapidity of both tau candidates for DTT and STT . . . . .	195
6.28	Azimuthal distance between both tau candidates for DTT and STT . . . . .	196
6.29	Missing transverse momentum and total sum of transverse energy for DTT and STT	197
6.30	Observed p-Value . . . . .	202
6.31	Exclusion limits for $m_h^{\text{max}}$ benchmark scenario using the 2011 data set . . . . .	206
6.32	Observed upper limit parametrized in $m_A$ and $\tan \beta$ . . . . .	208
6.33	Exclusion limits for the $m_h^{\text{mod-}}$ and $m_h^{\text{mod+}}$ benchmark scenarios using the 2011 data set . . . . .	209
6.34	Post-fix distributions of the $m_T^{\text{tot}}$ observable for the DTT and STT category . . .	210
6.35	Pull distributions . . . . .	212
6.36	Pull distribution summary . . . . .	213
6.37	Correlation matrix between the nuisance parameter . . . . .	214
6.38	Exclusion limits for $m_h^{\text{max}}$ benchmark scenario using the 2011 and 2012 data set .	215
6.39	Exclusion limits for $m_h^{\text{mod-}}$ and $m_h^{\text{mod+}}$ benchmark scenario using the 2011 and 2012 data set . . . . .	216
6.41	Expected 95 % CL sensitivities in the hMSSM model . . . . .	218
A.1	Development of the neutral, CP-even Higgs bosons masses . . . . .	219
A.2	Observables for tau lepton identification for 1-prong tau leptons . . . . .	220
A.3	Observables for tau lepton identification for multi-prong tau leptons . . . . .	221
A.4	$\Delta Z_{\text{PV,PU}}$ distributions for different data periods . . . . .	222
A.5	Profile distributions for $\sum p_T$ against $p_T^{\text{lead}}$ in the trans-max and trans-min region	223
A.6	Profile distributions for $N_{\text{ch}}$ against $p_T^{\text{lead}}$ in the trans-max and trans-min region	224
A.7	Cross sections for $H/A$ production within the $m_h^{\text{mod-}}$ and $m_h^{\text{mod+}}$ benchmark scenarios . . . . .	225
A.8	Pull distributions for the cross sections related nuisance parameter . . . . .	240
A.9	Pull distributions for nuisance parameter related to jets, $E_T^{\text{miss}}$ , luminosity and modeling . . . . .	241



# List of Tables

2.2	Overview about the SM matter content . . . . .	7
2.3	Parameter Settings for MSSM Benchmark Scenarios . . . . .	33
3.1	Run 1 parameter . . . . .	50
4.1	Jet Cleaning Selection Criteria for year 2010 . . . . .	62
4.2	Jet Cleaning Selection Criteria for year 2011 . . . . .	63
4.3	Tau identification observables for 1-prong and multi-prong . . . . .	70
5.1	Underlying Event Observables . . . . .	97
5.2	Underlying Event MC Samples . . . . .	99
5.3	UE Trigger . . . . .	101
5.4	Underlying Selection Criteria . . . . .	102
5.5	UE Event Numbers . . . . .	103
5.6	Systematic Uncertainties for the Inclusive Topology . . . . .	120
5.7	Systematic Uncertainties for the Exclusive Topology . . . . .	121
6.1	Combined cross sections times branching fractions within the $m_h^{\max}$ benchmark scenario . . . . .	141
6.2	Event yields for the baseline selection . . . . .	148
6.3	Trigger tags for the MSSM Higgs boson search . . . . .	148
6.4	Event Selection . . . . .	149
6.5	Final observed number of events and background predictions within the STT validation regions . . . . .	161
6.6	Muon trigger in the $W \rightarrow \mu\nu$ control region . . . . .	166
6.7	Final observed number of events and background predictions in the $W \rightarrow \mu\nu$ control region . . . . .	167
6.8	Event yields summary in the $W \rightarrow \mu\nu$ control region . . . . .	168
6.9	Misidentification efficiencies without trigger requirement . . . . .	175
6.10	Misidentification efficiencies with the EF_tau20_medium1 trigger . . . . .	175
6.11	Misidentification efficiencies with the EF_tau29_medium1 trigger . . . . .	176
6.12	Event yields summary in the di-jet control region . . . . .	178
6.13	Tau identification transfer factors for 1-prong tau candidates . . . . .	180
6.14	Tau identification transfer factors for 3-prong tau candidates . . . . .	180
6.15	Final observed number of events and background predictions in the Drell-Yan validation region . . . . .	182
6.16	Systematic uncertainties for the DTT selection . . . . .	186
6.17	Systematic uncertainties for STT selection . . . . .	187

6.18	Modeling uncertainties (in %) for the b-associated production of neutral MSSM Higgs bosons using the Sherpa Monte Carlo event generator. . . . .	189
6.19	Modeling uncertainties (in %) for the production of neutral MSSM Higgs bosons in gluon-gluon fusion processes using the POWHEG Monte Carlo event generator. . . . .	190
6.20	Final observed number of events and background predictions for DTT and STT selection regions . . . . .	191
6.21	Event yields summary for the DTT selection region . . . . .	192
6.22	Event yields summary for the STT selection region . . . . .	192
6.23	Upper limit $\tan \beta$ values for the $m_h^{\max}$ benchmark scenario . . . . .	207
6.24	Observed number of events and post-fit background predictions for DTT and STT categories . . . . .	211
A.1	Tau identification observables for 1-prong . . . . .	220
A.2	Tau identification observables for multi-prong . . . . .	221
A.3	Final observed number of events and background predictions within the DTT validation regions . . . . .	226
A.4	Event yield summary in the DTT validation region . . . . .	227
A.5	Event yield summary in the STT validation region . . . . .	228
A.6	Fail-identification efficiencies without trigger requirement . . . . .	229
A.7	Fail-identification efficiencies with the EF_tau20_medium1 trigger . . . . .	230
A.8	Fail-identification efficiencies with the EF_tau29_medium1 trigger . . . . .	230
A.9	Event yields summary in the Drell-Yan validation region . . . . .	232
A.10	MSSM Higgs boson signal samples . . . . .	233
A.11	Samples for the $Z \rightarrow \tau\tau$ and $W \rightarrow \tau\nu$ production . . . . .	234
A.12	Samples for the $Z \rightarrow ll$ and $W \rightarrow l\nu$ production . . . . .	235
A.13	Samples for the $W \rightarrow qq' + \text{jets}$ and $top$ production . . . . .	236
A.14	Samples for the production of two gauge bosons . . . . .	237
A.15	Upper limit $\tan \beta$ values for the $m_h^{\text{mod-}}$ benchmark scenario . . . . .	238
A.16	Upper limit $\tan \beta$ values for the $m_h^{\text{mod+}}$ benchmark scenario . . . . .	239
A.17	Legend for the nuisance parameter. . . . .	242

# Bibliography

- [1] J. Thomson, *XL. Cathode Rays*, Philosophical Magazine Series 5 **44** (1897) no. 269, 293–316, <http://dx.doi.org/10.1080/14786449708621070>.
- [2] H. Geiger and E. Marsden, *On a Diffuse Reflection of the  $\alpha$ -Particles*, Proceedings of the Royal Society of London A: Mathematical, Physical and Engineering Sciences **82** (1909) no. 557, 495–500, <http://rspa.royalsocietypublishing.org/content/82/557/495>.
- [3] H. Geiger, *The Scattering of the  $\alpha$ -Particles by Matter*, Proceedings of the Royal Society of London A: Mathematical, Physical and Engineering Sciences **83** (1910) no. 565, 492–504, <http://rspa.royalsocietypublishing.org/content/83/565/492>.
- [4] E. Rutherford, *LXXIX. The scattering of  $\alpha$  and  $\beta$  particles by matter and the structure of the atom*, Philosophical Magazine Series 6 **21** (1911) no. 125, 669–688, <http://dx.doi.org/10.1080/14786440508637080>.
- [5] G. Arnison et al., *Experimental observation of isolated large transverse energy electrons with associated missing energy at  $\sqrt{s} = 540$  GeV*, Physics Letters B **122** (1983) no. 1, 103 – 116, <http://www.sciencedirect.com/science/article/pii/0370269383911772>.
- [6] UA2 Collaboration, M. Banner et al., *Observation of Single Isolated Electrons of High Transverse Momentum in Events with Missing Transverse Energy at the CERN anti-p p Collider*, Phys. Lett. **122B** (1983) 476–485.
- [7] UA1 Collaboration, G. Arnison et al., *Experimental Observation of Lepton Pairs of Invariant Mass Around 95-GeV/c\*\*2 at the CERN SPS Collider*, Phys. Lett. **126B** (1983) 398–410.
- [8] UA2 Collaboration, P. Bagnaia et al., *Evidence for  $Z^0 \rightarrow e^+e^-$  at the CERN anti-p p Collider*, Phys. Lett. **B129** (1983) 130–140.
- [9] CDF Collaboration, F. Abe et al., *Observation of top quark production in  $\bar{p}p$  collisions*, Phys. Rev. Lett. **74** (1995) 2626–2631, [arXiv:hep-ex/9503002](https://arxiv.org/abs/hep-ex/9503002) [hep-ex].
- [10] ATLAS Collaboration, G. Aad et al., *Observation of a new particle in the search for the Standard Model Higgs boson with the ATLAS detector at the LHC*, Phys. Lett. **B716** (2013) 1–29, [arXiv:1207.7214](https://arxiv.org/abs/1207.7214) [hep-ex].
- [11] CMS Collaboration, S. Chatrchyan et al., *Observation of a new boson at a mass of 125 GeV with the CMS experiment at the LHC*, Phys. Lett. **B716** (2013) 30–61, [arXiv:1207.7235](https://arxiv.org/abs/1207.7235) [hep-ex].
- [12] Particle Data Group Collaboration, C. Patrignani et al., *Review of Particle Physics*, Chin. Phys. **C40** (2016) no. 10, 100001.

- [13] B. N. Taylor and A. Thompson, *The International System of Units (SI)*. National Institute of Standards and Technology Special Publication 330 (2008 Edition). National Institute of Standards and Technology / U.S. Department of Commerce, 2008.
- [14] A. Thompson and B. N. Taylor, *Guide for the Use of the International System of Units (SI)*. National Institute of Standards and Technology Special Publication 811 (2008 Edition). National Institute of Standards and Technology / U.S. Department of Commerce, 2008.
- [15] M. Gell-Mann, *A Schematic Model of Baryons and Mesons*, Phys. Lett. **8** (1964) 214–215.
- [16] G. Zweig, *An  $SU_3$  model for strong interaction symmetry and its breaking; Version 2*, <https://cds.cern.ch/record/570209>. Version 1 is CERN preprint 8182/TH.401, Jan. 17, 1964.
- [17] H. D. Politzer, *Reliable Perturbative Results for Strong Interactions?*, Phys. Rev. Lett. **30** (1973) 1346–1349.
- [18] D. J. Gross and F. Wilczek, *Ultraviolet Behavior of Nonabelian Gauge Theories*, Phys. Rev. Lett. **30** (1973) 1343–1346.
- [19] H. Fritzsch, M. Gell-Mann, and H. Leutwyler, *Advantages of the Color Octet Gluon Picture*, Phys. Lett. **B47** (1973) 365–368.
- [20] S. L. Glashow, *Partial-symmetries of weak interactions*, Nuclear Physics **22** (1961) no. 4, 579 – 588.
- [21] S. Weinberg, *A Model of Leptons*, Phys. Rev. Lett. **19** (Nov, 1967) 1264–1266.
- [22] A. Salam, *Weak and Electromagnetic Interactions*, in *Elementary particle theory*, N. Svartholm, ed., pp. 367–377. Almquist & Wiksell.
- [23] J. R. Ellis, N. E. Mavromatos, and D. V. Nanopoulos, *Search for quantum gravity*, Gen. Rel. Grav. **31** (1999) 1257–1262, [arXiv:gr-qc/9905048](https://arxiv.org/abs/gr-qc/9905048) [gr-qc].
- [24] T. Thiemann, *Modern canonical quantum general relativity*. Cambridge University Press, 2008. [arXiv:gr-qc/0110034](https://arxiv.org/abs/gr-qc/0110034) [gr-qc].  
<http://www.cambridge.org/catalogue/catalogue.asp?isbn=9780521842631>.
- [25] C. Rovelli, *Quantum Gravity*. Cambridge Monographs on Mathematical Physics. Cambridge University Press, 2004.
- [26] P. W. Higgs, *Broken Symmetries and the Masses of Gauge Bosons*, Phys. Rev. Lett. **13** (1964) 508–509.
- [27] F. Englert and R. Brout, *Broken Symmetry and the Mass of Gauge Vector Mesons*, Phys. Rev. Lett. **13** (1964) 321–323.
- [28] G. S. Guralnik, C. R. Hagen, and T. W. B. Kibble, *Global Conservation Laws and Massless Particles*, Phys. Rev. Lett. **13** (1964) 585–587.



- [29] P. W. Higgs, *Spontaneous Symmetry Breakdown without Massless Bosons*, Phys. Rev. **145** (1966) 1156–1163.
- [30] T. W. B. Kibble, *Symmetry breaking in nonAbelian gauge theories*, Phys. Rev. **155** (1967) 1554–1561.
- [31] A. Djouadi, *The Anatomy of electro-weak symmetry breaking. I: The Higgs boson in the standard model*, Phys. Rept. **457** (2008) 1–216, [arXiv:hep-ph/0503172](#) [hep-ph].
- [32] SLD Electroweak Group, DELPHI, LEP, ALEPH, SLD Heavy Flavour Group, OPAL, LEP Electroweak Working Group, L3 Collaboration, *A Combination of preliminary electroweak measurements and constraints on the standard model*, [arXiv:hep-ex/0412015](#) [hep-ex].
- [33] OPAL, DELPHI, LEP Working Group for Higgs boson searches, ALEPH, L3 Collaboration, R. Barate et al., *Search for the standard model Higgs boson at LEP*, Phys. Lett. **B565** (2003) 61–75, [arXiv:hep-ex/0306033](#) [hep-ex].
- [34] CDF Collaboration and D0 Collaboration Collaboration, T. Aaltonen et al., *Evidence for a Particle Produced in Association with Weak Bosons and Decaying to a Bottom-Antibottom Quark Pair in Higgs Boson Searches at the Tevatron*, Phys. Rev. Lett. **109** (Aug, 2012) 071804, <http://link.aps.org/doi/10.1103/PhysRevLett.109.071804>.
- [35] ATLAS, CMS Collaboration, G. Aad et al., *Combined Measurement of the Higgs Boson Mass in  $pp$  Collisions at  $\sqrt{s} = 7$  and 8 TeV with the ATLAS and CMS Experiments*, Phys. Rev. Lett. **114** (2015) 191803, [arXiv:1503.07589](#) [hep-ex].
- [36] ATLAS, CMS Collaboration, G. Aad et al., *Measurements of the Higgs boson production and decay rates and constraints on its couplings from a combined ATLAS and CMS analysis of the LHC  $pp$  collision data at  $\sqrt{s} = 7$  and 8 TeV*, JHEP **08** (2016) 045, [arXiv:1606.02266](#) [hep-ex].
- [37] J. D. Bjorken and E. A. Paschos, *Inelastic Electron-Proton and  $\gamma$ -Proton Scattering and the Structure of the Nucleon*, Phys. Rev. **185** (Sep, 1969) 1975–1982.
- [38] S. Alekhin, J. Blumlein, S. Klein, and S. Moch, *The 3, 4, and 5-flavor NNLO Parton from Deep-Inelastic-Scattering Data and at Hadron Colliders*, Phys. Rev. **D81** (2010) 014032, [arXiv:0908.2766](#) [hep-ph].
- [39] T. Gleisberg, S. Hoeche, F. Krauss, M. Schonherr, S. Schumann, F. Siegert, and J. Winter, *Event generation with SHERPA 1.1*, JHEP **02** (2009) 007, [arXiv:0811.4622](#) [hep-ph].
- [40] S. Agostinelli and et al., *Geant4—a simulation toolkit*, Nuclear Instruments and Methods in Physics Research Section A: Accelerators, Spectrometers, Detectors and Associated Equipment **506** (2003) no. 3, 250 – 303.
- [41] J. Allison, *Geant4 developments and applications*, IEEE Trans. Nucl. Sci. **53** (2006) 270, <http://cds.cern.ch/record/1035669>.
- [42] ATLAS Collaboration Collaboration, *ATLAS Computing: technical design report*. Technical Design Report ATLAS. CERN, Geneva, 2005. <https://cds.cern.ch/record/837738>.

- [43] P. Mato, *Status of the GAUDI event-processing framework*,  
<https://cds.cern.ch/record/1745147>.
- [44] G. Barrand et al., *GAUDI - A software architecture and framework for building HEP data processing applications*, Comput. Phys. Commun. **140** (2001) 45–55.
- [45] ATLAS Collaboration, G. Aad et al., *The ATLAS Simulation Infrastructure*, Eur. Phys. J. **C70** (2010) 823–874, [arXiv:1005.4568](https://arxiv.org/abs/1005.4568) [physics.ins-det].
- [46] ATLAS Collaboration, Z. Marshall, *Simulation of Pile-up in the ATLAS Experiment*, J. Phys. Conf. Ser. **513** (2014) 022024.
- [47] J. Ellis, *The Physics Landscape after the Higgs Discovery at the LHC*, in *10th Latin American Symposium on High Energy Physics (SILAFAE 2014) Medellin, Colombia, November 24-28, 2014*. 2015. [arXiv:1504.03654](https://arxiv.org/abs/1504.03654) [hep-ph].
- [48] J. R. Espinosa and C. Grojean, *Implications of the Higgs boson discovery*, Comptes Rendus Physique **16** (2015) no. 4, 394 – 406,  
<http://www.sciencedirect.com/science/article/pii/S1631070515000675>. Highlights of the LHC run 1 / Résultats marquants de la première période d’exploitation du GCH.
- [49] J. P. Miller, E. de Rafael, and B. L. Roberts, *Muon ( $g-2$ ): Experiment and theory*, Rept. Prog. Phys. **70** (2007) 795, [arXiv:hep-ph/0703049](https://arxiv.org/abs/hep-ph/0703049) [hep-ph].
- [50] F. Jegerlehner and A. Nyffeler, *The Muon  $g-2$* , Phys. Rept. **477** (2009) 1–110, [arXiv:0902.3360](https://arxiv.org/abs/0902.3360) [hep-ph].
- [51] *Muon ( $g-2$ ): Experiment and Theory*, Annual Review of Nuclear and Particle Science **62** (2012) no. 1, 237–264, <http://dx.doi.org/10.1146/annurev-nucl-031312-120340>.
- [52] P. Fayet, *About the origins of the supersymmetric standard model*, Nucl. Phys. Proc. Suppl. **101** (2001) 81–98, [arXiv:hep-ph/0107228](https://arxiv.org/abs/hep-ph/0107228) [hep-ph]. [,81(2001)].
- [53] Yu. A. Golfand and E. P. Likhtman, *Extension of the Algebra of Poincare Group Generators and Violation of  $p$  Invariance*, JETP Lett. **13** (1971) 323–326. [Pisma Zh. Eksp. Teor. Fiz.13,452(1971)].
- [54] D. V. Volkov and V. P. Akulov, *Is the Neutrino a Goldstone Particle?*, Phys. Lett. **B46** (1973) 109–110.
- [55] S. Ferrara, B. Zumino, and J. Wess, *Supergauge multiplets and superfields*, Physics Letters B **51** (1974) no. 3, 239 – 241,  
<http://www.sciencedirect.com/science/article/pii/0370269374902834>.
- [56] P. Fayet, *Supersymmetry and weak, electromagnetic and strong interactions*, Physics Letters B **64** (1976) no. 2, 159 – 162,  
<http://www.sciencedirect.com/science/article/pii/0370269376903191>.
- [57] P. Fayet, *Spontaneously broken supersymmetric theories of weak, electromagnetic and strong interactions*, Physics Letters B **69** (1977) no. 4, 489 – 494,  
<http://www.sciencedirect.com/science/article/pii/0370269377908528>.

- [58] S. P. Martin, *A Supersymmetry primer*, [arXiv:hep-ph/9709356](#) [hep-ph]. [Adv. Ser. Direct. High Energy Phys.18,1(1998)].
- [59] A. Djouadi, *The Anatomy of electro-weak symmetry breaking. II. The Higgs bosons in the minimal supersymmetric model*, Phys. Rept. **459** (2008) 1–241, [arXiv:hep-ph/0503173](#) [hep-ph].
- [60] G. R. Farrar and P. Fayet, *Phenomenology of the Production, Decay, and Detection of New Hadronic States Associated with Supersymmetry*, Phys. Lett. **B76** (1978) 575–579.
- [61] S. Dimopoulos and D. W. Sutter, *The Supersymmetric flavor problem*, Nucl. Phys. **B452** (1995) 496–512, [arXiv:hep-ph/9504415](#) [hep-ph].
- [62] J. R. Espinosa and M. Quiros, *Gauge unification and the supersymmetric light Higgs mass*, Phys. Rev. Lett. **81** (1998) 516–519, [arXiv:hep-ph/9804235](#) [hep-ph].
- [63] ALEPH, DELPHI, L3, OPAL, LEP Working Group for Higgs Boson Searches Collaboration, S. Schael et al., *Search for neutral MSSM Higgs bosons at LEP*, Eur.Phys.J. **C47** (2006) 547–587, [arXiv:hep-ex/0602042](#) [hep-ex].
- [64] <https://twiki.cern.ch/twiki/bin/view/LHCPhysics/CrossSections>, (2015-10-20).
- [65] E. Bagnaschi, F. Frensch, S. Heinemeyer, G. Lee, S. R. Liebler, M. Muhlleitner, A. R. Mc Carn, J. Quevillon, N. Rompotis, P. Slavich, M. Spira, C. Wagner, and R. Wolf, *Benchmark scenarios for low  $\tan\beta$  in the MSSM*, Tech. Rep. LHCHSWG-2015-002, CERN, Geneva, Aug, 2015. <https://cds.cern.ch/record/2039911>.
- [66] M. Carena and H. E. Haber, *Higgs boson theory and phenomenology*, Prog. Part. Nucl. Phys. **50** (2003) 63–152, [arXiv:hep-ph/0208209](#) [hep-ph].
- [67] LHC Higgs Cross Section Working Group Collaboration, S. Dittmaier et al., *Handbook of LHC Higgs Cross Sections: 1. Inclusive Observables*, [arXiv:1101.0593](#) [hep-ph].
- [68] J. M. Campbell, R. K. Ellis, F. Maltoni, and S. Willenbrock, *Higgs-Boson production in association with a single bottom quark*, Phys. Rev. **D67** (2003) 095002, [arXiv:hep-ph/0204093](#) [hep-ph].
- [69] S. Dawson, C. B. Jackson, L. Reina, and D. Wackerroth, *Higgs boson production with one bottom quark jet at hadron colliders*, Phys. Rev. Lett. **94** (2005) 031802, [arXiv:hep-ph/0408077](#) [hep-ph].
- [70] M. Beccaria, G. O. Davier, G. Macorini, E. Mirabella, L. Panizzi, F. M. Renard, and C. Verzegnassi, *Semi-inclusive bottom-Higgs production at LHC: The complete one-loop electroweak effect in the MSSM*, Phys. Rev. **D82** (2010) 093018, [arXiv:1005.0759](#) [hep-ph].
- [71] S. Dawson and C. B. Jackson, *SUSY QCD Corrections to Associated Higgs-bottom Quark Production*, Phys. Rev. **D77** (2008) 015019, [arXiv:0709.4519](#) [hep-ph].
- [72] R. Harlander, M. Kramer, and M. Schumacher, *Bottom-quark associated Higgs-boson production: reconciling the four- and five-flavour scheme approach*, [arXiv:1112.3478](#) [hep-ph].

- [73] J. Guasch, W. Hollik, and S. Penaranda, *Distinguishing Higgs models in  $H \rightarrow b\bar{b}/H \rightarrow \tau^+\tau^-$* , Phys. Lett. **B515** (2001) 367–374, [arXiv:hep-ph/0106027 \[hep-ph\]](#).
- [74] G. Deggrasi, S. Heinemeyer, W. Hollik, P. Slavich, and G. Weiglein, *Towards high precision predictions for the MSSM Higgs sector*, Eur. Phys. J. **C28** (2003) 133–143, [arXiv:hep-ph/0212020 \[hep-ph\]](#).
- [75] M. Carena, S. Heinemeyer, O. Stål, C. E. M. Wagner, and G. Weiglein, *MSSM Higgs Boson Searches at the LHC: Benchmark Scenarios after the Discovery of a Higgs-like Particle*, Eur. Phys. J. **C73** (2013) no. 9, 2552, [arXiv:1302.7033 \[hep-ph\]](#).
- [76] M. Carena, S. Heinemeyer, C. E. M. Wagner, and G. Weiglein, *Suggestions for improved benchmark scenarios for Higgs boson searches at LEP-2*, in *Workshop on New Theoretical Developments for Higgs Physics at LEP-2 Geneva, Switzerland, October 27, 1999*. 1999. [arXiv:hep-ph/9912223 \[hep-ph\]](#).
- [77] M. Carena, S. Heinemeyer, C. E. M. Wagner, and G. Weiglein, *Suggestions for benchmark scenarios for MSSM Higgs boson searches at hadron colliders*, Eur. Phys. J. **C26** (2003) 601–607, [arXiv:hep-ph/0202167 \[hep-ph\]](#).
- [78] L. Evans and P. Bryant, *LHC Machine*, JINST **3** (2008) S08001.
- [79] S. Myers, *The LEP collider, from design to approval and commissioning*, 1991. <http://doc.cern.ch/cernrep/1991/91-08/91-08.html>.
- [80] ATLAS Collaboration, G. Aad et al., *The ATLAS Experiment at the CERN Large Hadron Collider*, JINST **3** (2008) S08003.
- [81] CMS Collaboration, S. Chatrchyan et al., *The CMS experiment at the CERN LHC*, JINST **3** (2008) S08004.
- [82] ALICE Collaboration, K. Aamodt et al., *The ALICE experiment at the CERN LHC*, JINST **3** (2008) S08002.
- [83] LHCb Collaboration, A. A. Alves, Jr. et al., *The LHCb Detector at the LHC*, JINST **3** (2008) S08005.
- [84] LHCf Collaboration, O. Adriani et al., *The LHCf detector at the CERN Large Hadron Collider*, JINST **3** (2008) S08006.
- [85] TOTEM Collaboration, G. Anelli et al., *The TOTEM experiment at the CERN Large Hadron Collider*, JINST **3** (2008) S08007.
- [86] J.-L. Caron, *LHC Layout.. Schema general du LHC.*, AC Collection. Legacy of AC. Pictures from 1992 to 2002., Sep, 1997.
- [87] R. R. Wilson, *The Tevatron*, Phys. Today **30N10** (1977) 23–30.
- [88] C. Lefèvre, *The CERN accelerator complex. Complexe des accélérateurs du CERN*, Dec, 2008.

- [89] J. Pequenaio, *Computer generated image of the whole ATLAS detector*, Mar, 2008.
- [90] ATLAS Collaboration Collaboration, L. E. Committee, *ATLAS inner detector: Technical Design Report, 1*. Technical Design Report ATLAS. CERN, Geneva, 1997. <http://cds.cern.ch/record/331063>.
- [91] ATLAS Collaboration Collaboration, S. Haywood, L. Rossi, R. Nickerson, and A. Romaniouk, *ATLAS inner detector: Technical Design Report, 2*. Technical Design Report ATLAS. CERN, Geneva, 1997. <http://cds.cern.ch/record/331064>.
- [92] G. Aad et al., *ATLAS pixel detector electronics and sensors*, JINST **3** (2008) P07007.
- [93] A. Ahmad et al., *The Silicon microstrip sensors of the ATLAS semiconductor tracker*, Nucl. Instrum. Meth. **A578** (2007) 98–118.
- [94] ATLAS TRT Collaboration, E. Abat et al., *The ATLAS Transition Radiation Tracker (TRT) proportional drift tube: Design and performance*, JINST **3** (2008) P02013.
- [95] ATLAS TRT Collaboration, E. Abat et al., *The ATLAS TRT barrel detector*, JINST **3** (2008) P02014.
- [96] E. Abat et al., *The ATLAS TRT end-cap detectors*, JINST **3** (2008) P10003.
- [97] M. Capeans, G. Darbo, K. Einsweiler, M. Elsing, T. Flick, M. Garcia-Sciveres, C. Gemme, H. Pernegger, O. Rohne, and R. Vuillemet, *ATLAS Insertable B-Layer Technical Design Report*, Tech. Rep. CERN-LHCC-2010-013. ATLAS-TDR-19, CERN, Geneva, Sep, 2010. <https://cds.cern.ch/record/1291633>.
- [98] ATLAS Collaboration Collaboration, *Particle Identification Performance of the ATLAS Transition Radiation Tracker*, Tech. Rep. ATLAS-CONF-2011-128, CERN, Geneva, Sep, 2011. <http://cds.cern.ch/record/1383793>.
- [99] ATLAS Collaboration, *ATLAS liquid argon calorimeter: Technical design report*, <http://cds.cern.ch/record/331061>.
- [100] ATLAS Collaboration, M. Aleksa et al., *Construction, assembly and tests of the ATLAS electromagnetic end-cap calorimeters*, JINST **3** (2008) P06002.
- [101] ATLAS Collaboration, *ATLAS tile calorimeter: Technical design report*, <http://cds.cern.ch/record/331062>.
- [102] D. M. Gingrich et al., *Construction, assembly and testing of the ATLAS hadronic end-cap calorimeter*, JINST **2** (2007) P05005.
- [103] A. Artamonov et al., *The ATLAS forward calorimeters*, JINST **3** (2008) P02010.
- [104] J. Pequenaio, *Computer Generated image of the ATLAS calorimeter*, Mar, 2008.
- [105] B. Aubert et al., *Development and construction of large size signal electrodes for the ATLAS electromagnetic calorimeter*, Nucl. Instrum. Meth. **A539** (2005) 558–594.
- [106] J. P. Rutherford, *Signal degradation due to charge buildup in noble liquid ionization calorimeters*, Nucl. Instrum. Meth. **A482** (2002) 156–178.

- [107] ATLAS Collaboration Collaboration, *ATLAS muon spectrometer: Technical Design Report*. Technical Design Report ATLAS. CERN, Geneva, 1997.  
<https://cds.cern.ch/record/331068>.
- [108] J. Pequeno, *Computer generated image of the ATLAS Muons subsystem*, Mar, 2008.
- [109] *ECFA-CERN Workshop on large hadron collider in the LEP tunnel, Lausanne and CERN, Geneva, Switzerland, 21-27 Mar 1984: Proceedings. 1*. 1984.  
<http://www.slac.stanford.edu/spires/find/books/www?cl=QCD183:E2:1984>.
- [110] M. Bajko et al., *Report of the Task Force on the Incident of 19th September 2008 at the LHC*, Tech. Rep. LHC-PROJECT-Report-1168. CERN-LHC-PROJECT-Report-1168, CERN, Geneva, Mar, 2009. <https://cds.cern.ch/record/1168025>.
- [111] R. Alemany-Fernandez, E. Bravin, L. Drosdal, A. Gorzawski, V. Kain, M. Lamont, A. Macpherson, G. Papotti, M. Pojer, L. Ponce, S. Redaelli, G. Roy, M. Solfaroli Camillocci, W. Venturini, and J. Wenninger, *Operation and Configuration of the LHC in Run 1*, <https://cds.cern.ch/record/1631030>.
- [112] ATLAS Collaboration, G. Aad et al., *Improved luminosity determination in pp collisions at  $\sqrt{s} = 7$  TeV using the ATLAS detector at the LHC*, Eur.Phys.J. **C73** (2013) no. 8, 2518, [arXiv:1302.4393 \[hep-ex\]](#).
- [113] ATLAS Collaboration, [https://twiki.cern.ch/twiki/bin/view/AtlasPublic/LuminosityPublicResults#Publications\\_and\\_Conference\\_Resu](https://twiki.cern.ch/twiki/bin/view/AtlasPublic/LuminosityPublicResults#Publications_and_Conference_Resu), (2016-04-19).
- [114] ATLAS Collaboration, *Performance of the ATLAS Inner Detector Track and Vertex Reconstruction in the High Pile-Up LHC Environment*, Tech. Rep. ATLAS-CONF-2012-042, CERN, Geneva, Mar, 2012. <https://cds.cern.ch/record/1435196>.
- [115] T. Cornelissen, M. Elsing, I. Gavrilenko, W. Liebig, E. Moyse, and A. Salzburger, *The new ATLAS track reconstruction (NEWT)*, J. Phys. Conf. Ser. **119** (2008) 032014.
- [116] G. Piacquadio, K. Prokofiev, and A. Wildauer, *Primary vertex reconstruction in the ATLAS experiment at LHC*, J. Phys. Conf. Ser. **119** (2008) 032033.
- [117] E. Abat et al., *Combined performance studies for electrons at the 2004 ATLAS combined test-beam*, JINST **5** (2010) P11006.
- [118] M. Aharrouche et al., *Measurement of the response of the ATLAS liquid argon barrel calorimeter to electrons at the 2004 combined test-beam*, Nucl. Instrum. Meth. **A614** (2010) 400–432.
- [119] J. Colas et al., *Response Uniformity of the ATLAS Liquid Argon Electromagnetic Calorimeter*, Nucl. Instrum. Meth. **A582** (2007) 429–455, [arXiv:0709.1094 \[physics.ins-det\]](#).
- [120] ATLAS Electromagnetic Barrel Calorimeter Collaboration, M. Aharrouche et al., *Energy linearity and resolution of the ATLAS electromagnetic barrel calorimeter in an electron test-beam*, Nucl. Instrum. Meth. **A568** (2006) 601–623, [arXiv:physics/0608012 \[physics\]](#).

- [121] P. Adragna et al., *Testbeam studies of production modules of the ATLAS tile calorimeter*, Nucl. Instrum. Meth. **A606** (2009) 362–394.
- [122] ATLAS Liquid Argon EMEC/HEC Collaboration, C. Cojocaru et al., *Hadronic calibration of the ATLAS liquid argon end-cap calorimeter in the pseudorapidity region  $1.6 < |\eta| < 1.8$  in beam tests*, Nucl. Instrum. Meth. **A531** (2004) 481–514, [arXiv:physics/0407009 \[physics\]](#).
- [123] J. Pinfold et al., *Performance of the ATLAS liquid argon endcap calorimeter in the pseudorapidity region  $2.5 < |\eta| < 4.0$  in beam tests*, Nucl. Instrum. Meth. **A593** (2008) 324–342.
- [124] M. Aharrouché et al., *Study of the response of ATLAS electromagnetic liquid argon calorimeters to muons*, Nucl. Instrum. Meth. **A606** (2009) 419–431.
- [125] ATLAS Collaboration, G. Aad et al., *Electron performance measurements with the ATLAS detector using the 2010 LHC proton-proton collision data*, Eur. Phys. J. **C72** (2012) 1909, [arXiv:1110.3174 \[hep-ex\]](#).
- [126] T. Barillari, E. Bergeaas Kuutmann, T. Carli, J. Erdmann, P. Giovannini, K. J. Grahm, C. Issever, A. Jantsch, A. Kiryunin, K. Lohwasser, A. Maslennikov, S. Menke, H. Oberlack, G. Pospelov, E. Rauter, P. Schacht, F. Spanó, P. Speckmayer, P. Stavina, and P. Strízenec, *Local Hadronic Calibration*, Tech. Rep. ATL-LARG-PUB-2009-001-2. ATL-COM-LARG-2008-006. ATL-LARG-PUB-2009-001, CERN, Geneva, Jun, 2008. <https://cds.cern.ch/record/1112035>. Due to a report-number conflict with another document, the report-number ATL-LARG-PUB-2009-001-2 has been assigned.
- [127] ATLAS Collaboration, *Jet energy measurement and its systematic uncertainty in proton-proton collisions at  $\sqrt{s} = 7$  TeV with the ATLAS detector*, Eur. Phys. J. **C 75** (2015) 17, [arXiv:1406.0076 \[hep-ex\]](#).
- [128] W. Lampl, S. Laplace, D. Lelas, P. Loch, H. Ma, S. Menke, S. Rajagopalan, D. Rousseau, S. Snyder, and G. Unal, *Calorimeter Clustering Algorithms: Description and Performance*, ATL-LARG-PUB-2008-002, ATL-COM-LARG-2008-003.
- [129] ATLAS Collaboration, *Electron reconstruction and identification efficiency measurements with the ATLAS detector using the 2011 LHC proton-proton collision data*, Eur. Phys. J. **C 74** (2014) 2941, [arXiv:1404.2240 \[hep-ex\]](#).
- [130] ATLAS Collaboration, *Electron and photon energy calibration with the ATLAS detector using LHC Run 1 data*, Eur. Phys. J. **C 74** (2014) 3071, [arXiv:1407.5063 \[hep-ex\]](#).
- [131] ATLAS Collaboration, *Measurement of the muon reconstruction performance of the ATLAS detector using 2011 and 2012 LHC proton-proton collision data*, Eur. Phys. J. **C 74** (2014) 3130, [arXiv:1407.3935 \[hep-ex\]](#).
- [132] M. Cacciari, G. P. Salam, and G. Soyez, *The Anti- $k(t)$  jet clustering algorithm*, JHEP **04** (2008) 063, [arXiv:0802.1189 \[hep-ph\]](#).

- [133] M. Cacciari, G. P. Salam, and G. Soyez, *FastJet User Manual*, Eur. Phys. J. **C72** (2012) 1896, [arXiv:1111.6097 \[hep-ph\]](#).
- [134] M. Cacciari and G. P. Salam, *Dispelling the  $N^3$  myth for the  $k_t$  jet-finder*, Phys. Lett. **B641** (2006) 57–61, [arXiv:hep-ph/0512210 \[hep-ph\]](#).
- [135] ATLAS Collaboration, G. Aad et al., *Jet energy measurement and its systematic uncertainty in proton-proton collisions at  $\sqrt{s} = 7$  TeV with the ATLAS detector*, Eur. Phys. J. **C75** (2015) 17, [arXiv:1406.0076 \[hep-ex\]](#).
- [136] ATLAS Collaboration, G. Aad et al., *Jet energy measurement with the ATLAS detector in proton-proton collisions at  $\sqrt{s} = 7$  TeV*, Eur. Phys. J. **C73** (2013) no. 3, 2304, [arXiv:1112.6426 \[hep-ex\]](#).
- [137] ATLAS Collaboration, *Jet energy resolution in proton-proton collisions at  $\sqrt{s} = 7$  TeV recorded in 2010 with the ATLAS detector*, Eur. Phys. J. C **73** (2013) 2306, [arXiv:1210.6210 \[hep-ex\]](#).
- [138] ATLAS Collaboration, <https://twiki.cern.ch/twiki/pub/AtlasPublic/JetEtmisApproved2013Jer2011/AntiKt4EMJES.png>, (2016-06-16).
- [139] ATLAS Collaboration, *Data-Quality Requirements and Event Cleaning for Jets and Missing Transverse Energy Reconstruction with the ATLAS Detector in Proton-Proton Collisions at a Center-of-Mass Energy of  $\sqrt{s} = 7$  TeV*, .
- [140] ATLAS Collaboration, P. Strizenec, *Performance of the ATLAS Liquid Argon Calorimeter after three years of LHC operation and plans for a future upgrade*, JINST **9** (2014) C09007.
- [141] ATLAS Collaboration, G. Aad et al., *Identification and energy calibration of hadronically decaying tau leptons with the ATLAS experiment in pp collisions at  $\sqrt{s}=8$  TeV*, [arXiv:1412.7086 \[hep-ex\]](#).
- [142] ATLAS Collaboration, *Performance of the Reconstruction and Identification of Hadronic Tau Decays in ATLAS with 2011 Data*, .
- [143] ATLAS Collaboration, *Determination of the tau energy scale and the associated systematic uncertainty in proton-proton collisions at  $\sqrt{s} = 7$  TeV with the ATLAS detector at the LHC in 2011*, Tech. Rep. ATLAS-CONF-2012-054, CERN, Geneva, Jun, 2012. <http://cds.cern.ch/record/1453781>.
- [144] L. Breiman, J. H. Friedman, R. A. Olshen, and C. J. Stone, *Classification and regression trees*. Wadsworth, Belmont, CA (1984) .
- [145] Y. Freund and R. E. Schapire, *A Decision-Theoretic Generalization of On-Line Learning and an Application to Boosting*, Journal of Computer and System Sciences **55** (1997) no. 1, 119 – 139.
- [146] ATLAS Collaboration, *Performance of the Reconstruction and Identification of Hadronic Tau Decays with ATLAS*, Tech. Rep. ATLAS-CONF-2011-152, CERN, Geneva, Nov, 2011. <https://cds.cern.ch/record/1398195>.



- [147] *Identification of the Hadronic Decays of Tau Leptons in 2012 Data with the ATLAS Detector*, Tech. Rep. ATLAS-CONF-2013-064, CERN, Geneva, Jul, 2013.  
<https://cds.cern.ch/record/1562839>.
- [148] T. Sjostrand, S. Mrenna, and P. Z. Skands, *A Brief Introduction to PYTHIA 8.1*, Comput. Phys. Commun. **178** (2008) 852–867, [arXiv:0710.3820](https://arxiv.org/abs/0710.3820) [hep-ph].
- [149] J. L. Hewett and T. G. Rizzo, *Low-energy phenomenology of superstring-inspired  $\{E6\}$  models*, Physics Reports **183** (1989) 193 – 381,  
<http://www.sciencedirect.com/science/article/pii/0370157389900719>.
- [150] M. Cvetič and S. Godfrey, *Discovery and identification of extra gauge bosons*, [arXiv:hep-ph/9504216](https://arxiv.org/abs/hep-ph/9504216) [hep-ph].
- [151] A. Leike, *The Phenomenology of extra neutral gauge bosons*, Phys.Rept. **317** (1999) 143–250, [arXiv:hep-ph/9805494](https://arxiv.org/abs/hep-ph/9805494) [hep-ph].
- [152] T. G. Rizzo,  *$Z'$  phenomenology and the LHC*, [arXiv:hep-ph/0610104](https://arxiv.org/abs/hep-ph/0610104) [hep-ph].
- [153] R. Diener, S. Godfrey, and T. A. Martin, *Unravelling an Extra Neutral Gauge Boson at the LHC using Third Generation Fermions*, Phys.Rev. **D83** (2011) 115008,  
[arXiv:1006.2845](https://arxiv.org/abs/1006.2845) [hep-ph].
- [154] P. Langacker, *The Physics of Heavy  $Z'$  Gauge Bosons*, Rev.Mod.Phys. **81** (2009) 1199–1228, [arXiv:0801.1345](https://arxiv.org/abs/0801.1345) [hep-ph].
- [155] A. Hoecker, P. Speckmayer, J. Stelzer, J. Therhaag, E. von Toerne, and H. Voss, *TMVA: Toolkit for Multivariate Data Analysis*, PoS **ACAT** (2007) 040, [arXiv:physics/0703039](https://arxiv.org/abs/physics/0703039).
- [156] R. Brun and F. Rademakers, ROOT — *An object oriented data analysis framework*, Nuclear Instruments and Methods in Physics Research Section A: Accelerators, Spectrometers, Detectors and Associated Equipment **389** (1997) no. 1–2, 81 – 86. New Computing Techniques in Physics Research V.
- [157] ATLAS Collaboration, G. Aad et al., *Performance of Missing Transverse Momentum Reconstruction in Proton-Proton Collisions at 7 TeV with ATLAS*, Eur. Phys. J. **C72** (2012) 1844, [arXiv:1108.5602](https://arxiv.org/abs/1108.5602) [hep-ex].
- [158] ATLAS Collaboration,  
[https://atlas.web.cern.ch/Atlas/GROUPS/PHYSICS/CombinedSummaryPlots/SM/ATLAS\\_a\\_SMSummary\\_TotalXsect/ATLAS\\_a\\_SMSummary\\_TotalXsect.pdf](https://atlas.web.cern.ch/Atlas/GROUPS/PHYSICS/CombinedSummaryPlots/SM/ATLAS_a_SMSummary_TotalXsect/ATLAS_a_SMSummary_TotalXsect.pdf),  
(2015-06-24).
- [159] ATLAS Collaboration, *Performance of the Minimum Bias Trigger in p-p Collisions at  $\sqrt{s} = 900$  GeV*, 2010. <https://cds.cern.ch/record/1277657>.
- [160] ATLAS Collaboration, *Performance of the Minimum Bias Trigger in p-p Collisions at  $\sqrt{s} = 7$  TeV*, 2010. <https://cds.cern.ch/record/1281343>.
- [161] A. Artikov, D. Chokheli, J. Huston, B. Miller, and M. Nessi, *Minimum bias scintillator counter geometry*, tech. rep., AT-GE-ES-0001, 2004.

- [162] ATLAS Collaboration, *Performance of the ATLAS Jet Trigger in the Early  $\sqrt{s} = 7$  TeV Data*, 2010. <https://cds.cern.ch/record/1299109>.
- [163] L. Ancu, M. Begel, M. Campanelli, R. Chislett, G. Kasieczka, J. McFayden, J. Miguens, and A. Sfyrla, *Inclusive Jet Trigger Efficiencies for the Early 2011 Data*, Tech. Rep. ATL-COM-DAQ-2011-031, CERN, Geneva, May, 2011. <https://cds.cern.ch/record/1351823>.
- [164] ATLAS Collaboration, [https://twiki.cern.ch/twiki/pub/AtlasPublic/JetTriggerPublicResults/EF\\_J50\\_j70\\_j75.png](https://twiki.cern.ch/twiki/pub/AtlasPublic/JetTriggerPublicResults/EF_J50_j70_j75.png), (2015-06-22).
- [165] ATLAS Collaboration, *Performance of the ATLAS muon trigger in 2011*, 2012. <https://cds.cern.ch/record/1462601>.
- [166] ATLAS Collaboration, *Performance of the ATLAS tau trigger in 2011*, 2013. <https://cds.cern.ch/record/1510157>.
- [167] R. Feynman, *The Behavior of Hadron Collisions at Extreme Energies*, in *Special Relativity and Quantum Theory*, M. Noz and Y. Kim, eds., vol. 33 of *Fundamental Theories of Physics*, pp. 289–304. Springer Netherlands, 1988.
- [168] R. K. Ellis, W. J. Stirling, and B. Webber, *QCD and collider physics*, Camb.Monogr.Part.Phys.Nucl.Phys.Cosmol. **8** (1996) 1–435.
- [169] H.-L. Lai, M. Guzzi, J. Huston, Z. Li, P. M. Nadolsky, J. Pumplin, and C. P. Yuan, *New parton distributions for collider physics*, Phys. Rev. **D82** (2010) 074024, [arXiv:1007.2241](https://arxiv.org/abs/1007.2241) [hep-ph].
- [170] CDF Collaboration, D. Acosta et al., *The underlying event in hard interactions at the Tevatron  $\bar{p}p$  collider*, Phys. Rev. **D70** (2004) 072002, [arXiv:hep-ex/0404004](https://arxiv.org/abs/hep-ex/0404004) [hep-ex].
- [171] CDF Collaboration, T. Aaltonen et al., *Studying the Underlying Event in Drell-Yan and High Transverse Momentum Jet Production at the Tevatron*, Phys. Rev. **D82** (2010) 034001, [arXiv:1003.3146](https://arxiv.org/abs/1003.3146) [hep-ex].
- [172] ATLAS Collaboration, G. Aad et al., *Measurement of underlying event characteristics using charged particles in  $pp$  collisions at  $\sqrt{s} = 900\text{ GeV}$  and 7 TeV with the ATLAS detector*, Phys.Rev. **D83** (2011) 112001, [arXiv:1012.0791](https://arxiv.org/abs/1012.0791) [hep-ex].
- [173] ATLAS Collaboration, G. Aad et al., *Measurements of underlying-event properties using neutral and charged particles in  $pp$  collisions at 900 GeV and 7 TeV with the ATLAS detector at the LHC*, Eur.Phys.J. **C71** (2011) 1636, [arXiv:1103.1816](https://arxiv.org/abs/1103.1816) [hep-ex].
- [174] ATLAS Collaboration, G. Aad et al., *Underlying event characteristics and their dependence on jet size of charged-particle jet events in  $pp$  collisions at  $\sqrt{s} = 7$  TeV with the ATLAS detector*, Phys.Rev. **D86** (2012) 072004, [arXiv:1208.0563](https://arxiv.org/abs/1208.0563) [hep-ex].
- [175] ATLAS Collaboration, G. Aad et al., *Measurements of the pseudorapidity dependence of the total transverse energy in proton-proton collisions at  $\sqrt{s} = 7$  TeV with ATLAS*, JHEP **1211** (2012) 033, [arXiv:1208.6256](https://arxiv.org/abs/1208.6256) [hep-ex].

- [176] ALICE Collaboration, B. Abelev et al., *Underlying Event measurements in pp collisions at  $\sqrt{s} = 0.9$  and 7 TeV with the ALICE experiment at the LHC*, JHEP **07** (2012) 116, [arXiv:1112.2082 \[hep-ex\]](#).
- [177] CMS Collaboration, S. Chatrchyan et al., *Measurement of the Underlying Event Activity at the LHC with  $\sqrt{s} = 7$  TeV and Comparison with  $\sqrt{s} = 0.9$  TeV*, JHEP **09** (2011) 109, [arXiv:1107.0330 \[hep-ex\]](#).
- [178] CMS Collaboration, S. Chatrchyan et al., *Measurement of the underlying event activity in pp collisions at  $\sqrt{s} = 0.9$  and 7 TeV with the novel jet-area/median approach*, JHEP **08** (2012) 130, [arXiv:1207.2392 \[hep-ex\]](#).
- [179] CMS Collaboration, S. Chatrchyan et al., *Measurement of the underlying event in the Drell-Yan process in proton-proton collisions at  $\sqrt{s} = 7$  TeV*, Eur. Phys. J. **C72** (2012) 2080, [arXiv:1204.1411 \[hep-ex\]](#).
- [180] CMS Collaboration, S. Chatrchyan et al., *Study of the underlying event at forward rapidity in pp collisions at  $\sqrt{s} = 0.9, 2.76$ , and 7 TeV*, JHEP **04** (2013) 072, [arXiv:1302.2394 \[hep-ex\]](#).
- [181] CMS Collaboration, S. Chatrchyan et al., *Jet and underlying event properties as a function of charged-particle multiplicity in proton-proton collisions at  $\sqrt{s} = 7$  TeV*, Eur. Phys. J. **C73** (2013) no. 12, 2674, [arXiv:1310.4554 \[hep-ex\]](#).
- [182] CMS Collaboration, V. Khachatryan et al., *Measurement of the underlying event activity using charged-particle jets in proton-proton collisions at  $\sqrt{s} = 2.76$  TeV*, <https://cds.cern.ch/record/2037726>. Comments: Submitted to JHEP.
- [183] ATLAS Collaboration, G. Aad et al., *Measurement of the underlying event in jet events from 7 TeV proton-proton collisions with the ATLAS detector*, Eur.Phys.J. **C74** (2014) no. 8, 2965, [arXiv:1406.0392 \[hep-ex\]](#).
- [184] *ATLAS Run 1 Pythia8 tunes*, Tech. Rep. ATL-PHYS-PUB-2014-021, CERN, Geneva, Nov, 2014. <https://cds.cern.ch/record/1966419>.
- [185] ATLAS Collaboration, G. Aad et al., *Measurement of the inclusive jet cross-section in proton-proton collisions at  $\sqrt{s} = 7$  TeV using 4.5 fb<sup>-1</sup> of data with the ATLAS detector*, JHEP **1502** (2015) 153, [arXiv:1410.8857 \[hep-ex\]](#).
- [186] ATLAS Collaboration, G. Aad et al., *Measurement of dijet cross sections in pp collisions at 7 TeV centre-of-mass energy using the ATLAS detector*, JHEP **1405** (2014) 059, [arXiv:1312.3524 \[hep-ex\]](#).
- [187] ATLAS Collaboration, G. Aad et al., *Charged-particle multiplicities in pp interactions measured with the ATLAS detector at the LHC*, New J.Phys. **13** (2011) 053033, [arXiv:1012.5104 \[hep-ex\]](#).
- [188] T. Sjostrand, S. Mrenna, and P. Z. Skands, *PYTHIA 6.4 Physics and Manual*, JHEP **05** (2006) 026, [arXiv:hep-ph/0603175 \[hep-ph\]](#).

- [189] M. Bahr et al., *Herwig++ Physics and Manual*, Eur. Phys. J. **C58** (2008) 639–707, [arXiv:0803.0883 \[hep-ph\]](#).
- [190] G. Corcella, I. G. Knowles, G. Marchesini, S. Moretti, K. Odagiri, P. Richardson, M. H. Seymour, and B. R. Webber, *HERWIG 6: An Event generator for hadron emission reactions with interfering gluons (including supersymmetric processes)*, JHEP **01** (2001) 010, [arXiv:hep-ph/0011363 \[hep-ph\]](#).
- [191] J. M. Butterworth, J. R. Forshaw, and M. H. Seymour, *Multiparton interactions in photoproduction at HERA*, Z. Phys. **C72** (1996) 637–646, [arXiv:hep-ph/9601371 \[hep-ph\]](#).
- [192] M. L. Mangano, M. Moretti, F. Piccinini, R. Pittau, and A. D. Polosa, *ALPGEN, a generator for hard multiparton processes in hadronic collisions*, JHEP **07** (2003) 001, [arXiv:hep-ph/0206293 \[hep-ph\]](#).
- [193] P. Nason, *A New method for combining NLO QCD with shower Monte Carlo algorithms*, JHEP **11** (2004) 040, [arXiv:hep-ph/0409146 \[hep-ph\]](#).
- [194] S. Frixione, P. Nason, and C. Oleari, *Matching NLO QCD computations with Parton Shower simulations: the POWHEG method*, JHEP **11** (2007) 070, [arXiv:0709.2092 \[hep-ph\]](#).
- [195] S. Alioli, P. Nason, C. Oleari, and E. Re, *A general framework for implementing NLO calculations in shower Monte Carlo programs: the POWHEG BOX*, JHEP **06** (2010) 043, [arXiv:1002.2581 \[hep-ph\]](#).
- [196] A. Sherstnev and R. S. Thorne, *Parton Distributions for LO Generators*, Eur. Phys. J. **C55** (2008) 553–575, [arXiv:0711.2473 \[hep-ph\]](#).
- [197] ATLAS Collaboration, *New ATLAS event generator tunes to 2010 data*, <https://cds.cern.ch/record/1345343>.
- [198] HERWIG++ Collaboration, *HERWIG++ minimum-bias and underlying-event tunes*, [https://herwig.hepforge.org/trac/wiki/MB\\_\\_UE\\_\\_tunes](https://herwig.hepforge.org/trac/wiki/MB__UE__tunes).
- [199] ATLAS Collaboration, *Summary of ATLAS Pythia 8 tunes*, <https://cds.cern.ch/record/1474107>.
- [200] CTEQ Collaboration, H. L. Lai, J. Huston, S. Kuhlmann, J. Morfin, F. I. Olness, J. F. Owens, J. Pumplin, and W. K. Tung, *Global QCD analysis of parton structure of the nucleon: CTEQ5 parton distributions*, Eur. Phys. J. **C12** (2000) 375–392, [arXiv:hep-ph/9903282 \[hep-ph\]](#).
- [201] P. Z. Skands, *Tuning Monte Carlo generators: the Perugia Tunes*, Phys. Rev. D **82** (2010) 074018, [arXiv:1005.3457](#). Perugia 2011 tunes described in arXiv update.
- [202] CDF Collaboration, R. Field, *CDF Run II Monte-Carlo tunes*, in *TeV4LHC 2006 Workshop 4th meeting Batavia, Illinois, October 20-22, 2006*. 2006. [http://lss.fnal.gov/cgi-bin/find\\_paper.pl?pub-06-408](http://lss.fnal.gov/cgi-bin/find_paper.pl?pub-06-408).

- [203] A. Sherstnev and R. Thorne, *Different PDF approximations useful for LO Monte Carlo generators*, [arXiv:0807.2132](#).
- [204] S. Gieseke, C. A. Rohr, and A. Siodmok, *Multiple Partonic Interaction Developments in Herwig++*, [arXiv:1110.2675 \[hep-ph\]](#).
- [205] ATLAS Collaboration, *First tuning of HERWIG/JIMMY to ATLAS data*, <https://cds.cern.ch/record/1303025>.
- [206] J. Pumplin, D. R. Stump, J. Huston, H. L. Lai, P. M. Nadolsky, and W. K. Tung, *New generation of parton distributions with uncertainties from global QCD analysis*, JHEP **07** (2002) 012, [arXiv:hep-ph/0201195 \[hep-ph\]](#).
- [207] I. Nedelkov, *Improper problems in computational physics*, Computer Physics Communications **4** (1972) no. 2, 157 – 164.
- [208] V. Blobel, *An Unfolding method for high-energy physics experiments*, in *Advanced statistical techniques in particle physics. Proceedings, Conference, Durham, UK, March 18-22, 2002*, pp. 258–267. 2002. [arXiv:hep-ex/0208022 \[hep-ex\]](#).
- [209] J. W. Monk and C. Oropeza-Barrera, *The HBOM Method for Unfolding Detector Effects*, Nucl. Instrum. Meth. **A701** (2013) 17–24, [arXiv:1111.4896 \[hep-ex\]](#).
- [210] A. Hocker and V. Kartvelishvili, *SVD approach to data unfolding*, Nucl. Instrum. Meth. **A372** (1996) 469–481, [arXiv:hep-ph/9509307 \[hep-ph\]](#).
- [211] G. D’Agostini, *A Multidimensional unfolding method based on Bayes’ theorem*, Nucl. Instrum. Meth. **A362** (1995) 487–498.
- [212] B. Wynne, *ImagiRO: an implementation of Bayesian iterative unfolding for high energy physics*, ArXiv e-prints (Mar., 2012) , [arXiv:1203.4981 \[physics.data-an\]](#).
- [213] T. Adye, *Unfolding algorithms and tests using RooUnfold*, ArXiv e-prints (May, 2011) , [arXiv:1105.1160 \[physics.data-an\]](#).
- [214] F. Colecchia, J. Monk, E. Nurse, R. Prabhu, and P. Wijeratne, *Validation of the calorimeter energy response with  $\pi^0 \rightarrow \gamma\gamma$  candidates*, Tech. Rep. ATL-COM-CAL-2011-003, CERN, Geneva, Aug, 2011. <https://cds.cern.ch/record/1377411>.
- [215] A. Buckley, *Soft QCD in ATLAS: Measurements and modelling of multi-parton interactions*, Acta Phys. Polon. **B42** (2011) 2669–2696, [arXiv:1112.5477 \[hep-ph\]](#).
- [216] ATLAS Collaboration, G. Aad et al., *Measurement of distributions sensitive to the underlying event in inclusive Z-boson production in pp collisions at  $\sqrt{s} = 7$  TeV with the ATLAS detector*, Eur.Phys.J. **C74** (2014) no. 12, 3195, [arXiv:1409.3433 \[hep-ex\]](#).
- [217] CDF, D0 Collaboration, T. Aaltonen et al., *Search for Neutral Higgs Bosons in Events with Multiple Bottom Quarks at the Tevatron*, Phys. Rev. **D86** (2012) 091101, [arXiv:1207.2757 \[hep-ex\]](#).

- [218] Tevatron New Phenomena Higgs Working Group Collaboration, D. Benjamin et al., *Combined CDF and D0 Upper Limits on MSSM Higgs Boson Production in tau-tau Final States with up to 2.2 fb<sup>-1</sup>*, [arXiv:1003.3363](#) [[hep-ex](#)].
- [219] CDF Collaboration, A. Abulencia et al., *Search for charged Higgs bosons from top quark decays in  $p\bar{p}$  collisions at  $\sqrt{s} = 1.96$ -TeV.*, Phys. Rev. Lett. **96** (2006) 042003, [arXiv:hep-ex/0510065](#) [[hep-ex](#)].
- [220] D0 Collaboration Collaboration, V. M. Abazov et al., *Search for charged Higgs bosons in decays of top quarks*, Phys. Rev. D **80** (Sep, 2009) 051107.
- [221] CDF, D0 Collaboration, T. Aaltonen et al., *Higgs Boson Studies at the Tevatron*, Phys. Rev. **D88** (2013) no. 5, 052014, [arXiv:1303.6346](#) [[hep-ex](#)].
- [222] ATLAS Collaboration Collaboration, G. Aad et al., *Search for neutral MSSM Higgs bosons decaying to  $\tau^+\tau^-$  pairs in proton-proton collisions at  $\sqrt{s} = 7$  TeV with the ATLAS detector*, Phys. Lett. B **705** (Jul, 2011) 174–192. 20 p, <http://cds.cern.ch/record/1370459>.
- [223] ATLAS Collaboration, *Search for the neutral Higgs bosons of the Minimal Supersymmetric Standard Model in  $pp$  collisions at  $\sqrt{s} = 7$  TeV with the ATLAS detector*, JHEP **1302** (2013) 095, [arXiv:1211.6956](#) [[hep-ex](#)].
- [224] ATLAS Collaboration, G. Aad et al., *Search for neutral Higgs bosons of the minimal supersymmetric standard model in  $pp$  collisions at  $\sqrt{s} = 8$  TeV with the ATLAS detector*, JHEP **11** (2014) 056, [arXiv:1409.6064](#) [[hep-ex](#)].
- [225] *Search for Neutral Minimal Supersymmetric Standard Model Higgs Bosons  $H/A \rightarrow \tau\tau$  produced in  $pp$  collisions at  $\sqrt{s} = 13$  TeV with the ATLAS Detector*, Tech. Rep. ATLAS-CONF-2015-061, CERN, Geneva, Dec, 2015. <https://cds.cern.ch/record/2114827>.
- [226] S. Dittmaier et al., *Handbook of LHC Higgs Cross Sections: 2. Differential Distributions*, [arXiv:1201.3084](#) [[hep-ph](#)].
- [227] LHC Higgs Cross Section Working Group Collaboration, J. R. Andersen et al., *Handbook of LHC Higgs Cross Sections: 3. Higgs Properties*, [arXiv:1307.1347](#) [[hep-ph](#)].
- [228] M. Spira, *HIGLU: A program for the calculation of the total Higgs production cross-section at hadron colliders via gluon fusion including QCD corrections*, [arXiv:hep-ph/9510347](#) [[hep-ph](#)].
- [229] R. V. Harlander and W. B. Kilgore, *Next-to-next-to-leading order Higgs production at hadron colliders*, Phys. Rev. Lett. **88** (2002) 201801, [arXiv:hep-ph/0201206](#) [[hep-ph](#)].
- [230] R. V. Harlander and W. B. Kilgore, *Production of a pseudoscalar Higgs boson at hadron colliders at next-to-next-to leading order*, JHEP **10** (2002) 017, [arXiv:hep-ph/0208096](#) [[hep-ph](#)].
- [231] R. V. Harlander and W. B. Kilgore, *Higgs boson production in bottom quark fusion at next-to-next-to leading order*, Phys. Rev. **D68** (2003) 013001, [arXiv:hep-ph/0304035](#) [[hep-ph](#)].

- [232] S. Dittmaier, M. Kramer, 1, and M. Spira, *Higgs radiation off bottom quarks at the Tevatron and the CERN LHC*, Phys. Rev. **D70** (2004) 074010, [arXiv:hep-ph/0309204 \[hep-ph\]](#).
- [233] A. Djouadi, J. Kalinowski, and M. Spira, *HDECAY: A Program for Higgs boson decays in the standard model and its supersymmetric extension*, Comput. Phys. Commun. **108** (1998) 56–74, [arXiv:hep-ph/9704448 \[hep-ph\]](#).
- [234] M. Spira, *QCD effects in Higgs physics*, Fortsch. Phys. **46** (1998) 203–284, [arXiv:hep-ph/9705337 \[hep-ph\]](#).
- [235] J. M. Butterworth et al., *THE TOOLS AND MONTE CARLO WORKING GROUP Summary Report from the Les Houches 2009 Workshop on TeV Colliders*, in *Physics at TeV colliders. Proceedings, 6th Workshop, dedicated to Thomas Binoth, Les Houches, France, June 8-26, 2009*. 2010. [arXiv:1003.1643 \[hep-ph\]](#).
- [236] S. Heinemeyer, W. Hollik, and G. Weiglein, *FeynHiggs: A Program for the calculation of the masses of the neutral CP even Higgs bosons in the MSSM*, Comput. Phys. Commun. **124** (2000) 76–89, [arXiv:hep-ph/9812320 \[hep-ph\]](#).
- [237] S. Heinemeyer, W. Hollik, and G. Weiglein, *The Masses of the neutral CP - even Higgs bosons in the MSSM: Accurate analysis at the two loop level*, Eur. Phys. J. **C9** (1999) 343–366, [arXiv:hep-ph/9812472 \[hep-ph\]](#).
- [238] M. Frank, T. Hahn, S. Heinemeyer, W. Hollik, H. Rzehak, and G. Weiglein, *The Higgs Boson Masses and Mixings of the Complex MSSM in the Feynman-Diagrammatic Approach*, JHEP **02** (2007) 047, [arXiv:hep-ph/0611326 \[hep-ph\]](#).
- [239] T. Hahn, S. Heinemeyer, W. Hollik, H. Rzehak, and G. Weiglein, *FeynHiggs: A program for the calculation of MSSM Higgs-boson observables – Version 2.6.5*, Computer Physics Communications **180** (2009) no. 8, 1426 – 1427.
- [240] R. Hamberg, W. van Neerven, and T. Matsuura, *A complete calculation of the order  $\alpha_s^2$  correction to the Drell-Yan K-factor*, Nuclear Physics B **359** (1991) no. 2, 343 – 405.
- [241] C. Anastasiou, L. J. Dixon, K. Melnikov, and F. Petriello, *High precision QCD at hadron colliders: Electroweak gauge boson rapidity distributions at NNLO*, Phys. Rev. **D69** (2004) 094008, [arXiv:hep-ph/0312266 \[hep-ph\]](#).
- [242] S. Frixione and B. R. Webber, *Matching NLO QCD computations and parton shower simulations*, JHEP **06** (2002) 029, [arXiv:hep-ph/0204244 \[hep-ph\]](#).
- [243] S. Frixione, P. Nason, and B. R. Webber, *Matching NLO QCD and parton showers in heavy flavor production*, JHEP **08** (2003) 007, [arXiv:hep-ph/0305252 \[hep-ph\]](#).
- [244] S. Frixione, E. Laenen, P. Motylinski, and B. R. Webber, *Single-top production in MC@NLO*, JHEP **03** (2006) 092, [arXiv:hep-ph/0512250 \[hep-ph\]](#).
- [245] P. M. Nadolsky, H.-L. Lai, Q.-H. Cao, J. Huston, J. Pumplin, D. Stump, W.-K. Tung, and C. P. Yuan, *Implications of CTEQ global analysis for collider observables*, Phys. Rev. **D78** (2008) 013004, [arXiv:0802.0007 \[hep-ph\]](#).

- [246] M. Aliev, H. Lacker, U. Langenfeld, S. Moch, P. Uwer, and M. Wiedermann, *HATHOR: HAdronic Top and Heavy quarks crOss section calculatoR*, Comput. Phys. Commun. **182** (2011) 1034–1046, [arXiv:1007.1327 \[hep-ph\]](#).
- [247] B. P. Kersevan and E. Richter-Was, *The Monte Carlo event generator AcerMC versions 2.0 to 3.8 with interfaces to PYTHIA 6.4, HERWIG 6.5 and ARIADNE 4.1*, Comput. Phys. Commun. **184** (2013) 919–985, [arXiv:hep-ph/0405247 \[hep-ph\]](#).
- [248] N. Kidonakis, *Next-to-next-to-leading-order collinear and soft gluon corrections for t-channel single top quark production*, Phys. Rev. **D83** (2011) 091503, [arXiv:1103.2792 \[hep-ph\]](#).
- [249] N. Kidonakis, *Two-loop soft anomalous dimensions for single top quark associated production with a W- or H-*, Phys. Rev. **D82** (2010) 054018, [arXiv:1005.4451 \[hep-ph\]](#).
- [250] N. Kidonakis, *NNLL resummation for s-channel single top quark production*, Phys. Rev. **D81** (2010) 054028, [arXiv:1001.5034 \[hep-ph\]](#).
- [251] J. M. Campbell, R. K. Ellis, and F. Tramontano, *Single top production and decay at next-to-leading order*, Phys. Rev. **D70** (2004) 094012, [arXiv:hep-ph/0408158 \[hep-ph\]](#).
- [252] J. M. Campbell and F. Tramontano, *Next-to-leading order corrections to Wt production and decay*, Nucl. Phys. **B726** (2005) 109–130, [arXiv:hep-ph/0506289 \[hep-ph\]](#).
- [253] T. Binoth, M. Ciccolini, N. Kauer, and M. Kramer, *Gluon-induced W-boson pair production at the LHC*, JHEP **12** (2006) 046, [arXiv:hep-ph/0611170 \[hep-ph\]](#).
- [254] T. Binoth, N. Kauer, and P. Mertsch, *Gluon-induced QCD corrections to  $pp \rightarrow ZZ \rightarrow \ell\bar{\ell}\ell'\bar{\ell}'$* , in *Proceedings, 16th International Workshop on Deep Inelastic Scattering and Related Subjects (DIS 2008)*, p. 142. 2008. [arXiv:0807.0024 \[hep-ph\]](#).
- [255] J. M. Campbell, E. Castaneda-Miranda, Y. Fang, N. Kauer, B. Mellado, and S. L. Wu, *Normalizing Weak Boson Pair Production at the Large Hadron Collider*, Phys. Rev. **D80** (2009) 054023, [arXiv:0906.2500 \[hep-ph\]](#).
- [256] S. Jadach, J. H. Kuhn, and Z. Was, *TAUOLA: A Library of Monte Carlo programs to simulate decays of polarized tau leptons*, Comput. Phys. Commun. **64** (1990) 275–299.
- [257] E. Barberio, B. van Eijk, and Z. Was, *PHOTOS: A Universal Monte Carlo for QED radiative corrections in decays*, Comput. Phys. Commun. **66** (1991) 115–128.
- [258] A. Elagin, P. Murat, A. Pranko, and A. Safonov, *A New Mass Reconstruction Technique for Resonances Decaying to di-tau*, Nucl. Instrum. Meth. **A654** (2011) 481–489, [arXiv:1012.4686 \[hep-ex\]](#).
- [259] C. J. Clopper and E. S. Pearson, *The Use of Confidence or Fiducial Limits Illustrated in the Case of the Binomial*, Biometrika **26** (1934) no. 4, 404–413.
- [260] A. Buckley, J. Butterworth, L. Lonnblad, D. Grellscheid, H. Hoeth, J. Monk, H. Schulz, and F. Siegert, *Rivet user manual*, Comput. Phys. Commun. **184** (2013) 2803–2819, [arXiv:1003.0694 \[hep-ph\]](#).



- [261] ROOT Collaboration Collaboration, K. Cranmer, G. Lewis, L. Moneta, A. Shibata, and W. Verkerke, *HistFactory: A tool for creating statistical models for use with RooFit and RooStats*, Tech. Rep. CERN-OPEN-2012-016, New York U., New York, Jan, 2012. <https://cds.cern.ch/record/1456844>.
- [262] R. J. Barlow and C. Beeston, *Fitting using finite Monte Carlo samples*, Comput. Phys. Commun. **77** (1993) 219–228.
- [263] W. Verkerke and D. Kirkby, *The RooFit toolkit for data modeling*, ArXiv Physics e-prints (June, 2003) , [physics/0306116](#).
- [264] G. Cowan, K. Cranmer, E. Gross, and O. Vitells, *Asymptotic formulae for likelihood-based tests of new physics*, Eur. Phys. J. **C71** (2011) 1554, [arXiv:1007.1727](#) [[physics.data-an](#)]. [Erratum: Eur. Phys. J.C73,2501(2013)].
- [265] A. Wald, *Tests of Statistical Hypotheses Concerning Several Parameters When the Number of Observations is Large*, Transactions of the American Mathematical Society **54** (1943) no. 3, 426–482, <http://www.jstor.org/stable/1990256>.
- [266] A. L. Read, *Presentation of search results: The CL(s) technique*, J. Phys. **G28** (2002) 2693–2704. [,11(2002)].
- [267] O. Behnke, K. Kröninger, T. Schörner-Sadenius, and G. Schott, eds., *Data analysis in high energy physics*. Wiley-VCH, Weinheim, Germany, 2013.
- [268] ATLAS Collaboration, M. Aaboud et al., *Search for Minimal Supersymmetric Standard Model Higgs bosons H/A and for a Z' boson in the  $\tau\tau$  final state produced in pp collisions at  $\sqrt{s} = 13$  TeV with the ATLAS Detector*, Eur. Phys. J. **C76** (2016) no. 11, 585, [arXiv:1608.00890](#) [[hep-ex](#)].
- [269] ATLAS Collaboration Collaboration, *Search for Minimal Supersymmetric Standard Model Higgs Bosons H/A in the  $\tau\tau$  final state in up to  $13.3\text{ fb}^{-1}$  of pp collisions at  $\sqrt{s} = 13$  TeV with the ATLAS Detector*, Tech. Rep. ATLAS-CONF-2016-085, CERN, Geneva, Aug, 2016. <http://cds.cern.ch/record/2206278>.
- [270] A. Djouadi, L. Maiani, A. Polosa, J. Quevillon, and V. Riquer, *Fully covering the MSSM Higgs sector at the LHC*, JHEP **06** (2015) 168, [arXiv:1502.05653](#) [[hep-ph](#)].
- [271] A. Djouadi, L. Maiani, G. Moreau, A. Polosa, J. Quevillon, and V. Riquer, *The post-Higgs MSSM scenario: Habemus MSSM?*, Eur. Phys. J. **C73** (2013) 2650, [arXiv:1307.5205](#) [[hep-ph](#)].



# Danksagung

Ich möchte mich an dieser Stelle bei den vielen Menschen bedanken die mich während meiner Promotionszeit begleitet haben und ohne ich diese Arbeit nie hätte schaffen können.

Mein besonderer Dank gilt dabei meinem Doktorvater Prof. Arno Straessner, welcher mich nicht nur ermutigt hat auf dem Gebiet zu promovieren, sondern mich auch während der gesamten Zeit mit viel Geduld und Einsatz unterstützt hat.

Die Arbeit am Institut war vor allem durch eine freundliche und besonders humorvolle Atmosphäre ausgezeichnet, die während der gesamten Promotionszeit erhalten blieb. Ein derart nettes Arbeitsumfeld ist keineswegs immer selbstverständlich und umso mehr habe ich die Jahre im Institut genossen. Ich möchte mich bei der Gelegenheit bei meinen Kollegen und Freunden, insbesondere von der „Tau Arbeitsgruppe“ bedanken, mit denen ich mit viel Humor den Arbeitsalltag gemeistert habe und dir mir während der Zeit mit Rat und Tat zur Seite standen: Dirk, Lorentz, David, Felix, Marcus, Stefanie, Phillip, Wolfgang, Frank, Steffen, Christian und viele weitere. Ein besonderer Dank gilt dabei Prof. Michael Kobel sowie den vielen weiteren Kollegen welche das Institut am Laufen gehalten haben, unter anderem Tatjana, Kristin, Frau Schöler, Uta und Nicole.

Mit einer der schönsten Seiten der Promotion war die Zusammenarbeit mit den vielen unterschiedlichen Menschen aus allen Teilen der Welt, auch innerhalb von CERN und ATLAS. Bedanken möchte ich mich hierbei bei der underlying event Arbeitsgruppe, mit denen ich nicht nur während meiner Zeit als Diplomand gearbeitet habe, sondern insbesondere auch am Anfang meiner Doktorarbeitszeit: Deepak Kar, Andy Buckley und Benjamin Wynne. Ein weiterer Dank gilt den vielen Menschen denen ich während meiner Zusammenarbeit in der Tau, Higgs und SoftQCD - Arbeitsgruppe begegnet bin.

Last but not least, möchte ich mich noch bei meinen Eltern und Großeltern, meinem Bruder und meinen Freunden bedanken. Ohne euch hätte ich diese Arbeit nicht schaffen können.

Sebastian Wahrmund



# Versicherung

Hiermit versichere ich, dass ich die vorliegende Arbeit ohne unzulässige Hilfe Dritter und ohne Benutzung anderer als der angegebenen Hilfsmittel angefertigt habe; die aus fremden Quellen direkt oder indirekt übernommenen Gedanken sind als solche kenntlich gemacht. Die Arbeit wurde bisher weder im Inland noch im Ausland in gleicher oder ähnlicher Form einer anderen Prüfungsbehörde vorgelegt.

Die vorliegende Dissertation wurde am Institut für Kern- und Teilchenphysik der Technischen Universität Dresden unter der wissenschaftlichen Betreuung von Prof. Dr. Arno Straessner angefertigt.

Es haben keine früheren erfolglosen Promotionsverfahren stattgefunden.

Ich erkenne die Promotionsordnung der Fakultät Mathematik und Naturwissenschaften an der Technischen Universität Dresden vom 23.02.2011 in der Fassung vom 18.06.2014 an.

Dresden, den

---

*Dipl. Phys. Sebastian Wahrmund*